

# Investigation of Calmodulin/Target Interactions by Mass Spectrometry

Dissertation

zur Erlangung des  
Doktorgrades der Naturwissenschaften (Dr. rer. nat.)

vorgelegt der  
Naturwissenschaftlichen Fakultät I – Biowissenschaften

**Martin-Luther-Universität Halle-Wittenberg**



von Sabine Herbst

(geborene Schaks)

geboren am 10.06.1984 in Merseburg

Gutachter: 1. Prof. Dr. Andrea Sinz  
2. Prof. Dr. Gary Sawers  
3. Prof. Dr. Simone König

Datum der öffentlichen Verteidigung: 04.02.2014

# Table of Contents

Table of Contents	I
Abbreviations	V
List of Figures	VIII
Summary	1
1. INTRODUCTION	3
1.1. Biological Background	3
1.1.1. Calmodulin	4
1.1.2. Calmodulin Binding Motifs	5
1.1.3. Calmodulin Target Proteins Used in this Work	6
1.1.3.1. The Munc13 Protein Family and Synaptic Plasticity	6
1.1.3.2. Skeletal Muscle Myosin Light Chain Kinase	10
1.1.3.3. Adenylyl Cyclases 1 and 8	12
1.1.4. Orai1 and STIM1 - Additional Interaction Partners of AC8	13
1.2. Structural Investigation of Protein-Protein Interactions	15
1.2.1. Chemical Cross-Linking and Mass Spectrometry	15
1.2.1.1. Chemical Cross-Linking with Homobifunctional Cross-linkers	18
1.2.1.2. Chemical Cross-Linking with Heterobifunctional Cross-linkers	20
1.2.1.3. Structural Investigations with Photo-Reactive Amino Acids	21
1.2.2. Mass Spectrometry	22
1.2.2.1. MALDI-TOF Mass Spectrometry	22
1.2.2.2. ESI-LTQ-Orbitrap Mass Spectrometry	24
1.2.3. Circular Dichroism Spectroscopy	27
1.2.4. Isothermal Titration Calorimetry	29
1.2.5. Surface Plasmon Resonance Spectroscopy	30
1.2.6. Fluorescence (Förster) Resonance Energy Transfer	31
	I

2. MATERIAL &METHODS	33
2.1. Material	33
2.1.1. Plasmids	33
2.1.2. Oligonucleotides	34
2.1.3. Bacterial Strains and Human Cell Lines	35
2.1.4. Media and Antibiotics	36
2.1.5. Buffer Solutions	36
2.1.6. Enzymes	37
2.1.7. Proteins and Peptides	37
2.1.8. Cross-linking and Biotinylation Reagents	38
2.1.9. Chemicals	38
2.1.10. Kits	40
2.1.11. Equipment	40
2.1.12. Software	42
2.2. Molecular Biology Techniques	43
2.2.1. Preparation of Chemo-Competent Cells	43
2.2.2. Transformation of DNA in Chemo-Competent Cells	43
2.2.3. Isolation of Plasmid DNA from <i>E.coli</i>	43
2.2.4. Polymerase Chain Reaction	43
2.2.5. Site-directed Mutagenesis	44
2.2.6. DNA Digestion with Restriction Endonucleases	45
2.2.7. Agarose Gel Electrophoresis	45
2.2.8. Gel Extraction of DNA	45
2.2.9. Ligation	45
2.2.10. Sequencing	46
2.3. Cell Biology Techniques	46
2.3.1. Cell Culture and Transfection	46
2.3.1. Micro-FRET Analysis of Protein-Protein Interactions	46

2.4. Protein Chemistry	47
2.4.1. Expression of Munc13 Variants	47
2.4.2. Purification of Munc13 Variants	47
2.4.3. Buffer Exchange of Protein and Peptide Solutions	48
2.4.4. SDS-PAGE	48
2.4.5. <i>In-Gel</i> Digestion	49
2.4.6. Circular Dichroism Spectroscopy	50
2.4.7. Isothermal Titration Calorimetry	50
2.4.8. Surface Plasmon Resonance Spectroscopy	50
2.5. Chemical Cross-linking and Mass Spectrometric Analysis	51
2.5.1. Chemical Cross-linking with Homobifunctional Reagents	51
2.5.2. Chemical Cross-linking with Heterobifunctional Reagents	52
2.5.3. MALDI-TOF Mass Spectrometry	52
2.5.4. Nano-HPLC/MALDI-TOF/TOF Mass Spectrometry	52
2.5.5. Nano-HPLC/Nano-ESI-LTQ-Orbitrap Mass Spectrometry	53
2.5.6. <i>Offline</i> Nano-ESI Mass Spectrometry	53
2.5.7. Identification of Cross-linked Products	54
2.5.8. Modeling of CaM/Target Peptide Complexes	54
3. RESULTS	56
3.1. CaM/Munc13 Interaction	56
3.1.1. Structural Investigation of CaM/Munc13 Peptide Complexes	56
3.1.2. Expression and Purification of Munc13 Domains	64
3.1.2.1. Expression and Purification of bMunc13-2 and Munc13-3 Domains	65
3.1.2.2. Expression and Purification of Munc13-1 and ubMunc13-2 Domains	70
3.1.3. Cross-links between Munc13 Domains and CaM	71
3.1.4. Introduction of Bpa-Encoding Amber Stop Codons into Munc13	74
3.2. CaM/skMLCK Interaction	77
3.2.1. Circular Dichroism Spectroscopy	78

## Table of Contents

---

3.2.2. Cross-links between CaM and skMLCK Peptide Variants	79
3.2.3. Surface Plasmon Resonance Spectroscopy	84
3.3. Interaction of Adenylyl Cyclases with CaM and Orai1/STIM1	86
3.3.1. CaM Binding to AC1 and AC8	86
3.3.1.1. Circular Dichroism Spectroscopy	87
3.3.1.2. Isothermal Titration Calorimetry Measurements	88
3.3.1.3. <i>Offline</i> Nano-ESI-MS	89
3.3.1.4. Chemical Cross-linking of CaM and AC1/AC8 Peptides	91
3.3.2. Interaction of AC8 with Orai1 and STIM1	98
3.3.2.1. Fluorescence (Förster) Resonance Energy Transfer Experiments	98
4. DISCUSSION AND OUTLOOK	102
4.1. CaM/Munc13 Interaction	102
4.2. CaM/skMLCK Interaction	105
4.3. CaM/AC1 and AC8 Interaction	107
4.4. AC8/Orai1 and STIM1 Interaction	109
APPENDIX	i
Tables	i
Figures	ix
REFERENCES	xxiv
ACKNOWLEDGEMENT	xxxvi
PUBLICATIONS	xxxviii

## Abbreviations

AC	Adenylyl cyclase
ACN	Acetonitrile
AGC	Automatic gain control
amp <sup>R</sup>	Ampicilline resistance
API	Atmospheric pressure ionization
APS	Ammonium persulfate
bp	Base pair
Bpa	<i>p</i> -Benzoylphenylalanine
BS2G	Bis (sulfosuccinimidyl) glutarate
BS3	Bis (sulfosuccinimidyl) suberate
BSA	Bovine serum albumin
Ca <sup>2+</sup>	calcium/calcium ion
CaM	Calmodulin
CD	Circular dichroism
CFP	Cyan fluorescent protein
CID	Collision-induced dissociation
CMC	Critical micelle concentration
CRAC	Ca <sup>2+</sup> -release activated Ca <sup>2+</sup> current
CRM	Charged-residue model
C-Trap	Curved ion trap
Da	Dalton
DAG	Diacylglycerol
DC	Direct current
DDM	<i>n</i> -Dodecyl- $\beta$ - <i>D</i> -maltoside
DHB	2,5-Dihydroxybenzoic acid
DMSO	Dimethyl sulfoxide
DNA	Desoxyribonucleic acid
DTT	1,4-Dithiothreitol
<i>E. coli</i>	<i>Escherichia coli</i>
E <sub>kin</sub>	Kinetic energy
ER	Endoplasmatic reticulum
ESI	Electrospray ionization
FPLC	Fast protein liquid chromatography

## Abbreviations

---

FRET	Fluorescence (Förster) resonance energy transfer
FT	Fourier transformation
GST	Glutathione-S-transferase
IEM	Ion evaporation model
IPTG	<i>D</i> -Isopropylthiogalactose
ISD	In-source decay
ITC	Isothermal titration calorimetry
HCCA	$\alpha$ -Cyano-4-hydroxy cinnamic acid
HEK	Human embryonic kidney
HEPES	[4-(2-hydroxyethyl) piperazine] ethanesulfonic acid
HPLC	High performance liquid chromatography
$K_D$	Equilibrium dissociation constant
kDa	Kilodalton
LB	Lysogeny broth
LID	Laser-induced dissociation
LIFT	Laser-induced fragmentation technology (Bruker Daltonik)
LTQ	Linear triple quadrupole (Thermo Fisher Scientific)
MALDI	Matrix-assisted laser desorption/ionization
MEM	Minimal essential medium
MHD	Munc homology domain
MS	Mass spectrometry / Mass spectrometer / Mass spectrum
MS/MS	Tandem mass spectrometry
<i>m/z</i>	Mass-to-charge ratio
NFRET <sup>C</sup>	normalized and corrected FRET value
NHS	<i>N</i> -Hydroxysuccinimide
NMR	Nuclear magnetic resonance
OD	Optical density
ori	Origin of replication
PAGE	Polyacrylamide gel electrophoresis
PAL	Photo-affinity labeling
PBS	Phosphate buffered saline
PCR	Polymerase chain reaction
pdb	Protein data bank
PSD	Post-source decay

## Abbreviations

---

RF	Radio frequency
RMSD	Root mean square deviation
(t)RNA	(transfer) Ribonucleic acid
RP	Reversed phase
RU	Biacore response unit
SA	Sinapinic acid
Sulfo-SDA	Sulfosuccinimidyl 4,4'-azipentanoate
SDS	Sodium dodecyl sulfate
skMLCK	Skeletal muscle myosin light chain kinase
SNARE	Soluble <i>N</i> -ethylmaleimide-sensitive-factor attachment receptor
SOC	Store-operated Ca <sup>2+</sup>
SOCE	Store-operated Ca <sup>2+</sup> entry
SPR	Surface plasmon resonance
STD	Short-term depression
STE	Short-term enhancement
STIM1	Stromal interaction molecule 1
STP	Short-term plasticity
TEMED	<i>N,N,N',N'</i> -Tetramethylethylenediamine
TFA	Trifluoroacetic acid
TFE	2,2,2-Trifluoroethanol
TIC	Total ion current
TIS	Timed ion selector
TOF	Time-of-flight
Tris	Tris (hydroxymethyl) aminomethane
XL	Cross-link/Cross-linker
YFP	Yellow fluorescent protein

### *Proteinogenic amino acids*

Alanine Ala A	Glutamic acid Glu E	Methionine Met M	Tyrosine Tyr Y
Arginine Arg R	Glycine Gly G	Phenylalanine Phe F	Valine Val V
Asparagine Asn N	Histidine His H	Proline Pro P	
Aspartic acid Asp D	Isoleucine Ile I	Serine Ser S	
Cysteine Cys C	Leucine Leu L	Threonine Thr T	
Glutamine Gln Q	Lysine Lys K	Tryptophan Trp W	



## List of Figures

Figure 1. Amino acid sequence and 3D-structure of calmodulin. ....	4
Figure 2. CaM-binding motifs.....	6
Figure 3. Synaptic vesicle cycle.....	7
Figure 4. Domain structure of Munc13 proteins. ....	8
Figure 5. CaM/Munc13 binding motifs.....	9
Figure 6. Myosin light chain kinase (MLCK) function in muscle contraction. ....	10
Figure 7. Structure of the CaM/M13 peptide complex.....	11
Figure 8. Predicted structure of the AC family. ....	12
Figure 9. Store-operated Ca <sup>2+</sup> entry in response to store depletion. ....	14
Figure 10. Cross-linking strategies for structural investigation of proteins or protein complexes. ....	16
Figure 11. Reaction mechanism of amine-reactive sulfo-NHS ester cross-linkers. ....	17
Figure 12. Reaction mechanism of benzophenone cross-linkers. ....	17
Figure 13. Reaction scheme of a cross-linking reaction with homobifunctional cross-linkers. ....	18
Figure 14. Nomenclature of CID fragment ions according to <i>Roepstorff and Schilling</i> . ....	19
Figure 15. Reaction scheme of a cross-linking reaction with heterobifunctional cross-linkers. ....	20
Figure 16. Photo-reactive amino acids. ....	21
Figure 17. Schematic design of MALDI-TOF/TOF MS (Bruker Daltonik). ....	23
Figure 18. Electrospray ionization (ESI).....	25
Figure 19. Schematic design of the LTQ-OrbitrapXL mass spectrometer. ....	26
Figure 20. Far-UV CD spectra of different poly-Lys conformations. ....	28
Figure 21. Schematic set-up of a power compensating ITC. ....	29
Figure 22. Set-up of a surface plasmon resonance (SPR) sensor. ....	31
Figure 23. Munc13 peptides and cross-linking reaction scheme of SBC.....	57
Figure 24. SDS-PAGE analysis of CaM/Munc13-3 peptide cross-linking reactions.....	58
Figure 25. MALDI-TOF-MS of cross-linking reactions between CaM and the Munc13-3 peptide. ....	59
Figure 26. SDS-PAGE analysis of CaM/Munc13 cross-linking reactions.....	60
Figure 27. MS and MS/MS analysis of a cross-linked product between CaM and the bMunc13-2 peptide.....	62
Figure 28. Structures of CaM/Munc13 peptide complexes.....	63
Figure 29. Munc13 constructs.....	65
Figure 30. GST affinity purification of the GST-bMunc13-2 domain. ....	66
Figure 31. Thrombin cleavage of GST-Munc13. ....	67
Figure 32. FPLC chromatogram of a combined GST affinity and anion exchange purification.....	68
Figure 33. SDS-PAGE analysis after on-column thrombin cleavage of bMunc13-2 and Munc13-3 domains. ....	69
Figure 34. Cross-linking between bMunc13-2 and Munc13-3 domains and CaM. ....	71
Figure 35. MS and MS/MS analysis of a cross-linked product between CaM and bMunc13-2. ....	73
Figure 36. CD spectra of skMLCK peptide variants.....	78
Figure 37. SDS-PAGE of cross-linking reactions between CaM and the skMLCK F19E/L31W peptide.....	80

## List of Figures

---

Figure 38. MS and MS/MS analysis of a cross-linking reaction between CaM and the skMLCK F19E/L31W peptide. ....	82
Figure 39. Identified cross-linked products between CaM and the skMLCK F19E/L31W peptide. ....	83
Figure 40. Analysis of the binding of CaM to the skMLCK peptides by SPR.....	85
Figure 41. Schematic presentation of CaM binding to AC8. ....	86
Figure 42. Amino acid sequences of the AC peptides used in this work. ....	87
Figure 43. CD spectra of AC peptides. ....	88
Figure 44. ITC analysis of the CaM/AC8-Nt peptide interaction. ....	89
Figure 45. Interaction between CaM and AC peptides. ....	90
Figure 46. SDS-PAGE analysis of cross-linking reaction mixtures between CaM and AC peptides. ....	93
Figure 47. MS and MS/MS analysis of a cross-linking reaction between CaM and the AC8-Nt peptide.....	95
Figure 48. Model structures of the CaM/AC8 peptide complexes. ....	96
Figure 49. Detailed presentation of the binding of AC8 peptides to CaM. ....	97
Figure 50. FRET analysis of the interaction between YFP-AC8 and Orai1-CFP truncation variants. ....	99
Figure 51. FRET analysis of the interaction between STIM1-YFP / YFP-AC8 and CFP-tagged Orai isoforms. ....	101
Figure A1. Fragment ion mass spectrum of a cross-link between CaM and Munc13-1. ....	ix
Figure A2. Fragment ion mass spectrum of a cross-link between CaM and ubMunc13-2. ....	x
Figure A3. Fragment ion mass spectrum of a cross-link between CaM and Munc13-3. ....	x
Figure A4. Sequence of the GST-bMunc13-2 domain.....	xi
Figure A5. Sequence of the GST-Munc13-3 domain.....	xi
Figure A6. Cross-linking experiment between and CaM and GST-Munc13 domains.....	xii
Figure A7. SDS-PAGE analysis of cross-linking reactions between CaM and different skMLCK peptide variants. ....	xii
Figure A8. Fragment ion mass spectrum of a cross-link between CaM and the skMLCK peptide. ....	xiii
Figure A9. Identified cross-linked products between CaM and the skMLCK peptide. ....	xiv
Figure A10. Identified cross-linked products between CaM and the skMLCK F19A peptide. ....	xv
Figure A11. Identified cross-linked products between CaM and the skMLCK F19E peptide.....	xvi
Figure A12. Fragment ion mass spectrum of a cross-link between CaM and the skMLCK F19A peptide. ....	xvii
Figure A13. Fragment ion mass spectrum of a cross-link between CaM and the skMLCK F19E peptide.....	xviii
Figure A14. <i>Offline</i> nano-ESI-MS of a solution containing CaM and both AC8 peptides. ....	xix
Figure A15. Scheme of cross-linking reactions using sulfo-SDA.....	xix
Figure A16. MALDI-TOF-MS analysis of cross-linking reaction mixtures between CaM and AC peptides. ....	xx
Figure A17. Fragment ion mass spectrum of a cross-link between CaM and the AC8-C2b peptide. ....	xxi
Figure A18. ITC analysis of the interaction between CaM and the AC1-C1b peptide. ....	xxii
Figure A19. FRET between Orai1-CFP and STIM1-YFP. ....	xxiii
Figure A20. FRET between YFP-AC8 and Orai1-CFP in the presence of HA-STIM1. ....	xxiii

## List of Tables

Table 1. Synthetic oligonucleotides for sequencing.....	34
Table 2. Synthetic oligonucleotides for cloning.....	34
Table 3. Synthetic oligonucleotides for site directed mutagenesis.....	35
Table 4. PCR program for DNA amplification. ....	44
Table 5. Components of a 50 $\mu$ l-PCR reaction for site-directed mutagenesis.....	44
Table 6. Composition of resolving and stacking gels for SDS-PAGE.....	49
Table 7. Munc13 variants containing the amber stop codon.....	75
Table A1. CaM and CaM/target peptide complexes used in molecular modeling studies.....	i
Table A2. Intermolecular cross-links between CaM and Munc13 peptides.....	ii
Table A3. Intramolecular cross-links within CaM.....	iii
Table A4. Cross-linking sites identified between CaM and the skMLCK peptide. ....	iv
Table A5. Cross-linking sites identified between CaM and the skMLCK F19A peptide. ....	v
Table A6. Cross-linking sites identified between CaM and the skMLCK F19E peptide.....	vi
Table A7. Cross-linking sites identified between CaM and the skMLCK F19E/L31W peptide. ....	vii
Table A8. Cross-linking sites identified between CaM and the AC8-Nt peptide.....	vii
Table A9. Cross-linking sites identified between CaM and the AC8-C2b peptide.....	viii
Table A10. Cross-linking sites identified between CaM and both AC8 peptides.....	viii

## Summary

Investigation of protein-protein interactions to elucidate networks of signaling pathways is a key issue in biological research. A detailed knowledge about particular interactions and their impact on signal transduction is important for the development of new drugs. One prominent signaling molecule is calmodulin (CaM), a highly conserved  $\text{Ca}^{2+}$ -sensing protein that plays a role in a wide range of cellular processes. Therefore, analyzing the interactions between CaM and its target proteins is essential for a deeper understanding of  $\text{Ca}^{2+}$ -mediated regulation of signaling processes.

One set of CaM targets is the family of Munc13 proteins, which are key mediators of presynaptic short-term plasticity (STP) and are essential for vesicle priming. CaM complexes with short 21-amino acid peptides comprising the CaM-binding regions of the two homologous Munc13 isoforms, Munc13-1 and ubMunc13-2, were found to have a structure comparable to that of the complex between CaM and an NO synthase peptide. Chemical cross-linking in combination with high-resolution mass spectrometry (MS) was used to investigate the structure of CaM complexes formed with peptides representing the CaM-binding regions of the two other Munc13 isoforms, bMunc13-2 and Munc13-3. These experiments demonstrated a common CaM-binding mode for short peptides of all four Munc13 isoforms, which are characterized by a 1-5-8 CaM-binding motif and an antiparallel orientation of the Munc13 peptide in the CaM/peptide complex. Overexpression of larger Munc13 domains surrounding the CaM-binding regions and initial cross-linking studies of bMunc13-2 and CaM gave no hints on additional interaction sites between bMunc13-2 and CaM, apart from the confirmed CaM-binding motif.

Recently, a more extended CaM conformation was observed in the complex with longer 34-amino acid peptides of Munc13-1 and ubMunc13-2. A *C*-terminal elongation of the short Munc13 peptides containing a 1-5-8 CaM-binding motif had revealed an additional interaction site between a hydrophobic tryptophan at position 26 of the motif and the *N*-terminal domain of CaM, inducing an extended conformation of CaM within the CaM/peptide complex that had only been found in Munc13 so far. Given that short peptides are usually used in structural investigations of CaM/peptide complexes, which represent the minimal CaM-binding region, the question arises whether an extended CaM conformation can be induced within any CaM/peptide complex by simple *C*-terminal elongation of these CaM-binding peptides. Therefore, four peptides comprising the CaM-binding region of the skeletal

muscle myosin light chain kinase (skMLCK) were used in cross-linking experiments and surface plasmon resonance (SPR) spectroscopy measurements, demonstrating that C-terminal elongation of the skMLCK CaM-binding sequence does not induce a structure of CaM in the CaM/peptide complex comparable to that of Munc13. Additional amino acid exchanges in the skMLCK peptide at positions 14 and 26 of the CaM-binding motif to resemble the respective amino acids in the Munc13 motif showed that the 1-5-8-26 motif of Munc13 cannot be introduced in skMLCK peptides.

The third CaM interaction examined herein is the binding of CaM to adenylyl cyclases (AC) 1 and 8. Although both enzymes share a common predicted domain structure as well as their stimulation by CaM, the mechanism of CaM regulation differs between both proteins. In contrast to only one CaM-binding motif in AC1, AC8 exhibits two CaM-binding sites - one in the N-terminal region and one in the C-terminal C2b domain. A model had been proposed on the basis of recent findings describing the N-terminus of AC8 as CaM trap that binds to CaM even at resting  $\text{Ca}^{2+}$  concentrations, which increases the local CaM concentration in the environment of the C-terminal CaM-binding motif of AC8. Upon rising  $\text{Ca}^{2+}$  concentrations, CaM also binds to the C2b domain of AC8 and, thereby, activates the cAMP production of the enzyme. Using a combinatorial approach of circular dichroism (CD) spectroscopy, chemical cross-linking in combination with MS, and isothermal titration calorimetry (ITC) with two AC8 peptides comprising the CaM-binding regions of AC8, this model was supported by structural and thermodynamic information. From these experiments there is no evidence for a CaM complex with both AC8 peptides binding simultaneously, as had been hypothesized.

The interaction of AC8 with proteins in the plasma membrane and the ER was investigated by fluorescence (Förster) resonance energy transfer (FRET) measurements. AC8 is specifically stimulated by increasing  $\text{Ca}^{2+}$  concentrations resulting from store-operated  $\text{Ca}^{2+}$  entry (SOCE). Proteins involved in this process, Orai1 and STIM1, were thought to co-localize and interact with AC8, either directly or indirectly. In this study, AC8 binding to Orai1 was demonstrated to occur through their N-terminal regions. An additional interaction site in the transmembrane regions of both proteins was proposed on the basis of FRET experiments with a second isoform of the Orai protein family (Orai2). Furthermore, FRET measurements showed the influence of STIM1 on AC8/Orai1 binding.

# 1. INTRODUCTION

In their natural environment, most proteins are components of large protein complexes and networks, mediating functions such as signal transduction (1), modulation of protein activity (2) or conversion of energy into physical motion (3-4). Different methods have been developed to screen for, and to characterize, protein-protein interactions: examples include co-immunoprecipitation (co-IP) (5), yeast-two hybrid screening (6-7), tandem-affinity purification (TAP) (8), surface plasmon resonance (SPR) spectroscopy (9), isothermal titration calorimetry (ITC) (10), fluorescence (Förster) resonance energy transfer (FRET) (11), cryo-electron microscopy (12), nuclear magnetic resonance (NMR) spectroscopy (13-14), and X-ray crystallography (15-16), as well as chemical cross-linking in combination with mass spectrometry (MS) (17-19). Using these methods, our general understanding of biological processes in living cells has increased dramatically over the last few years. A detailed knowledge about the interplay of proteins within large protein networks is one of the most important issues to understand diseases and to develop novel drugs. In this work, the interaction of calmodulin (CaM), an important  $\text{Ca}^{2+}$ -sensor, with different target proteins was investigated. In order to extend existing knowledge in this field, in particular with regard to how  $\text{Ca}^{2+}$  signals are converted into various biochemical cellular responses, complementary biochemical and biophysical methods were used.

## 1.1. Biological Background

One of the most important signaling molecules in the cell is the calcium ion ( $\text{Ca}^{2+}$ ). The calcium concentration differs between the extra- and intracellular milieu by a factor of  $10^4$ , providing the potential for a  $\text{Ca}^{2+}$  influx through regulated channels and pumps upon specific stimuli (20). Free  $\text{Ca}^{2+}$  that streams into the cytoplasm is only available as a signaling molecule for a very short time before it is bound by different proteins or is transported into intracellular stores or outside the cell. This transient increase of the  $\text{Ca}^{2+}$  concentration induces a variety of biochemical changes such as vesicle exo- and endocytosis (synapses) (21-22), muscle contraction (muscle cells) (4) or activation of kinases (23) and phosphatases (24). Some of these processes are regulated directly by  $\text{Ca}^{2+}$  itself, whereas others are mediated by  $\text{Ca}^{2+}$ -binding proteins. A range of proteins is known, which bind  $\text{Ca}^{2+}$  in different ways and, therefore, are able to sense  $\text{Ca}^{2+}$  concentrations in their environment. Among these proteins,

CaM is a prominent example of a  $\text{Ca}^{2+}$  sensor, interacting with hundreds of target proteins and converting the  $\text{Ca}^{2+}$  signal into various cellular responses (25).

### 1.1.1. Calmodulin

Calmodulin (*calcium modulated protein*, CaM) was first discovered in 1970 by Cheung (26) and Kakiuchi (27) as a  $\text{Ca}^{2+}$ -sensing protein in the brain. In the following decades, the knowledge about CaM dramatically increased, as it was structurally characterized (28-30) and found to interact with a wide variety of target proteins. The amino acid sequence of CaM (Figure 1A) is evolutionarily highly conserved with 100% identity among all vertebrates (31-34) and only a few amino acid substitutions in fungi, plants, and invertebrates (e.g., 96% identity of vertebrate CaM with that of *C.elegans* (31)).

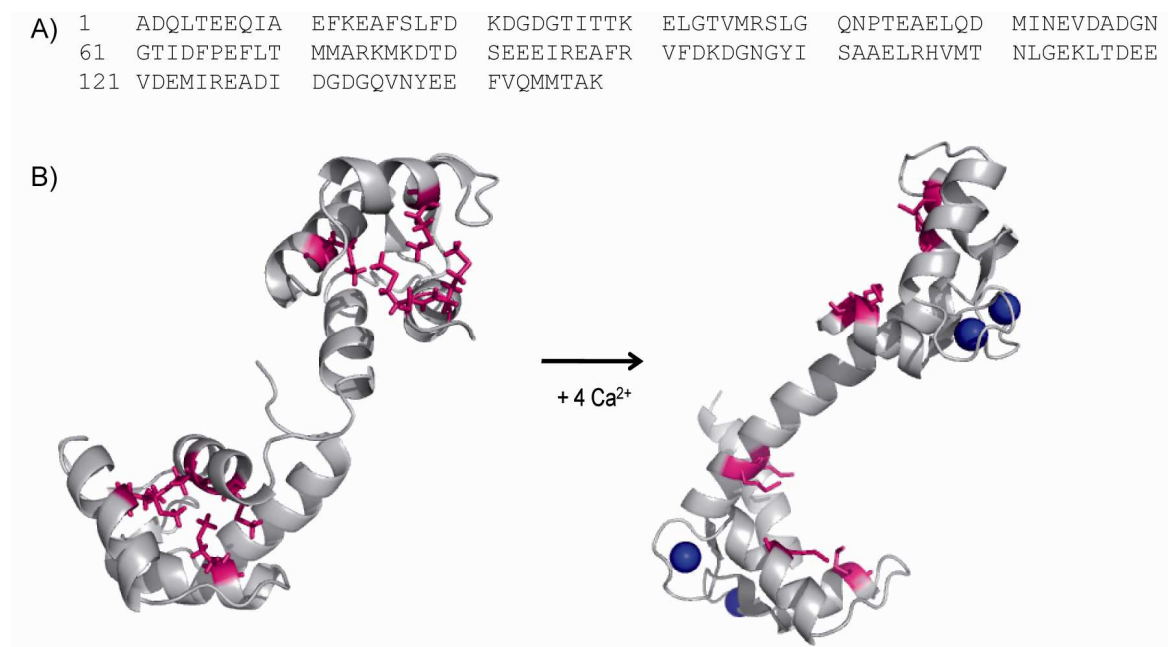


**Figure 1. Amino acid sequence and 3D-structure of calmodulin.** A) The amino acid sequence of CaM is highly conserved. The protein has an acidic pI value and is methionine-rich. B) The two domains of apo-CaM (left, pdb entry 1c1l, (35)) are extremely flexible relative to each other and the hydrophobic methionine residues (pink sticks) are hidden in the core of the domains. Upon  $\text{Ca}^{2+}$  binding, conformational changes lead to an opening of the CaM domains and, thereby, to an exposure of the hydrophobic binding pocket (right, holo-CaM, pdb entry 1dmo, (36)). The structures were illustrated with Pymol; CaM is shown in grey and  $\text{Ca}^{2+}$  in blue.

Structurally, CaM comprises two globular domains, linked by a flexible  $\alpha$ -helical linker region, each of them containing two EF-hand motifs that can bind four  $\text{Ca}^{2+}$  (Figure 1B). These motifs are helix-loop-helix structures that coordinate  $\text{Ca}^{2+}$  with different affinities depending on their sequence composition (37-39) and, therefore, are the key elements for CaM's  $\text{Ca}^{2+}$  sensitivity. EF-hand proteins are found in eukaryotes as well as in prokaryotes,

demonstrating that this motif is extremely well conserved for regulating or sensing  $\text{Ca}^{2+}$  concentrations (40-41).

Differences in affinity for  $\text{Ca}^{2+}$  of the four EF-hands of CaM (42-43) and the cooperativity of  $\text{Ca}^{2+}$  binding, enabled through a pairwise organization of the EF-hands (44), allow CaM to sense  $\text{Ca}^{2+}$  over a wide concentration range. While the *N*-terminal lobe of  $\text{Ca}^{2+}$ -free CaM (apo-CaM) exhibits a closed conformation where the two helices of the EF-hands are tightly packed, the *C*-terminal domain adopts a semi-open conformation, which slightly exposes the hydrophobic binding patch (45), allowing specific target proteins to bind CaM even in the absence of  $\text{Ca}^{2+}$  (Figure 1B, left). At nanomolar  $\text{Ca}^{2+}$  concentrations only the *C*-terminal CaM domain is  $\text{Ca}^{2+}$ -loaded ( $K_D$  (*C*-terminal lobe of CaM): 200 nM), whereas the *N*-terminal domain of CaM has an affinity of 2  $\mu\text{M}$  (42-43, 46).

Upon  $\text{Ca}^{2+}$  binding, significant structural rearrangements are induced in the relative orientation of (a) the helices in both CaM domains and (b) between the lobes, resulting in the exposure of hydrophobic methionine residues that form the target binding pocket (Figure 1B, right; (47-48)). These sequential structural changes in CaM permit various modes of target recognition and binding (25). For that reason, CaM is able to activate a number of proteins involved in versatile biological processes such as muscle contraction, cell proliferation, apoptosis, fertilization, and neurotransmitter release (25).

### 1.1.2. Calmodulin Binding Motifs

The ability of CaM to bind various different target proteins makes it one of the most important proteins in  $\text{Ca}^{2+}$  signaling. CaM-binding sites of target proteins comprise common structural and sequential features. These binding motifs (Figure 2) are characterized by a high propensity to form an amphiphilic  $\alpha$ -helix and contain hydrophobic anchor residues at distinct positions (49-51).

Four classes of CaM-binding motifs are known so far, which are further divided into subclasses and are named according to the positions of the bulky hydrophobic amino acids within the motif: 1-10, 1-14, 1-16, and IQ-motif (Figure 2). In addition to hydrophobic residues, basic amino acids determine the mode of target binding by the relative orientation of binding proteins and peptides in the complex with CaM (51).





**Figure 2. CaM-binding motifs.** CaM-binding motifs share only occasionally sequence homology, but contain hydrophobic residues at distinct positions of the motif (bold and underlined).

Although the above mentioned characteristics of CaM-binding motifs are common to many CaM targets, CaM-binding proteins have recently been found that do not share this binding behavior (52). Additionally, new classes of binding motifs were shown to induce alternative CaM conformations within the CaM/target peptide complexes (53-54). These findings demonstrate the structural flexibility of CaM and the diversity of its target binding modes, which are not completely understood so far, despite having been studied for several decades.

### 1.1.3. Calmodulin Target Proteins Used in this Work

In order to understand the conversion of the Ca<sup>2+</sup> signal into the diverse biological processes, a detailed knowledge about CaM/target interactions is indispensable. In this work, three protein systems were investigated in regard to their interaction with CaM.

#### 1.1.3.1. The Munc13 Protein Family and Synaptic Plasticity

One important family of CaM target proteins is the Munc13 family comprising Munc13-1, ubMunc13-2, bMunc13-2, and Munc13-3. These proteins were identified as mammalian homologs of the *Caenorhabditis elegans* Unc-13 proteins (55). Unc-13 mutants of the worm were discovered in a genetic screen for mutants with an uncoordinated (*unc*) phenotype that is characterized by an abnormal accumulation of acetylcholine and resistance to acetyltransferase inhibitors, interpreted as a deficiency in neurotransmitter release (56-58). In contrast to one single *Unc-13* gene in *C.elegans* and *drosophila* (59), mammals have at least three different *Munc13* genes (Munc13-1, Munc13-2, and Munc13-3) (55, 60). While Munc13-1, the most abundant isoform, and Munc13-3 are specifically expressed in neurons

and neuroendocrine cells, Munc13-2 occurs as brain-specific (bMunc13-2) and ubiquitous (ubMunc13-2) splice variants (61-62).

Munc13 proteins are important presynaptic regulators that participate in a number of processes including synaptic vesicle priming (63-64) and presynaptic short-term plasticity (STP) (65-66). Vesicle priming describes the maturation of membrane-docked vesicles to a fusion-competent form prior to exocytosis (Figure 3). Experiments with Munc13 double knockout mice showed that the MUN domain of Munc13 is sufficient to rescue vesicle release in these mice (67). This rescue of release is also achieved by a constitutively open mutant of the SNARE (soluble *N*-ethylmaleimide-sensitive-factor attachment receptor) protein syntaxin-1 (68), indicating a role of Munc13 in the conformational transition of syntaxin-1 from the closed to the open state. Although a direct interaction of Munc13 with syntaxin-1 was suggested initially (69-70), it was found later that Munc13 does not bind to isolated syntaxin-1 (67, 71), but to syntaxin-1/SNAP25 heterodimers (71-72). These results demonstrate the involvement of Munc13 in exocytotic events, like opening of syntaxin-1, which was recently proven *in-vivo* (73).

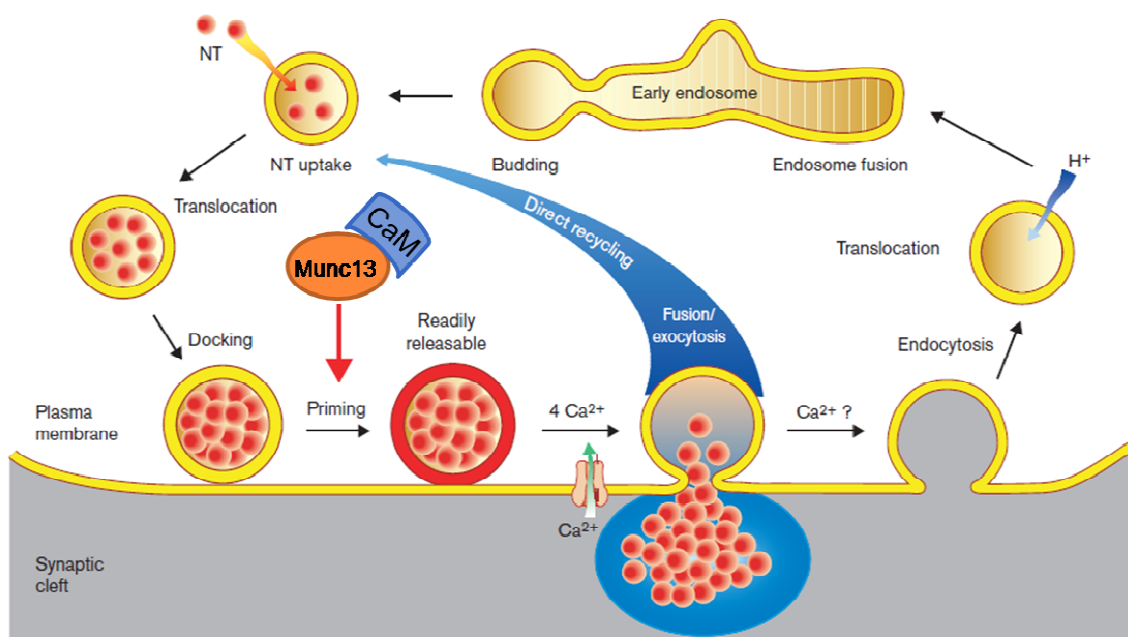


**Figure 3. Synaptic vesicle cycle.** Synaptic vesicles get loaded with neurotransmitter (NT) by active transport systems and are translocated to the presynaptic plasma membrane. Membrane-docked vesicles mature during the priming process, forming a pool of readily releasable vesicles. This step of the synaptic vesicle cycle is dependent on the presence of Munc13 proteins and is regulated by CaM. An increase in  $\text{Ca}^{2+}$  concentration causes the fusion of readily releasable vesicles with the presynaptic membrane and, thereby, a release of neurotransmitter in the synaptic cleft. Afterwards, synaptic vesicles are directly recycled via clathrin-mediated endocytosis. Adapted from Brose *et al.* 2000 (70).

A second Munc13-dependent presynaptic process is short-term plasticity (STP), a  $\text{Ca}^{2+}$ -dependent process describing the transient modification of synaptic performance, which can be expressed as short-term enhancement (STE) or short-term depression (STD) (74). The regulation of STP by Munc13, which is essential for processes such as learning and memory, is isoform-specific. Neurons expressing only ubMunc13-2 exhibit STE, while STD is found in Munc13-1 specific neurons, as shown in rescue experiments with double knockout mice (65). Moreover, the interaction of Munc13 proteins with CaM through the CaM-binding motif in the *N*-terminal region of Munc13 was found to be the link between residual  $\text{Ca}^{2+}$  concentrations and presynaptic plasticity phenomena (75). Experiments by Junge *et al.* revealed a stronger STD in Munc13-1-dependent neurons expressing a CaM-insensitive Munc13-1 variant, while expression of a CaM-insensitive ubMunc13-2 variant led to STD instead of STE in wild-type ubMunc13-2-expressing cells (75).

All Munc13 homologs share a highly conserved *C*-terminal region containing a C1 domain, which binds diacylglycerol (DAG) or phorbol esters and is, therefore, part of the DAG second messenger pathway (76), as well as two C2 domains, identified as protein or  $\text{Ca}^{2+}$ -dependent phospholipid binding site in many different proteins (77), but with unknown function in the Munc13 family (Figure 4). Munc13 proteins additionally possess two Munc13 homology domains (MHD) in the *C*-terminus (78) that form, together with flanking regions, an independently folding domain (MUN). This MUN domain is responsible for the priming activity of Munc13 proteins (67).

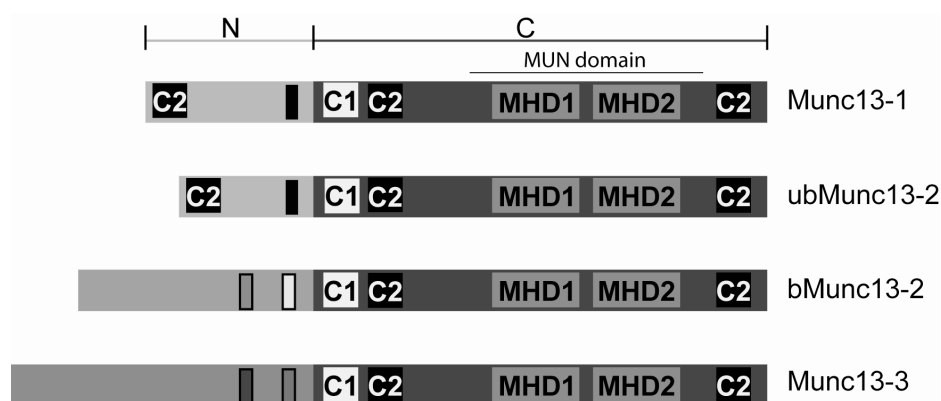


**Figure 4. Domain structure of Munc13 proteins.** All isoforms share a highly conserved *C*-terminal part (C, dark) that contains a C1 domain (white), two C2 domains (black) and two Munc Homology Domains (MHD1 and MHD2, grey) that together form the MUN domain. The *N*-terminus (N), containing an additional C2 domain (black) and the CaM-binding site (black bars), is homologous only between Munc13-1 and ubMunc13-2. The other isoforms (bMunc13-2 and Munc13-3) have unrelated *N*-termini with two predicted CaM-binding sites, each (bars). Adapted from Dimova *et al.* 2006 (79).

Besides the domain topology, high-resolution structural information is available for Munc13: The C-terminal C2 domain (pdb 3kwt and 3kwu, (80)), the C1 domain (pdb 1y8f, (81)) and a part of the MUN domain (pdb 3swh, (82)) have been structurally characterized by NMR spectroscopy or X-ray crystallography.

The N-terminal parts of Munc13-1 and ubMunc13-2 are structurally homologous - even to Unc13 of *C.elegans* - whereas the N-termini of bMunc13-2 and Munc13-3 are largely unrelated. However, biochemical studies have revealed that the CaM-binding site of all Munc13 isoforms is located in the non-conserved N-terminal region (75), allowing a discrete  $\text{Ca}^{2+}$ /CaM dependent regulation. For Munc13-1 and ubMunc13-2, a 21-amino acid stretch was identified as the minimal CaM-binding site, which shows a high propensity to form an  $\alpha$ -helical structure and contains bulky hydrophobic residues (Figure 5A; (79, 83)). Synthetic peptides representing this binding region had been found to bind to CaM in an antiparallel manner through a 1-5-8 CaM-binding motif, thereby creating a complex structure comparable to that of the CaM/NO synthase peptide complex (Figure 5B; (84)).

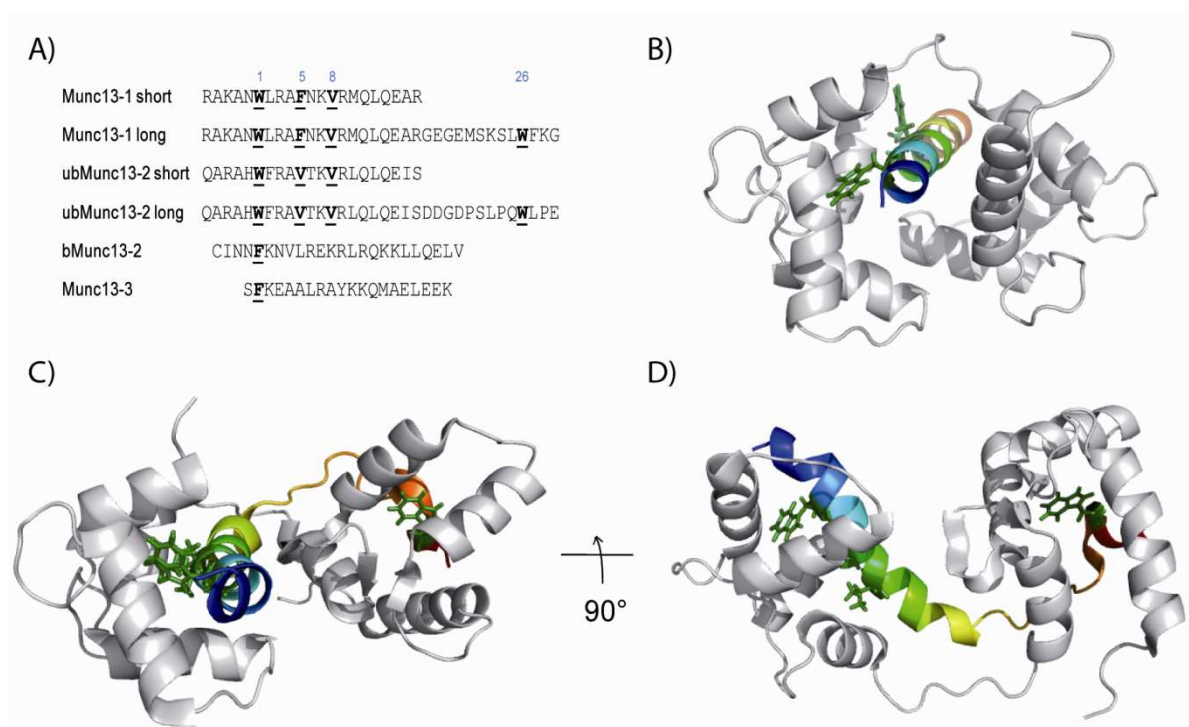


**Figure 5. CaM/Munc13 binding motifs.** A) Sequences of Munc13 peptides representing the CaM-binding sites of all Munc13 isoforms. Hydrophobic anchor residues in the CaM-binding motif are underlined and highlighted in bold. B) Structure of the complex between CaM and a short 21-aa Munc13-1 peptide (84). C, D) Structure of the complex between CaM and a longer 34-aa Munc13-1 peptide (pdb entry 2kdu) (54) viewed from two angles. CaM is presented in grey, the Munc13-1 peptide in rainbow colors. Hydrophobic anchor residues of the Munc13-1 peptide are depicted as green sticks. The structures were illustrated with Pymol.

However, after C-terminal elongation of these peptides, an additional bulky hydrophobic residue (Trp) at position 26 of the CaM-binding motif was found to additionally interact with the N-terminal CaM domain, forming a CaM/peptide complex with a more open conformation of CaM (Figure 5C, D). This presents a novel CaM-binding motif with hydrophobic amino acids at positions 1, 5, 8, and 26 (Figure 5A; (54)).

Bioinformatic analysis, based on biophysical and structural criteria as well as biochemical analysis, predicted two CaM-binding sites in bMunc13-2 and Munc13-3, each (Figure 4 (79)). Additional Ca<sup>2+</sup> titration and GST-pull down experiments indicated that only one of these CaM-binding sites is functional and that this region spatially aligns with the CaM-binding motifs of Munc13-1 and ubMunc13-2 (Figure 5A; (85)).

### 1.1.3.2. Skeletal Muscle Myosin Light Chain Kinase

A second CaM target protein investigated herein is the skeletal muscle myosin light chain kinase (skMLCK), an important mediator of muscle contraction. The skMLCK protein, expressed by the *MYLK2* gene in skeletal muscle (4, 86), is monomeric and has a distinct domain structure, containing an N-terminus with unknown function, a prototypical protein kinase catalytic core, and a regulatory segment in the C-terminus (Figure 6A). The regulatory domain of skMLCK includes an autoinhibitory sequence and the CaM-binding region (87-89).

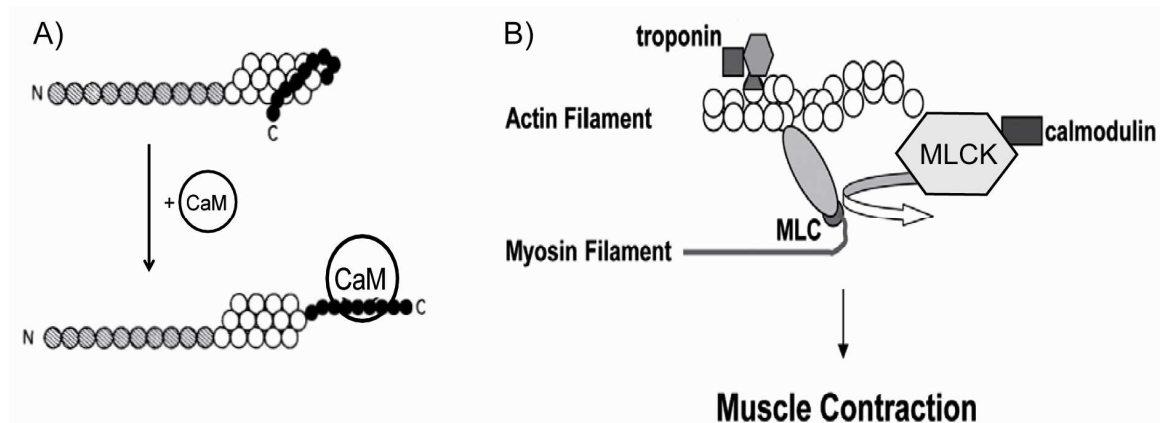


**Figure 6. Myosin light chain kinase (MLCK) function in muscle contraction.** A) The interaction of the regulatory segment (black) with the catalytic domain (white) of MLCK autoinhibits its function. The interaction of MLCK with CaM activates the protein. B) After Ca<sup>2+</sup>/CaM-dependent activation of MLCK, it phosphorylates the light chain of myosin (MLC) and, thereby, induces the movement of the myosin head. Adapted from Kennelly *et al.* 1987 (90) (A) and Takashima 2009 (91) (B).

In the absence of  $\text{Ca}^{2+}$ , the autoinhibitory motif makes numerous contacts with a part of the catalytic core and, by this means, blocks the catalytic cleft. Upon  $\text{Ca}^{2+}$ /CaM binding to the regulatory segment of skMLCK, conformational changes release the autoinhibitory sequence from the active site (Figure 6A; (92-93)). Consequently, the kinase substrate myosin is able to bind in the catalytic cleft and can be phosphorylated at a specific serine residue (94), which in turn leads to a movement of the myosin head and a modulation of force generation in sarcomers (Figure 6B; (4)).

Biochemical studies by Blumenthal *et al.* identified a peptide, called M13, from the C-terminus of skMLCK (amino acids 577-602 of rabbit skMLCK), as minimal CaM-binding sequence of the protein (88). In the subsequent years, the complex between M13 and CaM was intensively investigated using different methods (92-93, 95-97). The NMR structure of the CaM/M13 peptide complex, published in 1992 (98), illustrates that CaM wraps around the peptide and adopts a compact collapsed structure compared to peptide-free CaM (Figure 7; (30)). Kinetic studies revealed the association of the CaM/M13 complex to be limited by diffusion, while the dissociation is quite slow ( $0.03 \text{ s}^{-1}$ ) in the presence of  $\text{Ca}^{2+}$ . However, the dissociation is accelerated in the absence of  $\text{Ca}^{2+}$  (4). The dissociation constant ( $K_D$ ) of the CaM/skMLCK complex is in the low nanomolar range (4, 99). Additionally, mutagenesis of all amino acids within the M13 peptide using peptide arrays revealed that exchanging the hydrophobic residues, especially Trp-2 and Phe-15, to any other amino acid resulted in a decreased affinity of skMLCK to CaM (100), illustrating their importance for binding. Consequently, the CaM/skMLCK peptide complex (Figure 7) is one of the best studied examples for a target interaction with CaM via a 1-5-8-14 motif.

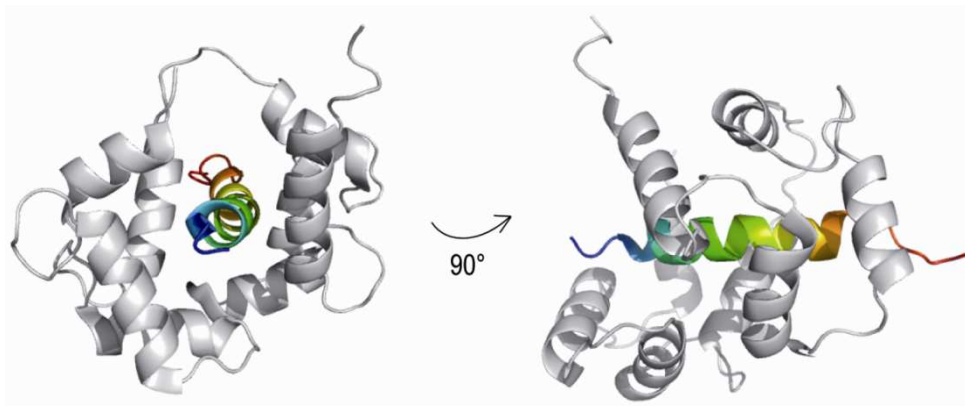


**Figure 7. Structure of the CaM/M13 peptide complex.** CaM (grey) wraps around the skMLCK (M13) peptide (rainbow colors), which causes the two CaM domains to interact. Hence, a compact structure of the CaM/skMLCK peptide complex is formed (pdb entry 2bbm (98)).

### 1.1.3.3. Adenylyl Cyclases 1 and 8

In mammals, ten members of the adenylyl cyclase (AC) family have been characterized (AC1-10), and all of them convert ATP into cAMP, an important second messenger. A common structure has been predicted for the nine membrane-bound ACs (AC1-9) (101), containing a small *N*-terminal domain, two transmembrane domains (each comprising 6  $\alpha$ -helices), and two cytosolic Cyclase-Homology-Domains (C1, C2) with a catalytic (C1a, C2a) and a regulatory subdomain (C1b, C2b) (Figure 8A). In 1997, the catalytic subdomains of AC5 and AC2 were crystallized, showing a structural homology to DNA polymerases with a  $\beta\alpha\beta\beta\alpha\beta$  fold (Figure 8B; (102-103)). This similarity is not surprising because both enzymes catalyze the attack of the hydroxyl group of C-3 of ribose on the phosphate of a nucleoside triphosphate and the formation of a C3 - C5 diester bond (104-105). Additionally, the AC structure clearly shows that dimerization of the two catalytic subdomains is needed to form the ATP-binding site at the interface between both domains (Figure 8). Although the domain topology is common to AC1-9, turn-over rates of the purified enzymes vary between 1 and 100 s<sup>-1</sup>, and  $K_M$  values for ATP binding range between 30 - 400  $\mu$ M (106).

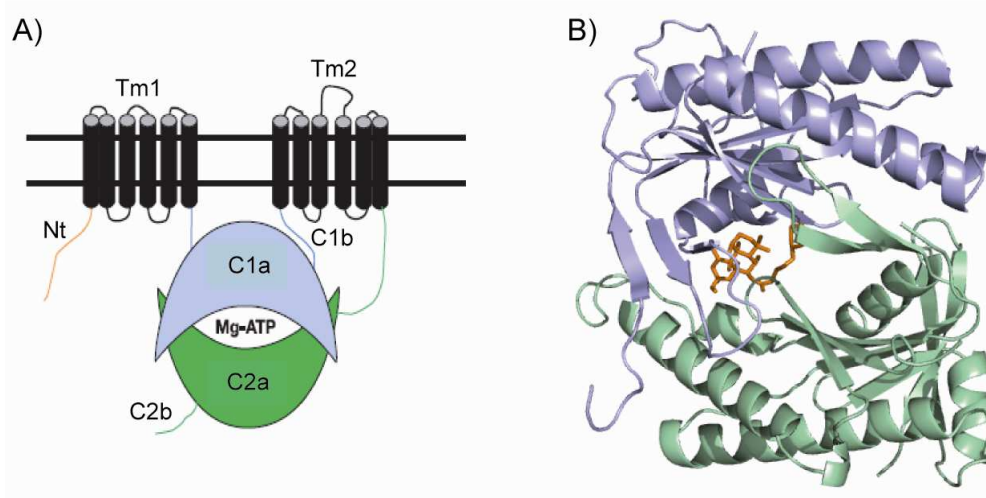


**Figure 8. Predicted structure of the AC family.** A) All ACs share a common domain structure, including a short *N*-terminal region (Nt), two transmembrane domains (Tm1 and Tm2, each containing 6  $\alpha$ -helices), and two cytosolic domains (C1 and C2), which are further divided into subdomains (C1a, b; C2a, b). Taken from Cooper 2003 (105). B) Crystal structure of the catalytic core of ACs with the stimulator forskolin bound at the interface between both subdomains (pdb entry 1azs) (102).

ACs are expressed in a tissue-specific manner and differently regulated by several factors, including  $G_{sa}$ , protein kinases A and C, and CaM (105). AC1 and AC8 are both activated by CaM, but the mechanism of stimulation differs between both isoforms (107). Although the CaM affinity of AC1 is higher, activation is slower compared to AC8, which might result

from the requirement of both CaM lobes binding to AC1 (107). Additionally, AC1 and AC8 differ in the number of CaM-binding sites. While AC1 binds CaM in the first cytosolic regulatory subdomain C1b (108-109), AC8 possesses two CaM-binding sites, one in the *N*-terminus and one in the *C*-terminal cytosolic regulatory subdomain C2b (110). CaM binding to AC8-Nt occurs via a typical 1-5-8-14 binding motif, but is not required for Ca<sup>2+</sup> stimulation of the catalytic activity *in vitro*, as evidenced by truncation studies (110-111). In contrast, deletion of the AC8-C2b domain leads to a superactive, but Ca<sup>2+</sup>-insensitive enzyme, indicating a disinhibitory mechanism for the activation of AC8 via CaM binding to the AC8-C2b IQ-like motif (112). Recent studies additionally showed that the *N*-terminus of AC8 binds to the *C*-terminal Ca<sup>2+</sup>-loaded CaM lobe, whereas AC8-C2b interacts with the *N*-terminal Ca<sup>2+</sup>-loaded domain of CaM (107). Therefore, a model was proposed, describing a pre-association of CaM to the *N*-terminus of AC8 via its 1-5-8-14 binding motif at resting-state Ca<sup>2+</sup> concentrations and a transfer of CaM to the IQ-like motif in the *C*-terminus of AC8 upon increasing Ca<sup>2+</sup> concentrations, which leads to the activation of cAMP production (112).

### 1.1.4. Orai1 and STIM1 - Additional Interaction Partners of AC8

AC8 displays a high selectivity for increasing Ca<sup>2+</sup> concentrations due to store-operated Ca<sup>2+</sup> entry (SOCE) (113-114). The transmembrane protein Orai1 has been identified as the major pore-subunit of store-operated Ca<sup>2+</sup> (SOC) channels (115-117) showing a Ca<sup>2+</sup>-release-activated Ca<sup>2+</sup> current (CRAC) (118-119). Three closely related Orai isoforms are known (Orai1, Orai2, and Orai3), sharing a set of acidic residues in the transmembrane regions that are responsible for a high Ca<sup>2+</sup> selectivity (Figure 9B; (115-117)). SOC channels are formed by tetramerization of Orai proteins through their transmembrane regions, thereby also forming heteromultimers containing different Orai isoforms, which might correlate with multiple channel subtypes (116, 120). Upon depletion of the Ca<sup>2+</sup> stores in the endoplasmic reticulum (ER), the SOC channels become activated by clustering of the ER Ca<sup>2+</sup> sensor protein STIM1 (stromal interaction molecule1) at junctions between the ER and the plasma membrane (Figure 9A; (121-122)). The STIM family, containing the two isoforms STIM1 and STIM2, comprises a Ca<sup>2+</sup> sensing, ER-oriented *N*-terminus and a long *C*-terminal part that interacts with the Orai protein family (Figure 9B; (123)). These two important proteins, Orai1 and STIM1, were shown to affect the activity of AC8 in human embryonic kidney (HEK) 293 cells and are thought to functionally colocalize with AC8 (114, 124). Additionally, recent experiments demonstrated a direct interaction between Orai1 and the *N*-terminus of AC8 (125).



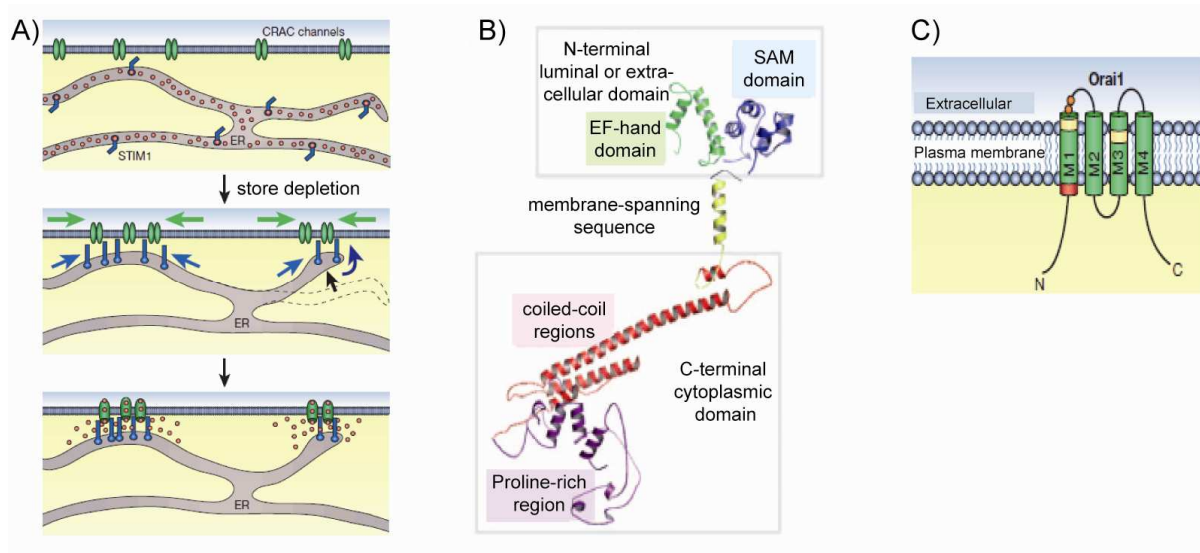


**Figure 9. Store-operated  $\text{Ca}^{2+}$  entry in response to store depletion.** A) Upon  $\text{Ca}^{2+}$  store depletion in the ER (grey), STIM1 (blue) accumulates at junctions between the ER and the plasma membrane, which leads to co-clustering of Orai1 (green) and, consequently, to CRAC channel opening and  $\text{Ca}^{2+}$  (red circles) influx. Adapted from Lewis 2007 (126). B) Homology model of the STIM1 structure (adapted from Spassova *et al.* 2006 (127)). C) Schematic representation of Orai1 in the plasma membrane, with acidic residues relevant for  $\text{Ca}^{2+}$  sensitivity highlighted in red and yellow (adapted from Lewis 2007 (126)).

## 1.2. Structural Investigation of Protein-Protein Interactions

Numerous methods have been developed to structurally, thermodynamically, or kinetically characterize protein-protein interactions, and to gain insights into the composition of protein complexes (5, 7-12, 14-15, 18). Complementary methods were implemented in this work to investigate three selected CaM/target interactions (Munc13, skMLCK, and AC1 and AC8) to extend our current knowledge on how a Ca<sup>2+</sup> signal is converted into different cellular responses. Furthermore, the co-localization and interaction of AC8 with Orai proteins and STIM1 was examined by FRET. In the following, the methods used in this work are described in more detail.

### 1.2.1. Chemical Cross-Linking and Mass Spectrometry

The combination of chemical cross-linking and mass spectrometry (MS) is an alternative technique to high-resolution methods, such as nuclear magnetic resonance (NMR) spectroscopy and X-ray crystallography, for the structural investigation of proteins and protein complexes (17, 128-129). This approach can be conducted following two different strategies, both starting by covalently connecting specific amino acids with cross-linking reagents within one protein (intramolecular) or between interacting proteins (intermolecular) (Figure 10, (17, 129)). In the bottom-up procedure, the cross-linked products are enzymatically digested and the resulting peptide mixtures can be analyzed by MS (Figure 10, left pathway). An alternative approach to analyze the cross-linked proteins or protein complexes is the top-down strategy. Here, intact cross-linked proteins are analyzed in the mass spectrometer using gas phase fragmentation (Figure 10, right pathway). Although only low-resolution 3D-structural information is obtained by chemical cross-linking, this method has several outstanding advantages. In contrast to the high-resolution 3D-structural techniques mentioned above, chemical cross-linking can be conducted with low protein concentrations (femtomol amounts) and in buffers that reflect the cellular environment much better than the solvents used for NMR spectroscopy or crystallization trials. Additionally, the size of a protein under investigation is theoretically unlimited (at least in a bottom-up procedure) and membrane proteins are also suitable for 3D-structural analysis. Furthermore, chemical cross-linking can be applied in living cells for investigation of protein-protein interactions in their cellular context (18). However, despite its great benefits, one major challenge of this technique is the complexity of the cross-linking reaction mixtures, which increases with size and number of the proteins under investigation. These difficulties can be met by an

enrichment of cross-linked species using strong cation exchange (130) or affinity chromatography (131-132), as well as the application of isotope-labeled cross-linkers (133-134) or proteins (135), and cleavable cross-linkers (136-138).

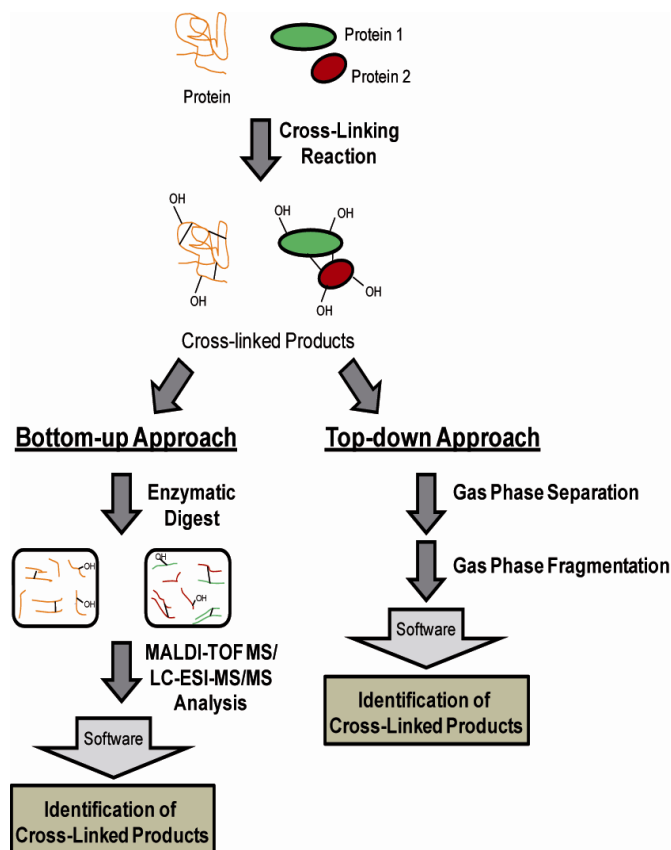


**Figure 10. Cross-linking strategies for structural investigation of proteins or protein complexes.** Both approaches, bottom-up (right) and top-down (left), start with the cross-linking reaction, in which covalent bonds are created between specific amino acids within one protein (intramolecular) or between interacting proteins (intermolecular). The cross-linked products are either enzymatically digested and analyzed by high resolution MS (bottom-up), or analyzed intact using gas phase fragmentation (top-down) in the mass spectrometer.

Various chemical reagents with different reactivities are available for application in chemical cross-linking experiments (139). Thereby, amine-reactive cross-linkers are most widely-used, often as water-soluble derivatives (i.e. sulfo-*N*-hydroxysuccinimide (NHS) esters). Sulfo-NHS esters mainly react with primary amine groups in proteins, which are present at the *N*-terminus or  $\epsilon$ -amino groups of lysines. These nucleophilic groups attack the carbonyl-C atom of the NHS ester moiety via an  $S_N2$  mechanism, forming a covalent amide or imide bond and releasing the NHS (Figure 11). Besides primary amines, hydroxyl groups of serine, threonine, and tyrosine residues (140-142) react with NHS esters. Other amine-reactive functional groups are carbodiimides, which constitute zero-length cross-linkers and mediate amide bond formation between carboxylic acid and amine groups.

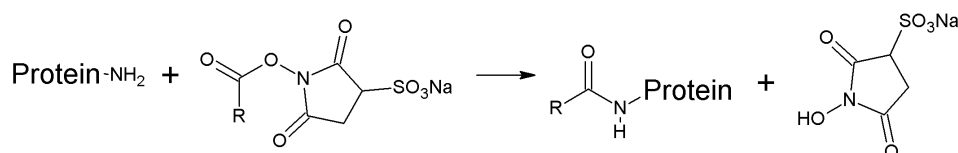


**Figure 11. Reaction mechanism of amine-reactive sulfo-NHS ester cross-linkers.** Primary amine groups in proteins attack the carbonyl-C atom of the sulfo-NHS ester and a new amide bond is formed, while sulfo-NHS functions as leaving group. Adapted from Sinz 2006 (17).

Another set of cross-linker reactivities includes photo-reactive groups, such as aryl azides, diazirines, and benzophenones. These functional groups react with target molecules upon UV irradiation. The irradiation wavelength should not cause any photolytic damage to the proteins under investigation. Highly reactive aryl azides and diazirines form short-lived nitrenes or carbenes that insert into C-H or heteroatom-H bonds (143). The benzophenone group has the advantage of biradical formation upon irradiation with long-wavelength UV light (~365 nm), which is reversible because no photo-dissociative mechanism is included in the activation process. Therefore, a benzophenone group that does not find a reaction partner during the life time of the biradical can be reactivated. The oxygen radical generated can then abstract a hydrogen radical from the protein and the formed alkyl radical further reacts by forming a C-C bond (Figure 12) (144). Although benzophenones were shown to react preferably with methionines (145-146), the number of reaction sites is much higher compared to amine-reactive sulfo-NHS groups.

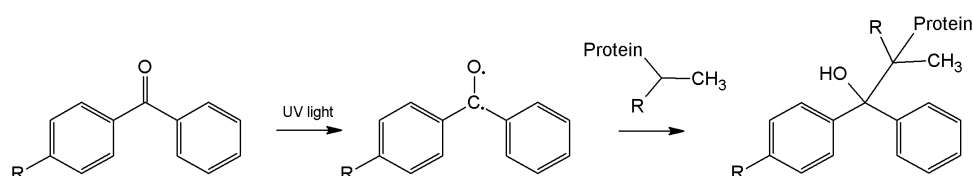


**Figure 12. Reaction mechanism of benzophenone cross-linkers.** A biradical is formed upon irradiation with UV light. The oxygen radical generated abstracts a hydrogen radical from the protein and the generated alkyl radical reacts by forming a new C-C bond. Adapted from Sinz 2006 (17).

In addition to their reactive groups, the numbers and distances of these groups (spacer lengths) are characteristic for each cross-linking reagent. Most cross-linkers have two reactive groups (bifunctional), which are either identical (homobifunctional) or different (heterobifunctional), and possess spacer lengths ranging from 6 up to 25 Å. Cross-linkers possessing a third reactive group (trifunctional) are often used for an enrichment of cross-linked species by affinity purification prior to the mass spectrometric analysis (17, 129).

### 1.2.1.1. Chemical Cross-Linking with Homobifunctional Cross-linkers

Two of the most commonly used homobifunctional, amine-reactive cross-linking reagents are bis(sulfosuccinimidyl)suberate ( $BS^3$ ) and bis(sulfosuccinimidyl)glutarate ( $BS^2G$ ), which have spacer lengths of 11.4 Å and 7.7 Å, respectively (147). These cross-linkers are dissolved in DMSO prior to adding them to the proteins to avoid hydrolysis of the NHS esters. A typical cross-linking reaction with  $BS^3$  or  $BS^2G$  is conducted in HEPES buffer at pH 7 - 7.5 for 30 min, but pH, reaction time, and concentrations of cross-linker and proteins have to be optimized for every single protein or protein complex under investigation (17). After a specified period of incubation, non-reacted cross-linker is quenched by addition of  $NH_4HCO_3$  and the cross-linking reaction mixtures are separated by one-dimensional SDS-PAGE (2.4.4.). In addition to SDS-PAGE, analysis of intact cross-linked proteins can be conducted by MALDI-TOF-MS (1.2.2.1.), especially during the optimization procedure. After colloidal Coomassie-staining of the SDS gel, bands representing cross-linked products (intramolecularly or intermolecularly cross-linked) are excised (Figure 13).

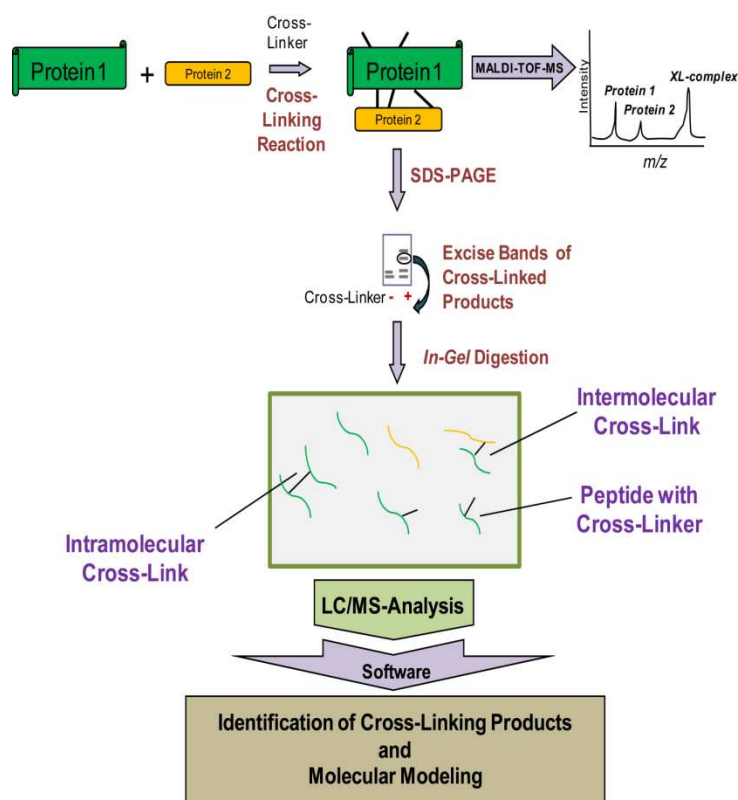


**Figure 13. Reaction scheme of a cross-linking reaction with homobifunctional cross-linkers.** Two or more proteins are covalently connected by a homobifunctional cross-linker. The cross-linked products are analyzed by MALDI-TOF-MS and SDS-PAGE, bands of interest are excised and *in-gel* digested. Subsequently, the resulting cross-linked peptide mixtures are analyzed by LC/MS. Cross-linked products are identified using customized software. Molecular modeling yields 3D-structural information based on the distance constraints obtained by cross-linking.

*In-gel* enzymatic digestion of the cross-linked products is carried out by addition of proteases such as trypsin, AspN, GluC or LysC, which cleave the proteins *N*- or *C*-terminal of specific amino acids. The protease or protease mixture used for *in-gel* digestion is selected in order to obtain maximal sequence coverage during MS analysis. Cross-linked peptide mixtures resulting from *in-gel* digestion are often very complex and can be enriched by strong cation exchange chromatography (130). Usually, the cross-linked peptides are separated by reversed phase (RP) chromatography on a C18 column before they are analyzed by nano-ESI-LTQ-Orbitrap-MS/MS (1.2.2.2.) or MALDI-TOF/TOF-MS/MS (1.2.2.1.) (Figure 13).

With the help of customized software, namely Xcalibur (Thermo Fisher Scientific), GPMW (148), CoolToolBox (Leo J. de Koning, University of Amsterdam, The Netherlands) or StavroX (149), cross-linked products are identified. Mass lists of a theoretical digest of cross-linked protein(s) are compared with experimentally obtained mass lists. Additionally, StavroX compares masses of fragment ions of a cross-linked peptide, calculated from theoretical fragmentation of each peptide bond (which is cleaved in collision-induced dissociation (CID) MS/MS experiments), with experimentally obtained masses. The nomenclature according to Roepstorff (150) and Schilling (151) was used for MS/MS fragments of cross-linked products (Figure 14).

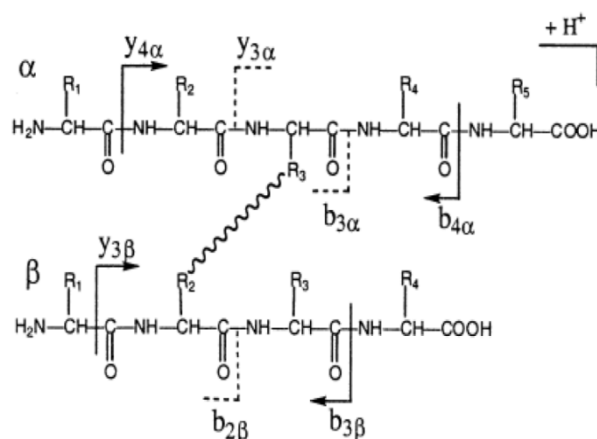


**Figure 14.** Nomenclature of CID fragment ions according to Roepstorff and Schilling. (Schilling *et al.* 2003 (151)).

To improve cross-link identification, the homobifunctional reagents, BS<sup>3</sup> and BS<sup>2</sup>G mentioned above, are commercially available as isotope-labeled, i.e., deuterated, variants (Thermo Fisher Scientific). Specific isotopic patterns of cross-linker-containing species improve their detection and particular fragmentation in the mass spectrometer. The distance constraints, obtained from cross-linking experiments, are used for molecular modeling to gain low-resolution structural information on the protein or protein complex under investigation (152) (Figure 13).

### 1.2.1.2. Chemical Cross-Linking with Heterobifunctional Cross-linkers

Cross-linking reactions with heterobifunctional reagents, such as the amine-/photo-reactive cross-linker *N*-succinimidyl-*p*-benzoyldihydrocinamate (SBC, (145)), are conducted in a two-step fashion (Figure 15).

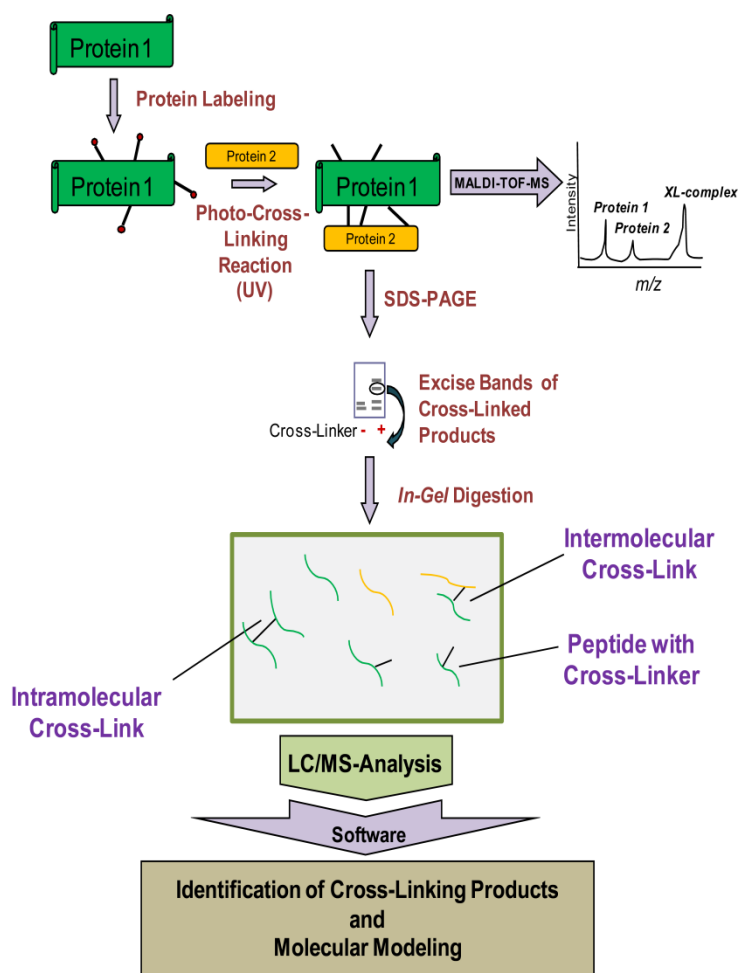


**Figure 15. Reaction scheme of a cross-linking reaction with heterobifunctional cross-linkers.** Protein 1 is labeled with the cross-linker in a first step. After removal of non-reacted cross-linker, protein 2 is added and the reaction mixture is UV-irradiated, thereby inducing the photo-reaction. The cross-linked products are analyzed by MALDI-TOF-MS and SDS-PAGE, bands of interest are excised and *in-gel* digested. Subsequently, the resulting cross-linked peptide mixtures are analyzed by LC/MS. Cross-linked products are identified using customized software. Molecular modeling yields 3D-structural information with the help of distance constraints obtained by cross-linking.

In the case of SBC, the amine-reactive NHS ester site of the cross-linker is reacted with protein 1 in a first step, resulting in a cross-linker-modified protein. After quenching and microfiltration for removal of non-reacted cross-linker, the interaction partner (protein 2) is added and the photo-reaction of the benzophenone group is induced by UV irradiation ( $\lambda \sim 365$  nm). Subsequent LC/MS analysis and identification of cross-linked products are carried out as described for homobifunctional cross-linkers (1.2.1.1.) (Figure 15, (145)). The

two-step reaction procedure with heterobifunctional cross-linkers minimizes the formation of high-molecular weight aggregates compared to homobifunctional reagents. Additionally, cross-linkers containing a photo-reactive group are advantageous because this moiety is stable towards UV light exposition and reacts less specifically with various amino acids, resulting in a high number of reaction sites (17).

### 1.2.1.3. Structural Investigations with Photo-Reactive Amino Acids

An alternative approach to the use of homo- or heterobifunctional cross-linking reagents is the use of photo-reactive amino acids. Their activation upon UV irradiation and their reaction mechanism are identical to the respective functional groups of cross-linking reagents (diazirines or bezophenones, see 1.2.1.). Unnatural photo-reactive residues, such as photo-Leu, photo-Met, or photo-Ile (Figure 16), are incorporated into proteins during translation in cell culture (153). For this, the photo-amino acid is added instead of the natural amino acid directly to the nutrient solution and is statistically incorporated at every position that encodes for Leu, Met, or Ile. For a more specific replacement of natural amino acids by photo-reactive residues, an extended genetic code can be used to incorporate *p*-benzoylphenylalanine (Bpa) (Figure 16) at the so-called amber stop codon. A specific tRNA : aminoacyl/tRNA synthetase pair was selected to guide the incorporation of Bpa in the protein sequence (154-156). The advantage of incorporating photo-reactive amino acids into proteins is the possibility to examine protein 3D-structures or to study interacting proteins in their cellular environment. Furthermore, the 3D-structural information obtained by cross-linked photo-reactive amino acids is useful, as the distance of linked residues is supposed to be maximal 8 Å (84). Therefore, binding interfaces can be precisely mapped.

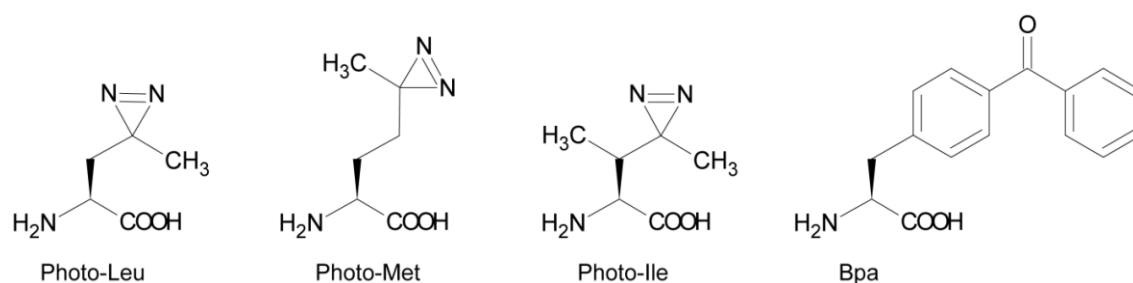


**Figure 16. Photo-reactive amino acids.** Amino acids photo-leucine, photo-methionine, and photo-isoleucine possess a diazirine group; Bpa contains a photo-reactive benzophenone.



## 1.2.2. Mass Spectrometry

Mass spectrometry (MS) is used in combination with chemical cross-linking owing to its high sensitivity, which allows a rapid analysis of the complex mixtures resulting from cross-linking experiments. The sample is ionized in the ion source (e.g. by matrix-assisted laser desorption/ionization (MALDI) or electrospray ionization (ESI)), the ions are separated according to their mass-to-charge ( $m/z$ ) ratio in the mass analyzer (e.g. time-of-flight (TOF), linear ion trap (LTQ) or orbitrap), and are detected.

### 1.2.2.1. MALDI-TOF Mass Spectrometry

The exact mechanism of MALDI is still under investigation and not yet understood in detail. In principle, analyte molecules are co-crystallized on a steel target with an organic matrix that absorbs UV laser energy. These matrices, first used by Karas and Hillenkamp (157-158), are mainly derivatives of cinnamic acid (e.g.  $\alpha$ -cyano-4-hydroxycinnamic acid (HCCA), 2,5-dihydroxybenzoic acid (DHB) (159) or sinapinic acid (SA)). Upon laser irradiation (Nd-YAG-laser or N<sub>2</sub> laser) of the sample in the vacuum of a MALDI source, the matrix molecules are excited. The excitation energy of the matrix relaxes into the crystal lattice and leads to an ablation of material from the upper layers of the sample, thereby delivering analyte and matrix molecules into the gas phase. Experimental studies provide evidence for an involvement of matrix molecules in the ionization of the analyte (160).

The combination of the pulsed MALDI technique with a time-of-flight (TOF) analyzer is one of the most frequently used analytical tools to investigate biomolecules. Even though the construction of a TOF analyzer was already described in the 1950s by Stephens (161), the technique became famous and commonly used only in the context of success of pulsed ionization methods, especially MALDI. Determination of the  $m/z$  ratio with a TOF analyzer is achieved by measuring the drift time of accelerated ions in a field-free path through the drift tube. In this manner, the  $m/z$  value is proportional to the drift time  $t$ :

$$E_{kin} = e \cdot z \cdot U = \frac{1}{2} m \cdot v^2 \quad (eq1)$$

$$v = \sqrt{\frac{2 \cdot e z U}{m}} \quad (eq2)$$

$$t = \frac{S}{v} \quad (eq3)$$

$$t = s \sqrt{\frac{m}{2 z e U}} \quad (eq4)$$

Variables:  $E_{kin}$  (kinetic energy),  $e$  (element electric charge),  $z$  (charge),  $U$  (acceleration voltage),  $m$  (mass of an ion),  $v$  (velocity), and  $s$  (length of flight tube).

Subsequently, two major improvements were introduced into MALDI-TOF instruments: the reflectron (162-163) and the delayed extraction technique (164-165). Due to a quite extended time of  $\sim 100$  ns for the desorption/ionization process, the starting times for ions of the same  $m/z$  might differ to a greater extent than the flight times of neighboring  $m/z$  values, leading to a limited resolution. For compensation of different starting times and positions or different kinetic energies, the reflectron was developed, an ion mirror consisting of annular electrodes with increasing potential (162-163). Ions submerge into the reflectron at the end of the flight tube until their kinetic energy reaches zero. Then, the ions are accelerated in the direction of the second flight tube before they reach the reflector detector (Figure 17). Since ions with a higher kinetic energy will penetrate the reflectron deeper, they will spend more time within the decelerating field. Therefore, a correction for spatial and starting energy distributions of ions with identical  $m/z$  values is possible, resulting in improved resolution (166-167).

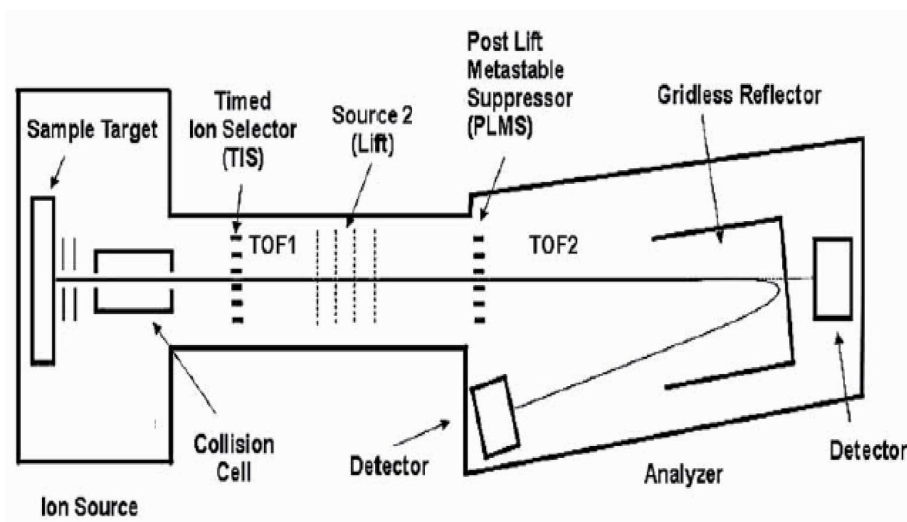


**Figure 17.** Schematic design of MALDI-TOF/TOF MS (Bruker Daltonik). Slightly modified from Suckau *et al.* 2003 (168).

Another possibility to achieve better resolution is delayed extraction. During a certain delay time (hundreds of nanoseconds) between generation and acceleration of ions in a MALDI-TOF MS, the ions are separated according to their initial velocities. Ions with a higher initial velocity move further than slower ions and are accelerated to a lesser extent, thereby compensating for their initial energy distributions (164-165).

Fragmentation of precursor ions (i.e., peptides resulting from a proteolytic digest) can be carried out at different positions in a MALDI-TOF instrument: laser-induced dissociation (LID), *in-source* decay (ISD), and *post-source* decay (PSD). In this work, LID was used for fragmentation of cross-linked peptides in order to identify the amino acids that had reacted with the cross-linker. Therefore, the laser power was increased to generate a larger number of ions, which fragment mainly at the peptide bond and are accelerated as so-called “ion families”. The fragment ions, which are formed from the same precursor after the first acceleration, possess the same kinetic energy and can be selected in a timed ion selector (TIS) before they enter the LIFT (laser-induced fragmentation technology) unit (168). There, the ion family is finally accelerated and the ions are separated according their  $m/z$  values in the TOF2 region (Figure 17).

As a conclusion, MALDI-TOF/TOF-MS/MS is a high-resolution technique to identify cross-linked and unmodified peptides. Additionally, intact proteins with high molecular masses (up to 150,000 u) can be measured if the TOF analyzer is operated in the linear mode (with the reflectron turned off; MALDI-TOF-MS). Therefore, it is used for monitoring the cross-linking reaction (in parallel to SDS-PAGE) and for analyzing cross-linked peptide mixtures after proteolytic digestion (Figure 13 Figure 15).

### 1.2.2.2. ESI-LTQ-Orbitrap Mass Spectrometry

Atmospheric pressure ionization (API) (169) allowed for the first time to transfer analyte molecules directly from solution into the gas phase. The ESI source designed by John Fenn in the 1980s (170-171) is based on the work of Dole and coworkers (172). It contains a stainless steel needle, which is held at a potential of 3 - 4 kV relative to a surrounding electrode (Figure 18A). The sample is conducted through the needle and is emitted in form of a Taylor cone as aerosol (173), from which the solvent is evaporated (Figure 18B). When the charge density on the surface of a formed droplet increases to the Rayleigh limit - the point where electrostatic repulsion exceeds the surface tension (174) - droplet jet fission can be observed (175-176). Two complementary theories describe the final formation of desolvated ions: the charged-residue model (CRM) and the ion evaporation model (IEM).

The CRM acts on the assumption that each nanodroplet, generated by various fissions, contains only one charge. This charge is transferred to the analyte upon complete loss of all solvent molecules, forming a charged desolvated analyte molecule (172, 177). In contrast, the

IEM describes the direct formation of charged desolvated ions by emission from a charged droplet (diameter  $\sim 8$  nm) at the Rayleigh limit. Thereby, the radius of the remaining droplet decreases, which leads to ion emission (178-179). The IEM is supported by the observation that extended molecules carry more charges than globular ions and that fast evaporation favors higher average charge states (180).

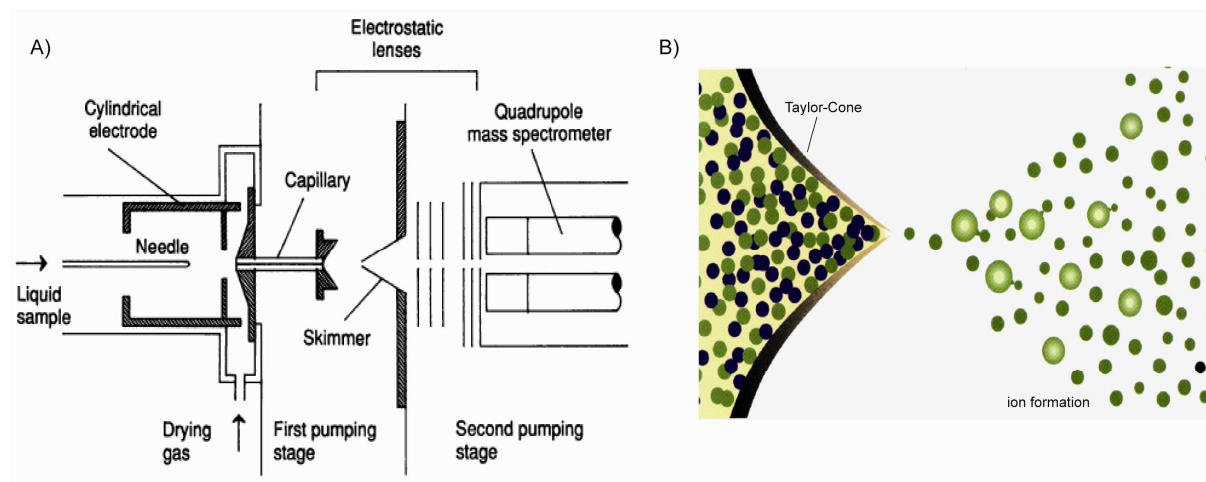


**Figure 18. Electrospray ionization (ESI).** A) Schematic design of an ESI source by J. Fenn (171). B) Ion formation in an ESI source from the Taylor cone. Slightly adapted from Fenn, 1989 (A) and Kebarle, 1993 (175) (B).

A reduction of sample volume and an increase in sensitivity were achieved by miniaturization of the ESI process to nano-ESI. For this, borosilicate glass capillaries with smaller inner diameters (5 - 30  $\mu\text{m}$ ) were developed, which produce smaller droplets at reduced flow rates (100 - 300 nl/min) (181-182).

The desolvated ions reach the mass spectrometer through a capillary and are transferred from a chamber with a vacuum of  $10^{-2}$  mbar through a skimmer and the transfer optics to the analyzer under strong vacuum ( $10^{-7}$  -  $10^{-8}$  mbar) (171). Analysis of the desolvated ions was carried out in this work either in the linear ion trap (LTQ, Thermo Fisher Scientific) or in the orbitrap analyzer of an LTQ-OrbitrapXL hybrid mass spectrometer. The LTQ is a linear quadrupole, which is capped by two terminal electrodes that carry a DC (direct current) voltage for ion storage in the axial direction (Figure 19). A radiofrequency (RF) potential at the four electrodes of the quadrupole stores the ions in the radial direction (183). Due to decreased space-charge effects through focusing of the ions in the  $z$  direction, the store capacity of linear ion traps is much higher than for three dimensional Paul traps where the ion cloud is focused at one point (184). Prevention of overcrowding of the LTQ is realized by automatic gain control (AGC) through short prescans, which determine the total ion current (TIC) in a specific mass range and enable a calculation of the injection time that is needed to

fill, but not overflow the trap (185). Analysis and detection of stored ions is achieved by radial ejection of the ions to lateral photo-multipliers through a change in the RF voltage. Another possibility to eject the stored ions is applying an additional alternating current (AC) voltage at the end electrodes, which leads to an oscillation of ions with a specific  $m/z$  value that are resonant and their selective ejection from the trap in  $z$  direction (183).

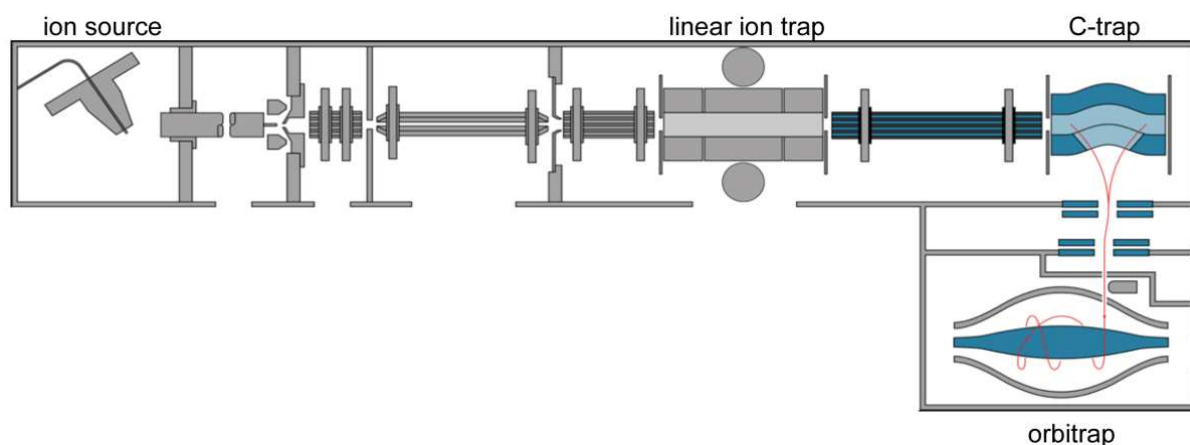


**Figure 19. Schematic design of the LTQ-OrbitrapXL mass spectrometer.** The hybrid mass spectrometer (Thermo Fisher Scientific) contains an ion source, a linear ion trap (LTQ), a curved trap (*C-trap*), and an orbitrap analyzer. The ion path (red) from the *C-trap* into the orbitrap and there around the central electrode is highlighted. Taken from Makarov *et al.* 2006 (186).

During the storage of ions with a specific  $m/z$  value, fragmentation of these ions can be conducted by CID. The ions are excited to a higher kinetic energy by an electric potential and then a collision gas (nitrogen or helium) is applied. Collisions between the neutral gas and the analyte ions lead to a conversion of kinetic to internal energy of the ion and to a rupture of the weakest bond, i.e., the peptide bond (187). Afterwards, the fragment ions are ejected according to their  $m/z$  values.

The second analyzer of the LTQ-OrbitrapXL mass spectrometer is an orbitrap. Although the underlying principle was described by Kingdom already in the 1930s (188), Makarov developed the first orbitrap analyzer in 1999 (189-190). The orbitrap consists of a central spindle-shaped electrode, which carries an electrical voltage of several kV, and a barrel-shaped outer electrode with a ground potential (Figure 19). Desolvated ions are transferred to the orbitrap through the LTQ and a curved trap (*C-trap*) where they are decelerated by collisional cooling using nitrogen gas. The special geometry of the *C-trap* and collisional cooling of the ions condense the ion package, which is then conveyed to the orbitrap through various optics and electrodes (190). Ions within the orbitrap rotate around the central electrode and oscillate axially in  $z$  direction with a frequency that is dependent on their  $m/z$  ratio (191):

$$\omega = \sqrt{\frac{z \cdot k}{m}} \quad (eq5)$$

The axial oscillation frequency ( $\omega$ ) of the ions in an orbitrap analyzer is indirectly proportional to the square root of their  $m/z$  ratio. The variable  $k$  is an instrument constant.

The outer electrodes of the orbitrap analyzer record an image current that represents the frequencies of the different ions that oscillate around the central electrode. Using Fourier transformation (FT) this frequency spectrum is converted into a mass spectrum (MS) (190).

In summary, the hybrid mass spectrometer LTQ-OrbitrapXL, which is equipped with an ESI source, combines a soft and continuous ionization technique (ESI) with a linear ion trap, which is highly sensitive, and a high resolution orbitrap analyzer (Figure 19). Most of the cross-linked peptide mixtures obtained in different cross-linking experiments during this work were analyzed by nano-ESI-LTQ-Orbitrap-MS/MS.

### 1.2.3. Circular Dichroism Spectroscopy

Analysis of the secondary structure of proteins and peptides, but also nucleic acids, can be achieved using circular dichroism (CD) spectroscopy.

The difference in absorption ( $\Delta A$ ) of right and left circularly polarized light by an analyte (Cotton effect) is measured in dependence of the wavelength. This absorption difference is due to an asymmetric composition of chromophores, e.g., of the peptide bond, which absorbs light in the far-UV range (170 - 200 nm). In proteins, secondary structural elements ( $\alpha$ -helices,  $\beta$ -sheets and random coils) make specific contributions to a CD spectrum (Figure 20), allowing conclusions about their appearance and quantity to be made (192).

The absorption  $A$  of non-polarized light by a substance is, according to Beer-Lambert's law (eq.6), dependent on the concentration ( $c$ ), the path length ( $d$ ), and the extinction coefficient ( $\epsilon$ ).

$$A(\lambda) = \log\left(\frac{I_0}{I}\right) = c \cdot d \cdot \epsilon \quad (eq6)$$

The absorption ( $A$ ) is dependent on the ratio between the intensity of incident light ( $I_0$ ) and transmitted light ( $I$ ).

According to equation 6, the difference in absorption of right (R) and left (L) circularly polarized light ( $\Delta A$ ) is calculated:

$$\Delta A(\lambda) = \log(I_L) - \log(I_R) = c \cdot d \cdot (\varepsilon_L(\lambda) - \varepsilon_R(\lambda)) \quad (\text{eq7})$$

Commonly, in CD spectroscopy measurements rather than  $\Delta A$ , the degree of ellipticity ( $\theta_D$ , eq.8) is reported, which can be converted into the concentration-corrected molar ellipticity ( $\theta_{MRW}$ , eq.9) for a better comparison of different experiments.

$$\theta_D = \frac{\ln 10}{4} \cdot (\varepsilon_L - \varepsilon_R) \cdot \frac{180}{\pi} [\text{deg}] \quad (\text{eq8})$$

$$\theta_{MRW} = \frac{\theta_D}{c \cdot d} [\text{deg} \cdot \text{cm}^2 \cdot \text{mol}^{-1}] \quad (\text{eq9})$$

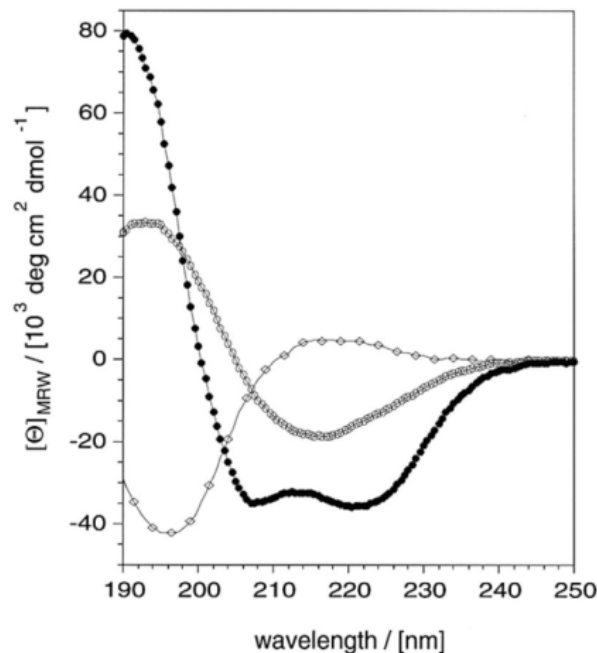


**Figure 20. Far-UV CD spectra of different poly-Lys conformations.** The dependence of the concentration-corrected molar ellipticity on the wavelength is depicted for different conformations of poly-Lys. The  $\alpha$ -helical conformation (black, filled circles) is found for freshly dissolved poly-Lys at pH 11.1, the  $\beta$ -sheet (grey, open circles) for poly-Lys at pH 11.1 after heating for 15 min at 52 °C, and the random-coil conformation (light grey diamonds) is observed for poly-Lys freshly dissolved in pure water (193-194). Taken from Fändrich *et al.* 2002 (194).

In some cases of protein interactions, a specific structure or structural motif of one or both binding partners is induced upon binding. One prominent example is CaM. Most of its targets have a high propensity to form  $\alpha$ -helical structures in the complex with CaM. Investigation of this propensity can be carried out with 2,2,2-trifluoroethanol (TFE). Addition of different amounts of TFE stabilizes the secondary structural elements of proteins or peptides (195) by weakening hydrogen bonds to the surrounding solution and, thereby, strengthening intramolecular interactions (196-197). Therefore, CD spectroscopy permits expeditious

acquisition of structural information and requires fairly small amounts of protein or peptide (in the ng to  $\mu\text{g}$  range), which makes it one of the most frequently used methods for analyzing protein secondary structures.

#### 1.2.4. Isothermal Titration Calorimetry

Isothermal titration calorimetry (ITC) is a method for characterization of protein-protein or protein-ligand interactions on a thermodynamic level. In one experiment, the enthalpy ( $\Delta H$ ), entropy ( $\Delta S$ ), the Gibbs free energy ( $\Delta G$ ), as well as the affinity ( $K_A$ ) and stoichiometry ( $N$ ) of a binding event can be determined with high accuracy (198-200).

A target molecule is titrated to a solution of its interaction partner in the reaction cell of a calorimeter and the power, applied to this cell to keep the temperature constant compared to a reference cell, is measured (Figure 21). The changes in power applied to the reaction cell depend on the heat absorbed or released during the binding reaction.

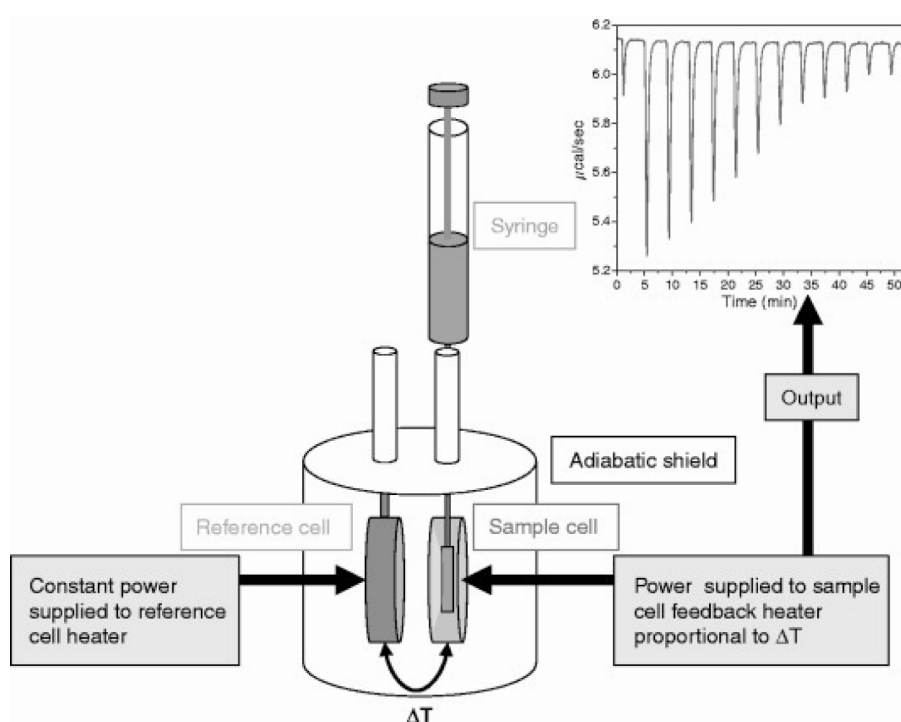


**Figure 21. Schematic set-up of a power compensating ITC.** Two cells (reference and sample cell) are embedded in an adiabatic shield. Power is supplied to the reaction cell to hold the temperature difference between reference and sample cell at zero ( $\Delta T=0$ ). Through a syringe, an interacting molecule is titrated to the protein solution in the reaction cell and the heat of the binding reaction is measured. Taken from Freyer *et al.* 2008 (201).

Parameters characterizing an interaction event can be determined by using the following equations (202):



$$\Delta G = -R \cdot T \cdot \ln K \quad (eq10)$$

$$\Delta G = \Delta H - T \cdot \Delta S \quad (eq11)$$

$G^0$  is the Gibbs free energy, R is the universal gas constant, T is the absolute temperature, K is the equilibrium constant, H is the enthalpy, and S is the entropy.

Advantages of ITC are the easy handling and the lack of limitations in buffers, pH, molecular weight, and temperature. Additionally, there is no need for labeling or immobilization of one or both interaction partners (203). Therefore, despite a few drawbacks, e.g., long measuring times and large sample volumes, ITC is widely used for thermodynamic characterization of protein interactions.

### 1.2.5. Surface Plasmon Resonance Spectroscopy

Investigations of protein-protein interaction by surface plasmon resonance (SPR) spectroscopy allow the investigator to gain insights into the kinetics of a binding event and to reveal information about the affinity of binding partners. In SPR, one protein is immobilized on a gold-coated surface, over which the interaction partner is flowing (Figure 22). Upon binding of the interacting protein, the immobilized mass increases. This results in a changed refractive index for totally reflected light at the surface/buffer interface, which is linear to the number of bound molecules (204). A typical set-up of an SPR sensor contains a prism, which is mounted on the gold-coated sensor chip (Figure 22). On the surface of the sensor chip where the protein of interest is immobilized, oscillating electrons are excited by light and form an electron density wave, leading to a reduction in intensity of totally reflected light at the plasmon resonance wavelength (205). Due to changes in the environment of these excited electrons (plasmons), the conditions change where light couples with the plasmons. This is measured as an altered resonance angle or resonance wavelength (204).

Although this high-throughput method is commonly used for determining binding kinetics of antigen/antibody complexes (204), immobilization of the protein of interest might cause difficulties for other proteins. This is because the immobilization of a protein does not necessarily lead to a surface coated with molecules of the same orientation. The kinetics of target binding might be affected. Another problem is the reduced flexibility of immobilized proteins and, therefore, a reduced accessibility of a small protein or peptide after immobilization. Nevertheless, SPR is a powerful method to determine the kinetics of a protein-protein interaction in a very sensitive, reproducible, and label-free manner (206).

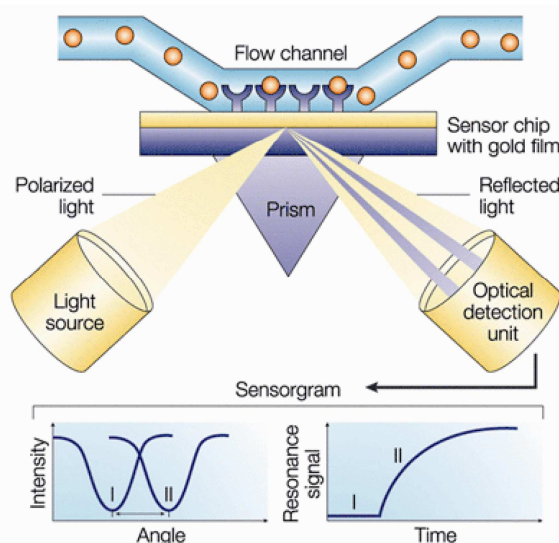


**Figure 22. Set-up of a surface plasmon resonance (SPR) sensor.** SPR spectroscopy detects changes in the refractive index at the surface of a gold-coated sensor chip, which are caused by alterations in the environment of excited plasmons, e.g., caused by binding of a target protein to an immobilized protein. Taken from Cooper 2002 (207).

### 1.2.6. Fluorescence (Förster) Resonance Energy Transfer

One method to examine protein-protein interactions in living cells is using fluorescence (Förster) resonance energy transfer (FRET). Non-radiative (dipole-dipole) transfer of energy from an excited donor chromophore to an acceptor chromophore is measured. Due to an inverse dependency of this energy transfer efficiency to the sixth power of the distance between donor and acceptor (eq.12), FRET provides the opportunity to investigate binding events between two proteins in their natural environment qualitatively and to calculate the distance of these interacting proteins. The distance of a donor-acceptor pair where the efficiency of the energy transfer is half-maximal ( $R_0$ ) is in most cases around 5 nm. Therefore, the threshold for an effective energy transfer is approximately 10 nm (11).

$$E = \frac{R_0^6}{(R_0^6 + r^6)} \quad (\text{eq12})$$

The efficiency of the non-radiative energy transfer from the donor to the acceptor molecule is inversely dependent on the sixth power of the distance ( $r^6$ ) between these two molecules.  $R_0$  is the distance between donor and acceptor where the energy transfer is 50%.

Commonly, the proteins of interest are genetically fused to a donor or acceptor molecule. Crucial for selecting a pair of fluorescent dyes is that the emission spectrum of the donor dye (e.g. cyan fluorescent protein, CFP) overlaps with the excitation spectrum of the acceptor (e.g. yellow fluorescent protein, YFP) to enable energy transfer. CFP and YFP - a pair of

fluorescent dyes derived from the green fluorescent protein (GFP) - are widely used and fulfill this requirement. Using a confocal laser-scanning microscope, digital images are acquired through three different channels (at three different wavelengths): the CFP, YFP, and the FRET channel. Through subtraction of background and bleed-through of CFP and YFP fluorescence to the FRET image, a corrected FRET<sup>C</sup> image is generated, containing the energy transfer information (208). Overall, besides some drawbacks, such as accumulation of tagged proteins due to their overexpression, photo-bleaching of YFP, or non-optimal orientations of the large fluorescent dyes at the interacting proteins (11), FRET is a fast and sensitive method to examine protein-protein interactions in different compartments of living cells.

## 2. MATERIAL & METHODS

### 2.1. Material

#### 2.1.1. Plasmids

*Munc13 constructs:*

pEGFP-Munc13-1 (full-length)	K. Dimova/O. Jahn, MPI Göttingen
pGEX-KG Munc13-1 (445-567)	K. Dimova/O. Jahn, MPI Göttingen
pGEX-Munc13-1 (445-567)	this study (3.1.2.)
pEGFP-ubMunc13-2 (full-length)	K. Dimova/O. Jahn, MPI Göttingen
pGEX-KG ubMunc13-2 (372-494)	K. Dimova/O. Jahn, MPI Göttingen
pGEX-ubMunc13-2 (372-494)	this study (3.1.2.)
pGEX-bMunc13-2(366-780)	K. Dimova/O. Jahn, MPI Göttingen
pGEX-bMunc13-2 (366-780)	Eurofins MWG Operon
pGEX-bMunc13-2 (366-780) F580Stop	this study(3.1.4.)
pGEX-bMunc13-2 (366-780) W619Stop	this study (3.1.4.)
pGEX-bMunc13-2 (366-780) F723Stop	this study (3.1.4.)
pGEX-bMunc13-2 (366-780) W775Stop	this study (3.1.4.)
pGEX-bMunc13-2 (366-780) F580Stop 1063TAA	this study (3.1.4.)
pGEX-bMunc13-2 (366-780) W619Stop 1063TAA	this study (3.1.4.)
pGEX-bMunc13-2 (366-780) F723Stop 1063TAA	this study (3.1.4.)
pGEX-bMunc13-2 (366-780) W775Stop 1063TAA	this study (3.1.4.)
pGEX-Munc13-3 (711-1063)	K. Dimova/O. Jahn, MPI Göttingen
pGEX-Munc13-3 (711-1063)	Eurofins MWG Operon
pGEX-Munc13-3 (711-1063) F962Stop	this study (3.1.4.)
pGEX-Munc13-3 (711-1063) F1012Stop	this study (3.1.4.)
pGEX-Munc13-3 (711-1063) F787Stop	this study (3.1.4.)
pGEX-Munc13-3 (711-1063) F823Stop	this study (3.1.4.)

*other constructs:*

pCMV6-Orai3	K. Everts, University of Cambridge
pCMV6-Orai2	K. Everts, University of Cambridge
pECFP-N1-AC8	D. Willoughby, University of Cambridge

pECFP-N1-Orai1	D. Willoughby, University of Cambridge
pECFP-N1-Orai1 $\Delta$ 20	D. Willoughby, University of Cambridge
pECFP-N1-Orai1 $\Delta$ 40	D. Willoughby, University of Cambridge
pECFP-N1-Orai1 $\Delta$ 60	D. Willoughby, University of Cambridge
pECFP-N1-Orai2	this study (3.3.2.1.)
pECFP-N1-Orai3	this study (3.3.2.1.)
pECFP-N1-STIM1	D. Willoughby, University of Cambridge
pcDNA-STIM-YFP	D. Willoughby, University of Cambridge
pEYFP-C1-AC8	K. Everts, University of Cambridge
pEYFP-C1-8M1	K. Everts, University of Cambridge
pIRESneo-HA-STIM1	D. Willoughby, University of Cambridge

### 2.1.2. Oligonucleotides

All oligonucleotides were purchased from Metabion International AG (Martinsried) and used without further purification.

#### *Sequencing primers:*

**Table 1. Synthetic oligonucleotides for sequencing.** Sequences of the primers are shown from 5' to 3' end.

<b>name</b>	<b>sequence</b>
<b>pGEX fw</b>	GGGCTGGCAAGCCACGTTTGGTG
<b>Munc rev</b>	TCAGTCACGATGCGGCCGCTCGA
<b>Munc rev2</b>	CGTCATCACCGAAACGCGCG
<b>pGEX KG fw</b>	CGACCATCCTCCAAAATCGG
<b>pGEX KG rev</b>	GGTTTTACCGTCATCACCG
<b>Ac23</b>	GATAGCGGTTTGA CTACCG

#### *Primers for cloning:*

**Table 2. Synthetic oligonucleotides for cloning.** Sequences of the primers are shown from 5' to 3' end.

<b>name</b>	<b>sequence</b>
<b>#458 (Orai2 into pECFP-N1)</b>	GCCTCGAGCCACCATGAGTGCTGAGCTTAAC
<b>#459 (Orai2 into pECFP-N1)</b>	GCGGATCCCGCAAGACCTGCAGGCTGCG
<b>#460 (Orai3 into pECFP-N1)</b>	GCCTCGAGCCACCATGAAGGGCGGCGAGG
<b>#461 (Orai3 into pECFP-N1)</b>	GCGGATCCCGCACAGCCTGCAGCTCC

*Mutagenesis primers:*

**Table 3. Synthetic oligonucleotides for site directed mutagenesis.** Sequences of the primers are shown from 5' to 3' end.

<b>name</b>	<b>inserted mutation</b>	<b>sequence</b>
<b>fw2</b>	GST-Munc13-3 F962Stop	GAGAATCCGACCTTCCTAGAAAGAAGCAGC
<b>rev2</b>	GST-Munc13-3 F962Stop	GCTGCTTCTTTCTAGGAAGGTCGGATTCTC
<b>fw3</b>	GST-Munc13-3 F1012Stop	CCGCACTCCAGGTGTAGGGTGGGGCTGGGCG
<b>rev3</b>	GST-Munc13-3 F1012Stop	CGCCCAGCCCCACCCTACACCTGGAGTGCGG
<b>fw4</b>	GST-bMunc13-2 1063TAA	CCCAGAAGGTAACCTCGAGCGGCCGCATCGG
<b>rev4</b>	GST-bMunc13-2 1063TAA	CCGATGCGGCCGCTCGAGTTACCTTCTGGG
<b>fw5</b>	GST-bMunc13-2 F723Stop	CAAATGCATCAACAATTAGAAAAACGTCCTAAGAG
<b>rev5</b>	GST-bMunc13-2 F723Stop	CTCTTAGGACGTTTTTCTAATTGTTGATGCATTTG
<b>fw7</b>	GST-bMunc13-2 W775Stop	CCCCTCCTTGCCCTCAGTAGCTCCCAGAAGGGCC
<b>rev7</b>	GST-bMunc13-2 W775Stop	GGCCCTTCTGGGAGCTACTGAGGCAAGGAGGGG
<b>fw9</b>	GST-bMunc13-2 F580Stop	CGAGCGATCCACCACTAGCGTTTGGCTCTTCAG
<b>rev9</b>	GST-bMunc13-2 F580Stop	CTGAAGAGCCAAACGCTAGTGGTGGATCGCTCG
<b>fw11</b>	GST-bMunc13-2 W619Stop	CAGTGATAGACTTCTTTAGACAGTAAGTTCAGG
<b>rev11</b>	GST-bMunc13-2 W619Stop	CCTGAACTTACTGTCTAAAGAAGTCTATCACTG
<b>fw13</b>	GST-Munc13-3 F787Stop	CCTTTAAGTTCCCCAAATAGGGATCCACTCTTCAG
<b>rev13</b>	GST-Munc13-3 F787Stop	CTGAAGAGTGGATCCCTATTTGGGGAACCTTAAAGG
<b>fw15</b>	GST-Munc13-3 F823Stop	CTTAATGGGGAGATAGCGGACATTGTCTCAG
<b>rev15</b>	GST-Munc13-3 F823Stop	CTGAGACAATGTCCGCTATCTCCCCATTAAG

**2.1.3. Bacterial Strains and Human Cell Lines**

*Bacterial strains:*

BL21 (DE3) Codon Plus	<i>E.coli</i> B, <i>F<sub>ompT</sub></i> <i>hsdS</i> ( <i>r<sub>B</sub></i> - <i>m<sub>B</sub></i> -) <i>dcm</i> <sup>+</sup> Tet <sup>r</sup> galλ(DE3) <i>endA</i> Hte [ <i>argU ile Y leuW Cam</i> <sup>r</sup> ]
DH5α	<i>E.coli</i> , F <sup>-</sup> <i>endA1</i> <i>glnV44</i> <i>thi-1</i> <i>recA1</i> <i>relA1</i> <i>gyrA96</i> <i>deoR</i> <i>nupG</i> Φ80 <i>dlacZ</i> ΔM15 Δ( <i>lacZYA-argF</i> )U169, <i>hsdR17</i> ( <i>r<sub>K</sub></i> <sup>-</sup> <i>m<sub>K</sub></i> <sup>+</sup> ), λ <sup>-</sup>
XL1-Blue	<i>E.coli</i> K12, <i>endA1</i> <i>recA1</i> <i>gyrA96</i> <i>thi-1</i> <i>hsdR17</i> <i>relA1</i> <i>supE44</i> lac [F <sup>+</sup> <i>proAB</i> lacI <sup>q</sup> ΔM15 Tn10(Tet <sup>r</sup> )]

*Human cell line:*

HEK293	human embryonic kidney 293 cells
--------	----------------------------------

### 2.1.4. Media and Antibiotics

LB medium (Lysogeny Broth):	10 g/l peptone, 5 g/l yeast extract, 10 g/l NaCl
MEM (minimal essential medium):	Sigma, Gillingham (UK)
Opti-MEM:	Sigma, Gillingham (UK)
Fetal bovine serum (FBS):	Sigma, Gillingham (UK)
Carbenicillin:	100 mg/ml in H <sub>2</sub> O, final concentration: 100 µg/ml
Tetracyclin:	25 mg/ml in H <sub>2</sub> O, final concentration: 12.5 µg/ml
Chloramphenicol:	30 mg/ml in ethanol, final concentration: 30 µg/ml
Kanamycin:	30 mg/ml in H <sub>2</sub> O, final concentration: 30 µg/ml
Penicillin:	10,000 U/ml, final concentration: 100 U/ml
Streptomycin:	10 mg/ml, final concentration: 100 µg/ml
Agar plates:	15 g/l agar-agar applied in LB medium

### 2.1.5. Buffer Solutions

PBS buffer:	137 mM NaCl, 2.7 mM KCl, 10 mM Na <sub>2</sub> HPO <sub>4</sub> , 1.76 mM KH <sub>2</sub> PO <sub>4</sub> , pH 7.4
TBE buffer (10x):	45 mM Tris, 45 mM H <sub>3</sub> BO <sub>3</sub> , 0.5 mM EDTA
DNA sample buffer:	0.25% (w/v) bromphenol blue, 0.25% (w/v) xylene cyanol blue
Buffer A:	40 mM Tris-HCl, 300 mM NaCl, 2 mM EDTA, pH 7.5
Buffer B:	buffer A + 10 mM GSH + 1 mM DTT
IEX B:	20 mM HEPES, 2 M NaCl, 1 mM EDTA, pH 7.4
Washing buffer:	20 mM HEPES, 140 mM NaCl, 2.7 mM KCl, 5 mM MgCl <sub>2</sub> , pH 7.4
ITC buffer:	20 mM HEPES, 1 mM CaCl <sub>2</sub> , 100 mM KCl, pH 7.4
Biacore buffer:	20 mM HEPES, 1 mM CaCl <sub>2</sub> , 150 mM NaCl, 0.05% (w/v) Tween-20, pH 7.4
Trypsin buffer:	12 ng/µl trypsin, 0.01% ProteaseMAX™ in 50 mM NH <sub>4</sub> HCO <sub>3</sub>
ProteaseMAX™ buffer:	0.01% ProteaseMax™ in 50 mM NH <sub>4</sub> HCO <sub>3</sub>
PBS/EDTA:	1 x PBS, 1 mM EDTA
HBS buffer:	10 mM HEPES, 140 mM NaCl, 4 mM KCl, 11 mM D-glucose, 0.2 mM MgCl <sub>2</sub> , pH 7.4
CD buffer:	100 mM K <sub>2</sub> HPO <sub>4</sub> /KH <sub>2</sub> PO <sub>4</sub> , pH 7.5

### 2.1.6. Enzymes

Phusion <sup>®</sup> DNA polymerase	Thermo Fisher Scientific (Ulm)
KOD Hot Start DNA polymerase	Novagen (Darmstadt)
T4 DNA ligase	New England-Biolabs (Hertfordshire)
ProteaseMAX <sup>™</sup>	Promega (Mannheim)
Trypsin (sequencing grade)	Promega (Mannheim)
EcoRI	Thermo Fisher Scientific (Ulm)
XhoI	New England-Biolabs (Hertfordshire)
BamHI	New England-Biolabs (Hertfordshire)
Deoxyribonuclease (DNase)	Carl Roth (Karlsruhe)
Thrombin (human plasma)	Calbiochem (Bad Soden)

### 2.1.7. Proteins and Peptides

*Calbiochem (Bad Soden):*

Calmodulin (CaM) (bovine)

1 Ac-ADQLTEEQIA EFKEAFSLFD KDGDGTITTK ELGTVMRSLG QNPTEAELQD  
 51 MINEVDADGN GTIDFPEFLT MMARKMKDTD SEEEIREAFR VFDKDGNGYI  
 101 SAAELRHVMT NLGEkLTDEE VDEMIREADI DGDGQVNYEE FVQMMTAK

The protein is *N*-terminally acetylated (Ac-) and trimethylated at Lys-115 (k) as shown by peptide mass fingerprint analysis.

*amresco<sup>®</sup> (Solon, USA):*

Glutathione (GSH):  $\gamma$ -L-glutamyl-L-cysteinyl-glycine

*Synthesis by Olaf Jahn, MPI Göttingen:*

Munc13-1 peptide	RAKANWLRAF <sup>N</sup> KV <sup>R</sup> MQLQEAR
ubMunc13-2 peptide	QARAHWFRAV <sup>T</sup> TKV <sup>R</sup> LQLQEIS
bMunc13-2 peptide*	Cam-CINNFKNV <sup>L</sup> REK <sup>R</sup> LRQ <sup>K</sup> KL <sup>L</sup> QELV
Munc13-3 peptide*	Cam-CSFKEAALRAY <sup>K</sup> KQ <sup>M</sup> AEELEEK
skMLCK peptide	LMKRRW <sup>K</sup> KNFIAVSAAN <sup>R</sup> FK <sup>K</sup> ISSSGALMALGV
skMLCK F19A peptide	LMKRRW <sup>K</sup> KNFIAVSAAN <sup>R</sup> AK <sup>K</sup> ISSSGALMALGV
skMLCK F19E peptide	LMKRRW <sup>K</sup> KNFIAVSAAN <sup>R</sup> E <sup>K</sup> KISSSGALMALGV
skMLCK F19E/L31W peptide	LMKRRW <sup>K</sup> KNFIAVSAAN <sup>R</sup> E <sup>K</sup> KISSSGALMAWGV

\*The peptide is *N*-terminally carbamidomethylated (Cam-).



### *JPT Peptide Technologies GmbH (Berlin):*

AC1-C1b peptide AC-IKPAKRMKFKTVCYLLVQLMHCRKMFKA-NH<sub>2</sub>

AC8-Nt peptide AC-GSRPQRLWQTAVRHITTEQRFIHHGH-NH<sub>2</sub>

AC8-C2b peptide AC-YSLAAVVLGLVQSLNRQRQKQLLNE-NH<sub>2</sub>

The peptides are N-terminally acetylated (Ac-) and C-terminally amidated (-NH<sub>2</sub>).

### *Sigma (Taufkirchen):*

Lysozyme (chicken)

Cytochrome C (porcine)

Myoglobin (*Equus caballus*)

These proteins were used for MALDI-TOF-MS calibration.

## 2.1.8. Cross-linking and Biotinylation Reagents

### *Thermo Fisher Scientific (Darmstadt):*

D<sub>0</sub>-bis(sulfosuccinimidyl)glutarate (D<sub>0</sub>-BS<sup>2</sup>G)

D<sub>4</sub>-bis(sulfosuccinimidyl)glutarate (D<sub>4</sub>-BS<sup>2</sup>G)

Sulfosuccinimidyl 4,4'-azipentanoate (Sulfo-SDA)

EZ-Link NHS-LC-Biotin (LC-Biotin)

### *Synthesis by Fabian Krauth (Sinz lab, Halle):*

N-succinimidyl-p-benzoyldihydrocinnamate (SBC) (145)

## 2.1.9. Chemicals

Acetonitrile HPLC gradient grade, HiPerSolv		VWR
Acrylamide/bisacrylamide solution (37.5:1) 40 % (w/v)		Roth
Ammonium acetate	(CH <sub>3</sub> COONH <sub>4</sub> )	Sigma-Aldrich
Ammoniumhydrogencarbonate	(NH <sub>4</sub> HCO <sub>3</sub> )	Sigma-Aldrich
Ammoniumpersulfate	(APS)	Sigma-Aldrich
Boric acid	(H <sub>3</sub> BO <sub>3</sub> )	Roth
Calcium chloride	(CaCl <sub>2</sub> )	Roth
Complete Protease Inhibitor Cocktail Tablets		Roche
Coomassie-Brilliant-Blue G250		Sigma-Aldrich
Coomassie-Brilliant-Blue R250		Sigma-Aldrich
α-Cyano-4-hydroxycinnamic acid	(HCCA)	Sigma-Aldrich

## Material & Methods

---

Deoxyribonucleic acid triphosphates	(dNTPs)	Thermo Fisher Scientific
<i>D</i> -Glucose		Sigma-Aldrich
2,5-Dihydroxybenzoic acid	(DHB)	Sigma-Aldrich
Dimethylsulfoxide	(DMSO)	Thermo Fisher Scientific
Dithiothreitol	(DTT)	AppliChem
DNA ladder (1 kb, 100 bp)		Thermo Fisher Scientific
<i>n</i> -Dodecyl- $\beta$ - <i>D</i> -maltoside	(DDM)	Roth
Ethanol		Merck
Ethyleneglycol tetraacetic acid	(EGTA)	Sigma-Aldrich
Ethylenediaminetetraacetic acid	(EDTA)	Sigma-Aldrich
Formic acid	(FA)	Roth
GelGreen™ Nucleic Acid Gel Stain		Biotium
Hydrochloric acid, 0.1 M (endotoxin free)		Sigma-Aldrich
[4-(2-Hydroxyethyl) piperazine] ethanesulfonic acid	(HEPES)	Roth
Isopropanol		Merck
Isopropyl- $\beta$ - <i>D</i> -1-thiogalactopyranoside	(IPTG)	Roth
Laemmli sample buffer		Bio-Rad
L-Glutamine		Sigma-Aldrich
Lipofectamine™ 2000		Invitrogen
Magnesium chloride	(MgCl <sub>2</sub> )	Thermo Fisher Scientific
Magnesium sulfate	(MgSO <sub>4</sub> )	Sigma-Aldrich
Peptide Calibration Standard II mono		Bruker Daltonik
Phenylmethylsulfonyl fluoride	(PMSF)	Roth
Phosphate buffered saline (tablets)	(PBS)	amresco®
$\epsilon$ -Poly- <i>L</i> -lysine		Sigma-Aldrich
Potassium chloride	(KCl)	Roth
Protein Calibration Standard I and II		Bruker Daltonik
Protein ladder (PageRuler™ Unstained)		Thermo Fisher Scientific
Sinapinic acid (3,5-dimethoxy-4-hydroxycinnamic acid)	(SA)	Sigma-Aldrich

Sodium chloride	(NaCl)	Roth
Sodium dodecylsulfate	(SDS)	Roth
<i>N,N,N',N'</i> -Tetramethylethylenediamine	(TEMED)	Roth
Thapsigargin	(Tg)	Calbiochem
Trifluoroacetic acid	(TFA)	Merck
2,2,2-Trifluoroethanol	(TFE)	Sigma-Aldrich
Tris(hydroxymethyl)aminomethane	(Tris)	Roth
Tris(hydroxymethyl)aminomethanehydrochloride	(Tris-HCl)	Roth
Triton X-100		Roth
Tween-20		Serva

### 2.1.10. Kits

Plasmid Mini-Prep Kit	Jena Bioscience
PCR Purification Kit	Jena Bioscience
QIAquick Gel Extraction Kit	Qiagen

### 2.1.11. Equipment

#### *Systems:*

MALDI-TOF/TOF-MS:	Ultraflex III (Bruker Daltonik, Bremen) with SmartBeam laser™ (Bruker Daltonik, Bremen) and fraction collector Proteineer fc (Bruker Daltonik, Bremen)
ESI-LTQ-Orbitrap-MS:	LTQ Orbitrap XL (Thermo Fisher Scientific, Bremen) with a nano-ESI-Source (Proxeon, Odense, Denmark)
Nano-HPLC systems:	<ul style="list-style-type: none"> <li>▪ Ultimate 3000 (Dionex, Idstein)</li> <li>▪ Ultimate (Dionex, Idstein)</li> </ul> with Ultimate Micro Pump, Ultimate UV-Detector, Ultimate SWITCHOS II, and Famos Micro-Autosampler
▪ Trapping columns	Acclaim PepMap, C18, 100 μm x 20 mm, 5 μm, 100 Å Acclaim PepMap, C18, 300 μm x 5 mm, 5 μm, 100 Å (Dionex Idstein)
▪ Separation columns	Acclaim PepMap, C18, 75 μm x 200 mm, 3 μm, 100 Å Acclaim PepMap, C18, 75 μm x 150 mm, 3 μm, 100 Å (Dionex, Idstein)

## Material & Methods

---

Cell disruption system	type Basic-Z, Constant Systems Ltd. (Northamptonshire, UK)
FPLC system	ÄKTA FPLC with fraction collector Frac-920 (GE Healthcare, Munich)
Biacore <sup>®</sup> T100	GE Healthcare, Munich
CD spectrometer	J-810 Circular Dichroism (Jasco, Groß-Umstadt)
Calorimeter	VP-ITC (MicroCal, Prague, CZ)
Electrophoresis systems	▪ DNA electrophoresis chamber Mini-Sub-Cell GT (Bio-Rad, Munich) ▪ gel electrophoresis apparatus Mini-Protean Tetra Cell with power supply POWERPACK 300 (Bio-Rad, Munich)
Gel documentation system	Gel Doc XR (Bio-Rad, München)
UV-spectrophotometers	▪ Ultrospec 1100 pro (GE Healthcare, Munich) ▪ NanoVue <sup>™</sup> Plus (GE Healthcare, Bucks, UK)
Centrifuges	▪ Optimal <sup>™</sup> L-90K (Beckmann Coulter, Krefeld) ▪ Avanti <sup>™</sup> J-20 XP (Beckmann Coulter, Krefeld) ▪ miVac Duo vacuum concentrator (GeneVac, Ipswich, UK)
Water purification system	▪ DirectQ5 (Millipore, Eschborn) ▪ Pacific-UP/UPW (ThermoFisher Scientific-TKA, Niederelbert)
Microscope	Nikon eclipse TE2000 inverted microscope equipped with a 40 x oil immersion objective (Nikon, Surrey, UK), connected to an Andor Ixon+ EMCCD camera (Andor, Belfast, UK) via an Optosplit (505DC) (Cairn Research, Kent, UK)

### *Miscellaneous:*

Amicon <sup>®</sup> Ultra centrifugal units (3K, 10K)	Millipore, Eschborn
Autoclave V75	Systec, Wettenberg
Float-A-Lyzer G2	Spectrum, Breda, NL
GSTrapFF, 1 ml	GE Healthcare, Munich
HiTrap Q XL, 1 ml	GE Healthcare, Munich
Micro columns ZipTipC4 and C18	Millipore, Eschborn
pH meter MV 870	Präcitronic, Dresden
MJ Research PTC-150 Minicycler	Bio-Rad, Hertfordshire, UK
Thermocycler TPersonal	Biometra, Göttingen

### 2.1.12. Software

CoolToolBox	Software for identification of cross-linked products (Leo J. de Koning, University of Amsterdam, The Netherlands)
Flex Analysis 3.3	Software for visualization and processing of mass spectra (Bruker Daltonik)
Flex Control 3.3	Acquisition of MALDI-TOF/TOF-MS(/MS) data (Bruker Daltonik)
Gentle	Software program for visualization and processing of DNA and protein sequences (Magnus Manske, University of Cologne)
Hystar 3.2	Software for control and coordination of HPLC systems and mass spectrometer (Bruker Daltonik)
Mascot	Evaluation software for mass spectrometry data (MS and MS/MS), <i>in-house</i> license, <a href="http://www.matrixscience.com">www.matrixscience.com</a>
Max chelator	Software for calculation of free $\text{Ca}^{2+}$ concentrations ( <a href="http://maxchelator.stanford.edu/">http://maxchelator.stanford.edu/</a> )
Patchdock server	Web server for docking of two molecules using distance constraints ( <a href="http://bioinfo3d.cs.tau.ac.il/PatchDock/">http://bioinfo3d.cs.tau.ac.il/PatchDock/</a> )
ProteomeDiscoverer 1.0	Software for analysis of MS, MS/MS and LC-MS data (Thermo Fisher Scientific)
PSIPRED, SAM-T08 web server	Software for secondary structure prediction, ( <a href="http://bioinf.cs.ucl.ac.uk/psipred/">http://bioinf.cs.ucl.ac.uk/psipred/</a> ) ( <a href="http://compbio.soe.ucsc.edu/SAM_T08/T08-query.html">http://compbio.soe.ucsc.edu/SAM_T08/T08-query.html</a> )
Pymol 0.99rc6	3D-grafic software for visualization and processing of protein structures (DeLano Scientific LLC, US)
StavroX versions 2.0.6 and 2.3.1.	Software for analysis and identification of cross-linking products (Michael Götze, University Halle-Wittenberg, (149))
Qual Browser 2.07	Software for visualization and processing of mass spectra (Thermo Fisher Scientific)

## **2.2. Molecular Biology Techniques**

### **2.2.1. Preparation of Chemo-Competent Cells**

Chemo-competent cells were prepared following the protocol of the CaCl<sub>2</sub>-method by Sambrook & Russell (209). Briefly, 200 ml LB medium were inoculated with 5 ml of an overnight culture of XL1-Blue, DH5 $\alpha$ , or BL21 (DE3) Codon Plus cells and cultivated at 37 °C to an optical density OD<sub>600</sub> between 0.4 and 0.7. Then, the cells were centrifuged for 15 min at 5000 rpm (4 °C). The cell pellet was resuspended in 50 ml of a 0.1 M CaCl<sub>2</sub> solution (sterile and ice cold) and incubated for 90 - 120 min on ice. Afterwards, the suspension was centrifuged again (15 min, 5000 rpm, 4 °C) and the cell pellet was resuspended in 2 ml of 0.1 M CaCl<sub>2</sub>. Following incubation for another 90 - 120 min on ice, glycerol was added to a final concentration of 10% (v/v), the cells were rapidly frozen in liquid nitrogen, and stored in 200  $\mu$ l-aliquots at -80 °C.

### **2.2.2. Transformation of DNA in Chemo-Competent Cells**

One aliquot (200  $\mu$ l) of chemo-competent cells was thawed on ice before 1 - 2  $\mu$ l plasmid DNA were added. After incubation on ice for 30 min, a 90 s-heat shock was performed at 42 °C. Subsequently, 800  $\mu$ l of LB medium were added to the cells. In the case of constructs with a kanamycin resistance, the cells were then incubated for 1 h at 37 °C (for constructs with ampicillin resistance incubation time was shortened to 10 - 30 min). 100  $\mu$ l of cell suspension were applied to agar plates containing the respective antibiotic agent and cultured overnight at 37 °C to select for cells carrying the DNA of interest.

### **2.2.3. Isolation of Plasmid DNA from *E.coli***

Plasmid DNA was isolated from 3 to 5 ml of an overnight-culture of XL1-Blue or DH5 $\alpha$  cells containing the DNA of interest. The cells were harvested and the DNA was isolated using the Plasmid Mini-Prep Kit (Jena Bioscience) according to the manufacturer's protocol. The elution was performed with 40  $\mu$ l *MilliQ* water.

### **2.2.4. Polymerase Chain Reaction**

*In-vitro* amplification of DNA was carried out by polymerase chain reaction (PCR). A 50  $\mu$ l-PCR reaction contained approximately 50 ng template DNA, 100 pmol of forward and reverse

primers, 4 mM MgSO<sub>4</sub>, 2 mM of each dNTP, and 1 U polymerase (Phusion<sup>®</sup>DNA polymerase or KOD Hot Start DNA polymerase, 2.1.6.). The program in the thermocycler (2.1.11.) is shown in Table 4:

**Table 4. PCR program for DNA amplification.**

reaction step	temperature	time	number of cycles
denaturation	98 °C	30 s	1
denaturation	98 °C	10 s	
primer annealing	55-60 °C	30 s	25
elongation	72 °C	45 s-1 min 30 s	
final elongation	72 °C	5 min	1
storage	4-10 °C	∞	

Annealing temperatures were chosen 5 °C lower than calculated and elongation times were adapted to the respective polymerase and DNA used in the reaction. In the case of a cloning procedure, PCR reactions were purified using the QIAquick Gel Extraction Kit (Qiagen). Visualization of the PCR reactions was carried out by agarose gel electrophoresis (2.2.7.).

### 2.2.5. Site-directed Mutagenesis

PCR reactions for site-directed mutagenesis were prepared as depicted in Table 5. The PCR program is shown in Table 4. Visualization of the PCR products was carried out by agarose gel electrophoresis (2.2.7.).

**Table 5. Components of a 50 µl-PCR reaction for site-directed mutagenesis.**

Volume	component
1 µl	template DNA
1 µl	dNTPs
2 µl	forward primer
2 µl	reverse primer
10 µl	10 x GC polymerase buffer
1 µl	Phusion <sup>®</sup> DNA polymerase
31 µl	MilliQ water

After transformation of the PCR reactions (2 - 10 µl) into *E.coli* chemo-competent cells (2.2.2.) and antibiotic selection of cells containing the DNA of interest, the mutated DNA was isolated (2.2.3.) and sequenced (2.2.10.).

### **2.2.6. DNA Digestion with Restriction Endonucleases**

Analytical DNA digestions were performed for sequence confirmation of a vector of interest, while preparative DNA digestion by endonucleases was carried out as a substep of a cloning procedure. A typical 50  $\mu$ l-digestion in *MilliQ* water contained 4  $\mu$ g of DNA (in the case of a vector plasmid) or 30  $\mu$ l of a PCR reaction (in the case of subcloning), 5  $\mu$ l of the recommended buffer (New England Biolabs), 0.5  $\mu$ l BSA (if recommended for the respective restriction enzyme), and 1 - 2 U of the restriction enzymes (EcoRI, BamHI or XhoI, respectively). Incubation of analytical digests was carried out at 37 °C for 3 h, while preparative digests were incubated overnight at 37 °C. Visualization of the DNA digestion was performed using agarose gel electrophoresis (2.2.7.).

### **2.2.7. Agarose Gel Electrophoresis**

Separation of DNA according to their molecular size was performed using 1 or 1.2% (w/v) agarose gels in 0.5 x TBE buffer (2.1.5.). The DNA was mixed with DNA sample buffer (2.1.5.) and loaded onto the gel. Electrophoretic separation was conducted at 200 V. Detection of the DNA in the gels was carried out with UV light (gel documentation system Gel Doc XR, 2.1.11.) after a 30 min-incubation of the gels in a staining solution containing GelGreen™ (15  $\mu$ l of a 10000 x stock solution), 45 ml *MilliQ* water, and 5 ml NaCl [1 M]. Alternatively, ethidium bromide was used.

### **2.2.8. Gel Extraction of DNA**

Bands of interest were excised from the agarose gels and the DNA was extracted using the QIAquick Gel Extraction Kit (Qiagen). Extraction was performed following the manufacturer's protocol, except for the elution step, in which *MilliQ* water (35  $\mu$ l) was used instead of the elution buffer. Concentration determination of the extracted DNA was performed spectrophotometrically ( $\lambda = 260$  nm) (NanoVue™ Plus or Ultrospec 1100 pro, 2.1.11.).

### **2.2.9. Ligation**

Digested plasmid and insert with compatible ends were mixed at molar ratios of 1:2 or 1:4 and added to a 20  $\mu$ l-reaction with T4 DNA ligase (2.1.6.) in the recommended buffer. The ligation reaction was allowed to proceed overnight at 16 °C. Afterwards, 10  $\mu$ l of the reaction



mixtures were transformed into *E.coli* chemo-competent cells (2.2.2.) for antibiotic selection of cells containing the DNA of interest. Subsequently, the DNA was isolated (2.2.3.) and sequenced (2.2.10.).

### **2.2.10. Sequencing**

All DNAs used and generated in this work were sequenced by the Sequence Laboratories Göttingen (Munc13 constructs) or the Department of Biochemistry in Cambridge, UK (Orai2 and 3 constructs). Analysis of the sequencing results was performed using the software program *Gentle*.

## **2.3. Cell Biology Techniques**

### **2.3.1. Cell Culture and Transfection**

Cultivation of HEK293 cells (European Collection of Cell Cultures, Porton Down, UK) was performed in minimal essential medium (2.1.4.) supplemented with 10% (v/v) fetal bovine serum (FBS, 2.1.4.), 100 U/ml penicillin, 100 µg/ml streptomycin, and 2 mM L-glutamine. The cells were grown at 37 °C in a humidified atmosphere (95% air and 5% CO<sub>2</sub>). Dilution of the cells was carried out in PBS/EDTA buffer (2.1.5.), which was added to the flask after removing the medium, in which the cells were grown. The cells were collected, centrifuged, and resuspended in fresh medium (see above). For transient transfection, untransfected HEK293 cells were plated onto 25-mm coverslips coated with ε-poly-L-lysine. After the cells had reached a confluence of ~60%, 2 µg of cDNA (1 µg of the YFP-tagged protein and 1 µg of the CFP construct) were transfected using Lipofectamine™ 2000 according to the manufacturer's protocol.

### **2.3.1. Micro-FRET Analysis of Protein-Protein Interactions**

Two or three days after transfection, FRET analysis of the interaction of two constructs (YFP and CFP-tagged) was performed on a Nikon eclipse TE2000 inverted microscope equipped with a 40 x oil immersion objective. To separate CFP (470 nm) and YFP (535 nm) emission images, the microscope was connected to an Andor Ixon+ EMCCD camera via an Optosplit (505DC). Prior to FRET analysis, the medium was removed from the coverslips and HBS buffer (2.1.5.), supplemented with 1.5 mM CaCl<sub>2</sub>, was applied. The coverslips were placed

into the microscope and washed several times with HBS buffer to remove cells that were only loosely attached. After focussing on the cells, images were acquired and analyzed according to the three-cube micro-FRET method (208). First, a number of live cell images were collected from cells expressing CFP or YFP alone to calculate the values for CFP and YFP bleed-through into the FRET signal. In the case of cells co-expressing CFP- and YFP-tagged proteins of interest, three separate live cell images were acquired: (1) the CFP image (435 nm excitation/470 nm emission), (2) the YFP image (500 nm excitation/535 nm emission), and (3) the uncorrected FRET image (435 nm excitation/535 nm emission). After background subtraction of all three images, the FRET image was corrected for CFP (59%) and YFP (11.2%) bleed-through to get a corrected pseudocolor FRET image, FRET<sup>c</sup>. For quantification of the FRET signals from different constructs, normalized NFRET<sup>c</sup> values were obtained by dividing the average intensities of the FRET<sup>c</sup> images by the product of the CFP and YFP image intensities. All FRET experiments were additionally conducted under conditions of Ca<sup>2+</sup> store depletion by adding HBS buffer containing 1 μM thapsigargin (Tg) to the coverslips.

## 2.4. Protein Chemistry

### 2.4.1. Expression of Munc13 Variants

A 50 - 100 ml-overnight culture of *E.coli* BL21 (DE3) Codon Plus cells containing the DNA of the protein of interest was divided and transferred into two beakers each containing 2.5 l LB medium. For antibiotic selection, carbenicillin (100 μg/ml) was supplemented to the medium and cells were grown at 37 °C until the optical density (OD<sub>600</sub>) reached a value between 0.4 and 0.6. Then, protein synthesis was induced by the addition of 0.1 - 1 mM IPTG and incubation was performed for 4 - 16 hrs at 18 - 37 °C. The amount of the protein - synthesized and located either in the soluble fraction or as inclusion bodies - was visualized by SDS-PAGE (2.4.4.).

### 2.4.2. Purification of Munc13 Variants

Cells were harvested by centrifugation at 5,000 rpm, 4 °C for 20 min. The cell pellet was washed with cold PBS buffer, frozen at -20 °C, and stored overnight to gently break the cell walls. After resuspension of the cell pellet in buffer A (2.1.5.) and addition of Complete Protease Inhibitor Cocktail (1 tablet in 50 ml cell suspension) and 1 mM DTT, disruption of

the cells was performed using the cell disruption system type Basic-Z (Constant Systems Ltd.) at a pressure of 2.3 kbar. Then, 0.5 mM PMSF and 0.1% (v/v) Triton X-100 were added and the solution was incubated on ice for 30 min. Fragments of the cell wall, cell organelles and other particles were pelleted by centrifugation at 40,000 rpm for 45 min. The supernatant was loaded on a GST-affinity column (GSTrapFF, 1 ml) at a flow rate of 0.2 ml/min using an ÄKTA FPLC system (2.1.11.). Further purification was performed either by (1) on-column cleavage of the GST tag by thrombin (0.33 mg/ml in washing buffer (2.1.5.) containing 1% (w/v) DDM) overnight and elution of the untagged Munc13 (flow rate: 0.5 ml/min) or (2) by elution of the GST-tagged Munc13, buffer-exchange, thrombin cleavage (2 - 16 U in washing buffer containing 1% (w/v) DDM) overnight at 8 °C and subsequent separation of the untagged protein from the GST tag by anion exchange chromatography (HiTrap Q XL column, 1 ml). The amount and purity of Munc13 proteins were determined by SDS-PAGE (2.4.4.). Determination of the protein concentration was performed spectrophotometrically (Ultrospec 1100 pro, 2.1.11.).

### **2.4.3. Buffer Exchange of Protein and Peptide Solutions**

Different systems were used for buffer exchange of peptide and protein solutions. Dialysis of peptides prior to SPR, ITC, and CD measurements was performed using Float-A-Lyzer G2 (2.1.11.) with a molecular weight cutoff of 100-500 Da or 500-1,000 Da according to the manufacturer's protocol. Peptide solutions used in *offline* nano-ESI-MS experiments were subjected to microfiltration (Amicon Ultra centrifugal units (3 K), Millipore, Schwalbach). Peptide solutions were transferred to the filtration units and centrifuged at 13,000 x g for 30 min. After three washing steps with buffer, peptides were eluted by centrifugation for 7 min at 4,000 x g. The same protocol was applied for buffer exchange of protein solutions for ITC, SPR, and *offline* nano-ESI-MS measurements using Amicon Ultra centrifugal units (10 K) (2.1.11.). Concentrations of the resulting peptide and protein solutions were determined spectrophotometrically ( $\lambda = 280$  nm) (Ultrospec 1100 pro, 2.1.11.).

### **2.4.4. SDS-PAGE**

Protein separation according to apparent molecular size was performed by sodium dodecyl sulfate polyacrylamide gel electrophoresis (SDS-PAGE). The compositions of resolving and stacking gels are shown in Table 6. Protein samples were mixed (1:1 (v/v)) with

*Laemmli* buffer supplemented with  $\beta$ -mercaptoethanol and loaded on an SDS gel, before the electrophoretic separation was carried out at 100 V for 15 min and at 200 V for 35 - 45 min.

**Table 6. Composition of resolving and stacking gels for SDS-PAGE.** Volumes are given for preparing two SDS gels.

	resolving gel 12%	resolving gel 15%	stacking gel 5%
<b>acrylamide/bis-acrylamide solution 40% (w/v)</b>	3000 $\mu$ l	3750 $\mu$ l	650 $\mu$ l
<b>1.5 M Tris-HCl, pH 8.8</b>	2500 $\mu$ l	2500 $\mu$ l	-
<b>0.5 M Tris-HCl, pH 6.8</b>	-	-	1250 $\mu$ l
<b>MilliQ water</b>	4340 $\mu$ l	3590 $\mu$ l	3000 $\mu$ l
<b>10% (v/v) SDS</b>	100 $\mu$ l	100 $\mu$ l	50 $\mu$ l
<b>TEMED</b>	10 $\mu$ l	10 $\mu$ l	10 $\mu$ l
<b>10% (v/v) APS</b>	50 $\mu$ l	50 $\mu$ l	25 $\mu$ l

Following electrophoresis, the gels were stained using a colloidal Coomassie-Blue-Silver staining protocol (210):

*Fixing solution:* 40% (v/v) MeOH, 10% (v/v) acetic acid

*Staining solution:* 2% (v/v) solution A, 98% (v/v) solution B

solution A: 5% (w/v) Coomassie-Brilliant-Blue G250 in *MilliQ*-H<sub>2</sub>O

solution B: 2% (w/v) orthophosphoric acid, 20% (w/v) (NH<sub>4</sub>)<sub>2</sub>SO<sub>4</sub> in *MilliQ*-H<sub>2</sub>O

*Destaining:* *MilliQ*-H<sub>2</sub>O

The gels were incubated in the fixing solution for 1 h, washed three times with *MilliQ* water, and transferred to the staining solution for incubation overnight. Destaining was performed by shaking the gels in *MilliQ* water.

#### 2.4.5. *In-Gel* Digestion

Bands of interest were excised from an SDS gel, cut into pieces of ca. 1 mm<sup>3</sup> volume, and washed with 100  $\mu$ l *MilliQ* water, twice with 100  $\mu$ l of 50% (v/v) ACN in *MilliQ* water, and incubated for 10 min. The supernatant was removed after each washing step. Afterwards, 80  $\mu$ l of ACN were added and the supernatant was removed after 5 min incubation. Subsequently, 80  $\mu$ l of NH<sub>4</sub>HCO<sub>3</sub> were added, an additional 80  $\mu$ l of ACN were added after 5 min, and the mixture was incubated for 10 min. After removing the supernatant, the gel pieces were dried in a vacuum concentrator for 30 min (2.1.11.) and (if not used immediately)

stored at -20 °C after shock freezing. For proteolysis, 20 µl of trypsin buffer (2.1.5.) were added to the gel pieces and the mixture was incubated for 10 min on ice. After addition of 30 µl ProteaseMAX™ buffer (2.1.5.), proteolysis was allowed to proceed at 37 °C for 2 - 4 hrs. The supernatant was transferred into a new reaction vessel, 1 µl 10% (v/v) TFA was added for trypsin inactivation, and analysis of the peptide mixture was performed immediately by nano-HPLC/nano-ESI-Orbitrap-MS/MS (2.5.5.) or nano-HPLC/MALDI-TOF/TOF-MS/MS (2.5.4.).

### **2.4.6. Circular Dichroism Spectroscopy**

Peptides were dialyzed (2.4.3.) against the CD buffer (2.1.5.) prior to circular dichroism (CD) spectroscopic analysis on a Jasco J-810 Circular Dichroism spectrometer (2.1.11.). The peptide concentration was determined spectrophotometrically at 280 nm. Far-UV CD spectra were recorded at 4 °C in a 0.5 nm fused silica cuvette by accumulating 20 far-UV spectra from 200 to 260 nm in the presence of 0 - 40% (v/v) TFE. A scan rate of 20 nm/min, a 4 s-response, and a bandwidth of 1 nm were used for data acquisition. CD data were processed with the software program Spectrum Manager I.

### **2.4.7. Isothermal Titration Calorimetry**

Proteins and peptides were dialyzed (2.4.3.) against the same buffer (ITC buffer, 2.1.5.) and degassed before their interaction was analyzed by isothermal titration calorimetry (ITC) in cooperation with S. Pfennig (University Halle-Wittenberg). A 5 - 10 µM-solution of CaM was placed into the reaction cell of a VP-ITC system (2.1.11.), while a 50 - 100 µM-solution of the peptide of interest was filled into the ITC syringe. The peptide was titrated to the CaM solution by 10 µl-injections in 5 min-intervals. Heats of dilution were measured by titration of a buffer without peptide to the CaM solution. This reference curve was subtracted from the peptide titration curve. The temperature was set to 25 °C throughout all measurements.

### **2.4.8. Surface Plasmon Resonance Spectroscopy**

The CaM-binding affinities of different skMLCK variants were determined by surface plasmon resonance (SPR) spectroscopy on a Biacore T100 instrument (2.1.11.) in cooperation with M. Schneider (University Halle-Wittenberg). The skMLCK peptides were *N*-terminally biotinylated using EZ-Link NHS-LC-Biotin (2.1.8.). Peptide : biotinylation reagent ratios varied between 1:10 and 10:1 (w/w). The biotinylation reaction was conducted in PBS buffer

(pH 6.5) and allowed to proceed for 30 min on ice, before excess of biotinylation reagent was quenched with 10 - 20 mM  $\text{NH}_4\text{HCO}_3$  (final concentration) and removed by microfiltration (2.4.3). MALDI-TOF mass spectrometry (2.5.3.) was used to confirm mono-biotinylation of all peptides. Following biotinylation, the peptides were immobilized on a Series S Sensor Chip SA (GE Healthcare, Freiburg) according to the manufacturer's protocol. A solution of 1 M NaCl with 50 mM NaOH was applied to the chip to remove non-covalently bound streptavidin. Afterwards, the peptide solutions were injected using a flow rate of 5  $\mu\text{l}/\text{min}$  until the immobilization rate reached 350 RU (RU: arbitrary response units). For the skMLCK F19E peptide, the maximum immobilization level was 250 RU. All measurements were performed at 25 °C using the Biacore buffer (2.1.5.), in which CaM was diluted to different concentrations (100 pM - 20  $\mu\text{M}$ ). CaM solutions were injected over the chip surface at a flow rate of 12  $\mu\text{l}/\text{min}$  for 1750 s. Biacore buffer (2.1.5.) was used as a blank. Regeneration of the chip was performed for 2 min at a flow rate of 12  $\mu\text{l}/\text{min}$  with 20 mM HEPES buffer (pH 7.4) containing 10 mM EGTA and 0.05% (v/v) Tween20. Steady state responses were calculated by double referencing and averaging the data over 10 s at the end of the association injection. Equilibrium dissociation constants ( $K_D$ ) were determined by fitting the steady-state data to equation 13 using SigmaPlot 11.0.

$$R_{eq} = R_{max}C/(K_D + C) + NC \quad (eq13)$$

$R_{eq}$  is the steady state response,  $K_D$  the equilibrium dissociation constant,  $C$  the CaM concentration,  $R_{max}$  the saturation binding response of the high-affinity binding phase, and  $N$  is the slope of the observed linear binding phase.

## 2.5. Chemical Cross-linking and Mass Spectrometric Analysis

### 2.5.1. Chemical Cross-linking with Homobifunctional Reagents

CaM (10  $\mu\text{M}$ ) was incubated for 10 min at room temperature in a buffer containing 10 - 20 mM HEPES and  $\text{Ca}^{2+}$  concentrations between 30 nM and 1 mM.  $\text{Ca}^{2+}$  concentrations in the nanomolar range were obtained using a  $\text{Ca}^{2+}$ /chelator (EGTA) system (calculated using the Max chelator software, 2.1.12.). The respective CaM target peptide was added and incubated with the CaM solution for 30 min at room temperature to form the CaM/peptide complexes. Cross-linking reactions were started by addition of a 50-fold molar excess of the homobifunctional amine-reactive cross-linker BS<sup>2</sup>G (bis(sulfosuccinimidyl)glutarate). The

cross-linking reactions were allowed to proceed for 30 min at room temperature, before non-reacted BS<sup>2</sup>G was quenched with NH<sub>4</sub>HCO<sub>3</sub> (final concentration 20 mM).

### 2.5.2. Chemical Cross-linking with Heterobifunctional Reagents

Cross-linking reactions with the heterobifunctional amine- and photo-reactive cross-linkers SBC (*N*-succinimidyl-*p*-benzoyldihydrocinamate) and sulfo-SDA (sulfosuccinimidyl 4,4'-azipentanoate) were conducted in a two-step fashion. CaM was diluted to 10 μM in 20 mM HEPES buffer (pH 7.4) containing 30 nM to 1 mM Ca<sup>2+</sup>. Nanomolar Ca<sup>2+</sup> concentrations were obtained by using a Ca<sup>2+</sup>/chelator (EGTA) system (calculated using the Max chelator software, 2.1.12.). After incubation at room temperature for 10 min, CaM was reacted with the amine-reactive site of the cross-linker (200 - 500 μM). Excess cross-linker was quenched with NH<sub>4</sub>HCO<sub>3</sub> (final concentration 20 mM) and removed by microfiltration using Amicon Ultra Centrifugation Units (10 K) (2.4.3.). Then, the CaM target peptide (10 μM) or protein (~10 μM) was added to the cross-linker-modified CaM. The mixture was incubated at room temperature for 30 min and then irradiated with long-wavelength UV light (maximum at 365 nm, irradiation energies 0, 4000, and 8000 mJ/cm<sup>2</sup>) to yield photo-cross-linked products.

### 2.5.3. MALDI-TOF Mass Spectrometry

Analysis of intact cross-linked samples was performed by MALDI-TOF-MS on an Ultraflex III mass spectrometer (2.1.11.) operated in the linear, positive ionization mode (*m/z* range 5,000 - 25,000). Cross-linking reaction mixtures were desalted prior to analysis with the help of ZipTipC4 micro columns (2.1.11.) and spotted on a steel target. Sinapinic acid (SA) or 2,5-dihydroxybenzoic acid (DHB) were used as matrices. Spectra from up to 2,000 laser shots were accumulated to one spectrum using FlexControl version 3.3 and processed with FlexAnalysis version 3.3 (2.1.12.).

### 2.5.4. Nano-HPLC/MALDI-TOF/TOF Mass Spectrometry

Tryptic peptide mixtures of the cross-linking reactions containing CaM and Munc13-1 or ubMunc13-2 were separated by nano-HPLC (Ultimate 3000, 2.1.11.) prior to MALDI-TOF/TOF-MS/MS analysis. Samples were concentrated on a trapping column (RP C18, 5 mm x 300 μm, 5 μm, 100 Å) with 0.1% (v/v) TFA at a flow rate of 30 μl/min, eluted onto the separation column (RP C18, 150 mm x 75 μm, 3 μm, 100 Å) and separated using a 90-min gradient from 5% (v/v) to 42.5% (v/v) acetonitrile (ACN) at a flow rate of 300 nl/min.

The eluates were fractionated onto a Bruker 800/384 AnchorChip target (Bruker Daltonik) using an LC/MALDI fraction collector (Proteinier fc, 2.1.11.) controlled via HyStar 3.2. (2.1.12.). Per spot, 1.1  $\mu$ l of matrix [0.71 mg/l HCCA in 90% (v/v) ACN, 0.1% (v/v) TFA, and 1 mM  $\text{NH}_4\text{H}_2\text{PO}_4$ ] was added. MALDI-TOF/TOF-MS/MS measurements were conducted in positive ionization and reflection mode on an Ultraflex III instrument (2.1.11.). Mass spectra were externally calibrated using Peptide Calibration Standard II (2.1.9.). Data were acquired with WarpLC 1.2 using FlexControl (2.1.12) and FlexAnalysis (2.1.12) scripts for data processing. For each spot, mass spectra were recorded in the range  $m/z$  800 - 5,000 by accumulating 2,000 laser shots. The three most intense peaks (signal-to-noise threshold > 10) of each full scan were selected for fragmentation; for every spot, a maximum of seven MS/MS measurements were performed.

### **2.5.5. Nano-HPLC/Nano-ESI-LTQ-Orbitrap Mass Spectrometry**

Fractionation of tryptic peptide mixtures was conducted on an Ultimate nano-HPLC system (2.1.11.). After desalting the samples on the trapping column (C18, 100  $\mu$ m x 20 mm, 5  $\mu$ m, 100  $\text{\AA}$ , 2.1.11.) for 15 min with 0.1% (v/v) TFA, the peptides were eluted onto the separation column (C18, 75  $\mu$ m x 200 mm, 3  $\mu$ m, 100  $\text{\AA}$ ). Separation was carried out by applying a 90-min gradient 0 - 50% B (A: 5% (v/v) ACN containing 0.1% (v/v) FA; B: 80% (v/v) ACN containing 0.08% (v/v) FA) at a flow rate of 300 nl/min. The nano-HPLC system was directly coupled to the nano-ESI source (2.1.11.) of an LTQ-OrbitrapXL hybrid mass spectrometer (2.1.11), which was operated in positive ionization mode. MS data were acquired in data-dependent MS/MS mode: The five most intense signals of the full scan mass spectrum (orbitrap, R = 60,000) were isolated (isolation window 2.5 Th) and fragmented by CID in the linear ion trap (LTQ). Detection of less abundant ions was allowed by applying dynamic exclusion (exclusion duration 120 s, after three repeats of fragmentation of one precursor). Data acquisition was controlled via XCalibur 2.0.7 (2.1.12.) in combination with DCMS link 2.0 (Dionex, Idstein, Germany).

### **2.5.6. Offline Nano-ESI Mass Spectrometry**

All protein and peptide solutions used in *offline* nano-ESI-MS experiments were dialyzed against 20 mM  $\text{NH}_4\text{CH}_3\text{COO}$  (2.4.3.). For binding experiments with CaM target peptides (AC8, AC1, skMLCK, and Munc13), reaction mixtures containing 10  $\mu$ M peptide, 10  $\mu$ M CaM, and 1 mM  $\text{CaCl}_2$  or/and EGTA (200  $\mu$ M - 10 mM) were analyzed. Five  $\mu$ l of protein or



protein/peptide solution were filled into a metal-coated borosilica emitter (Proxeon, Odense, Denmark) and sprayed into an LTQ-OrbitrapXL mass spectrometer equipped with a nano-ESI source (2.1.11.). Mass spectra were acquired in the orbitrap ( $R = 100,000$ ) in the  $m/z$  range 1,500 - 3,500 in positive ionization mode and signals were deconvoluted with Xcalibur 2.0.7 (2.1.12.).

### 2.5.7. Identification of Cross-linked Products

Mass spectrometry data (MS and MS/MS) were analyzed using either GPMW 8.2 (148) in combination with the software tool CoolToolBox (211) or the *in-house* software program StavroX version 2.0.6 or 2.3.1 (2.1.12., (149)) together with XCalibur 2.0.7 (2.1.12.). Mass deviation was set to 3 ppm, the maximal number of missed cleavages was set to 3 after Lys and Arg, and the signal-to-noise ratio was defined to be higher than 2. For cross-linking studies with homobifunctional amine-reactive cross-linkers, Lys, Ser, and Thr residues in the proteins/peptides were considered as potential reaction sites of the NHS group. In the case of structural analysis with the heterobifunctional cross-linkers SBC and SDA, Lys residues of CaM and Met, Ala, Ile, Leu, Lys, Arg, Phe, Pro residues of the target peptides (Munc13, skMLCK, AC8, or AC1) were assumed as potential reaction sites of the NHS or benzophenone/diazirine groups, respectively. In addition to the analysis with software tools, all cross-links were verified manually.

### 2.5.8. Modeling of CaM/Target Peptide Complexes

Modeling of the CaM/Munc13 peptide complexes was done in cooperation with S. Kalkhof (Helmholtz-Zentrum für Umweltforschung, Leipzig). The structures of the Munc13 peptides were modeled using the PepFold program (212) on the basis of secondary structure prediction from JuFo (213) and PSIPRED (214). These structures and different CaM structures from various CaM/peptide complex structures (pdb entries: 1cdl, 1ckk, 1qs7, 1qtx, 1wrz, 2bbm, 2f3y, and 2o60; see Table A1) were used as a starting point for fast global docking studies with the PatchDock server (215). Distance constraints obtained by the cross-linking experiments were implemented as follows: The  $C\alpha$ - $C\alpha$  distances of cross-linked amino acids by BS<sup>3</sup> or SBC were set to  $\leq 25$  Å, while Lys- $C\alpha$  – Met- $C\epsilon$  distances obtained by photo-affinity labeling (K. Dimova, MPI for Experimental Medicine, Göttingen) were assumed to be  $\leq 8$  Å. PatchDock solutions were refined by local searches using the RosettaDock server (216), in which 2,000 structures were independently calculated and energetically scored. The

final model was selected from the 10 energetically most favored structures on the basis of its root mean square deviations (RMSD) from the input structure and, additionally, by manually evaluating the suitability of the distance constraints. In the case of structural investigations of CaM/AC8 and AC1 peptide complexes, docking studies were performed using the PatchDock server only (215). The structures of the AC8 and AC1 peptides were predicted with PSIPRED (214) and modeled using the SAM-T08 web server. For docking, different CaM structures were used (2kdu, 2bbm, and a fusion of the *N*-terminal CaM domain of 1cfd and the *C*-terminal CaM domain of 1prw; see Table A1), thereby accounting for a variety of conformations CaM adopts in CaM/peptide complexes at different  $\text{Ca}^{2+}$  concentrations. Distance constraints were implemented as mentioned above. Additionally Lys- $\text{C}\alpha$  – X- $\text{C}\alpha$  distances were assumed to be  $\leq 20 \text{ \AA}$  in the case of SDA-linked residues. The final model was selected based on an optimum agreement with all experimental distance constraints. The cross-links obtained in the experiments with CaM and skMLCK peptide variants were just evaluated in three structures (2kdu, 2bbm, and a fusion between the *N*-terminal CaM domain of 1cfd and the *C*-terminal CaM domain of 1prw; see Table A1), inspecting the conformance of the distance constraints using the software program Pymol ([www.pymol.org](http://www.pymol.org)).

## 3. RESULTS

### 3.1. CaM/Munc13 Interaction

The interaction between Munc13 proteins and CaM was found to be the link between residual  $\text{Ca}^{2+}$  signaling and presynaptic plasticity (75). CaM-binding regions of the homologous Munc13 isoforms, Munc13-1 and ubMunc13-2, were identified in the *N*-terminal domains of Munc13 proteins (79, 83). Investigation of CaM complexes with peptides representing these binding regions revealed a 1-5-8 CaM-binding motif and an antiparallel orientation of the Munc13 peptides within a CaM complex that was structurally comparable to that of the CaM/NO synthase peptide complex (84). In recent NMR experiments with Munc13 peptides that were *C*-terminally elongated, an additional interaction site was found between a tryptophan at position 26 of the CaM-binding motif and the *N*-terminal CaM domain (54). This new binding mode via a 1-5-8-26 motif leads to an extended conformation of CaM in contrast to the collapsed CaM structure in the CaM/NO synthase peptide complex (54). Additionally, bioinformatic predictions revealed two CaM-binding sites in bMunc13-2 and in Munc13-3 (79). Recent biochemical analysis had shown that only these binding sites are functional, which spatially align with those of Munc13-1 and ubMunc13-2 (85). In this work, chemical cross-linking in combination with high-resolution MS was employed to characterize the CaM binding of Munc13-derived peptides representing the functional CaM-binding regions of Munc13-1, ubMunc13-2, bMunc13-2, and Munc13-3. Larger domains of all four Munc13 isoforms, surrounding their CaM-binding regions, were overexpressed and purified in order to gain further insights into the interaction of CaM with Munc13 proteins.

#### 3.1.1. Structural Investigation of CaM/Munc13 Peptide Complexes

Munc13 peptides, composed of 21 to 24 amino acids, representing the minimal CaM-binding sites of Munc13 proteins (Figure 23A), were used in cross-linking experiments to investigate their complexes with CaM on a structural level. The heterobifunctional amine- and photo-reactive cross-linker SBC (145) was used in a two-step reaction to covalently connect lysine side chains of CaM with amino acids in the respective Munc13 peptide (Figure 23B). First, the amine-reactive site of the cross-linker (NHS-ester) was reacted with CaM, and after quenching the reaction with  $\text{NH}_4\text{HCO}_3$ , excess cross-linker was removed by microfiltration. Then, the Munc13 peptide was added to the cross-linker-labeled CaM and the mixtures were irradiated with long-wavelength UV light (maximum at 365 nm) to activate the benzophenone

group of the cross-linker and to induce the photo-reaction (1.2.1.2. and 2.5.2.). As the photo-reaction is not completely specific, a large number of amino acids can be expected to react.

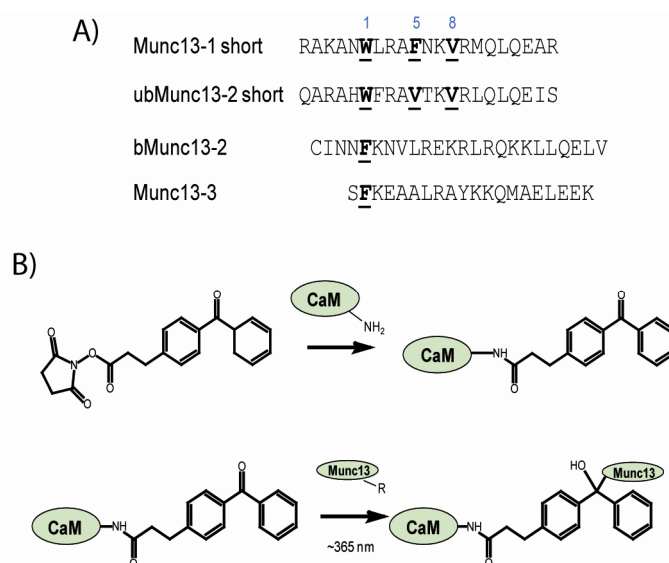


**Figure 23. Munc13 peptides and cross-linking reaction scheme of SBC.** A) Amino acid sequences of peptides representing the CaM-binding sites of all four Munc13 isoforms. The hydrophobic anchor residues are highlighted in bold and underlined; the numbers illustrate their positions in the CaM-binding motif. B) Reaction scheme of the heterobifunctional amine-/photoreactive cross-linker SBC. Adapted from Krauth *et al.* 2009 (145).

Previous photo-affinity labeling (PAL) experiments (79) had revealed a free  $\text{Ca}^{2+}$  concentration of ca. 30 nM was necessary to yield maximal photo-adduct formation. To investigate whether this  $\text{Ca}^{2+}$  concentration is also optimal to yield a maximum amount of cross-linked products for the heterobifunctional cross-linker SBC, cross-linking experiments using a 20- or 50-fold molar excess of SBC were performed at free  $\text{Ca}^{2+}$  concentrations of 10, 30, and 100 nM, which were adjusted by a  $\text{Ca}^{2+}$ /chelator (EGTA) system. Cross-linking reaction mixtures were separated on an SDS gel and the bands representing the 1:1 CaM/peptide complex migrating at ca. 22 kDa were compared between the different cross-linking samples (Figure 24).

Results of the SDS-PAGE analysis of the cross-linking reactions between CaM and Munc13 peptides (shown for Munc13-3 in Figure 24) illustrate a slightly lower yield of cross-linked 1:1 complexes between CaM and the Munc13 peptide in reactions with a 20-fold molar excess of SBC compared with reactions with a 50-fold excess. Two different irradiation energies (4000 and 8000  $\text{mJ}/\text{cm}^2$ ) were selected to induce the photo-reaction, which resulted in slightly different yields of cross-linked complexes. After irradiation of the reaction mixtures of all four Munc13 peptides with 4000  $\text{mJ}/\text{cm}^2$ , a band representing the 1:1 CaM/Munc13 peptide complex was visible in the reactions containing 10 nM and 30 nM

## Results

$\text{Ca}^{2+}$ , which became more intense, but at the same time more diffuse, after irradiation with  $8000 \text{ mJ/cm}^2$ . These diffuse bands, shown for Munc13-3 (Figure 24, lanes 7, 8, and 14, 15), which were most intense in the reactions containing  $30 \text{ nM Ca}^{2+}$ , indicated the highest degree of cross-linking, leading to various adducts with slightly different migration behaviors. CaM in water (Figure 24, lanes 9 and 16) had a different mobility on the SDS gel compared to CaM in the  $\text{Ca}^{2+}$  and peptide-containing reactions. This might result from different conformations that CaM adopts with or without a peptide bound. In the CaM migrating at ca.  $17 \text{ kDa}$  the peptide-bound conformation had been fixed by the cross-linking reagent, although SBC did not covalently link CaM and the Munc13-3 peptide. In contrast, the conformation of peptide-free CaM in water is different and migrates faster within the SDS gel. The performed cross-linking experiments confirmed that CaM/Munc13-3 peptide complex formation is most efficient at a  $\text{Ca}^{2+}$  concentration of  $30 \text{ nM}$  (Figure 24, middle panel), which was also true for the other Munc13 peptides and is in agreement with previous photo-affinity labeling studies (79). Although the intensity differences between the bands of the 1:1 complexes of CaM and the Munc13-3 peptide at  $10$  and  $30 \text{ nM Ca}^{2+}$  are only subtle (Figure 24), it can be concluded that a free  $\text{Ca}^{2+}$  concentration of  $30 \text{ nM}$  is the optimum condition for conducting the cross-linking reactions.

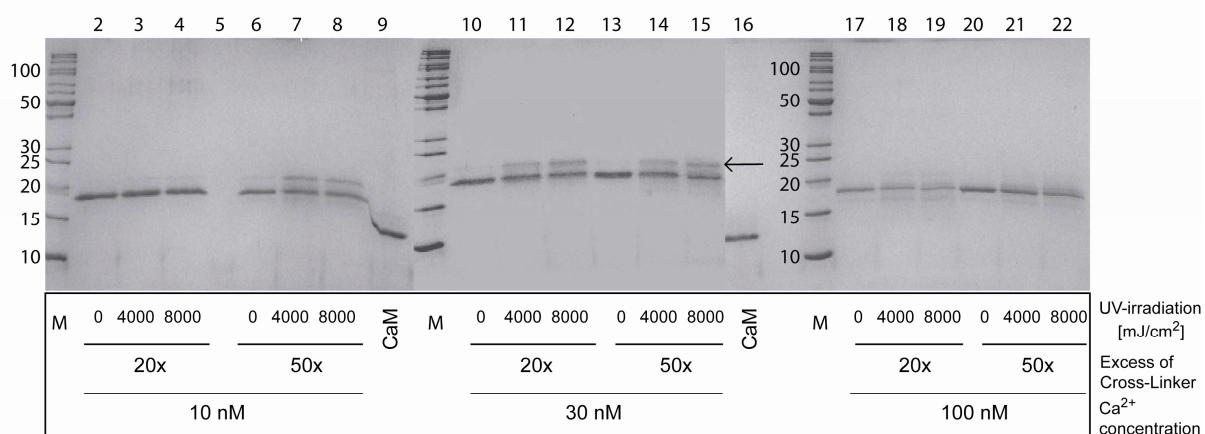


**Figure 24. SDS-PAGE analysis of CaM/Munc13-3 peptide cross-linking reactions.** Cross-linking reactions between CaM and Munc13-3 peptide conducted at different  $\text{Ca}^{2+}$  concentrations ( $10 \text{ nM}$ , left;  $30 \text{ nM}$ , middle;  $100 \text{ nM}$ , right) with a 20- or 50-fold molar excess of the cross-linker SBC. The amount of cross-linked complexes after irradiation (bands migrating at ca.  $22 \text{ kDa}$ , arrow) was maximal at a  $\text{Ca}^{2+}$  concentration of  $30 \text{ nM}$  (middle panel). Bands migrating at around  $17 \text{ kDa}$  represent cross-linker-labeled CaM. Lanes 9 and 16: CaM (in water). M: molecular weight marker.

After determination of the optimum  $\text{Ca}^{2+}$  concentration to yield a maximal amount of cross-linked product, additional cross-linking experiments were performed with the aim of generating distance constraints for molecular modeling of the CaM/Munc13 peptide

complexes of all four Munc13 isoforms. Again, the heterobifunctional cross-linker SBC was used in a 20- and 50-fold molar excess, and irradiation energies of 4000 and 8000 mJ/cm<sup>2</sup> were applied. The Ca<sup>2+</sup> concentration within the cross-linking reactions was adjusted to 30 nM, to maximize yields of complex formation between CaM and the Munc13 peptide. Cross-linking reaction mixtures were separated by one-dimensional SDS-PAGE (2.4.4.), and, additionally, analyzed by MALDI-TOF-MS (2.5.3.) to monitor the yield and stoichiometry of cross-linked CaM/Munc13 peptide complexes. The generated MALDI-TOF mass spectra were dominated by signals of labeled, but non-cross-linked CaM. Signals corresponding to cross-linked complexes between CaM and the Munc13 peptide were detected with relatively low intensity (shown for CaM and Munc13-3 peptide, Figure 25). Nevertheless, CaM/peptide cross-linking adducts, primarily with a 1:1 stoichiometry, were detected for all four Munc13 peptides under investigation (data not shown).

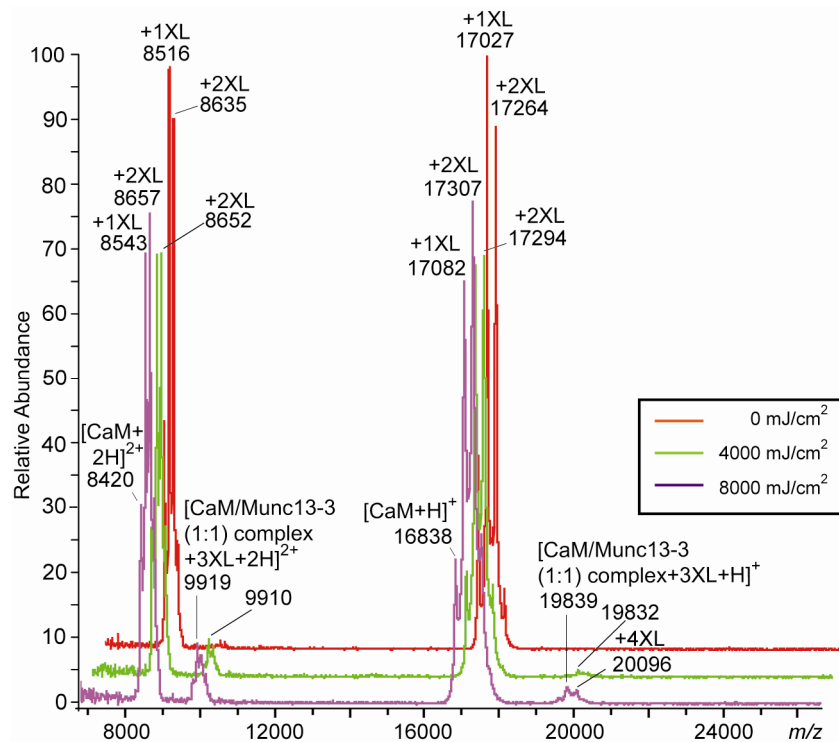


**Figure 25. MALDI-TOF-MS of cross-linking reactions between CaM and the Munc13-3 peptide.** Three MALDI-TOF mass spectra of the cross-linking reaction mixtures (50-fold excess of SBC, 30 min NHS ester reaction time, and irradiation energies of 0, 4000 or 8000 mJ/cm<sup>2</sup>) are shown for CaM and the Munc13-3 peptide. The spectra are dominated by the signal representing cross-linker-labeled CaM (CaM+XL). After UV-irradiation of the cross-linking reaction mixtures (green and purple spectra), a signal appears representing 1:1 complexes between CaM and the Munc13-3 peptide.

In addition to mass spectrometric analysis, intact cross-linking mixtures were separated on an SDS gel, which resulted in distinct bands for cross-linker-labeled CaM or cross-linked 1:1 CaM/Munc13 peptide complexes (Figure 26). Although the amount of cross-linked

## Results

complexes differed slightly between Munc13 isoforms, CaM binding was observed for all Munc13 peptides, confirming that these Munc13 peptides used herein represent the Munc13 regions, which are sufficient for CaM binding. Intensities of the bands for the Munc13 peptides differ between the four Munc13 isoforms, which might result from the fact that the peptides migrate in the migration front of the SDS gel, leading to partial leakage from the gel. SDS-PAGE analysis of the cross-linking reactions of bMunc13-2 showed cross-linked complexes between the peptide and CaM even in non-irradiated reaction mixtures (Figure 26, irradiation energy 0 mJ/cm<sup>2</sup>). In these cases, the benzophenone groups of SBC had already been activated to a certain extent by ambient light before irradiation.

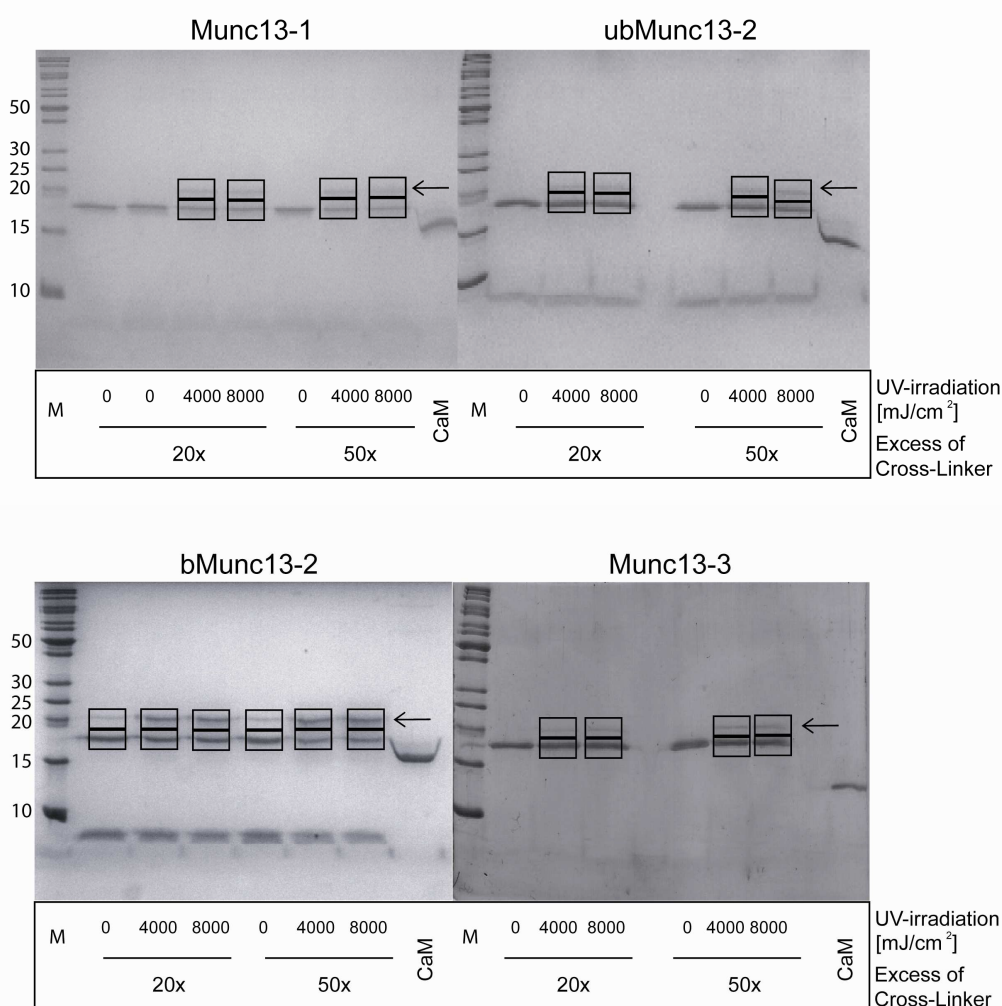


**Figure 26. SDS-PAGE analysis of CaM/Munc13 cross-linking reactions.** The cross-linking reactions were conducted at a free Ca<sup>2+</sup> concentration of 30 nM to maximize the yield of cross-linked CaM/Munc13 peptide complexes. Bands migrating at ca. 22 kDa (marked with arrows) represent cross-linked complexes between CaM and the Munc13 peptide, while bands migrating at ca. 17 kDa represent cross-linker-labeled CaM. CaM (in water) was used as reference. Bands, which were excised and *in-gel* digested are framed by black boxes. M: molecular weight marker.

The bands of the 1:1 CaM/Munc13 peptide complexes (Figure 26, upper black boxes) were excised and *in-gel* digested with trypsin and its enhancer ProteaseMax<sup>TM</sup> (2.4.5.). Afterwards,

the extracted proteolytic peptide mixtures were analyzed by nano-HPLC/MALDI-TOF/TOF-MS/MS (2.5.4.) and nano-HPLC/nano-ESI-LTQ-Orbitrap-MS/MS (2.5.5.).

Assignment of cross-linked CaM/Munc13 peptides revealed different numbers of identified intra- and intermolecular cross-linked products for the four Munc13 variants under investigation. Nevertheless, analogous contact sites with CaM were found for all four Munc13 variants (Table A2 and Table A3).

The cross-linked products identified for Munc13-1 and ubMunc13-2 peptides are consistent with previous data and validate the recently postulated model of the CaM/Munc13-1 and CaM/ubMunc13-2 peptide complexes (84).

Furthermore, for the two Munc13 variants bMunc13-2 and Munc13-3, which had not been studied so far, four and 13 cross-links were identified, respectively, and the contact sites between these two Munc13 peptides and CaM are similar to the cross-links found for Munc13-1 and ubMunc13-2. The amine-reactive site of the cross-linker SBC (NHS-group) had reacted with the *N*-terminal lobe (amino acids 21, 30), the central  $\alpha$ -helix (amino acids 75, 77), and the *C*-terminal domain (amino acid 94) of CaM, which is consistent with previous studies. In the second cross-linking reaction step, the benzophenone group of SBC had mainly reacted with lysine, leucine, alanine, isoleucine, and phenylalanine in the Munc13 peptides (Table A2).

Two cross-links, identified between CaM and Munc13-1, in which the amine-reactive site of SBC had reacted with the Munc13 peptide, demonstrate that quenching and removal of excess cross-linker was not complete in these reactions, before the Munc13-1 peptide was added. Therefore, SBC was able to react with its amine-reactive site with the Munc13-1 peptide. However, in the cross-linking reactions with the other Munc13 isoforms such “reverse” cross-links were not identified.

MS and fragment ion MS data of a cross-linked product between CaM and bMunc13-2 are shown in Figure 27. Eventhough the signal of the cross-linked product did not dominate the mass spectrum, this cross-link was unambiguously identified by MS/MS sequencing due to dynamic exclusion of highly abundant peptide masses (2.5.5.). Spectra of cross-linked products between CaM and all other Munc13 isoforms are illustrated in the appendix (Figure A1, Figure A2, and Figure A3).



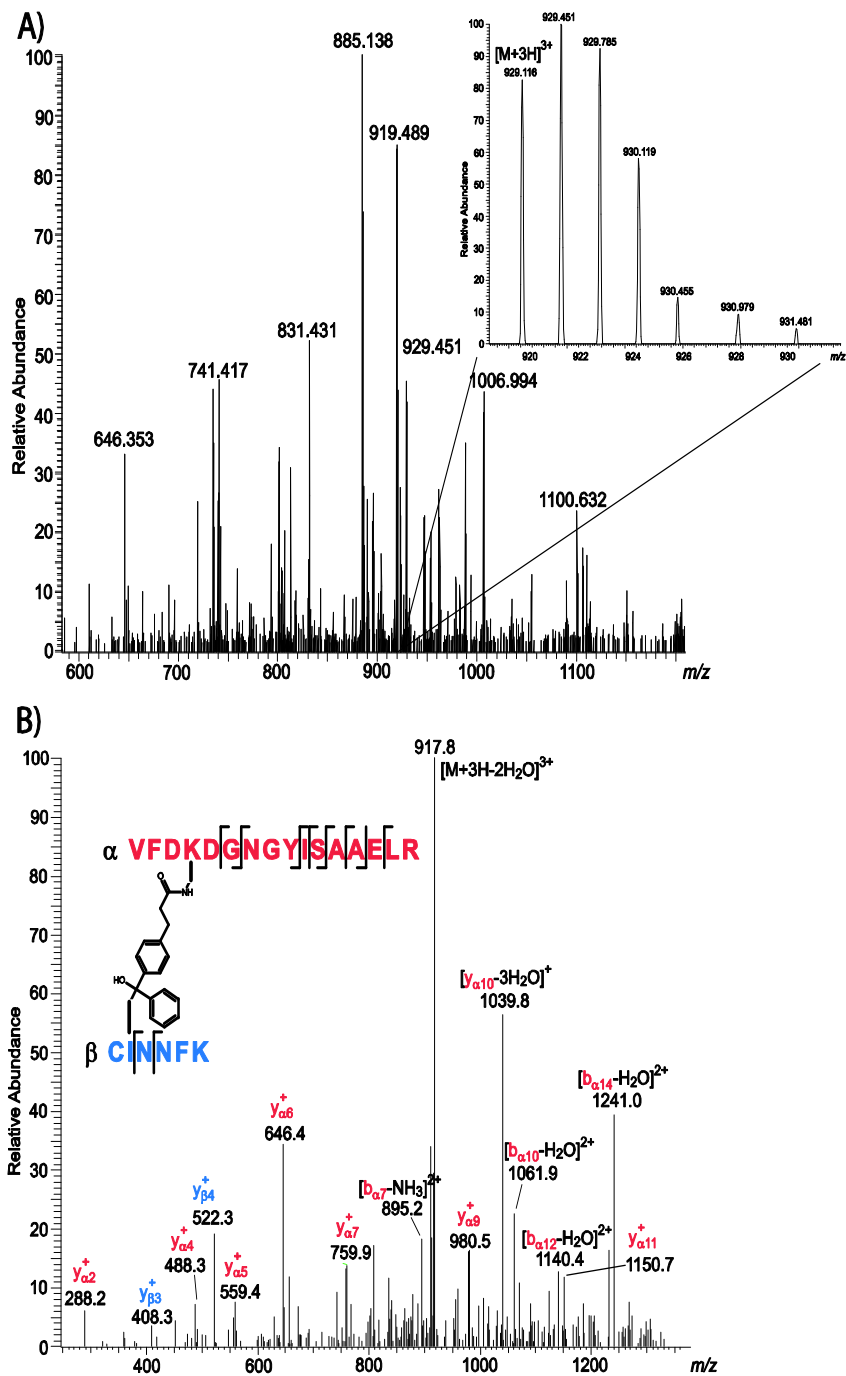


**Figure 27. MS and MS/MS analysis of a cross-linked product between CaM and the bMunc13-2 peptide.** Nano-HPLC/nano-ESI-LTQ-Orbitrap-MS/MS analysis of a cross-linked peptide mixture between CaM and the bMunc13-2 peptide (20-fold molar excess of SBC, 30 min, irradiation  $4000\text{mJ}/\text{cm}^2$ ). A) Mass spectrum recorded at 72.0 min. The 3+ signal of the cross-linked product at  $m/z$  929.451 is shown enlarged. B) Fragment ion mass spectrum of the cross-linked product between lysine-94 of CaM ( $\alpha$ -sequence 91-106, red) and isoleucine-2 of b-Munc13-2 ( $\beta$ -sequence 1-6, blue).

The distance constraints obtained by chemical cross-linking and previous PAL experiments (K. Dimova, MPI Göttingen) were used as a basis for molecular modeling studies to generate structures of all four CaM/Munc13 peptide complexes (Figure 28).

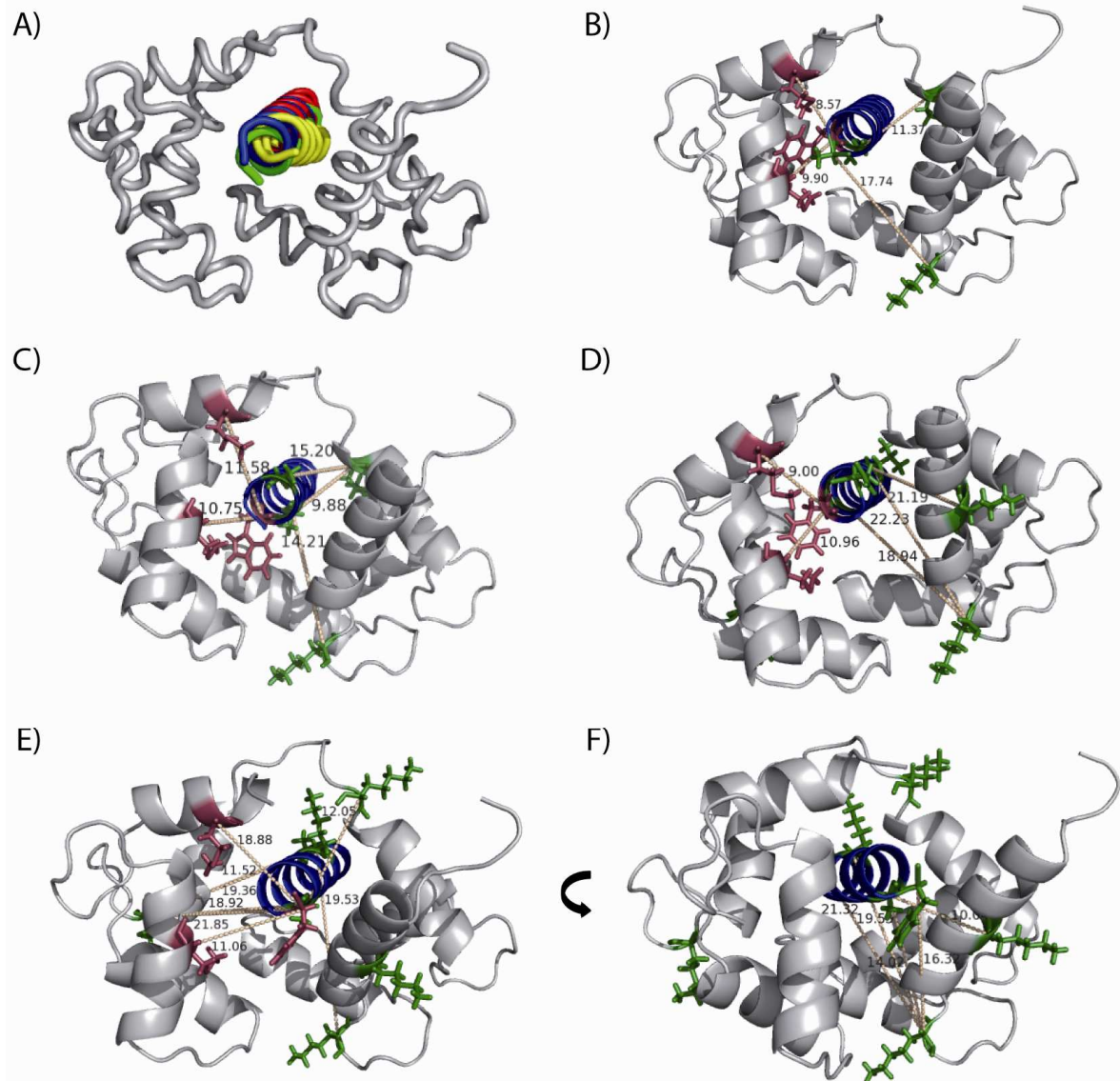


**Figure 28. Structures of CaM/Munc13 peptide complexes.** Structures of CaM complexes with four Munc13 peptides (Munc13-1, ubMunc13-2, bMunc13-2, and Munc13-3) were modeled on the basis of the CaM/NO synthase peptide complex (pdb 2o60). A) Superposition of CaM/Munc13 peptide complexes of all four Munc13 isoforms demonstrating a common CaM-binding mode for all Munc13 peptides. Cross-links obtained for the CaM complexes with B) Munc13-1, C) ubMunc13-2, D) bMunc13-2, and E, F) Munc13-3 are shown as dotted lines with the  $\text{C}\alpha$ - $\text{C}\alpha$  distances between connected amino acids (green sticks) given in Å. Additionally, the PAL constraints (K. Dimova, University Göttingen) are illustrated (connected residues are shown as purple sticks). CaM is shown in grey, the Munc13 peptides in color (A) or in blue (B-F). Adapted from Lipstein *et al.*, 2012 (85).

For modeling of the Munc13-1 and ubMunc13-2 peptide complexes with CaM, the cross-links found in previous experiments with the cross-linkers  $\text{BS}^3$  and  $\text{BS}^2\text{G}$  (84) were combined with those obtained with SBC (Table A2). In the molecular modeling studies (2.5.8.),  $\text{C}\alpha$ - $\text{C}\alpha$  distances of  $\text{BS}^3$  or SBC-cross-linked amino acids were set to  $\leq 25$  Å, while Lys- $\text{C}\alpha$  - Met-C $\epsilon$  distances obtained by PAL experiments were assumed to be  $\leq 8$  Å.

The structures of all Munc13 peptides were modeled using the PepFold program (212). An  $\alpha$ -helical structure of all Munc13 peptides could later be confirmed by CD spectroscopy (K. Kölbl, University Halle-Wittenberg, (85)). Afterwards, a fast global docking of the four Munc13 peptide structures to various CaM structures was performed using the Patchdock server (2.1.12.). Then, the resulting models were refined by local searches using the RosettaDock server (216). Final models for the CaM/Munc13 peptide complexes were selected based on the RMSD from the starting structure and the conformance with experimental distance constraints (2.5.8.). The resulting model structures for Munc13-1 and ubMunc13-2 (Figure 28B, C) with the highest score, which best accommodated all cross-links, are those based on the structure of the CaM/neuronal NO synthase peptide complex (pdb 2o60). These models are in agreement with previously determined structures (84), demonstrating that Munc13-1 and ubMunc13-2 peptides bind to CaM via a 1-5-8 motif in antiparallel orientation, forming a complex structure comparable to that of the CaM/NO synthase peptide complex. Interestingly, the model structures determined for the complexes between CaM and bMunc13-2 and Munc13-3 also show an antiparallel binding mode of both peptides (Figure 28D - F) comparable to that of Munc13-1 and ubMunc13-2 (Figure 28B, C). Although the 1-5-8 CaM-binding motif is not obvious in the bMunc13-2 and Munc13-3 peptides (Figure 23), the binding mode of all Munc13 isoforms is similar, as evidenced by an alignment of the four CaM/Munc13 peptide complexes (Figure 28A). Moreover, intramolecular cross-links between the *N*- and the *C*-terminal CaM domain (Table A3) confirm a collapsed conformation of CaM in the complex, comparable to that of the CaM/NO synthase peptide complex, in which both domains of CaM are in close proximity and can be connected by the cross-linker SBC (145).

In summary, chemical cross-linking in combination with MS, PAL, and molecular modeling revealed a common CaM-binding mode for all four Munc13 isoforms, which is characterized by an antiparallel orientation of the  $\alpha$ -helical Munc13 peptide in the CaM/Munc13 complex.

### 3.1.2. Expression and Purification of Munc13 Domains

Recent NMR studies had revealed an additional interaction site between a tryptophan residue of *C*-terminally elongated (34-amino acid) Munc13-1 and ubMunc13-2 peptides with the *N*-terminal domain of CaM (54). Apparently, the CaM-binding mode of these longer Munc13 peptides is characterized by an interaction via a novel 1-5-8-26 CaM-binding motif. Moreover, the CaM conformation in these CaM/Munc13 peptide complexes (pdb 2kdu, (54))

is extended compared to that in the complexes with the shorter (21 to 24-amino acid) peptides described above (3.1.1.). The intriguing question arises whether the 1-5-8-26 motif is also found in bMunc13-2 and Munc13-3 and if additional contact sites are present between the *N*-terminus of Munc13 and CaM. In order to address this question, Munc13 domains comprising the *N*-terminal region of Munc13 (Figure 29) were overexpressed as GST fusion proteins and purified to investigate their interaction with CaM.

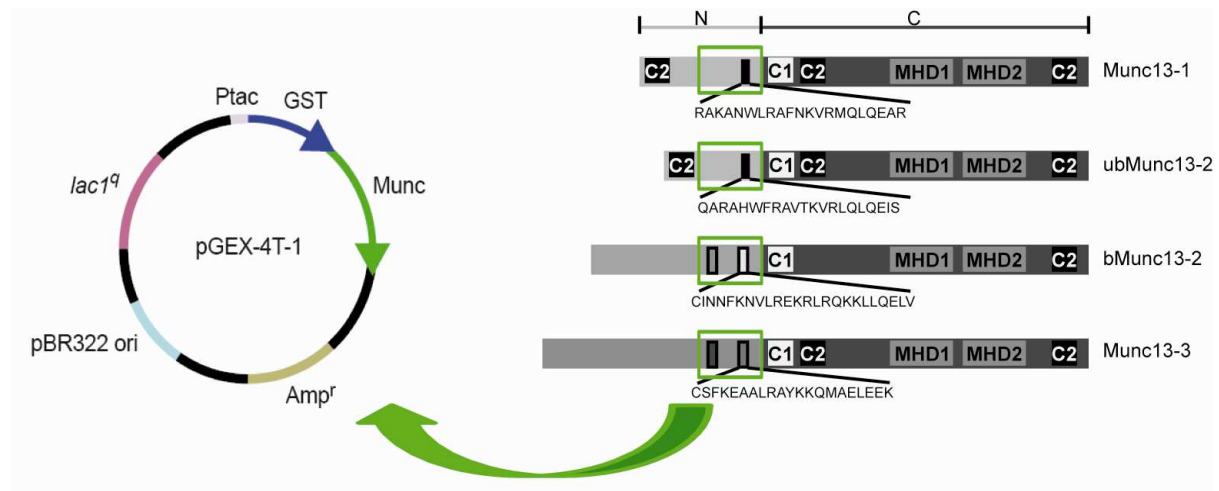


**Figure 29. Munc13 constructs.** The *C*-terminal parts of the *N*-terminal Munc13 domains (green boxes) were overexpressed as GST fusion proteins using a pGEX-4T-1 plasmid (with an ampicillin resistance ( $Amp^r$ ), a pBR322 origin of replication (*ori*), a Lac operon ( $lac1^q$ ), and a tac promoter region (*Ptac*)). The Munc13 domains contain the minimal CaM-binding regions of Munc13 proteins (amino acid sequences, from which the Munc13 peptides (3.1.1., Figure 23) are derived, are shown). Adapted from Dimova *et al.* 2006 (79) and the addgene vector database (<http://www.addgene.org/vector-database/2876/>).

### 3.1.2.1. Expression and Purification of bMunc13-2 and Munc13-3 Domains

First, constructs of bMunc13-2 (aa 366 - 780, Figure A4) and Munc13-3 (aa 711 - 1063, Figure A5) (217) were overexpressed in *E.coli* BL21 (DE3) Codon Plus cells (Figure 29). Cultivation conditions (namely, temperature, IPTG concentration, and time of overexpression) were optimized to yield maximal amounts of Munc13 proteins. Cells were grown at 37 °C until the optical density ( $OD_{600}$ ) reached a value between 0.4 and 0.6. Then, *Munc13* gene expression was induced by addition of 0.1 - 1 mM IPTG and allowed to proceed for 4 hrs, 6 hrs, or overnight at 18 °C or 37 °C. Optimum conditions were found to be those that allowed the cells to produce the desired protein slowly (4 hrs at 18 °C, induction with 0.1 mM IPTG) (2.4.1.). The purification of the Munc13 domains was optimized in a second step (2.4.2.). After harvesting and lysing the cells, cell debris was pelleted and the supernatant was loaded on a GST column using an ÄKTA-FPLC system (2.1.11.). The resulting fractions of the washing and elution steps were analyzed on an SDS gel (2.4.4.),

demonstrating that the GST fusion proteins co-eluted with a number of impurities (Figure 30). Characterization of the bands migrating between 25 and 50 kDa was performed by *in-gel* digestion (2.4.5.) and nano-HPLC/nano-ESI-LTQ-Orbitrap-MS/MS (2.5.5.), revealing that these impurities are C-terminally truncated GST-Munc13 constructs. These shorter GST-Munc13 proteins might result from proteolytic cleavage (in the cells or during the purification procedure) or, alternatively, they represent incompletely synthesized proteins due to malfunctions in transcription or translation. To circumvent these problems, low concentrations of ethanol (0.5 - 1% (v/v)) were added to the cell cultures upon induction, which should slightly stress the cells and induce an increased expression of chaperones, resulting in larger amounts of correctly folded protein and, thus, protect Munc13 from proteolysis. However, neither the addition of ethanol during overexpression of the proteins, nor the application of different protease inhibitors in all purification steps led to reduced amounts of truncated Munc13 domains, necessitating an additional purification step.

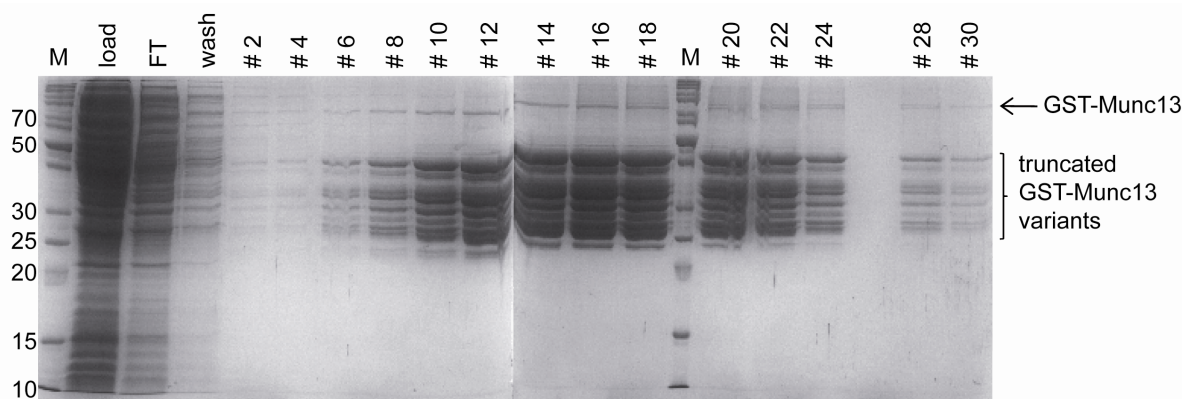


**Figure 30. GST affinity purification of the GST-bMunc13-2 domain.** SDS-PAGE analysis of the GST affinity purification revealed that the GST-Munc13 domain co-eluted with truncated GST-Munc13 variants. M: molecular weight marker, FT: flow-through fraction.

GST is a 26-kDa protein, which might interfere with the CaM interaction of Munc13 domains if it is not removed. Thus, a thrombin cleavage site had been inserted into the fusion protein between the amino acid sequences of GST and Munc13. This cleavage site has the sequence H-H-P-R[-K]-X-X, with H being hydrophobic residues and X being non-acidic amino acids (218). The Munc13 constructs used in this study comprise an optimal thrombin cleavage site with the sequence LVPRGS (Figure A4 and Figure A5). However, thrombin cleavage of pooled elution fractions of the GST affinity purification step revealed only minor amounts of full-length, untagged Munc13 protein (Figure 31), which do not differ between reactions containing 1 or 2 U thrombin (slight intensity differences between the bands are only due to

slight differences in the amounts loaded on the SDS gel). A band for thrombin, which should migrate at 37 kDa, was not visible because the amount was too low to be detected.

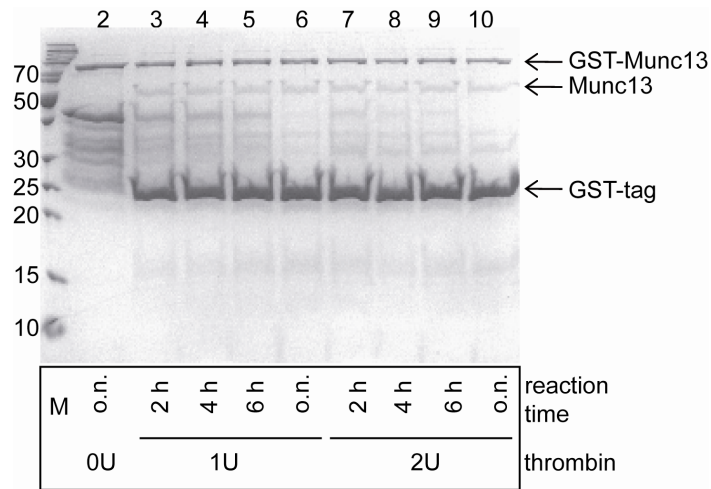


**Figure 31. Thrombin cleavage of GST-Munc13.** Cleavage of the GST tag was performed with 0, 1 or 2 U thrombin and was allowed to proceed for 2, 4, 6 hrs, or overnight (o.n.). A band representing untagged Munc13 is visible in all reactions containing thrombin (1U, 2U). In lane 2, an aliquot of the pooled elution fractions from the GST affinity purification (Figure 30) is shown. M: molecular weight marker.

Membrane-associated proteins like Munc13 can be stabilized by the presence of detergents such as Triton X-100 or DDM (*n*-dodecyl- $\beta$ -*D*-maltoside). Therefore, the thrombin cleavage reactions were repeated with different amounts of DDM or Triton X-100, resulting in slightly higher amounts of untagged Munc13 protein. The cleaved GST tag, thrombin, and the truncated Munc13 proteins had to be removed from full-length Munc13 in a subsequent purification step (Figure 32).

A combination of GST affinity and anion exchange chromatography was chosen to purify the full-length, untagged Munc13 protein. On the GST affinity column, the free GST tag as well as GST-Munc13 fusion proteins should bind, while thrombin, other impurities, and untagged Munc13 protein will not bind to the column and they can be separated by their isoelectric points on a second downstream column (anion exchange).

As shown in Figure 32, separation of the GST flow-through fraction resulted in three peaks during anion exchange chromatography, but unfortunately, SDS-PAGE analysis (2.4.4.) revealed that the concentrations of the proteins were below the detection limit (data not shown).

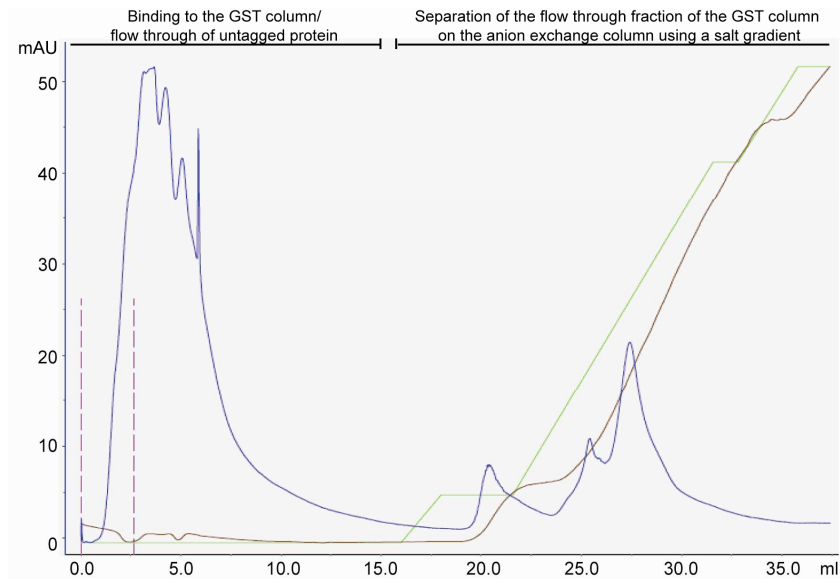


**Figure 32. FPLC chromatogram of a combined GST affinity and anion exchange purification.** Separation of thrombin cleavage reaction products by a combination of GST affinity and anion exchange chromatography. The untagged Munc13 protein, thrombin, and other impurities flowed through the GST column and were separated by their isoelectric points on the second column (anion-exchange) if a salt step gradient was applied. The absorption at 280 nm (blue), the concentration of buffer IEX B (2.1.5.) (green), and the conductivity (brown) are presented.

For optimization of the purification procedure, the truncated GST-Munc13 proteins should be removed prior to the thrombin cleavage reaction to enhance cleavage of the full-length fusion protein. Therefore, pooled elution fractions of the GST affinity purification step (before thrombin cleavage) were separated by anion exchange chromatography. Due to differences in their isoelectric points, the truncated Munc13 domains should not bind to the anion exchange column, while the majority of the full-length fusion protein should bind to the column and can be eluted separately by applying a salt gradient (219). The challenge with this purification procedure originated from the buffer exchange after the anion exchange chromatography, which was necessary to lower the salt concentration prior to thrombin cleavage, resulting in high sample losses.

Since truncated Munc13 domains might result from incomplete transcription and translation processes, the DNA of the Munc13 constructs should comprise codons, which are optimized for expression in *E.coli*. The nucleotide sequences of the respective Munc13 domains were derived from the full-length mammalian proteins. Therefore, an adaption of the DNA codons to those used in *E.coli* might lead to enhanced translation and, thus, to a reduced amount of truncated Munc13 domains. Adapted DNAs of GST-bMunc13-2 and GST-Munc13-3 domains were transformed into *E.coli* BL21 (DE3) Codon Plus cells and the proteins were overexpressed under the conditions described above. Additionally, the circumvention of

## Results

frequent buffer exchanges was achieved by on-column thrombin cleavage of the GST fusion protein. For this, thrombin was added to the washing buffer (2.1.5., containing 0.5% DDM), which was applied to the GST column after binding the GST-Munc13 proteins to the column, and the column was incubated with this thrombin-containing buffer A overnight (2.4.2.). Elution of the non-bound fraction from the GST column followed by SDS-PAGE analysis (2.4.4.) revealed high amounts of untagged Munc13 domains, yet impurities remained (Figure 33, fractions #ET1-7). Both the GST tag and untagged Munc13 were eluted with reduced glutathione (fractions #GST1-5 or 7), indicating a non-covalent interaction between both proteins.

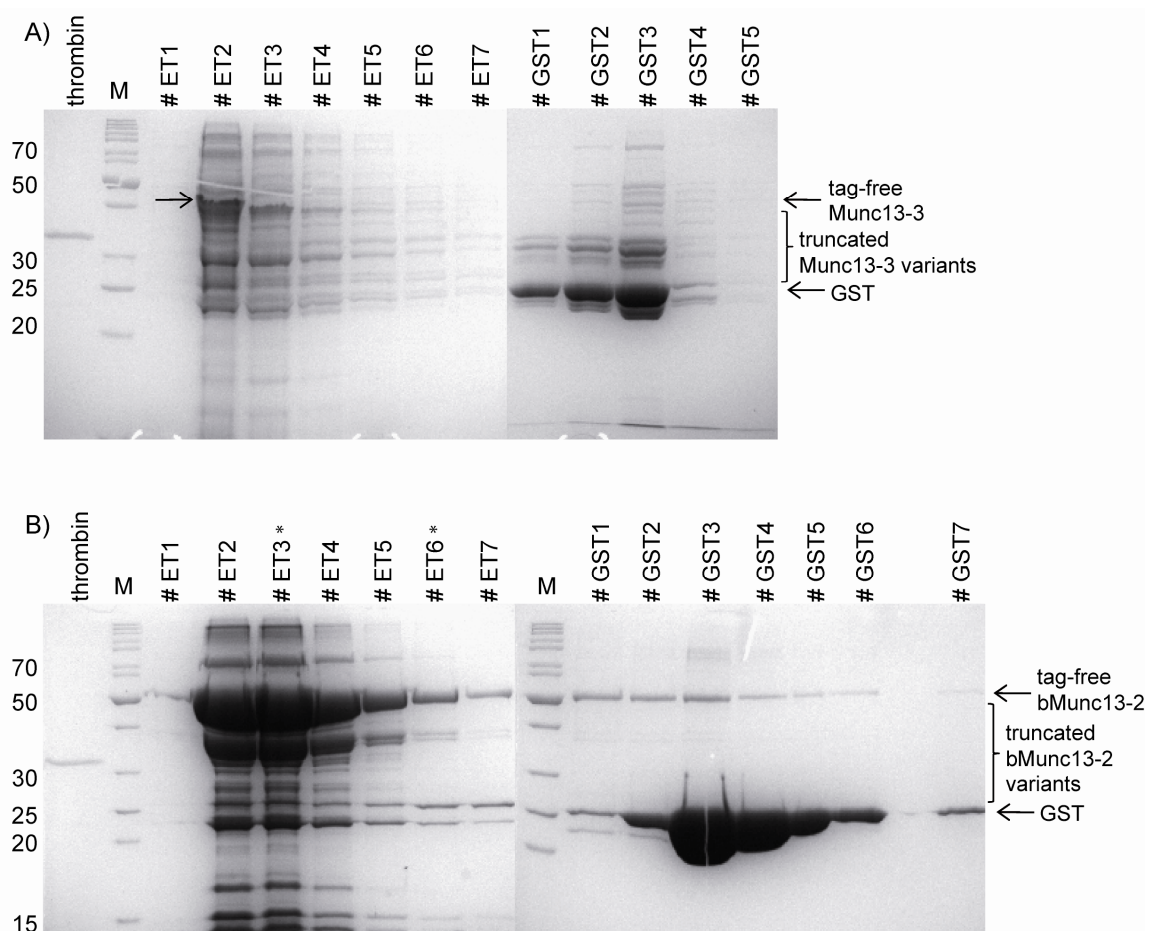


**Figure 33. SDS-PAGE analysis after on-column thrombin cleavage of bMunc13-2 and Munc13-3 domains.** After thrombin cleavage overnight, the unbound fraction was eluted from the GST column (fractions #ET1-7). As a second step, the proteins that had bound to the GST column were eluted with reduced glutathione (fractions #GST1-5 or 7). A) Purification of the Munc13-3 domain and B) purification of the bMunc13-2 domain is shown. M: molecular weight marker, ET: elution after thrombin cleavage.

In order to remove truncated Munc13 domains and thrombin, two elution fractions (Figure 33B, fractions #ET3 and 6, asterisks) were arbitrarily chosen and pooled to test the purification of untagged bMunc13-2 by a combination of GST affinity and anion exchange



chromatography. Although most impurities were successfully removed, the concentration of the untagged bMunc13-2 was low after purification and the subsequent desalting step. Elution fractions from the first GST affinity column (#GST1-4, Figure 33B) containing the majority of the co-eluted, untagged bMunc13-2 were pooled and separated by anion exchange chromatography. Nevertheless, no pure untagged bMunc13-2 protein was obtained. Therefore, these purification procedures were not continued with Munc13-3.

In conclusion, untagged bMunc13-2 and Munc13-3 domains were obtained by GST affinity purification and on-column thrombin cleavage in a buffer containing 0.5% DDM. Although this purification procedure yielded high amounts of Munc13 domains, impurities - mainly from GST and truncated Munc13 domains - could not be removed without significant protein losses.

### **3.1.2.2. Expression and Purification of Munc13-1 and ubMunc13-2 Domains**

In parallel to bMunc13-2 and Munc13-3, overexpression of GST-Munc13-1 and GST-ubMunc13-2 domains was performed in *E.coli* BL21 (DE3) Codon Plus cells. As full-length proteins could not be obtained using the conditions described for GST-bMunc13-2 and GST-Munc13-3, optimization of the expression was attempted by varying the cultivation temperature, medium, IPTG concentration, and through the use of different additives (e.g. sugars) (219). Despite these attempts, no conditions could be identified that allowed full-length GST-Munc13-1 and GST-ubMunc13-2 domains to be obtained. These problems in overexpressing GST-Munc13-1 and GST-ubMunc13-2 might have been caused by the DNA constructs used, in which the nucleotide sequence of Munc13-1 and ubMunc13-2 was inserted into a pGEX-KG vector (K. Dimova, MPI for Experimental Medicine Göttingen) compared to bMunc13-2 and Munc13-3 whose DNA was inserted into a pGEX-4T-1 vector (Figure 29). Hence, the DNA fragments encoding Munc13-1 and ubMunc13-2 domains were amplified from the full-length Munc13 constructs by PCR (2.2.4.), digested with restriction endonucleases (2.2.6.), purified by agarose gel electrophoresis (2.2.7.), extracted (2.2.8.), and ligated into the pGEX-4T-1 vector (2.2.9) (219). The resulting DNA constructs were transformed into chemo-competent *E.coli* XL-1 Blue cells (2.2.2.) the corresponding plasmid isolated (2.2.3.) and the insert DNA sequenced (2.2.10.). This subcloning strategy was only successful for Munc13-1. The plasmid encoding Munc13-1 was transformed into *E.coli* BL21 (DE3) Codon Plus cells (2.2.2.) and protein synthesis was allowed to proceed (2.4.1.). Unfortunately, however, no full-length protein was obtained (219). Thus, as it was shown for

bMunc13-2 and Munc13-3, optimization of the *Munc13-1* and *ubMunc13-2* genes to *E.coli*'s codon usage seems to be indispensable and might improve the overexpression of complete GST-Munc13-1 and GST-ubMunc13-2 domains.

### 3.1.3. Cross-links between Munc13 Domains and CaM

Chemical cross-linking in combination with MS was used to investigate the interaction of bMunc13-2 and Munc13-3 domains with CaM. Although cross-linking experiments are preferably performed with pure proteins, this method has the advantage that identification of cross-linked products is also feasible with protein solutions containing impurities. In general, the cross-linking reaction mixtures are separated by one-dimensional SDS-PAGE (2.4.4.), bands of interest are excised and *in-gel* digested (2.4.5.). Afterwards, the resulting peptide mixtures are analyzed by MS. In the case of untagged bMunc13-2 and Munc13-3 domains, the protein solutions contained a number of impurities (Figure 33A and B, fractions #ET2, each). Nevertheless, in the range between 50 and 70 kDa, where a cross-linked product between CaM and the Munc13 domains is expected, a new band arising from cross-linking should be readily visible (Figure 33 and Figure 34).

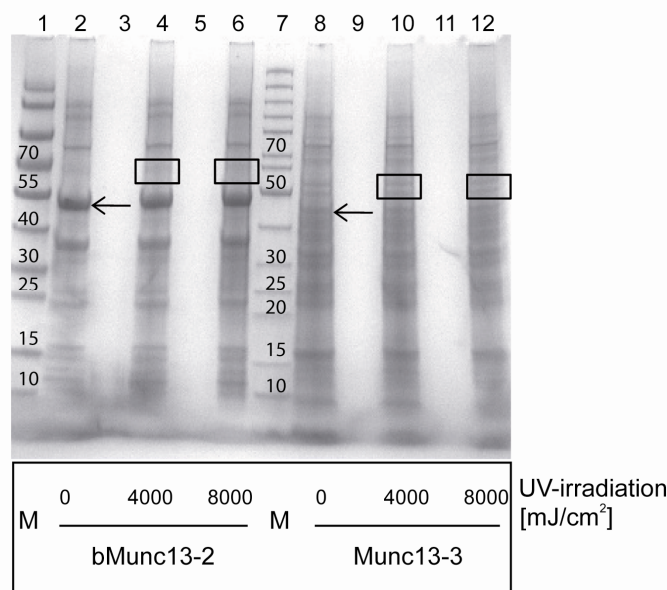


**Figure 34. Cross-linking between bMunc13-2 and Munc13-3 domains and CaM.** Cross-linking reactions conducted with SBC (amine-reactive site 30 min, 50-fold excess) were irradiated with UV-A light (0, 4000 or 8000 mJ/cm<sup>2</sup>). A gradient gel (4 - 15% resolving gel) was used for SDS-PAGE analysis to improve separation. Between 40 and 50 kDa, a band representing the GST-free Munc13 domains was detected (arrow). In the case of reaction with bMunc13-2, weak bands at 60 kDa were visible after irradiation that might represent the CaM/Munc13 complex (black boxes). For Munc13-3, the bands between 50 and 70 kDa did not change upon irradiation, which indicates that they do not represent the CaM/Munc13 complex. The bands, which were excised for *in-gel* digestion and MS analysis, are highlighted by black boxes. Lanes 1 and 7 contain molecular weight marker.

The cross-linking experiments were conducted with the heterobifunctional cross-linker SBC (145) in a 50-fold molar excess. First, the amine-reactive site was reacted with CaM for 30 min - as has already been described for the cross-linking experiments with the Munc13 peptides (3.1.1.). Due to the impurities present in the solution, the concentrations of the bMunc13-2 and Munc13-3 domains could not be unambiguously determined, but they were estimated to range between 10 to 20  $\mu$ M. Solutions of the Munc13 domains were added to SBC-labeled CaM and incubated for 30 min, before the reaction mixtures were irradiated with UV light (~365 nm). SDS-PAGE analysis revealed a thin band at 60 kDa for bMunc13-2, which might represent a cross-linked product between CaM and the Munc13 domains (Figure 34). This band is also present in the non-irradiated reaction mixture, which might indicate an activation of the benzophenone group of SBC by ambient light. For Munc13-3 it was difficult to determine the formation of cross-linked products with CaM, as a distinct band was not visible for untagged Munc13-3. Instead, bands representing impurities or truncated Munc13-3 constructs (Figure 33, fraction #ET2) indicate that the untagged protein is unstable. Bands that might represent a cross-linked product between bMunc13-2 and CaM or where a cross-linked product between Munc13-3 and CaM should migrate were excised, *in-gel* digested (2.4.5.), and analyzed by MS.

Nano-HPLC/nano-ESI-LTQ-Orbitrap-MS/MS analysis of the gel bands of Munc13-3 did not reveal cross-linked products. A distinct band on the SDS gel (Figure 34), which might have indicated the formation of such a product, was not visible. However, the parts of the gel where a cross-linked product between Munc13-3 and CaM should have migrated (Figure 34, black boxes) were nevertheless analyzed to confirm that no cross-link had been formed and was identified by MS, which is much more sensitive than the staining of the SDS gel. Although both proteins, CaM and Munc13-3, were identified in the excised bands, the interaction between them could not be confirmed by analysis of the MS data. MS analysis of the band corresponding to the CaM/bMunc13-2 complex revealed one intermolecular cross-link (Figure 35). Interestingly, the adduct shown in Figure 35 contains a part of the sequence of the confirmed CaM-binding motif of bMunc13-2 (see amino acid sequence, 3.1.1., Figure 23). Apparently, this region of the bMunc13-2 domain had reacted with the amine-reactive site of the cross-linker, whereas Ile-125 in CaM had reacted with the benzophenone group, indicating that the cross-linker had not been removed completely after the labeling of CaM.

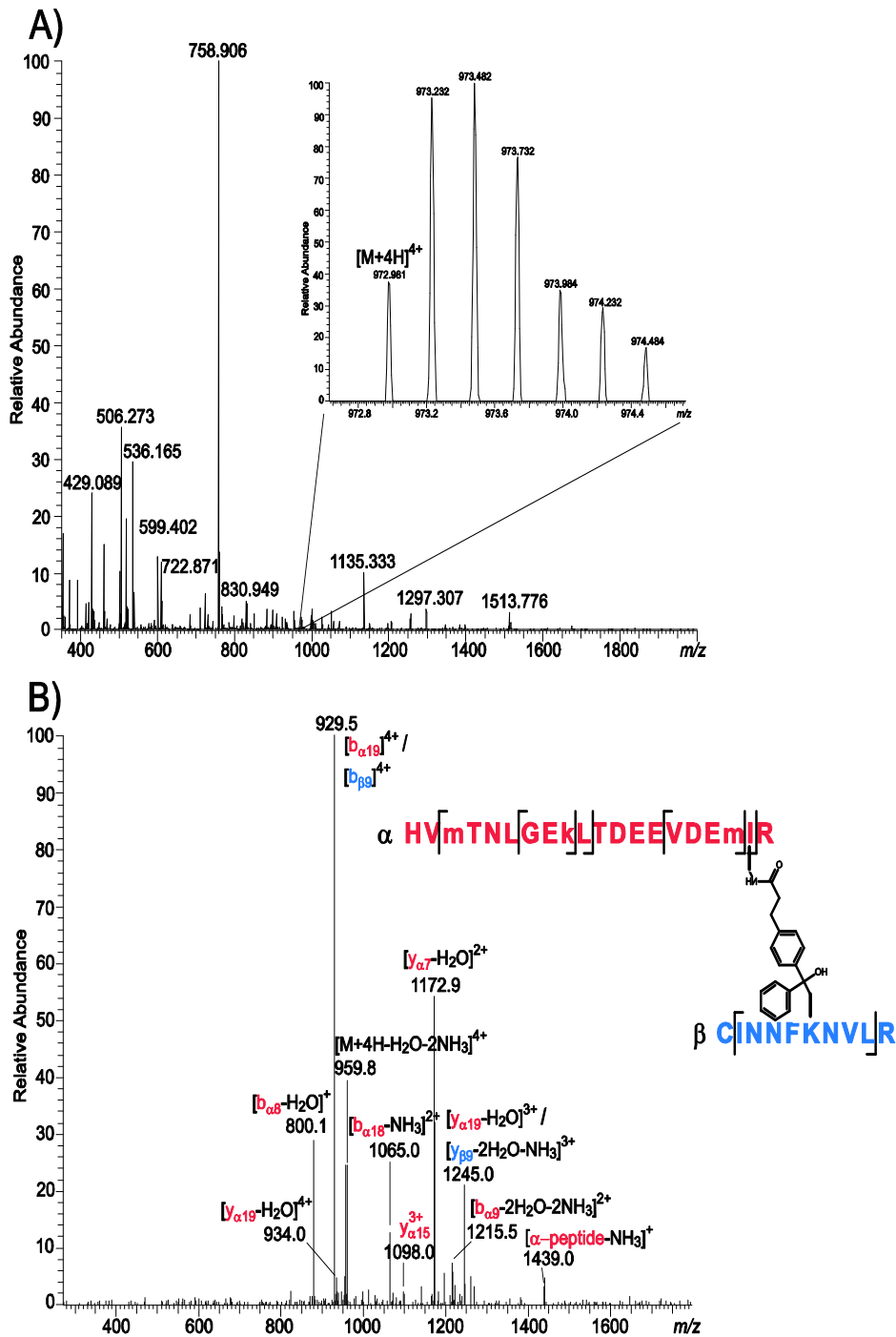


**Figure 35.** MS and MS/MS analysis of a cross-linked product between CaM and bMunc13-2. Nano-HPLC/nano-ESI-LTQ-Orbitrap-MS/MS analysis of a cross-linked peptide mixture between CaM and the bMunc13-2 domain (50-fold molar excess of SBC, 30 min, irradiation 8000mJ/cm<sup>2</sup>). A) Mass spectrum recorded at 80.7 min. The 4+ signal of the cross-linked product at  $m/z$  972.981 is shown enlarged. B) Fragment ion mass spectrum of the adduct between Lys-358 of bMunc13-2 ( $\beta$ -sequence 353-362, blue) and Ile-125 of CaM ( $\alpha$ -sequence 107-126, red). m: oxidized Met, k: trimethylated Lys.

Although one cross-link is certainly not sufficient to draw detailed conclusions on the interaction between CaM and bMunc13-2, this preliminary result confirms the CaM-binding motif in bMunc13-2. Nevertheless, the identified cross-linking product gives a first hint that the bMunc13-2 domain interacts with CaM through the CaM-binding motif, which was found

by bioinformatic prediction and was confirmed by biochemical studies and cross-linking experiments (3.1.1.). One drawback was that GST was also found in the analyzed gel band of the CaM/bMunc13-2 complex, indicating that the tag is apparently present throughout the gel lane.

Due to the instability of the GST-free Munc13 domains, especially Munc13-3, the cross-linking experiments were repeated with GST-tagged proteins. Therefore, the GST-bMunc13-2 and GST-Munc13-3 fusion proteins were purified as described (GST affinity and anion exchange chromatography, 3.1.2.) and used in cross-linking experiments with CaM. These experiments revealed similar results compared to those with the untagged proteins. SDS-PAGE analysis of the cross-linking reaction mixtures (Figure A6) showed bands representing the GST-bMunc13-2 and GST-Munc13-3 fusion proteins and bands for the CaM/bMunc13-2 complex, which appeared upon UV-irradiation. In the case of Munc13-3, a band migrating at ca. 75 kDa corresponds to the GST-Munc13-3 fusion protein, however, a distinct band corresponding to the CaM/Munc13-3 complex was not detected. MS and MS/MS analysis of the excised bands confirmed the cross-link for GST-bMunc13-2 that had already been identified in the experiments with untagged bMunc13-2 (Figure 35). Again, for GST-Munc13-3 no cross-link was identified.

In conclusion, investigation of the interaction between CaM and Munc13-3 did not reveal any cross-linking products, which might be due to the instability of this domain. For bMunc13-2, the importance of the already identified CaM-binding motif was confirmed.

### **3.1.4. Introduction of Bpa-Encoding Amber Stop Codons into Munc13**

The distance constraints obtained by chemical cross-linking with SBC are in the range of 15 - 25 Å. A more precise identification of an interaction site is achieved by using shorter spacers between the reactive groups of the cross-linker or, alternatively, by introduction of unnatural photo-reactive amino acids such as *p*-benzoylphenylalanine (Bpa, 1.2.1.3.) into the protein. Upon UV-irradiation, these amino acids react with other residues in their environment, thereby bridging C $\alpha$ -C $\alpha$  distances of up to 8 Å. Constraints obtained by the photo-reaction can be used in molecular modeling studies to allow a more detailed structural analysis of interaction sites in protein complexes.

Thus, DNA codons of hydrophobic residues at important anchor positions of the known CaM-binding motifs were exchanged to the amber stop codon (UAG) in order to incorporate Bpa

## Results

during the overexpression of Munc13 domains according to the method developed in the Schultz group (154). Different variants of GST-bMunc13-2 and GST-Munc13-3 domains, containing one amber stop codon were established by site directed mutagenesis (2.2.5.). DNA constructs of domains of bMunc13-2 (aa 366 - 780, Figure A4) and Munc13-3 (aa 711 - 1063, Figure A5) (217) that had already been used for overexpression of these variants (3.1.2.) were used as templates in the PCR reactions. After optimization of the PCR reaction, several variants were created (Table 7). Upon sequencing, it was observed that in the DNAs of GST-bMunc13-2 the translation stop codon of the construct was also UAG, the amber stop codon. For this reason, pairs of primers were designed to exchange this translation stop codon UAG to UAA, which does not interfere with Bpa incorporation.

**Table 7. Munc13 variants containing the amber stop codon.** Codons of different bulky hydrophobic residues, which are confirmed to be the anchor residues of the CaM-binding motif or which present potential additional interaction sites of the Munc13 domains with CaM, were exchanged to the amber stop codon that encodes Bpa.

Construct	Residue exchanged to Bpa	Position of the anchor residue in the CaM binding motif
pGEX-bMunc13-2 (366-780) F580Stop	F580	position 1 of the 2nd predicted motif
pGEX-bMunc13-2 (366-780) W619Stop	W619	potential second bulky anchor residue of the 2nd predicted motif
pGEX-bMunc13-2 (366-780) F723Stop	F723	position 1 of the confirmed motif
pGEX-bMunc13-2 (366-780) W775Stop	W775	potential second bulky anchor residue of the confirmed motif
pGEX-bMunc13-2 (366-780) F580Stop 1063TAA	F580	position 1 of the 2nd predicted motif
pGEX-bMunc13-2 (366-780) W619Stop 1063TAA	W619	potential second bulky anchor residue of the 2nd predicted motif
pGEX-bMunc13-2 (366-780) F723Stop 1063TAA	F723	position 1 of the confirmed motif
pGEX-bMunc13-2 (366-780) W775Stop 1063TAA	W775	potential second bulky anchor residue of the confirmed motif
pGEX-Munc13-3 (711-1063) F787Stop	F787	position 1 of the 2nd predicted motif
pGEX-Munc13-3 (711-1063) F823Stop	F823	potential second bulky anchor residue of the 2nd predicted motif
pGEX-Munc13-3 (711-1063) F962Stop	F962	position 1 of the confirmed motif
pGEX-Munc13-3 (711-1063) F1012Stop	F1012	potential second bulky anchor residue of the confirmed motif

Residues F723 (bMunc13-2) and F962 (Munc13-3) represent anchor residues at position one of the confirmed CaM-binding motifs. The exchange of these two amino acids to Bpa and the use of photo-cross-linking reactions should allow detailed insights into the interaction site between bMunc13-2 and Munc13-3 domains and CaM to be gained. Additional residues in the Munc13 domains (Table 7) were exchanged to Bpa to investigate their role as potential

CaM-interaction sites of bMunc13-2 and Munc13-3. Although at position 26 of the CaM-binding motif of bMunc13-2 and Munc13-3 no bulky hydrophobic residues are located, bulky amino acids close to position 26 of each investigated CaM-binding motif were exchanged to Bpa. An investigation into whether an additional CaM interaction site of bMunc13-2 and Munc13-3 can be detected, which is comparable to the unique 1-5-8-26 motif of Munc13-1 and ubMunc13-2, should be conducted in the future using the purified variants in photo-cross-linking experiments.

For bMunc13-2 and Munc13-3, a second CaM-binding motif in the *N*-terminal region of the proteins had been predicted. Preliminary biochemical studies had indicated that these motifs are not functional as Ca<sup>2+</sup>-dependent CaM interaction sites. In order to confirm these predictions, amino acids at distinct positions of these motifs were also exchanged to Bpa.

In summary, 12 variants containing the amber stop codon were constructed from the template DNAs of GST-bMunc13-2 and GST-Munc13-3 domains. As the template DNA was not optimized for *E.coli*'s codon usage, this might lead to an impaired overexpression of these variants as described for the proteins without Bpa (3.1.2.). Therefore, overexpression and purification of these variants was not conducted. In future experiments, site-directed mutagenesis (2.2.5.) should be repeated with the adapted template DNA that allows an improved overexpression of GST-bMunc13-2 and GST-Munc13-3 domains in *E.coli*. Afterwards these variants should be overexpressed and purified and their interaction with CaM should be investigated by photo-cross-linking.

### 3.2. CaM/skMLCK Interaction

Investigations of CaM/target interactions are commonly performed with peptides representing the minimal CaM-binding sequence. In recent NMR studies of the CaM/Munc13 peptide complex, a CaM-binding peptide of Munc13 was used, which was *C*-terminally elongated (54), compared to the one used in previous cross-linking studies (84). The NMR structure (pdb 2kdu) had revealed a more extended conformation of CaM in the CaM/peptide complex, compared to that found in the model structures derived from cross-linking experiments with shorter Munc13 peptides (54). In the CaM complex with the longer Munc13 peptide, a second bulky hydrophobic anchor residue at position 26 of the CaM-binding motif, which is not present in the shorter peptide, was found to interact with the *N*-terminal CaM domain (54). The following questions arise: I) is this novel 1-5-8-26 CaM-binding motif of Munc13 also found in other CaM targets?; II) can the 1-5-8-26 motif be introduced in other CaM target peptides by simple *C*-terminal elongation and amino acid exchanges?

A classical, well-characterized CaM target is the skeletal muscle myosin light chain kinase (skMLCK). The minimal CaM-binding region was narrowed down to a 26-amino acid peptide (M13), possessing a 1-5-8-14 CaM-binding motif (88, 98). For this study, four different skMLCK peptides were constructed with a *C*-terminal elongation compared to M13 and amino acid exchanges at positions 14 and 26 of the CaM-binding motif. Replacement of Phe-19 (corresponding to position 14 of the motif) with alanine (skMLCK F19A) or glutamate (skMLCK F19E) should remove the second anchor residue at this position and, in the case of skMLCK F19E, mimic the respective amino acid of Munc13 (Glu). The additional exchange of Leu-31 (position 26 of the motif) to tryptophan (skMLCK F19E/L31W) introduces a second bulky hydrophobic anchor residue, thereby mimicking the 1-5-8-26 CaM-binding motif of Munc13.

Recently, a general model was proposed for the conformations CaM can adopt in its complexes with target peptides and proteins. This model describes the dependence of the CaM conformation on the distance between the first and second hydrophobic anchor residue, leading to a more extended CaM conformation if this distance increases (53). In the skMLCK F19E/L31W peptide variant used in this study, the second bulky anchor residue is *C*-terminally shifted (position 14 → position 26) compared to the skMLCK peptide, which should lead to different CaM conformations in the CaM/skMLCK peptide complex compared to the complex between CaM and the skMLCK F19E/L31W peptide.



A combination of CD spectroscopy, chemical cross-linking, and surface plasmon resonance (SPR) spectroscopy was used for a structural and kinetic investigation of CaM binding to the four different skMLCK peptide variants.

### 3.2.1. Circular Dichroism Spectroscopy

CaM target regions usually have a high propensity to form  $\alpha$ -helical structures. In order to investigate the secondary structure of the four skMLCK peptide variants, circular dichroism (CD) spectroscopy was performed. The skMLCK peptides were dialyzed against phosphate buffer (pH 7.5, 2.1.5.) and far-UV CD spectra (Figure 36) were recorded on a Jasco J-810 CD spectrometer (2.1.11. and 2.4.6.).

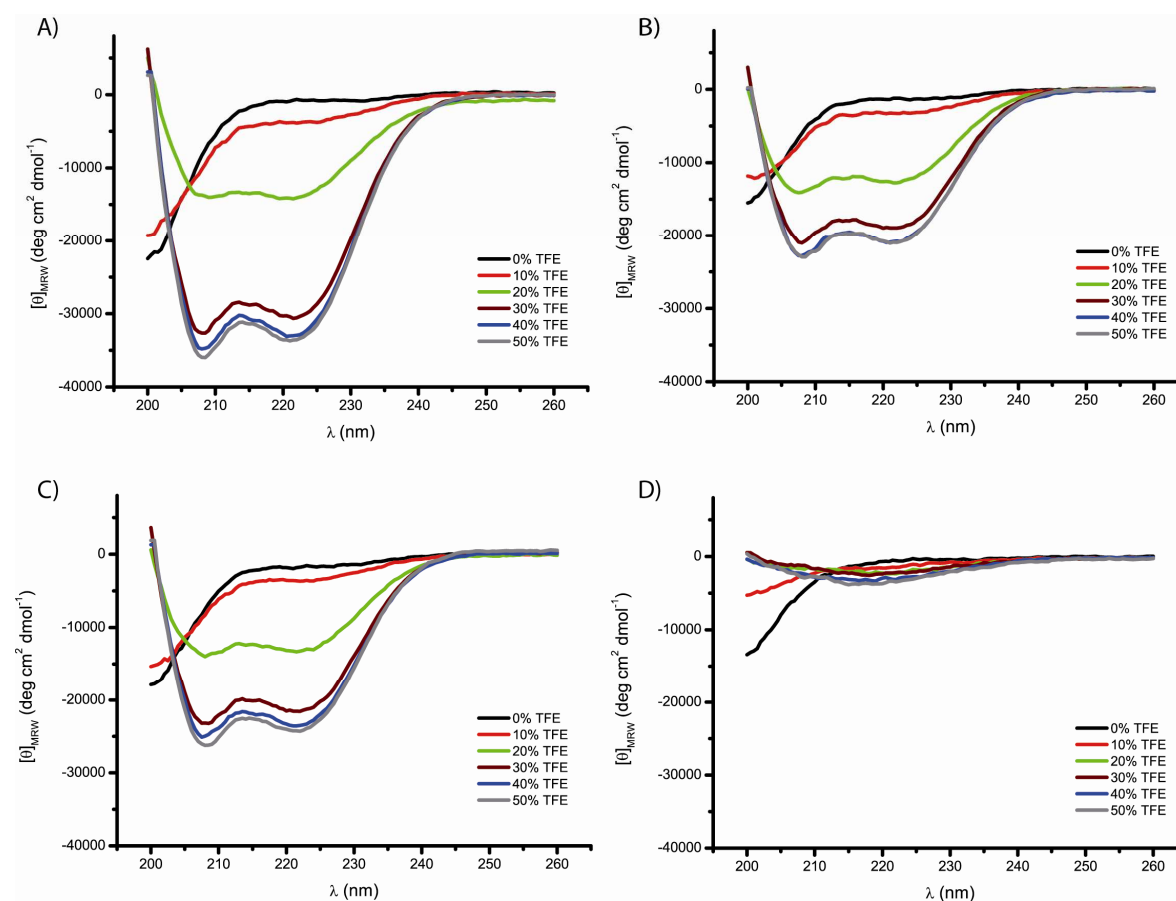


**Figure 36. CD spectra of skMLCK peptide variants.** Far-UV CD spectra were recorded between 200 and 260 nm for A) the skMLCK peptide, B) the skMLCK F19A peptide, C) the skMLCK F19E peptide, and D) the skMLCK F19E/L31W peptide. Different amounts of TFE [% (v/v)] were added to evaluate the propensity of the peptide variants to form an  $\alpha$ -helical structure (195).

All four skMLCK peptide variants possess a random-coil structure under the buffer conditions used (2.1.5.) (Figure 36, black spectra). Upon TFE addition, the structures of all peptides changed (Figure 36, colored spectra). With increasing TFE concentrations, an  $\alpha$ -helical

structure was induced in the skMLCK peptide, reaching a maximum  $\alpha$ -helical content at 40% (v/v) TFE (Figure 36A). Similar results were obtained for the two peptide variants with single amino acid exchanges at position 14 of the CaM-binding motif, skMLCK F19A and skMLCK F19E, indicating that the replacement of the phenylalanine residue at this position has no major impact on the secondary structure of the peptides (Figure 36B, C). In the case of the skMLCK F19E/L31W peptide, the amino acid exchanges resulted in considerable structural changes and a dramatic decrease of the peptide's propensity to form an  $\alpha$ -helix (Figure 36D), as had already been suspected by secondary structure predictions (PSIPREP).

In conclusion, the CD experiments revealed a high propensity of skMLCK, skMLCK F19A, and skMLCK F19E to form an  $\alpha$ -helical structure. In contrast, the skMLCK F19E/L31W peptide showed major differences in secondary structure and a decreased propensity to form an  $\alpha$ -helix. This raises the question whether these structural variations between the peptides have an effect on the structures of the respective CaM/peptide complexes.

### 3.2.2. Cross-links between CaM and skMLCK Peptide Variants

Structural investigation of the complexes between CaM and four different skMLCK peptide variants was performed by chemical cross-linking in combination with MS. As a first step, the influence of  $\text{Ca}^{2+}$  on the CaM/skMLCK peptide interaction was analyzed.  $\text{Ca}^{2+}$  titration experiments, conducted with the homobifunctional cross-linker BS<sup>2</sup>G, showed that CaM/skMLCK peptide complexes are formed at low (nanomolar) and high (millimolar)  $\text{Ca}^{2+}$  concentrations, but they seem to differ in their structures as evidenced by variations in their electrophoretic mobilities in SDS-PAGE analysis (220). Therefore, a more detailed structural examination of the CaM/peptide complexes at two different  $\text{Ca}^{2+}$  concentrations (30 nM and 1 mM) was conducted using the homobifunctional cross-linker BS<sup>2</sup>G and the heterobifunctional cross-linker SBC yielding complementary structural information.

Analysis of BS<sup>2</sup>G and SBC cross-linking reactions by SDS-PAGE (2.4.4.) showed bands for cross-linker-modified CaM (~17 kDa) and CaM/peptide complexes (~22 kDa), respectively (Figure 37). For skMLCK F19E/L31W and the other skMLCK variants (Figure A7), distinct bands for 1:1 CaM/peptide complexes were visible for the reactions conducted with 30 nM  $\text{Ca}^{2+}$ , while corresponding bands were more diverse for reactions with 1 mM  $\text{Ca}^{2+}$ . This had already been found in  $\text{Ca}^{2+}$  titration experiments (220). Additionally, the 1:1 CaM/peptide complexes formed at 30 nM or 1 mM  $\text{Ca}^{2+}$  differ in their electrophoretic mobilities, indicating

different conformations of the complexes. The bands corresponding to CaM/peptide (1:1) complexes were excised, washed, and *in-gel* digested (2.4.5.), and the resulting peptide mixtures were analyzed by nano-HPLC/nano-ESI-LTQ-Orbitrap-MS/MS (2.5.5.).

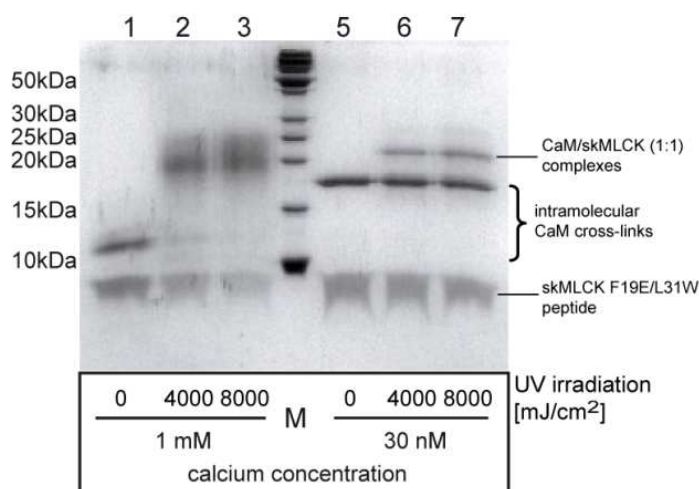


**Figure 37. SDS-PAGE of cross-linking reactions between CaM and the skMLCK F19E/L31W peptide.** The cross-linking reactions were conducted with SBC at free Ca<sup>2+</sup> concentrations of 30 nM and 1 mM and irradiated with UV-A light (maximum at 365 nm, irradiation energies of 0, 4000 or 8000 mJ/cm<sup>2</sup>). Bands migrating at ca. 22 kDa represent cross-linked 1:1 complexes between CaM and the skMLCK F19E/L31W peptide, while bands migrating at ca. 17 kDa correspond to cross-linker-labeled CaM. M: molecular weight marker.

MS analysis of the cross-linking reaction mixtures identified a number of cross-links between CaM and all four skMLCK peptide variants under investigation (Table A4, Table A5, Table A6, and Table A7). For the skMLCK peptide, Lys-21 and 30 in the *N*-terminal lobe of CaM, Lys-75 and 77 in the central linker region, and Lys-94 in the *C*-terminal CaM domain were connected through different residues of the peptide (Table A4), which is consistent with cross-linking studies using the shorter skMLCK M13 peptide (97). As an example, the cross-link between Lys-21 of CaM and Ala-12 of the skMLCK peptide is shown in Figure A8.  $\text{C}\alpha$ - $\text{C}\alpha$  distances between cross-linked amino acids were assumed to be up to 25 Å for both cross-linking reagents (SBC and BS<sup>2</sup>G) (84-85). These distance constraints are in agreement with the NMR structure of the CaM/M13 peptide complex (pdb 2bbm, (98)) shown in Figure A9A, B). Some slightly longer distances (up to 31 Å) can be explained by the inherent flexibility of the helix and both CaM lobes. These findings, and the fact that the  $\text{C}\alpha$ - $\text{C}\alpha$  distances between connected residues of the skMLCK peptide and the *N*-terminal CaM are not in agreement with the NMR structure of the CaM/Munc13 complex (pdb 2kdu, (54), Figure A9C), clearly indicate that CaM is collapsed around the skMLCK peptide in the complex. Furthermore, the structure of the CaM/skMLCK peptide complex does not depend

on the  $\text{Ca}^{2+}$  concentration as evidenced by similar cross-linking products found in reactions with low (30 nM) and high (1 mM)  $\text{Ca}^{2+}$  concentrations (Table A4).

Cross-links identified in the reactions with skMLCK F19A and skMLCK F19E (Table A5 and Table A6) lead to the same conclusions as for the skMLCK peptide. The  $\text{Ca}\alpha$ - $\text{Ca}\alpha$  distance constraints are in agreement with the NMR structure of the CaM/M13 peptide complex (98) (Figure A10 and Figure A11) and are not consistent with the extended CaM conformation in the CaM/Munc13 peptide complex (54) (Figure A10C and Figure A11C). Representative cross-linked products are shown in Figure A12 and Figure A13. According to these results, the exchange of the hydrophobic anchor residue at position 14 of the CaM-binding motif (Phe-19) to alanine or glutamate does not induce a structure similar to that of the CaM/Munc13 peptide complex.

Analysis of the cross-links between CaM and the skMLCK F19E/L31W peptide revealed a number of cross-linked products (Table A7). The cross-link between Lys-94 of CaM and Leu-1 of the skMLCK F19E/L31W peptide is shown in Figure 38. As for the other skMLCK peptide variants, all cross-links identified were in agreement with the CaM/M13 peptide complex structure (Figure 39A, B). Moreover, the distance constraints are not consistent with the CaM/Munc13 peptide complex, which exhibits a more extended CaM conformation (Figure 39C). These results indicate that even a skMLCK peptide, which strongly resembles the 1-5-8-26 CaM-binding motif of Munc13, can not induce a complex structure comparable to that of the CaM/Munc13 peptide complex.

At nanomolar  $\text{Ca}^{2+}$  concentrations, CaM is only half-saturated with  $\text{Ca}^{2+}$ . In order to generate the structure of half  $\text{Ca}^{2+}$ -loaded CaM bound to the skMLCK F19E/L31W peptide, the *N*-terminus of apo-CaM (pdb 2l53, (221)) was docked with the *C*-terminus of holo-CaM (pdb 2bbm, (98)). Afterwards, the cross-links obtained at a  $\text{Ca}^{2+}$  concentration of 30 nM were evaluated for their agreement with this half- $\text{Ca}^{2+}$ -loaded structure (Figure 39D). The distance constraints between the *C*-terminal CaM domain and the peptide are consistent with the structure of half  $\text{Ca}^{2+}$ -loaded CaM, while the distance between the skMLCK peptide and amino acids in the *N*-terminal lobe of CaM cannot be bridged by the cross-linkers. Due to the fact that the two CaM domains were simply docked and no further structural refinement was performed, it cannot be excluded that the structure of half  $\text{Ca}^{2+}$ -loaded CaM is more compact, which would be in agreement with all cross-links.

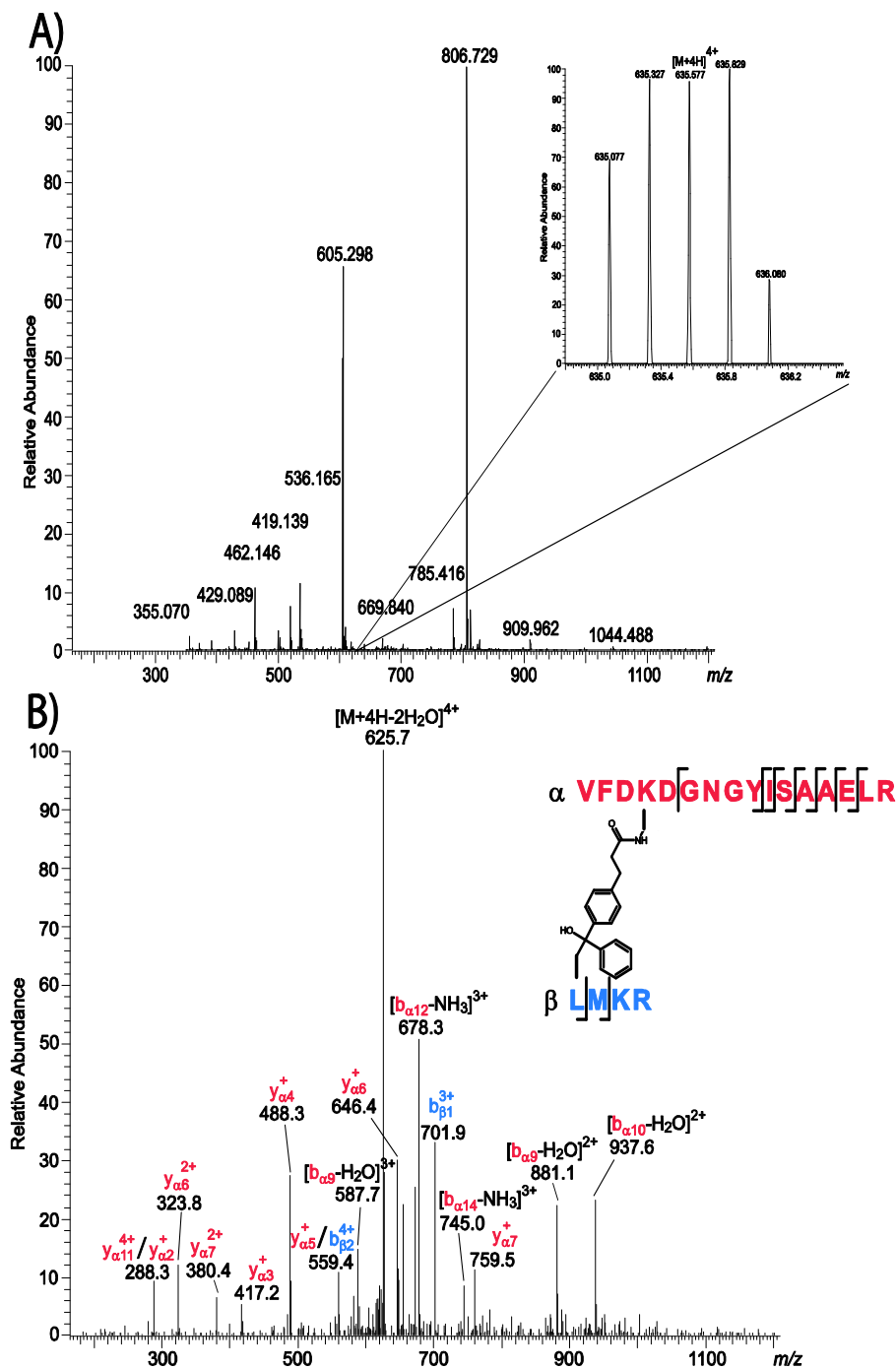


**Figure 38.** MS and MS/MS analysis of a cross-linking reaction between CaM and the skMLCK F19E/L31W peptide. The cross-linking reaction was conducted with a 50-fold molar excess of SBC for 30 min at 1 mM  $Ca^{2+}$  (irradiation: 8000  $mJ/cm^2$ ). A) The mass spectrum was recorded at a retention time of 59.94 min. The 4+ signal of the cross-linked product at  $m/z$  635.577 is highlighted. B) Fragment ion mass spectrum of the adduct between Lys-94 of CaM ( $\alpha$ -sequence 91-106, red) and Leu-1 of the skMLCK F19E/L31W peptide ( $\beta$ -sequence 1-4, blue).

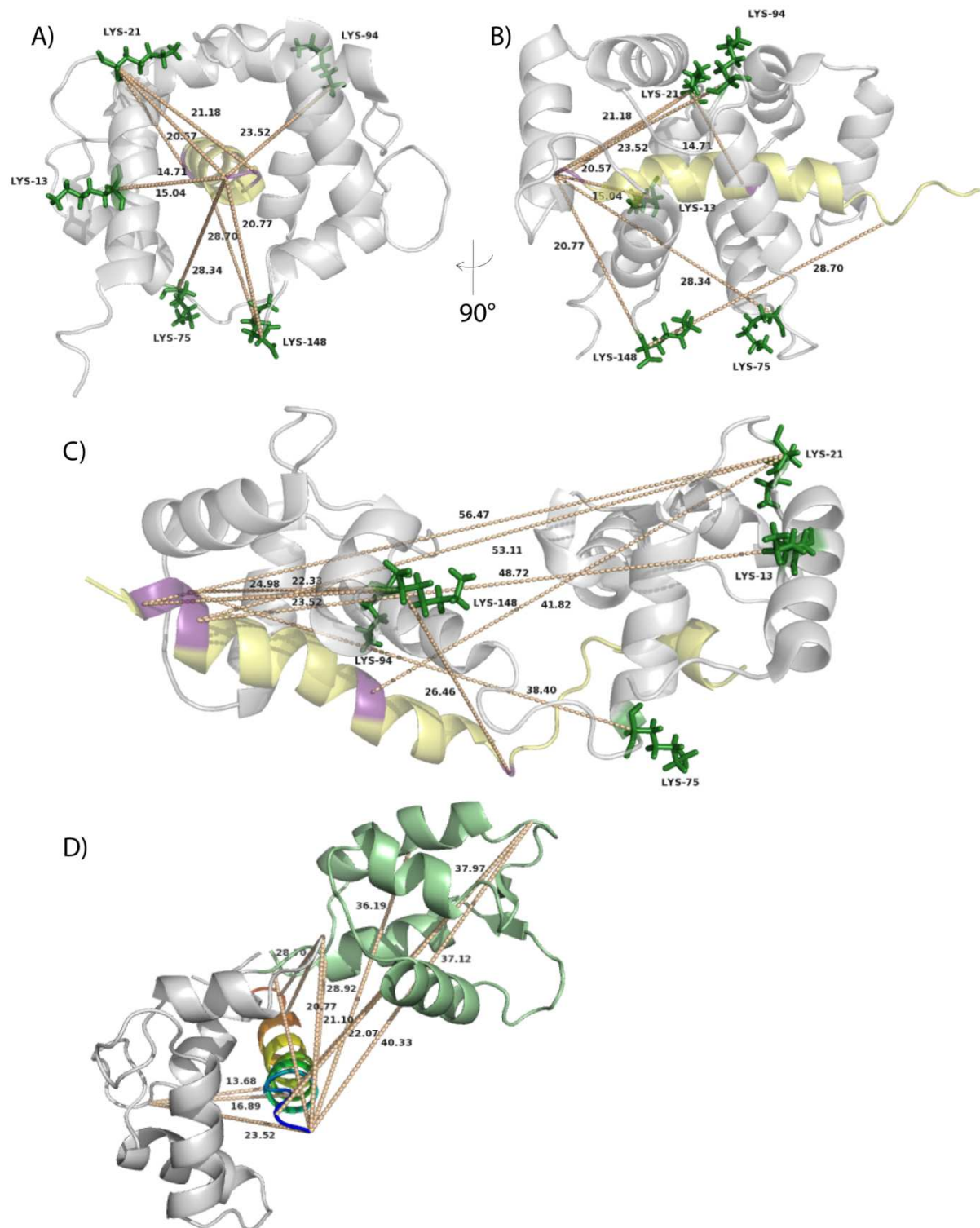


**Figure 39. Identified cross-linked products between CaM and the skMLCK F19E/L31W peptide.**  $\text{Ca-Ca}$  distances (in Å) between cross-linked amino acids, identified at 1 mM  $\text{Ca}^{2+}$ , are depicted as dotted lines in the NMR structures of A), B) the CaM/M13 peptide complex (pdb 2bbm, (98); viewed from two angles and C) the CaM/Munc13-1 peptide complex (pdb 2kdu, (54)). CaM is colored in grey, the peptide is shown in yellow. Reacted amino acids in CaM are displayed as green sticks, while those of the peptide are shown in purple. D)  $\text{Ca-Ca}$  distances of cross-linked amino acids identified at 30 nM  $\text{Ca}^{2+}$  are depicted in the half- $\text{Ca}^{2+}$ -loaded CaM (N-terminal domain of apo-CaM (pdb 2i53, (221), aa 1-77; green) and C-terminal domain of holo-CaM (pdb 2bbm, (98), aa 78-147; grey)). The skMLCK F19E/L31W peptide is shown in rainbow colors.

In summary, the cross-linking experiments, conducted at  $\text{Ca}^{2+}$  concentrations of 30 nM and 1 mM with two different cross-linking reagents, revealed that the 1-5-8-26 CaM-binding motif of Munc13 cannot be induced in the skMLCK peptides by C-terminal elongation of the peptide and amino acid exchanges. Even the skMLCK peptide, which closely mimics the sequence of Munc13's 1-5-8-26 motif did not induce an extended CaM conformation as found for the CaM/Munc13 peptide complex (54). All four skMLCK peptide variants under investigation created complexes with CaM that are in agreement with the NMR structure of the CaM/M13 peptide complex (98).

### 3.2.3. Surface Plasmon Resonance Spectroscopy

In addition to the structural characterization of the CaM/skMLCK peptide complexes, the binding affinities between CaM and all four skMLCK peptides were examined by surface plasmon resonance (SPR) spectroscopy. The skMLCK M13 peptide has a dissociation constant ( $K_D$ ) for CaM binding of <10 nM (88), which had also been found for the Munc13-1 peptide by NMR titration experiments (54). SPR measurements were performed with the four skMLCK peptide variants immobilized (2.4.8.) and CaM in the running buffer to determine the dissociation constants. Comparison of the obtained  $K_D$  values for the skMLCK peptide variants with these of the skMLCK M13 and Munc13-1 peptides for CaM binding, should clarify the influence of the exchanged anchor residues (Phe-19, Leu-31) on CaM affinity.

SPR measurements of the dissociation constant between the C-terminally elongated skMLCK peptide and CaM revealed a  $K_D$  value in the nanomolar range (4.2 ( $\pm$ 0.6) nM; Figure 40A) comparable to the shorter skMLCK M13 peptide, indicating that the additional C-terminal residues do not influence the binding behavior of the skMLCK peptide. Aside from the high-affinity binding event, a second linear phase of the dependence of the steady state response on the CaM concentration was detected (Figure 40A), suggesting a low-affinity binding event. In previous cross-linking studies, the binding of an additional CaM target peptide to a 1:1 CaM/peptide complex had been described as a non-specific binding event (79, 84), which might also be the case herein. The CaM affinity determined for the skMLCK F19A peptide was found to be reduced compared to the skMLCK peptide, as evidenced by a  $K_D$  of 85 ( $\pm$ 9) nM (Figure 40B), underlining the importance of the phenylalanine residue at position 14 of the CaM-binding motif of skMLCK. These results are confirmed by the fact that the exchange of the hydrophobic phenylalanine to an acidic glutamate residue in the skMLCK peptide F19E further reduces the binding affinity of the skMLCK peptide to CaM. In the case

of the skMLCK F19E peptide, only the linear binding phase was observed, while the high-affinity binding event was no longer detectable (Figure 40C). Moreover, an additional exchange of the leucine residue at position 26 of the CaM-binding motif to tryptophan (skMLCK F19E/L31W peptide) showed an essentially identical result (Figure 40D), demonstrating that a tryptophan residue is not able to function as second anchor site in skMLCK.

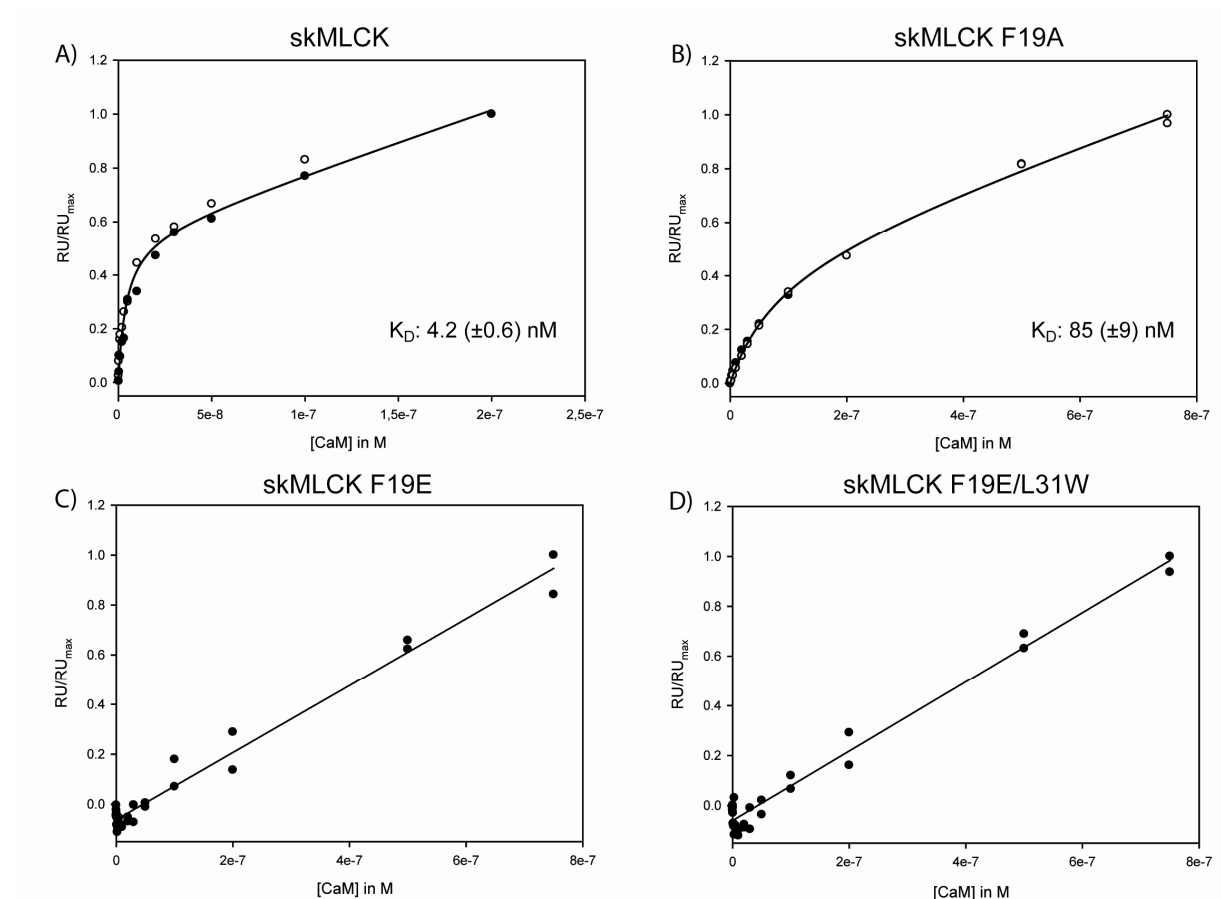


**Figure 40.** Analysis of the binding of CaM to the skMLCK peptides by SPR. The dependence of the steady-state response on the CaM concentration is illustrated for (A) the skMLCK peptide, (B) skMLCK F19A, (C) skMLCK F19E, and (D) skMLCK F19E/L31W. The dissociation constants ( $K_D$ ) for skMLCK and skMLCK F19A, determined by fitting the data (eq13 (2.4.8.)): solid lines), are given  $\pm$  standard error from two individual binding curve measurements (filled and open circles). For skMLCK F19E and skMLCK F19E/L31W only the linear binding event was detected.

It is therefore concluded that the extraordinary 1-5-8-26 CaM-binding motif of Munc13 cannot be introduced in the classical CaM target skMLCK by C-terminal elongation and amino acid exchanges.



### 3.3. Interaction of Adenylyl Cyclases with CaM and Orai1/STIM1

Adenylyl cyclases (ACs) are regulated by a number of different factors such as  $G_{so}$ , protein kinases, and  $Ca^{2+}$  (105). Although the membrane-bound AC isoforms (AC1-9) possess a common predicted structure (101), they are differently regulated. AC1 and AC8 are both stimulated by  $Ca^{2+}$  in a CaM-dependent manner, but their mechanisms of activation by CaM are different (107). In order to extend the current knowledge about the CaM interaction with AC1 and AC8, different methods were used, namely, CD spectroscopy, ITC, and chemical cross-linking/MS. Furthermore, the interaction of AC8 with the store-operated  $Ca^{2+}$  (SOC) channel protein Orai1 and the endoplasmic reticulum (ER)  $Ca^{2+}$  sensor STIM1 was investigated by FRET to gain insights into the mechanism of store-operated  $Ca^{2+}$  entry (SOCE).

#### 3.3.1. CaM Binding to AC1 and AC8

The two AC isoforms, AC1 and AC8, are both stimulated by CaM and comprise diverse mechanisms of regulation by the  $Ca^{2+}$  sensor. While CaM binding to AC1 occurs in the C1b subdomain (108-109), AC8 exhibits two CaM-binding motifs - one in the *N*-terminus and one in the C2b subdomain (110) (Figure 41).

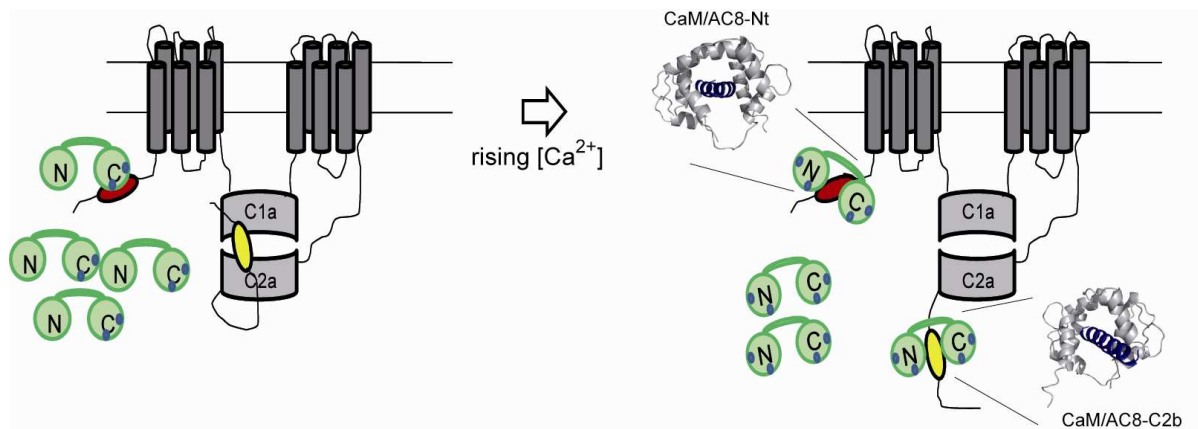


**Figure 41. Schematic presentation of CaM binding to AC8.** AC8 possesses two CaM-binding motifs, an *N*-terminal one (red ellipse, AC8-Nt) and one in the C2b domain (yellow ellipse, AC8-C2b). The catalytic center is formed by an interaction between the C1a and C2a domains (grey). AC8 is membrane-anchored by two bundles of six  $\alpha$ -helices (cylinders). At low  $Ca^{2+}$  concentrations half- $Ca^{2+}$ -loaded CaM (green) binds to AC8-Nt only, while AC8-C2b is bound to the catalytic center of AC8, inhibiting the cAMP production. At higher  $Ca^{2+}$  concentrations,  $Ca^{2+}$ -CaM also binds to AC8-C2b, activating the cAMP production.

The *N*-terminus of AC8 exhibits a typical 1-5-8-14 CaM-binding motif and was found to interact with the Ca<sup>2+</sup>-loaded *C*-terminal lobe of CaM. In contrast, the AC8-C2b domain interacts with the Ca<sup>2+</sup>-loaded *N*-terminal CaM lobe via an IQ-like motif (110, 222). These findings, and the fact that the *N*-terminal CaM-binding motif of AC8 is not necessarily required for the Ca<sup>2+</sup> sensitivity of the protein, support a model that describes the *N*-terminus of AC8 as CaM trap, which transfers the CaM molecule to the *C*-terminal AC8-C2b domain, thereby activating cAMP production (112) (Figure 41). This model raises the question whether both CaM-binding regions of AC8 bind simultaneously during the transfer of CaM from the *N*-terminus to the C2b domain of AC8 or whether the *N*-terminus of AC8 only serves to raise the local CaM concentration in the environment of AC8-C2b to ensure a fast activation of the enzymatic function. In order to gain more detailed insights into the mechanism of CaM-dependent activation of AC1 and AC8, a structural and thermodynamic characterization of the CaM complexes with peptides comprising the CaM-binding regions of both ACs was carried out using CD spectroscopy, ITC, and chemical cross-linking/MS.

### 3.3.1.1. Circular Dichroism Spectroscopy

Secondary structure predictions using PSIPRED revealed that the peptides comprising the CaM-binding regions of AC1 and AC8 (Figure 42) show high propensities to form  $\alpha$ -helical structures, which is typical for CaM targets (49-50). Experimental confirmation of these predictions was delivered by circular dichroism (CD) spectroscopy (2.4.6.).

AC8-Nt	(M <sub>r</sub> = 3065.51)	GSRPQRL <b><u>L</u></b> WQTAV <b><u>R</u></b> H <b><u>I</u></b> TEQRF <b><u>I</u></b> HGH
AC8-C2b	(M <sub>r</sub> = 2882.35)	YSLAAVVLGL <b><u>VQ</u></b> SLNRQRQQLNE
AC1-C1b	(M <sub>r</sub> = 3454.41)	IKPAKRM <b><u>K</u></b> FKTVCYLLVQLMHC <b><u>R</u></b> KM <b><u>F</u></b> KA

**Figure 42. Amino acid sequences of the AC peptides used in this work.** AC8 exhibits two CaM-binding regions - one 1-5-8-14 motif in the *N*-terminus (AC8-Nt) and an IQ-like motif in the C2b subdomain (AC8-C2b). In contrast, AC1 possesses only one CaM-binding (1-18) motif in the C1b subdomain (AC1-C1b). The hydrophobic anchor residues are highlighted in bold and underlined and the relative molecular masses (M<sub>r</sub>) are shown in brackets.

As illustrated in Figure 43, both AC8 peptides and the AC1 peptide show a high propensity to form  $\alpha$ -helices. With raising TFE concentrations, the minima of the CD signal at 208 and 220 nm become more pronounced, indicating that an  $\alpha$ -helical structure is induced. Differences between the peptides consist in the TFE concentrations that are required to reach the maximum  $\alpha$ -helical content, indicating that AC8-Nt has the highest propensity to form an  $\alpha$ -helix, while for AC8-C2b and AC1-C1b this propensity is less pronounced.

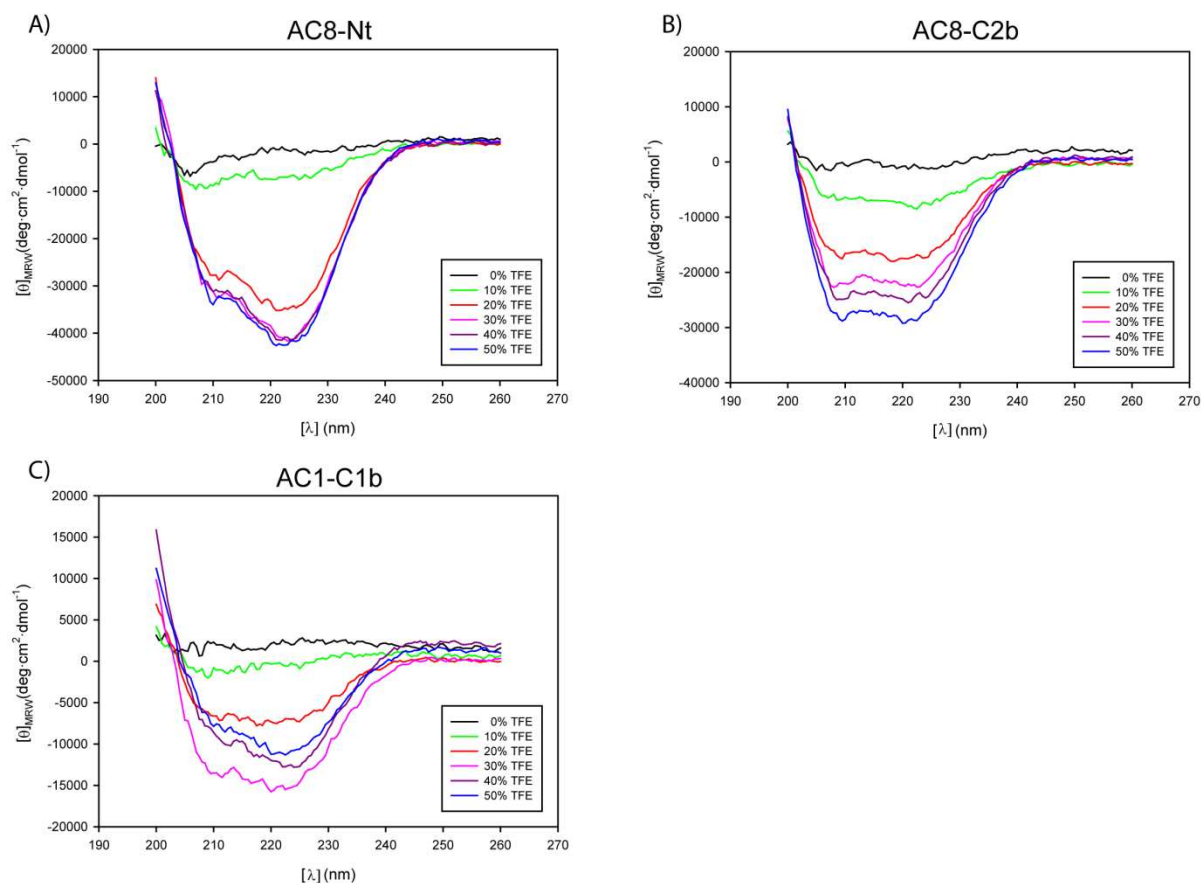


**Figure 43. CD spectra of AC peptides.** Far-UV CD spectra were recorded between 200 and 260 nm for A) AC8-Nt, B) AC8-C2b, and C) AC1-C1b. The addition of different TFE concentrations [% (v/v)] allows an estimate of the propensity of the peptide variants to form  $\alpha$ -helical structures.

### 3.3.1.2. Isothermal Titration Calorimetry Measurements

In addition to secondary structure investigations of the AC peptides by CD spectroscopy, the CaM interaction with peptides of AC1 and AC8 comprising the CaM-binding regions was thermodynamically characterized by isothermal titration calorimetry (ITC). The AC peptides were titrated into a CaM solution in the ITC reaction cell.

Analysis of the interaction between CaM and the AC8-Nt peptide revealed one binding event with a stoichiometry of nearly 1:1 ( $N = 1.23 \pm 0.01$ ) and a dissociation constant ( $K_D$ ) in the nanomolar range ( $30.12 \pm 8.95$  nM) (Figure 44), which is comparable to typical CaM targets (4, 99). A strongly negative value for the changes in enthalpy indicates an enthalpically driven binding event, which lowers the flexibility of CaM during complex formation, as evidenced by the negative value for the changes in entropy. For the AC8-C2b peptide, the CaM affinity was too low to obtain reliable data in the ITC experiments (data not shown), confirming the differences in CaM-binding affinities between AC8-Nt and AC8-C2b in *offline* nano-ESI-MS studies (3.3.1.3.). The AC8-C2b peptide was also titrated to a preformed CaM/AC8-Nt

peptide complex to investigate whether both AC8 peptides can bind simultaneously to CaM or whether AC8-Nt can transfer CaM to AC8-C2b, as had been hypothesized (112). In agreement with the results from *offline* nano-ESI-MS (3.3.1.3.) and cross-linking experiments (3.3.1.4.), no simultaneous CaM binding of both AC8 peptides was observed (data not shown). In the case of the AC1-C1b peptide titrated to CaM, a binding event was detected at a stoichiometry of 1:10, which indicates an oligomerization of AC1-C1b peptides (Figure A18).

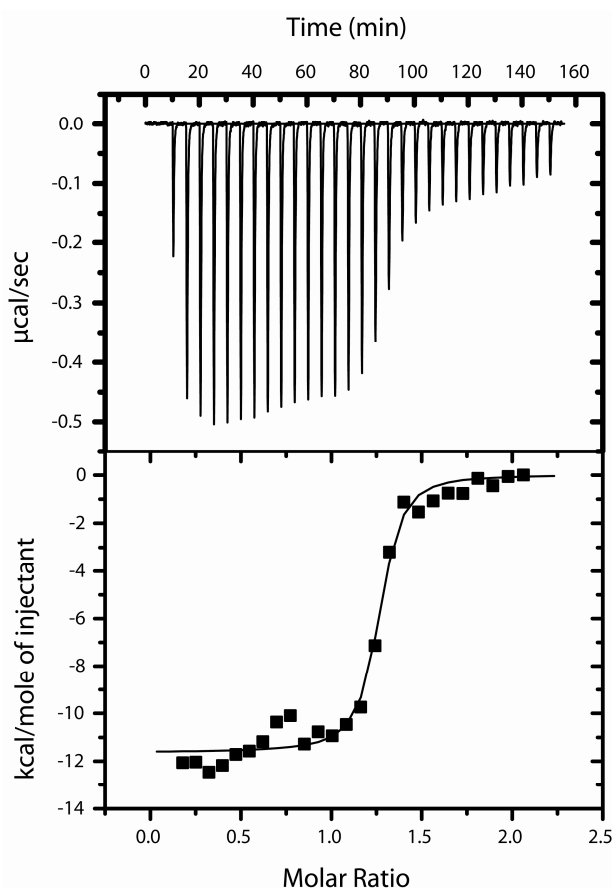


**Figure 44. ITC analysis of the CaM/AC8-Nt peptide interaction.** The AC8-Nt peptide (100  $\mu\text{M}$  in the syringe) was titrated to CaM (10  $\mu\text{M}$  in the reaction cell). One binding event was detectable with a  $K_D$  of  $30.12 \pm 8.95$  nM, stoichiometry  $N = 1.23 \pm 0.01$ ,  $\Delta H = -11.6 \pm 0.18$  kJ/mol, and  $\Delta S = -19.09$  J/mol/K.

### 3.3.1.3. *Offline* Nano-ESI-MS

In order to address the differences in CaM-dependent activation of AC1 and AC8, CaM binding of peptides comprising the CaM-binding regions of the two isoforms was examined at two different  $\text{Ca}^{2+}$  concentrations. AC peptides (Figure 42) were added to a CaM solution containing either 200  $\mu\text{M}$  EGTA (free  $[\text{Ca}^{2+}]$  ca. 2.4 nM; low  $\text{Ca}^{2+}$  concentration) or 1 mM  $\text{Ca}^{2+}$  (high  $\text{Ca}^{2+}$  concentration) and the mixtures were analyzed by *offline* nano-ESI-MS (2.5.6., Figure 45).

## Results

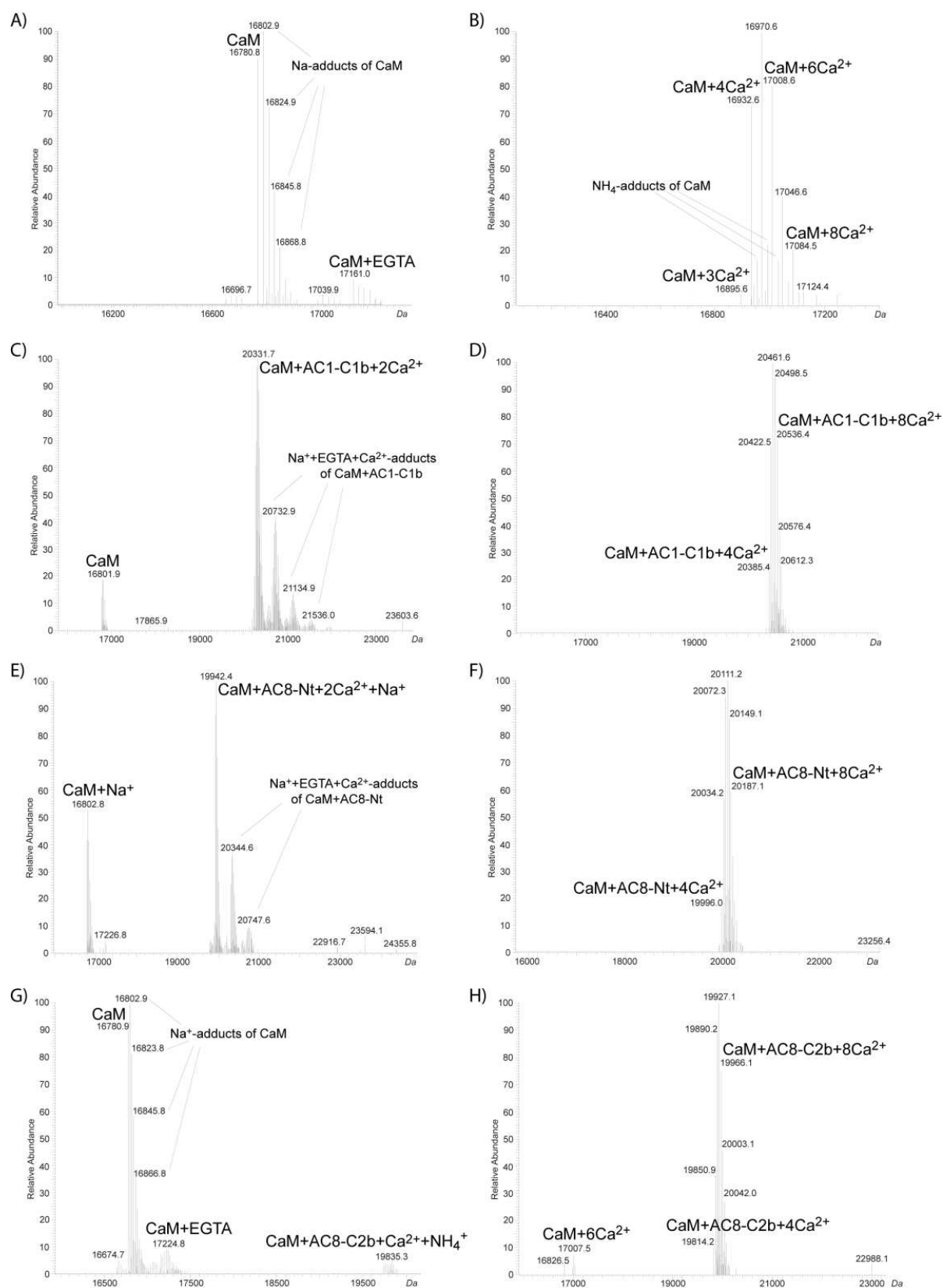


**Figure 45. Interaction between CaM and AC peptides.** *Offline nano-ESI-MS experiments of CaM solutions in the absence (A, B) or presence of AC peptides (C - H) were performed at low (200  $\mu$ M EGTA; free  $\text{Ca}^{2+}$  concentration ca. 2.4 nM; A, C, E, G) or high  $\text{Ca}^{2+}$  concentrations (1 mM  $\text{Ca}^{2+}$ ; B, D, F, H). Deconvoluted mass spectra, presenting singly charged species, show CaM complex formation with AC1-C1b (B, C), AC8-Nt (E, F), and AC8-C2b (G, H). Taken from Masada *et al.* 2012 (222).*

At a  $\text{Ca}^{2+}$  concentration of 1 mM, CaM is fully loaded with  $\text{Ca}^{2+}$ . In addition to the four  $\text{Ca}^{2+}$  ions that are specifically coordinated via the EF-hands of CaM, up to six  $\text{Ca}^{2+}$  ions are bound non-specifically to CaM. This is often observed for cations such as calcium, sodium, ammonium or potassium (Figure 45B). In contrast, upon addition of 200  $\mu\text{M}$  EGTA, CaM was detected in the  $\text{Ca}^{2+}$ -free form with only sodium ions or EGTA molecules, which were probably non-specifically attached to CaM (Figure 45A) (222). CaM complex formation was shown for all three AC peptides at low (Figure 45C, E, G) and high  $\text{Ca}^{2+}$  concentrations (Figure 45D, F, H). No signal was visible for  $\text{Ca}^{2+}$ -loaded CaM in the solutions containing 200  $\mu\text{M}$  EGTA without peptide (Figure 45A) (222). Nevertheless, CaM/peptide complexes with two coordinated  $\text{Ca}^{2+}$  ions were observed in the solutions containing 200  $\mu\text{M}$  EGTA (Figure 45C, E, G). This confirms that the affinity of CaM for  $\text{Ca}^{2+}$  is increased when a target peptide is bound. The peak intensities of CaM/peptide complexes are higher in comparison to peptide-free CaM in the presence of 1 mM  $\text{Ca}^{2+}$  (Figure 45D, F, H). As shown in Figure 45D and F, no signal for the non-peptide-bound CaM was detectable for AC1-C1b and AC8-Nt, which indicates a higher CaM affinity of these peptides in the presence of  $\text{Ca}^{2+}$ . In the solutions containing EGTA, the ratio between signal intensities of the CaM/peptide complex to peptide-free CaM was highest for AC1-C1b and lowest for AC8-C2b, which indicates that the relative affinities of the peptides for CaM are as follows: AC1-C1b > AC8-Nt > AC8-C2b (222). In order to investigate whether both AC8 peptides can bind simultaneously to CaM, both peptides were added to a CaM solution containing either 1 mM  $\text{Ca}^{2+}$  or 200  $\mu\text{M}$  EGTA (Figure A14). No signals were detectable that correspond to a 1:2 complex between CaM and both AC8 peptides (Figure A14), which underlines that there is no simultaneous binding of both CaM-binding motifs of AC8 to CaM. This emphasizes the assumption that the *N*-terminus of AC8 raises the local CaM concentration in the environment of AC8-C2b, but does not directly transfer the CaM molecule (Figure 41).

### 3.3.1.4. Chemical Cross-linking of CaM and AC1/AC8 Peptides

Two complementary heterobifunctional cross-linkers, SBC and sulfo-SDA (Figure A15), were used for structural investigation of the interaction between CaM and the AC1/AC8 peptides. The cross-linking reactions were conducted in a two-step fashion in the presence or in the absence of  $\text{Ca}^{2+}$ . First, the amine-reactive site of the cross-linker was reacted with CaM. After quenching and separation of excess cross-linker, samples were irradiated with UV light (4000 or 8000  $\text{mJ}/\text{cm}^2$ ; 2.5.2.). High  $\text{Ca}^{2+}$  concentrations were adjusted by addition of slightly more than 1 mM  $\text{CaCl}_2$  (1.4 mM), while addition of 10 mM EGTA resulted in  $\text{Ca}^{2+}$ -free

solutions. Intact reaction mixtures were analyzed by SDS-PAGE (2.4.4.) and MALDI-TOF-MS (2.5.3.).

MS measurements revealed different amounts of cross-linked CaM/peptide complexes for the three AC peptides (Figure A16). In the presence of  $\text{Ca}^{2+}$ , the signal of the CaM/AC8-Nt peptide complex was slightly higher than that of cross-linker-labeled CaM. Additionally, a signal was observed representing a 1:2 complex, in which two AC8-Nt peptides bind to one CaM molecule (Figure A16A). Apparently, the second AC8-Nt peptide binds non-specifically to the CaM/AC8-Nt peptide complex, as has already been described for other CaM target peptides such as Munc13-1 (84). In the reaction mixtures containing 10 mM EGTA where literally no free  $\text{Ca}^{2+}$  is present, the signal intensity of cross-linker-modified CaM was significantly higher than that of the CaM/AC8-Nt peptide complex (data not shown). This observation confirms the results of the *offline* nano-ESI-MS measurements, which had revealed a higher affinity of CaM to AC peptides at higher  $\text{Ca}^{2+}$  concentrations. For the AC8-C2b peptide, the signal of the cross-linker-labeled CaM was higher compared to that of the CaM/AC8-C2b peptide complex, and a 1:2 complex was not detected (Figure A16B). Reaction mixtures containing both AC8 peptides were analyzed (Figure A16C) and confirmed the findings of the *offline* nano-ESI-MS experiments where no CaM complex was found with both peptides binding simultaneously (Figure A14). Essentially, identical signals were obtained in the reaction mixtures with the AC8-Nt peptide alone (Figure A16A), indicating that a 1:2 complex containing both AC8 peptides is not formed in the cross-linking experiments. However, it cannot be ruled out completely that the broad signal, labeled with CaM/2AC8-Nt (Figure A16C), corresponds to a mixed species between CaM and either of the two AC8 peptides.

MALDI-TOF-MS analysis of the reaction mixtures containing the AC1-C1b peptide revealed signals of cross-linker-modified CaM, but not for a complex between CaM and the AC1-C1b peptide (Figure A16D). This result was unexpected because in the *offline* nano-ESI-MS experiments a non-covalent CaM/AC1-C1b peptide complex had been detected. One explanation might be that addition of the cross-linking reagent (SBC or sulfo-SDA) caused oligomerization of the AC1-C1b peptide, as observed in the SDS-PAGE analysis (Figure 46).

SDS-PAGE analysis of the cross-linking reactions with 1.4 mM  $\text{Ca}^{2+}$  before irradiation ( $0 \text{ mJ/cm}^2$ ) showed bands at around 15 kDa corresponding to the different  $\text{Ca}^{2+}$ -loaded states of CaM, which are not present in the absence of  $\text{Ca}^{2+}$  (10 mM EGTA) (Figure 46). Upon

## Results

irradiation with UV-A light, the photo-reaction was induced and bands representing CaM/AC peptide complexes were observed. In the presence of  $\text{Ca}^{2+}$  (Figure 46A), the cross-linked complexes showed different electrophoretic mobilities on the SDS gel, while distinct bands were visible in the absence of  $\text{Ca}^{2+}$  (10 mM EGTA) (Figure 46B).

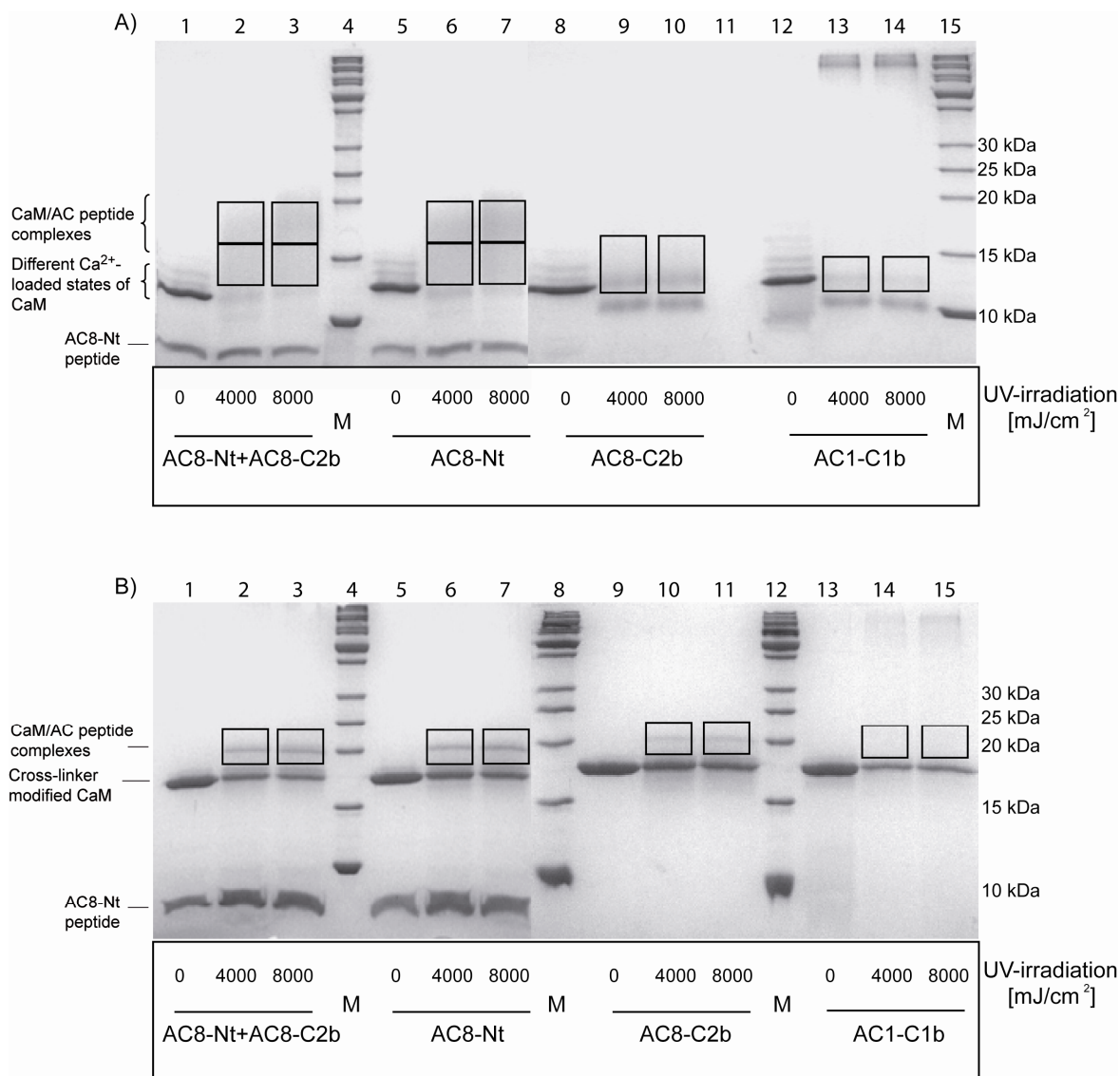


**Figure 46. SDS-PAGE analysis of cross-linking reaction mixtures between CaM and AC peptides.** The cross-linking reactions were conducted at a 50-fold molar excess of SBC in the presence of A) 1.4 mM  $\text{Ca}^{2+}$  or B) 10 mM EGTA. Reaction mixtures were irradiated with UV-A light (0, 4000, or 8000  $\text{mJ/cm}^2$ ). Please note that  $\text{Ca}^{2+}$ -loaded CaM and CaM complexes exhibit higher mobilities on the SDS gel due to their more compact structures compared to the  $\text{Ca}^{2+}$ -free states.

For AC8-C2b and AC1-C1b, bands migrating at ca. 11 kDa were detected in the presence of  $\text{Ca}^{2+}$  (Figure 46A), which correspond to intramolecularly cross-linked CaM species that exhibit higher electrophoretic mobilities compared to non-modified CaM. Additionally, a band was observed for the AC8-Nt peptide in the reactions conducted with this peptide, while the AC8-C2b peptide was too small to be detected. In the reactions containing the AC1-C1b



peptide, high-molecular weight aggregates were visible, indicating an oligomerization of the AC1-C1b peptide, which is in agreement with the ITC measurements (3.3.1.4.) and explains that no band was observed for the monomeric peptide. This might also be the reason for the absence of cross-linked products between CaM and the peptide (Figure A16).

For the reactions containing one or both of the AC8 peptides, the bands representing the CaM/AC8 peptide complexes were excised, washed, and *in-gel* digested (2.4.5.). The resulting peptide mixtures were analyzed by nano-HPLC/nano-ESI-LTQ-Orbitrap-MS/MS (2.5.5.).

Several cross-linked products were identified for the reactions between CaM and the AC8-Nt (Table A8) and AC8-C2b (Table A9). Two examples are presented in Figure 47Figure A17. In the cross-linked products, Lys-21, Lys-77, Lys-94, and Lys-148 residues of CaM were found to be connected with different amino acids in the AC8-Nt peptide. In particular, the benzophenone group of SBC reacted mainly with isoleucine and arginine residues, whereas glutamate and valine were found to have reacted with sulfo-SDA.

For the AC8-C2b peptide, similar cross-linked products were identified, which also showed differences in the reactivities of SBC and sulfo-SDA (Table A9). Most of the cross-links were found in the reaction mixtures containing 1.4 mM  $\text{Ca}^{2+}$ , while only a few cross-links were identified in the absence of  $\text{Ca}^{2+}$ . This confirms recent results of GST-pulldown experiments, which revealed an AC8 interaction with CaM only (for AC8-Nt peptide) or mainly (for AC8-C2b peptide) in the presence of  $\text{Ca}^{2+}$  (222).

In the reactions containing both AC8 peptides, mainly cross-links between CaM and the AC8-Nt peptide were detected (Table A10), as had been expected from MALDI-TOF-MS data (Figure A16). The cross-links identified in these reactions are similar to those found in the reactions containing only one AC8 peptide, indicating that the interaction interfaces within CaM/AC8 peptide complexes are comparable in both reactions. Moreover, these findings confirm the results of the *offline* nano-ESI-MS experiments (Figure 45), which showed a higher CaM affinity for the AC8-Nt peptide.

The distance constraints obtained in the cross-linking reactions of the AC8 peptides were used for molecular modeling studies (2.5.8.).

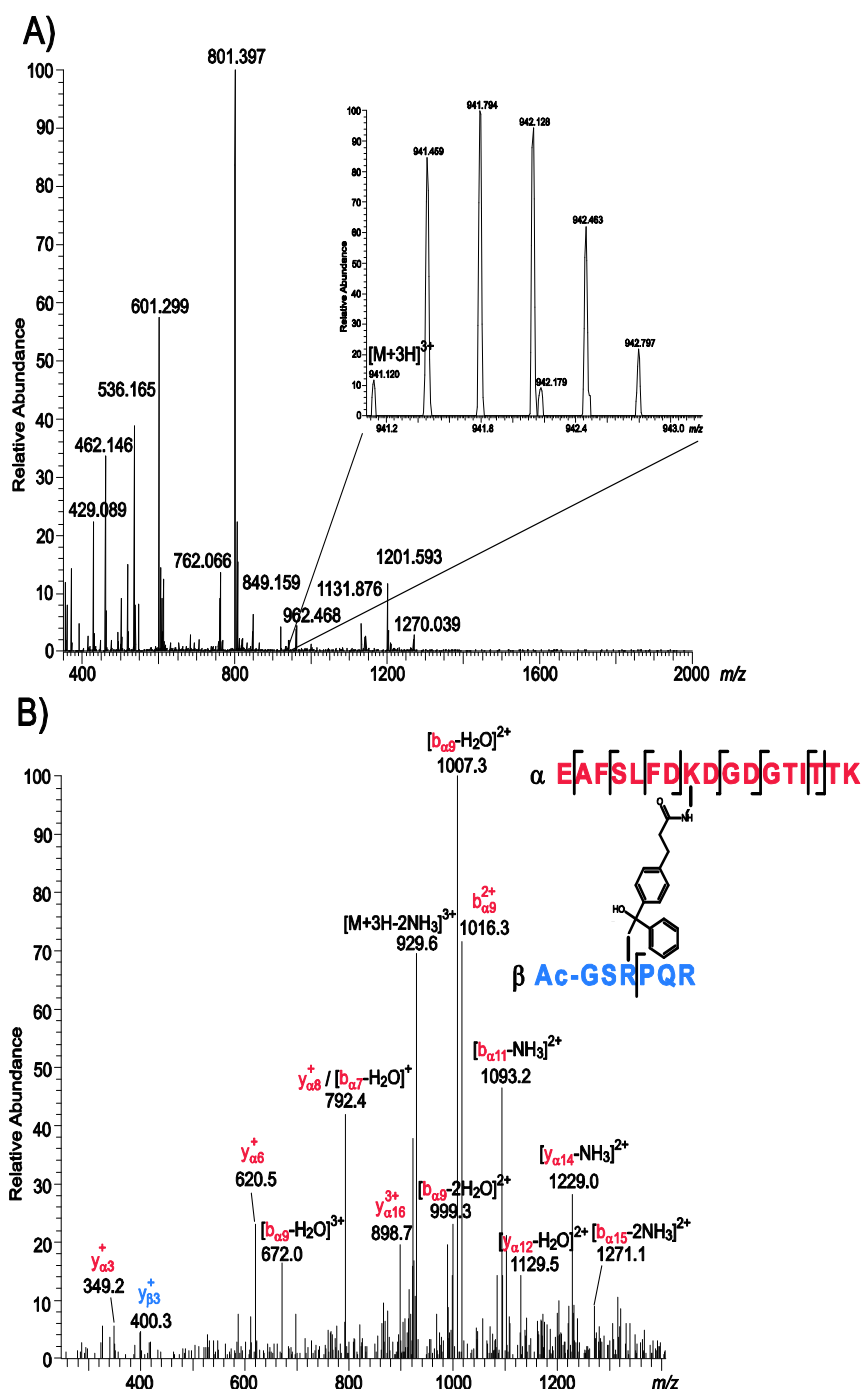


**Figure 47.** MS and MS/MS analysis of a cross-linking reaction between CaM and the AC8-Nt peptide. The cross-linking reaction was conducted with a 50-fold molar excess of SBC for 30 min at 1.4 mM  $Ca^{2+}$ ; the mixture was irradiated with UV-A light ( $8000 \text{ mJ/cm}^2$ ). A) The  $3+$  signal of the cross-linked product at  $m/z$  941.120 is annotated in the highlighted part of the spectrum recorded at a retention time of 67.9 min. B) Fragment ion mass spectrum (CID-MS/MS) of the adduct between Lys-21 of CaM ( $\alpha$ -sequence 14-30, red) and Arg-3 of the *N*-terminally acetylated (Ac-) AC8-Nt peptide ( $\beta$ -sequence 1-6, blue).

The structures of AC8 peptides were modeled and confirmed the CD experiments that had indicated  $\alpha$ -helical structures for both AC8 peptides were formed (3.3.1.1.). Different CaM structures were used for the docking models (pdb entries 2kdu, 2bbm, as well as a fusion construct of the *N*-terminal CaM domain of 1cfd and the *C*-terminal CaM domain of 1prw;

pdb entries defined in Table A1) that represent different conformations CaM can adopt in different CaM/peptide complexes at different  $\text{Ca}^{2+}$  concentrations. The assembled  $\text{Ca}$ - $\text{Ca}$  distances of cross-linked amino acids were set to  $\leq 25 \text{ \AA}$  (SBC) and  $\leq 20 \text{ \AA}$  (sulfo-SDA). The final model was selected based on an optimal agreement with all experimentally obtained distance constraints (Figure 48).

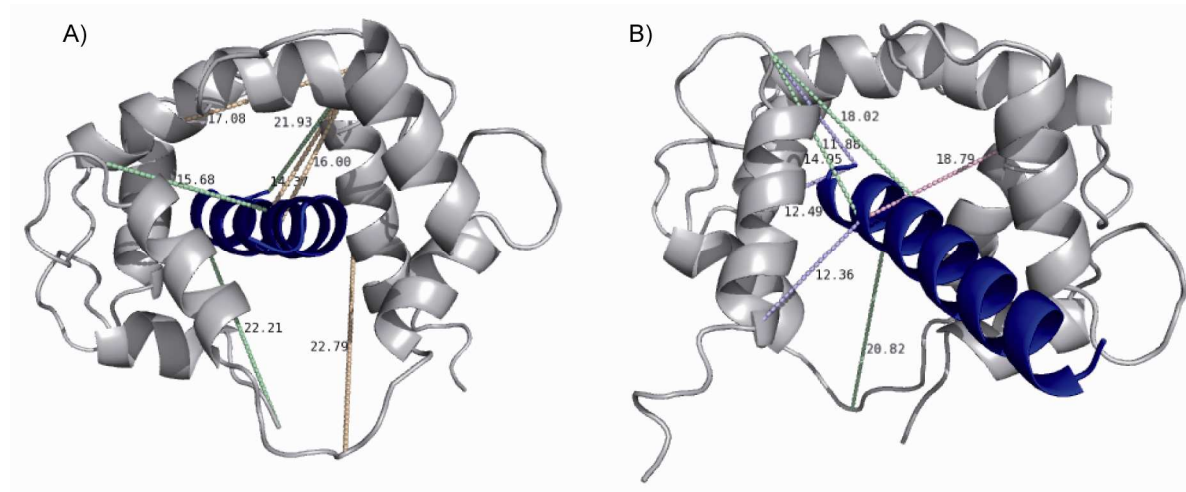


**Figure 48. Model structures of the CaM/AC8 peptide complexes.** The complex between CaM and A) AC8-Nt or B) AC8-C2b is similar to the structure of the CaM/skMLCK M13 peptide complex (pdb 2bbm, (98)). CaM is shown in grey, the AC8 peptides are shown in blue.  $\text{Ca}$ - $\text{Ca}$  distances (in  $\text{\AA}$ ) between the connected amino acids are illustrated as dotted lines.

It could be demonstrated for both AC8 peptides that the CaM/peptide complex structure showing the best conformance with all identified cross-links, is based on the structure of the CaM/skMLCK M13 peptide complex (pdb 2bbm). Although the CaM-binding motifs of the two AC8 peptides are different, the overall structure of the complex with CaM is clearly similar for both AC8 peptides. The two CaM/AC8 peptide complexes differed only in the orientation of the anchor amino acids of the AC8 peptides: The first three hydrophobic residues of the 1-5-8-14 motif of AC8-Nt are oriented towards the methionines of the C-terminal CaM lobe (Met-109, 124, 144, and 145) and the phenylalanine in position 14 binds to the N-terminal CaM domain. On the other hand, the AC8-C2b peptide interacts via its IQ-like motif mainly with the N-terminal CaM lobe (Met-36, 51, 71, and 72) (Figure 49). These results confirm recent findings (107, 222), showing that the N-terminal CaM domain has to be  $\text{Ca}^{2+}$ -loaded to allow for AC8-C2b peptide binding, while for AC8-Nt binding the C-terminal CaM lobe has to be  $\text{Ca}^{2+}$ -loaded.

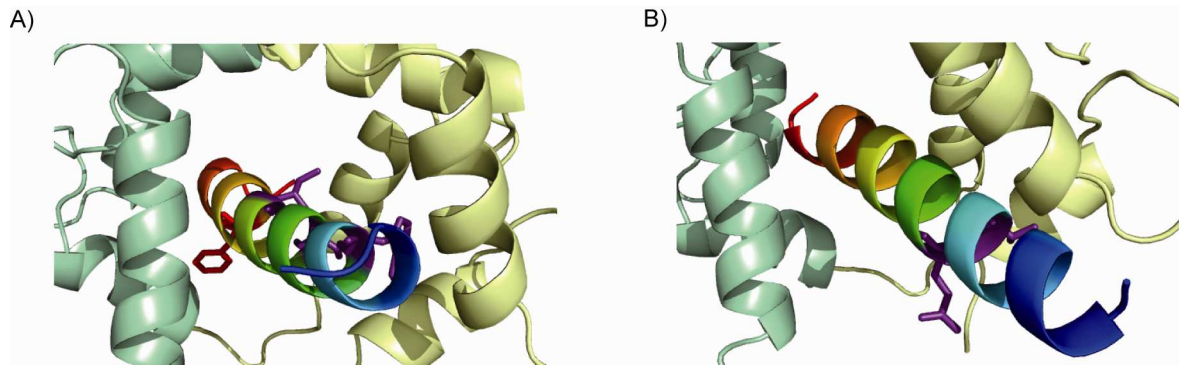


**Figure 49. Detailed presentation of the binding of AC8 peptides to CaM.** The complex between CaM and A) AC8-Nt or B) AC8-C2b is similar to the structure of the CaM/skMLCK M13 peptide complex (pdb 2bbm, (98)). The *N*-terminal domain of CaM is shown in green, the *C*-terminal CaM lobe in yellow, and the AC8 peptides are shown in rainbow colors. The hydrophobic anchor amino acids of the AC8 peptides are shown as purple sticks.

In conclusion, ITC, *offline* ESI-MS, and cross-linking experiments indicate that the CaM affinity of the three AC peptides, comprising the CaM-binding regions of AC1 and AC8, is higher in the presence than in the absence of  $\text{Ca}^{2+}$  ions. The order of relative CaM affinities is the following: AC1-C1b > AC8-Nt > AC8-C2b (222). Furthermore, the structures of the CaM/AC8 peptide complexes of AC8-Nt and AC8-C2b were found to be comparable to the CaM/skMLCK M13 peptide complex with an antiparallel binding mode of the peptide. The binding affinity of AC8-Nt is in the nanomolar range, as evidenced by ITC measurements. Additionally, the mechanism of AC8 regulation by CaM apparently does not include a 1:2 complex, in which both AC8 CaM-binding motifs bind simultaneously to CaM. Therefore, it was shown that AC8-Nt does not directly transfer the CaM molecule to AC8-C2b, but raises the local CaM concentration in the vicinity of AC8-C2b. This might be necessary to allow a fast activation of AC8 by ensuring that AC8-C2b does not have to compete with other CaM target proteins because of a high CaM concentration in its environment (222).

### 3.3.2. Interaction of AC8 with Orai1 and STIM1

AC8 is not only regulated by the  $\text{Ca}^{2+}/\text{CaM}$  system, but also by an increase in  $\text{Ca}^{2+}$  levels originating from store-operated  $\text{Ca}^{2+}$  entry (SOCE) (113-114), which are both sensed by proteins located in the plasma membrane or the membrane of the ER, namely Orai1 and STIM1. Due to the fact that AC8 is sensitive towards SOCE, the interaction of Orai1 and STIM1 with AC8 was investigated to gain insights into the mechanism of AC8 regulation by  $\text{Ca}^{2+}$  ions originating from SOCE. In recent experiments, Orai1, identified as the major pore-subunit of SOC channels (115-117), was found to interact with the *N*-terminal region of AC8. A second protein that was shown to affect the activity of AC8 in human embryonic kidney (HEK) 293 cells is STIM1 (114, 124). FRET experiments with STIM1 and different truncated variants of Orai1 and AC8 were conducted to shed light onto the interaction of these three proteins and the effects of Orai1 and STIM1 on AC8 regulation.

#### 3.3.2.1. Fluorescence (Förster) Resonance Energy Transfer Experiments

The interaction of Orai1 and STIM1 had been studied using fluorescence (Förster) resonance energy transfer (FRET) and was found to occur upon  $\text{Ca}^{2+}$  store depletion by thapsigargin (Tg) (125, 223). Tg is a non-competitive inhibitor of a class of  $\text{Ca}^{2+}$ -ATPases in the ER and the sarcoplasmic reticulum, which are responsible for pumping  $\text{Ca}^{2+}$  into the  $\text{Ca}^{2+}$  stores. By addition of Tg, these enzymes are blocked and  $\text{Ca}^{2+}$  stores are depleted, leading to clustering of STIM1 at ER-plasma membrane junctions and to an interaction between STIM1 and Orai1. Investigation of the known interaction between Orai1-CFP and STIM1-YFP by FRET was used as positive control.

First, CFP bleed-through into the YFP channel and YFP cross-excitation of CFP were calculated to correct the FRET images (data not shown). The correction factors obtained for CFP (59%) and YFP (11.2%) bleed-through were in agreement with the values calculated in previous experiments (63% and 5.7% (224)). Likewise, FRET analysis of the interaction between Orai1-CFP and STIM1-YFP revealed normalized, corrected FRET (NFRET<sub>C</sub>) values indicating that the proteins mainly interact upon  $\text{Ca}^{2+}$  store depletion, which is consistent with previous experiments (125) (Figure A19).

The interaction between AC8 and Orai1 had recently been identified to occur in a  $\text{Ca}^{2+}$ -independent manner via the *N*-terminal regions of both proteins, as evidenced by peptide array, GST-pulldown, FRET, and knockdown experiments (125). To further narrow down the

interaction site between AC8 and Orai1, different *N*-terminal truncation variants were analyzed by FRET together with the full-length proteins. Since deletion of more than the 73 *N*-terminal residues from Orai1 causes a disruption of the channelling function (223), only 20, 40, or 60 amino acids were deleted in the truncated variants. First, STIM1 interaction with these truncated Orai1 proteins was analyzed by FRET. Not surprisingly, as Orai1/STIM1 interaction had been found to occur in the *C*-terminal part of Orai1 (223), the experiments showed FRET signals comparable to those observed with the full-length Orai1 protein (data not shown). For the Orai1 $\Delta$ 40 variant, the expression in HEK293 cells recorded in the absence of Tg was too low to obtain NFRET<sub>C</sub> values. Therefore, this experiment will have to be repeated. FRET measurements of the Orai1/AC8 interaction showed no significant differences in the FRET signals between AC8 interactions with full-length Orai1 or *N*-terminally truncated Orai1 variants (Figure 50).

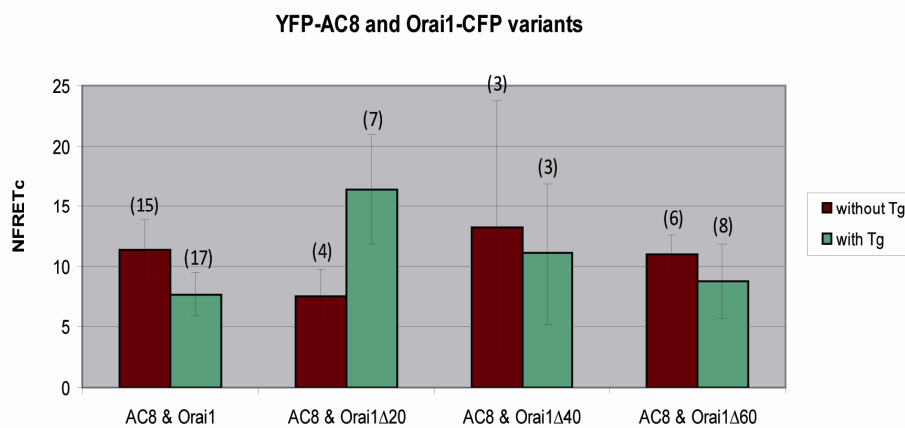


**Figure 50. FRET analysis of the interaction between YFP-AC8 and Orai1-CFP truncation variants.** The experiments were conducted under two different conditions: with (green) and without (red)  $\text{Ca}^{2+}$  store depletion by thapsigargin (Tg). The numbers in brackets represent the numbers of single cells, which were averaged.

Due to a high variation between the single cells in the experiment, the errors are large. Therefore, the experiment was repeated as follows: For a better visualization of  $\text{Ca}^{2+}$  store depletion upon Tg addition, HA-tagged STIM1 was overexpressed in HEK293 cells in addition to AC8 and the Orai1 variants, to facilitate formation of detectable ER-plasma membrane junctions, called puncta. Analysis of the FRET signal in these cells revealed different results compared to the experiment without STIM1, showing decreased FRET signals upon Tg addition (Figure A20). These preliminary findings indicate an effect of STIM1 on Orai1/AC8 interaction, which might be caused by a direct interaction of STIM1 with the *N*-terminus of AC8 (where the Orai1 interaction site is also located) or a structural change of the AC8 interaction site within Orai1 upon STIM1 binding.

Recent peptide array analysis of the interaction site between AC8 and Orai1 had identified an arginine-rich sequence stretch (GSRRS) of Orai1 to be crucial for Orai1/AC8 interaction. This sequence comprises amino acid 26 - 30 of Orai1 and its deletion should cause a decreased FRET signal in interaction studies. Results obtained in this work (Figure 50 and Figure A20) show no significant differences between Orai1 $\Delta$ 40, Orai1 $\Delta$ 60, and the full-length protein in respect to AC8 interaction, which might indicate the presence of a second AC8 binding site in the Orai1 protein that is located outside the cytosolic amino acid sequences investigated in the peptide array. For further analysis of the interaction between Orai1 and AC8 via their *N*-termini, the AC8 truncation variant AC8M1, lacking the first 106 amino acids, was investigated by FRET. These measurements showed NFRET<sub>C</sub> values that were not reduced compared to those of the experiments with the full-length proteins (data not shown). Although this FRET analysis was only performed once and has to be repeated in order to draw reliable conclusions, the results give a first hint that there has to be an interaction of AC8 and Orai1 beyond the one identified in their *N*-terminal regions. To test the hypothesis of a second AC8 binding site in the transmembrane regions or the extracellular loop of Orai1, the two other Orai isoforms (Orai2 and 3) were investigated. The Orai isoforms are homologous in their sequences, except for their *N*-terminal regions. Therefore, an AC8 interaction site beyond the *N*-terminus should be similar in all three Orai isoforms, leading to comparable NFRET<sub>C</sub> values. Constructs of Orai2 and Orai3 were cloned for overexpression of CFP-tagged proteins and FRET experiments were conducted with Orai2-CFP and STIM1-YFP or YFP-AC8 to investigate their interactions (Figure 51).

In the case of the Orai2/STIM1 interaction, a higher FRET signal was obtained before store depletion compared to Orai1/STIM1, which was due to CFP signals in the ER, indicating that Orai2 is expressed in identical amounts in the ER and the plasma membrane. Analysis of the interaction between AC8 and Orai2 showed no differences in detected FRET signals compared to AC8/Orai1 FRET experiments (Figure 51). These preliminary results indicate that there is a second AC8 binding site in the Orai1 protein beyond the *N*-terminal region, which is also present in Orai2.

In FRET measurements with the Orai3-CFP construct, Orai3 overexpression was only observed in the ER, which is not consistent with previous studies where heteromultimers of Orai isoforms were observed in the plasma membrane. Since the experiments in this work were only conducted once, the results have to be confirmed by repeating the FRET measurements.

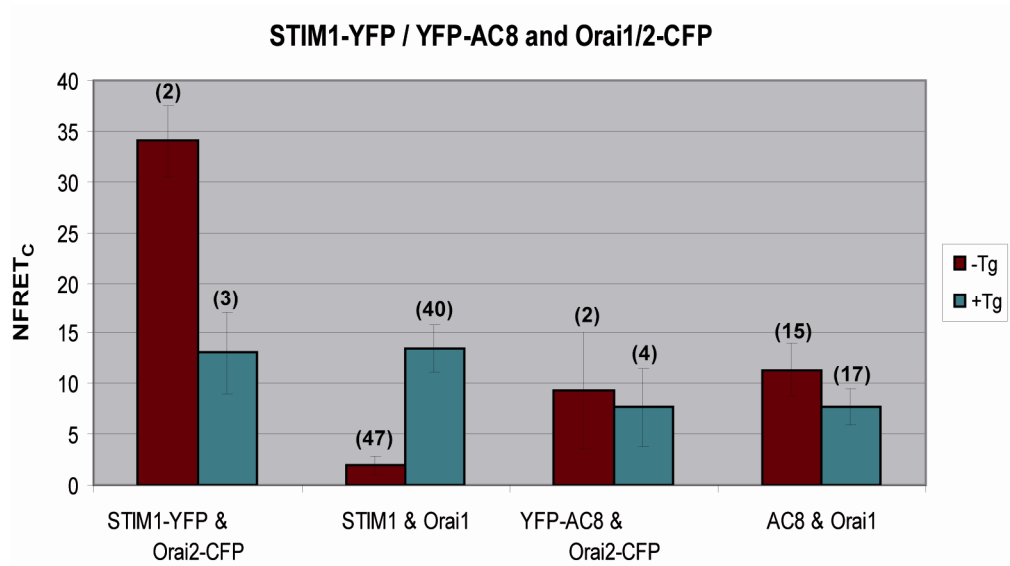


**Figure 51. FRET analysis of the interaction between STIM1-YFP / YFP-AC8 and CFP-tagged Orai isoforms.** Calculated NFRET<sub>C</sub> values for experiments conducted with (green) or without (red) addition of thapsigargin (Tg) are shown. The numbers in brackets represent the numbers of single cells, which were averaged.

In summary, the interaction of AC8 with Orai1 was shown not to be restricted to the *N*-terminal regions, as had been suggested by peptide array and GST-pull down experiments, but there exists evidence that a second AC8 binding site is present in the transmembrane or extracellular domains of Orai1.



## 4. DISCUSSION AND OUTLOOK

In order to extend our current knowledge on how the  $\text{Ca}^{2+}$  signal is converted into different cellular responses, three different CaM/target complexes (CaM/Munc13, skMLCK, AC1 and AC8) were investigated. AC8 is not only regulated by  $\text{Ca}^{2+}$ /CaM, but also by increasing  $\text{Ca}^{2+}$  concentrations originating from store operated  $\text{Ca}^{2+}$  entry (SOCE), which are sensed by STIM1 and Orai1. Therefore, the interactions between these proteins and AC8 were additionally investigated to gain further insights into AC8 regulation by SOCE.

### 4.1. CaM/Munc13 Interaction

Previous cross-linking and PAL studies on the CaM interaction with peptides comprising the CaM-binding regions of the two homologous Munc13 isoforms, Munc13-1 and ubMunc13-2, had revealed the formation of a CaM/peptide complex at  $\text{Ca}^{2+}$  concentrations in the low nanomolar range (30 nM) (79, 84). The structures of the CaM complexes created with these two Munc13 peptides were similar to the complex between CaM and a peptide derived from the NO synthase, showing an antiparallel orientation of the peptide. In those studies, a 1-5-8 CaM-binding motif had been identified in the Munc13 peptides (84).

In this work, cross-linking studies with peptides comprising the CaM-binding sites of all four Munc13 isoforms (Munc13-1, ubMunc13-2, bMunc13-2, and Munc13-3) were performed to investigate and compare the structures of the different CaM/Munc13 peptide complexes. Cross-linking experiments between CaM and all four Munc13 peptides, conducted at three different  $\text{Ca}^{2+}$  concentrations (10, 30, and 100 nM), showed that 30 nM  $\text{Ca}^{2+}$  is optimal for complex formation (Figure 24), which had also been found for Munc13-1 and ubMunc13-2 (84). Further experiments revealed cross-linked products between CaM and the Munc13 peptides (Table A2) and within the CaM molecule (Table A3), which allowed molecular modeling of the four CaM/Munc13 peptide complexes (Figure 28). The resulting structures of CaM/Munc13 peptide complexes demonstrate that peptides of all four Munc13 isoforms exhibit similar CaM-binding modes, which are characterized by an antiparallel orientation of the Munc13 peptide within the CaM/peptide complexes. As had previously been shown for Munc13-1 and ubMunc13-2 (84), the model structures of the CaM/Munc13 peptide complexes are comparable to that of the complex between CaM and an NO synthase peptide (85). These results confirm that the different synaptic plasticity phenomena observed for different Munc13 isoforms (65) do not result from variations in the structures of the

respective CaM/Munc13 complexes (85) and that the optimal  $\text{Ca}^{2+}$  concentration for CaM complex formation is similar for all Munc13 isoforms. Regulation of the function of Munc13 proteins, if not realized on the structural level, is apparently based on variations of the CaM affinities between different Munc13 isoforms. This hypothesis should be confirmed by performing ITC and SPR measurements. Moreover, it would be interesting to compare the short (21 to 24-amino acid) Munc13 peptides with their C-terminally elongated (34-amino acid) counterparts regarding their CaM affinities. As such, the influence of the additional hydrophobic anchor residue at position 26 of the novel 1-5-8-26 CaM-binding motif in Munc13-1 and ubMunc13-2, which had recently been identified (54), would be revealed. In addition to studying the CaM affinities of the four Munc13 isoforms, their affinities for other interacting proteins of the synaptic release machinery (e.g. Munc18 or syntaxin-1) could differ between the Munc13 isoforms, leading to variations in synaptic regulation. Furthermore, the composition of the synaptic release machinery might differ between synapses expressing different Munc13 isoforms. According to Ma *et al.* (73), the composition of these release complexes could be investigated by a combination of NMR and fluorescence spectroscopy, but also by cross-linking/MS.

In the NMR structures of the CaM/(34-aa) peptide complexes of Munc13-1 and ubMunc13-2, CaM adopts a more extended conformation compared to the complexes with shorter Munc13 peptides (54, 85). The question arises whether the novel 1-5-8-26 CaM-binding motif of Munc13-1 and ubMunc13-2 and the extended CaM conformation in the CaM/peptide complexes are also observed for bMunc13-2 and Munc13-3.

To address this question and to elucidate whether additional CaM interaction sites might be identified in the Munc13 isoforms, GST-tagged domains of the N-terminal Munc13 regions (Figure 29) were overexpressed in *E.coli* and purified. Various cultivation conditions were tested and the purification procedure was optimized. The greatest challenge arose from the occurrence of shorter Munc13 variants, which had to be separated from full-length Munc13 domains (Figure 30). Separation of these truncated variants resulted in high protein losses. Additionally, different attempts to reduce the speed of translation in *E.coli* cells to allow expression of full-length proteins did not reduce the amount of truncated Munc13 variants. The reason might be that in *E.coli* tRNAs encoding specific amino acids (especially Arg, Lys, and Pro) of the mammalian constructs are present at low concentrations, leading to an impaired translation process. Using DNA for the Munc13 constructs, in which the codons are optimized for usage in *E.coli* as well as on-column cleavage of the GST tag by thrombin to

avoid buffer exchange steps, yielded protein fractions containing high amounts of untagged Munc13 domains. Nevertheless, impurities, mainly originating from truncated Munc13 variants, were observed (Figure 33). These findings indicate that not only an impaired translation of Munc13 domains is responsible for the presence of truncated Munc13 variants, but also that proteolytic digestion during overexpression and purification of the proteins is an issue that has to be considered.

On the one hand, separation of truncated GST-Munc13 domains from full-length GST proteins resulted in protein losses. Otherwise, molecular masses and isoelectric points of full-length and truncated untagged Munc13 domains differ only slightly, making their separation difficult. For these reasons, cross-linking experiments were performed without further purification of the fractions containing the highest amounts of untagged Munc13 domains. Analysis of cross-linking reaction mixtures containing the bMunc13-2 domain revealed one cross-linked product that confirms the previously determined CaM-binding site (Figure 35). Although these results are still preliminary and clearly a higher number of cross-links (especially intramolecular ones within the Munc13 domain) is needed to draw reliable conclusions, identification of the known CaM-binding site of full-length bMunc13-2 underlines the strength of the cross-linking approach.

In addition to the occurrence of truncated Munc13 variants during overexpression and purification of Munc13 domains, the stability of the tag-free proteins was a major issue. Munc13 proteins are membrane associated proteins and, therefore, comprise hydrophobic regions. Addition of detergents such as Triton X-100 [0.1% (v/v)] and DDM [0.1 - 1% (v/v)], revealed reasonably stable untagged Munc13 domains, but high detergent concentrations above the critical micelle concentration (CMC) might have hindered the removal of truncated Munc13 variants. Therefore, a purification protocol would be favored, where no Triton X-100 is added after cell disruption. Instead of using detergents, a pH shift could be envisioned to lower the electrostatic interactions of the Munc13 proteins (peripheral membrane proteins) with membrane-spanning proteins after cell disruption and the head groups of the plasma membrane (225). Alternatively, low concentrations of glycerol or polyethylenglycol might be used to stabilize the untagged Munc13 proteins.

Using site-directed mutagenesis, different bMunc13-2 and Munc13-3 variants were constructed containing an amber stop codon that encodes the photo-reactive amino acid Bpa (Table 7). These variants do not yet comprise the optimal codon usage for overexpression in

*E.coli*, which could lead to problems during expression and purification. Hence, overexpression and purification of the Bpa-variants was not conducted. Nevertheless, overexpression and purification of Bpa-variants containing *E.coli*-optimized codons, will allow a more detailed investigation of the interaction between CaM and bMunc13-2 and Munc13-3 to be conducted.

Furthermore, a peptide array could be envisioned to supplement the cross-linking experiments with Munc13 domains and to identify potential additional CaM interaction sites. Although only linear binding motifs can be identified with this method, it should allow identification of CaM-binding regions in the Munc13 domains because CaM-binding motifs are usually linear (25).

In conclusion, the knowledge gained concerning the CaM/Munc13 interaction of the homologous isoforms, Munc13-1 and ubMunc13-2, was extended and novel insights into the CaM interaction were achieved for the non-homologous isoforms, bMunc13-2 and Munc13-3. Although different synaptic phenomena are observed for the four Munc13 isoforms, their interaction modes with CaM are similar, at least on the structural level.

### **4.2. CaM/skMLCK Interaction**

Previous studies had shown that *C*-terminally elongated Munc13 peptides exhibit a novel 1-5-8-26 CaM-binding motif, which is not found in shorter Munc13 peptides. The structures of the resulting CaM/Munc13 peptide complexes differ in the conformation that CaM can adopt in the complex. While CaM exhibits a compact structure in complex with short Munc13 peptides, the conformation of CaM is more extended in the complex with *C*-terminally elongated Munc13 peptides (pbd 2kdu, (54)). Usually, short peptides are used in CaM/target interaction studies, which comprise the minimal CaM-binding region alone. This raised the question whether *C*-terminal elongation of a classical CaM target peptide, skMLCK, combined with amino acid exchanges to resemble the 1-5-8-26 motif of Munc13 results in an altered CaM complex structure, in which CaM exhibits a conformation comparable to that of the CaM/Munc13 peptide complex.

CD experiments, cross-linking studies, and SPR measurements with peptide variants comprising the CaM-binding region of the classical CaM target skMLCK (termed M13) were performed to address this question. These skMLCK peptides were *C*-terminally elongated

compared to M13 (98). Furthermore, amino acid exchanges in the skMLCK peptides were performed at positions 14 and 26 of the CaM-binding motif to resemble the 1-5-8-26 motif of Munc13. CD secondary structure analysis of four peptide variants, skMLCK, skMLCK F19A, skMLCK F19E, and skMLCK F19/L31W, revealed a high propensity to form  $\alpha$ -helical structures for all peptides, except for skMLCK F19E/L31W. In contrast, analysis of cross-linking reaction mixtures between the skMLCK peptide variants and CaM showed that the structures of CaM/peptide complexes of all four skMLCK peptides are similar and comparable to the CaM/M13 peptide complex (Figure 39, Figure A9, Figure A10, Figure A11). The distance constraints obtained in the cross-linking experiments clearly demonstrate that an extended CaM conformation comparable to that of the CaM/Munc13 peptide complex (54) does not exist for any of the four CaM/skMLCK peptide complexes. Even in the skMLCK F19E/L31W peptide, which contains hydrophobic anchor residues at positions 1, 5, 8, and 26, cross-linked amino acids between the peptide and the *N*-terminal CaM lobe do not agree with the NMR structure of the CaM/Munc13 peptide complex (pdb 2kdu) (Figure 39). Therefore, it is concluded that the 1-5-8-26 CaM-binding motif of Munc13 cannot be introduced in skMLCK by *C*-terminal elongation of the CaM-binding motif and amino acid exchanges. Additionally, these findings demonstrate that the hydrophobic anchor residues and the basic cluster are not the only determinants for the CaM-binding mode of a target peptide.

Although chemical cross-linking revealed that the structures of the CaM/skMLCK peptide complexes are similar between the four skMLCK peptide variants, SPR measurements revealed differences in the CaM affinities of the variants. *C*-terminal elongation of the skMLCK peptide did not result in a changed CaM affinity compared to M13, while exchange of the hydrophobic anchor residue in position 14 of the CaM-binding motif to alanine (skMLCK F19A) resulted in a reduced CaM affinity (Figure 40). For both peptides, skMLCK and skMLCK F19A, a high- and a low-affinity (linear) binding phase was observed, indicating that a second skMLCK peptide might bind to hydrophobic patches on the CaM surface beyond the methionine-rich peptide binding pocket, as was described previously (79, 84). In the case of the skMLCK F19E peptide variant, in which the phenylalanine at position 14 was exchanged to glutamate, which is present in Munc13, the high-affinity binding phase was no longer detectable in the concentration range (up to 10  $\mu$ M) investigated. A drastically reduced CaM-binding affinity was observed for the skMLCK F19E (Figure 40) compared to M13 and the Munc13 peptide. Moreover, the additional introduction of a bulky hydrophobic tryptophan at position 26 of the CaM-binding motif did not restore high-affinity binding,

indicating that the 1-5-8-26 motif of Munc13 cannot be introduced into the skMLCK peptide. These results underline the importance of the hydrophobic anchor residue at position 14 of the skMLCK CaM-binding motif, which had previously been confirmed by peptide array analysis (100). Apparently, the CaM-binding mode of a target peptide is not exclusively determined by its hydrophobic anchor amino acids or by the basic cluster, but also by the amino acids in between. In a recent study, the distance between the major hydrophobic anchor residues of the CaM-binding motif was found to be decisive for the conformation CaM adopts in the CaM/target complex. The larger this distance, the more open the CaM conformation. In this work, it was shown that the identity and distance of the hydrophobic anchor amino acids does not exclusively determine the CaM conformation within the CaM/target complex. For further investigation, Munc13 peptides with amino acid exchanges at positions 14 and 26 of the CaM-binding motif (e.g. Glu14→Phe and Trp26→Ala) could be synthesized and tested in cross-linking experiments to evaluate whether the CaM conformation in the CaM/Munc13 peptide complexes with these peptide variants is extended or closed.

### 4.3. CaM/AC1 and AC8 Interaction

AC1 and AC8 are both stimulated by CaM, but the mechanism of regulation by the Ca<sup>2+</sup> sensor is different for both proteins (107). While AC1 possesses only one CaM-binding region, AC8 exhibits a 1-5-8-14 motif in the *N*-terminus (AC8-Nt) and an IQ-like CaM-binding motif in the C2b domain (AC8-C2b) (Figure 41). CD measurements of peptides comprising the CaM-binding regions of AC1 and AC8 showed that the propensity to form an  $\alpha$ -helical structure is highest for AC8-Nt, whereas for AC1 and AC8-C2b this propensity is lower, as evidenced by the TFE concentrations that were needed to reach maximal  $\alpha$ -helical content. In *offline* nano-ESI-MS experiments with the AC1 and AC8 peptides, CaM affinities were ranked as follows: AC1-C1b > AC8-Nt > AC8-C2b (222). The different CaM affinities of the two AC8 peptides were confirmed by ITC measurements, which revealed a  $K_D$  value for the CaM/AC8-Nt interaction in the nanomolar range. For AC8-C2b, a significantly lower CaM-binding affinity was observed. These differences in CaM-binding affinities might be caused by different CaM-binding modes of both AC8 peptides. Cross-linking experiments and molecular docking studies showed that the structures of both CaM/AC8peptide complexes are comparable to the structure of the CaM/skMLCK M13 peptide complex, with an antiparallel orientation of the target peptide within the complex. Although these complexes are similar with respect to their overall structures, there are subtle differences in the interactions between

the hydrophobic anchor residues of the AC8 peptides and the CaM lobes. While the amino acids at positions 1, 5, and 8 of AC8-Nt interact with the methionine residues of the C-terminal CaM domain, Phe-13 and Ile-14 are oriented towards the N-terminal methionines. In contrast, the AC8-C2b peptide mainly interacts with the N-terminal CaM lobe via Val and Gln residues of the IQ-like motif. These differences in the orientation of the named hydrophobic residues in the AC8 peptides confirm recent findings where a Ca<sup>2+</sup>-loaded N-terminal CaM domain was shown to be a requirement for AC8-C2b peptide binding, while the C-terminal CaM lobe has to be Ca<sup>2+</sup>-loaded for AC8-Nt peptide binding (107, 222). Moreover, the cross-linking and ITC results showed that the CaM affinity of a CaM target peptide depends on the orientation of the hydrophobic anchor residues of the target peptide within the CaM/peptide complex.

Nevertheless, the current model of AC8 regulation by CaM that describes AC8-Nt as a CaM trap was confirmed and extended. AC8-Nt seems to increase the local CaM concentration in the environment of AC8-C2b by binding to CaM with high affinity, even at low Ca<sup>2+</sup> concentrations. Upon raising the Ca<sup>2+</sup> concentration, the N-terminal CaM lobe is loaded with Ca<sup>2+</sup> and binds to AC8-C2b, thereby activating cAMP production of AC8. This activation is fast because AC8-C2b does not have to compete with other CaM targets due to a high CaM concentration in its environment.

In the case of the AC1 peptide, the thermodynamic parameters of CaM binding and the structure of the CaM/AC1 peptide complex could not be determined due to oligomerization of the peptide. In ITC measurements, CaM binding of oligomers with up to 10 AC1 peptides was detected (Figure A18) and SDS-PAGE analysis of the cross-linking reaction mixtures revealed high-molecular weight oligomers (Figure 46). These findings stand in contrast with the *offline* nano-ESI-MS experiments, which showed oligomerization of the AC1 peptide only when the peptide was added in a 10:1 (w/w) excess to CaM. Nevertheless, a tendency to oligomerize was observed in all experiments conducted. The reason why no 1:1 CaM/AC1 peptide complex was detected in the cross-linking reactions might be due to the higher oligomerization tendency of the AC1 peptide after addition of the cross-linker. Furthermore, in the ITC experiments 100 mM KCl was added to enhance complex formation, which might result in a higher oligomerization tendency of the AC1 peptide. For AC8-Nt, addition of 100 mM KCl was necessary to increase the ionic strength and, thus, to enhance complex formation, which was rarely observed without addition of salt. As ITC experiments of CaM and the AC1 peptide in the absence of KCl would not have been comparable to the AC8

measurements, they were not performed. One possibility to circumvent oligomerization would be to conduct SPR experiments, in which the AC1 peptide is immobilized and CaM affinities are determined with a buffer containing 100 mM KCl. It could be envisioned to study the structure of the CaM/AC1 peptide complex by NMR experiments, in which no cross-linking reagent is needed and conditions comparable to those of the *offline* nano-ESI-MS experiments could be used.

#### 4.4. AC8/Orai1 and STIM1 Interaction

In addition to the regulation of AC8 by Ca<sup>2+</sup>/CaM, there is also regulation by increasing Ca<sup>2+</sup> concentrations resulting from SOCE (113-114). The proteins STIM1 and Orai1, which are involved in SOCE, had previously been found to functionally colocalize with AC8 (114, 124). The localization of AC8 at regions of the plasma membrane, which contain Orai1, a protein that forms junctions between the ER and the plasma membrane with STIM1, brings AC8 into vicinity of the location of Ca<sup>2+</sup> ion entry during Ca<sup>2+</sup> store refilling. This allows a fast activation of AC8 upon store-operated Ca<sup>2+</sup> influx. On the basis of previous experiments that had shown an interaction between the *N*-termini of AC8 and Orai1, FRET measurements were performed with truncated variants of AC8 and Orai1 (125).

The experiments with full-length YFP-AC8 and CFP-tagged, *N*-terminally truncated Orai1 variants revealed no significant changes in the FRET signals for the variants compared to full-length Orai1 (Figure 50). Also, no differences in NFRET<sub>C</sub> values were detected before and after Tg-induced store depletion. In contrast, upon additional overexpression of HA-tagged STIM1 together with YFP-AC8 and the CFP-Orai1 variants, NFRET<sub>C</sub> values were lower after store depletion with Tg, compared to those without Tg (Figure A20). These data indicate an influence of STIM1 on the AC8/Orai1 interaction, either through a direct interaction of STIM1 with the *N*-terminus of AC8 (where the AC8/Orai1 interaction mainly takes place) or via an induction of a conformational change of the AC8 binding site in Orai1, which needs to be further investigated.

CFP-tagged constructs of two additional Orai isoforms, Orai2 and Orai3, were used in FRET experiments with YFP-AC8 to investigate whether there is an additional interaction site between AC8 and Orai1 beyond the *N*-terminus of both proteins. Different NFRET<sub>C</sub> values of the interaction with AC8 would be expected for the three Orai isoforms if the interaction between AC8 and Orai1 were restricted to their *N*-terminal regions. The reason for this is that



the *N*-terminal sequence of Orai1 is missing in the otherwise homologous proteins Orai2 and Orai3. However, no significant differences were observed between the interactions of Orai1 and Orai2 with AC8, indicating that a second AC8 interaction site is located beyond the *N*-terminus of Orai1 (Figure 51). This was confirmed by an interaction that was observed between *N*-terminally truncated AC8 (AC8M1) and Orai2.

Clearly, FRET experiments will have to be repeated to confirm the preliminary results obtained in this work. In future studies, the interaction between AC8, Orai1, and STIM1 could be investigated by peptide array analysis or electron microscopy. The expression and/or purification of at least one of these proteins will be challenging because they are integral membrane proteins. *In-vivo* cross-linking studies using unnatural amino acids, like Bpa, at various positions in the proteins will give further insights into the interaction sites between AC8, Orai1, and STIM1, and will, therefore, allow conclusions to be drawn about the regulation of AC8 by SOCE.

## APPENDIX

### Tables

Table A1. CaM and CaM/target peptide complexes used in molecular modeling studies.

pdb entry	structure
1cdl	Ca <sup>2+</sup> -CaM bound to a peptide analog of the CaM-binding region of chicken smooth muscle myosin light chain kinase (smMLCK)
1cfd	Ca <sup>2+</sup> - free CaM (Xenopus laevis)
1ckk	Ca <sup>2+</sup> -CaM in complex with Ca <sup>2+</sup> -CaM-dependent kinase kinase
1prw	closed compact structure of native Ca <sup>2+</sup> -CaM (bovine)
1qs7	Ca <sup>2+</sup> -CaM/rs20 peptide complex
1qtx	Ca <sup>2+</sup> -CaM/rs20 peptide complex
1wrz	Ca <sup>2+</sup> -CaM complexed with a peptide from a human death-associated protein kinase
2bbm	Ca <sup>2+</sup> -CaM /skMLCK M13 peptide complex
2f3y	Ca <sup>2+</sup> -CaM bound to the hydrophobic IQ domain of the cardiac Ca(v)1.2 calcium channel
2l53	apo-CaM in complex with the IQ motif of Human Cardiac Sodium Channel NaV1.5
2kdu	Ca <sup>2+</sup> -CaM /Munc13-1 peptide complex
2o06	Ca <sup>2+</sup> -CaM bound to a peptide from neuronal nitric oxide synthase

Table A2. Intermolecular cross-links between CaM and Munc13 peptides.

[M+H] <sup>+</sup> <sub>exp.</sub>	[M+H] <sup>+</sup> <sub>theor.</sub>	CaM	Munc13-1	ubMunc13-2	bMunc13-2	Munc13-3
1375.730	1375.775	K75 75KMK <sup>77</sup>	A10/F11 10AFNKVR <sup>15</sup>			
2163.062 (1 Met oxid.)	2163.069 (1 Met oxid.)	K30 22DGDGTTTKELGTVMR <sup>37</sup>	A3 3AK <sup>4</sup>			
2454.225	2454.219	K21 14EAFSLFDKDGDTITTK <sup>30</sup>	A2 1RAK <sup>3</sup>			
1059.540	1059.591	K75 75KMK <sup>77</sup>		A10 10AVTK <sup>13</sup>		
1357.732	1357.687	K75 75KMK <sup>77</sup>		A5/F8 5AHWFR <sup>9</sup>		
2753.404	2753.403	K21 14EAFSLFDKDGDTITTK <sup>30</sup>		A10/K13 10AVTKVR <sup>15</sup>		
2781.419	2781.409	K21 14EAFSLFDKDGDTITTK <sup>30</sup>			K12 11EKRLR <sup>15</sup>	
2785.332	2785.329	K94 91VFDKDGNGYISAAELR <sup>106</sup>			I2 1CINNFK <sup>6</sup>	
2691.393	2691.388	K94 91VFDKDGNGYISAAELR <sup>106</sup>			K12 11EKRLR <sup>15</sup>	
2748.410	2748.399	K94 91VFDKDGNGYISAAELR <sup>106</sup>			L9 7NVLREK <sup>12</sup>	
2709.235 (1 Met oxid.)	2709.227 (1 Met oxid.)	K75/77 75KMKDSEEEIR <sup>86</sup>				M15/A16 14QMAELEEK <sup>21</sup>
2967.430	2967.408	K94 91VFDKDGNGYISAAELR <sup>106</sup>				M15/A16/L18 14QMAELEEK <sup>21</sup>
2911.463	2911.462	K94 91VFDKDGNGYISAAELR <sup>106</sup>				A6/A7/L8 5EAALRAYK <sup>12</sup>
3039.563	3039.557	K94 91VFDKDGNGYISAAELR <sup>106</sup>				A6/A7 5EAALRAYKK <sup>13</sup>
3057.433	3057.429	K21 14EAFSLFDKDGDTITTK <sup>30</sup>				M15/A16/L18 14QMAELEEK <sup>21</sup>
3068.393	3068.386	K77 76MKDSEEEIREAFR <sup>90</sup>				M15/A16 14QMAELEEK <sup>21</sup>
3071.415	3071.422	K77 76MKDSEEEIR <sup>86</sup>				A10 10AYKKQMAELEEK <sup>21</sup>
3095.507	3095.503	K94 91VFDKDGNGYISAAELR <sup>106</sup>				K13/M15/A16/L18 13QMAELEEK <sup>21</sup>
3129.584	3129.578	K21 14EAFSLFDKDGDTITTK <sup>30</sup>				A6/A7/L8 5EAALRAYKK <sup>13</sup>
3185.526	3185.523	K21 14EAFSLFDKDGDTITTK <sup>30</sup>				K13/M15/A16 13QMAELEEK <sup>21</sup>
3457.705	3457.698	K94 91VFDKDGNGYISAAELR <sup>106</sup>				A10/K12/K13/M15 10AYKKQMAELEEK <sup>21</sup>
4014.002 (1 Met oxid.)	4013.955 (1 Met oxid.)	K94 91VFDKDGNGYISAAELR <sup>106</sup>				A6/A7/L8 5EAALRAYKKQMAELEEK <sup>21</sup>
4674.323	4674.314	K21 1ADQLTEEQIAEFKEAFSLFDK <sup>30</sup>				A6/A7/L8 5EAALRAYKK <sup>13</sup>
2062.970	2062.972	I85 78DTDSEEEIR <sup>86</sup>	K12 9AFNKVR <sup>14</sup>			
2748.384	2748.377	I27 22DGDGTTTTK <sup>30</sup>	K12 9AFNKVR <sup>14</sup>			

Table A3. Intramolecular cross-links within CaM.

$[M+H]^+$ <sub>exp.</sub>	$[M+H]^+$ <sub>theor.</sub>	CaM	CaM2
4407.114	4407.116	K94 <sup>91</sup> VFDKDGNGYISAAELR <sup>106</sup>	M109/L112 <sup>107</sup> HVMTNLGEKLTDEEVDEMIR <sup>126</sup>
2795.392	2795.371	K94 <sup>91</sup> VFDKDGNGYISAAELR <sup>106</sup>	L32/M36 <sup>31</sup> ELGTVMR <sup>37</sup>
2981.392	2981.383	K75/77 <sup>75</sup> KMKDTSDEEEIR <sup>86</sup>	I100 <sup>95</sup> DGNGYISAAELR <sup>106</sup>
4391.152	4391.121	K94 <sup>91</sup> VFDKDGNGYISAAELR <sup>106</sup>	M109 <sup>107</sup> HVMTNLGEKLTDEEVDEMIR <sup>126</sup>
4481.18	4481.141 (4497.136)	K21 <sup>14</sup> EAFSLFDKDGDTITTK <sup>30</sup>	M109 <sup>107</sup> HVMTNLGEKLTDEEVDEMIR <sup>126</sup>



**Table A5. Cross-linking sites identified between CaM and the skMLCK F19A peptide.**

<i>m/z</i> measured	[M+H] <sup>+</sup> theor.	Charge state	Mass deviation (ppm)	[Ca <sup>2+</sup> ]	CaM	CaM	skMLCK F19A	Fragments	Sample
549.787	2196.13	4+	-1.0	1mM	K94 <sup>91</sup> VFDKDGNGYISAAELR <sup>106</sup>		K20 <sup>19</sup> AKK <sup>21</sup>	Y <sub>62</sub> -Y <sub>63</sub> -Y <sub>64</sub> OR b <sub>58</sub> -Y <sub>67</sub> OR b <sub>111</sub> -Y <sub>66</sub> -Y <sub>67</sub> -Y <sub>61</sub> -b <sub>66</sub> -b <sub>67</sub> -b <sub>69</sub> -b <sub>108</sub> -b <sub>112</sub> -b <sub>113</sub> -b <sub>114</sub>	BS <sup>2</sup> G
575.033	2297.108	4+	0.5	1mM	K77 <sup>76</sup> MKDTDSEEEIREAFR <sup>90</sup>		K20 <sup>19</sup> AKK <sup>21</sup>	Y <sub>61</sub> -Y <sub>63</sub> -Y <sub>610</sub> -Y <sub>611</sub> -Y <sub>612</sub> -Y <sub>613</sub> -Y <sub>614</sub> -b <sub>62</sub> -b <sub>65</sub> -b <sub>62</sub> -NH <sub>2</sub> -b <sub>611</sub> -NH <sub>2</sub> -b <sub>62</sub>	BS <sup>2</sup> G
588.544	2351.156 (1 Met oxid.)	4+	-2.8	30nM / 1mM	K75 <sup>79</sup> KMK <sup>77</sup>		K30 <sup>22</sup> DGGDTITTKELGTVMR <sup>37</sup>	Y <sub>68</sub> -Y <sub>69</sub> -Y <sub>613</sub> -Y <sub>614</sub> -Y <sub>67</sub> -H <sub>2</sub> O, Y <sub>612</sub> -H <sub>2</sub> O, b <sub>63</sub>	SBC4, SBC8
603.793	2412.15	4+	-0.4	1mM	K77 <sup>76</sup> MKDTDSEEEIREAFR <sup>90</sup>		K7 <sup>6</sup> WK <sup>7</sup>	Y <sub>63</sub> -Y <sub>66</sub> -Y <sub>617</sub> -Y <sub>618</sub> -Y <sub>611</sub> -Y <sub>612</sub> -Y <sub>613</sub> -Y <sub>615</sub> -b <sub>63</sub> -H <sub>2</sub> O, b <sub>610</sub>	BS <sup>2</sup> G
699.598	2795.371	4+	0.6	1mM	K94 <sup>91</sup> VFDKDGNGYISAAELR <sup>106</sup>	M36 <sup>31</sup> ELGTVMR <sup>37</sup>		Y <sub>62</sub> -Y <sub>63</sub> -Y <sub>64</sub> -Y <sub>65</sub> -Y <sub>67</sub> -Y <sub>69</sub> -Y <sub>67</sub> -Y <sub>69</sub> -Y <sub>65</sub> -H <sub>2</sub> O, b <sub>66</sub> -2H <sub>2</sub> O, b <sub>66</sub> -2NH <sub>2</sub> , b <sub>610</sub> -H <sub>2</sub> O, b <sub>611</sub> -H <sub>2</sub> O, H <sub>2</sub> O, b <sub>612</sub> -3H <sub>2</sub> O	SBC4, SBC8
1032.181	3095.539	3+	-2.2	30nM	K94 <sup>91</sup> VFDKDGNGYISAAELR <sup>106</sup>		M30 <sup>22</sup> ISSGALMALGV <sup>33</sup>	Y <sub>63</sub> -Y <sub>64</sub> -Y <sub>65</sub> -Y <sub>66</sub> -Y <sub>67</sub> -Y <sub>69</sub> -b <sub>63</sub> -b <sub>64</sub> OR Y <sub>69</sub> OR b <sub>69</sub> -b <sub>67</sub> -2H <sub>2</sub> O, b <sub>612</sub> -H <sub>2</sub> O, b <sub>613</sub> -H <sub>2</sub> O, b <sub>615</sub> -H <sub>2</sub> O OR b <sub>618</sub> -H <sub>2</sub> O, b <sub>618</sub> -H <sub>2</sub> O	SBC4, SBC8
1044.817	3132.432	3+	0.9	1mM	K148 <sup>128</sup> EADIDGQGVNYEEFVQMMTA K <sup>148</sup>		K3 <sup>1</sup> LMKR <sup>4</sup>	Y <sub>69</sub> -Y <sub>619</sub> -Y <sub>612</sub> -Y <sub>613</sub> -Y <sub>614</sub> -Y <sub>615</sub> -Y <sub>616</sub> -Y <sub>617</sub> -Y <sub>618</sub> -Y <sub>620</sub> -b <sub>64</sub> -H <sub>2</sub> O, b <sub>69</sub> -b <sub>610</sub> -H <sub>2</sub> O	BS <sup>2</sup> G
640.132	3196.633	5+	-1.6	30nM	K94 <sup>81</sup> EAFRVFDKDGNGYISAAELR <sup>106</sup>		L1 <sup>1</sup> LMKRR <sup>5</sup>	Y <sub>611</sub> -Y <sub>620</sub> OR Y <sub>64</sub> -H <sub>2</sub> O, Y <sub>613</sub> -2H <sub>2</sub> O, Y <sub>614</sub> -2H <sub>2</sub> O, b <sub>625</sub> , b <sub>67</sub> , b <sub>610</sub> -2H <sub>2</sub> O, b <sub>611</sub> -2H <sub>2</sub> O	SBC8
1074.209	3223.634	3+	0.5	30nM	K94 <sup>91</sup> VFDKDGNGYISAAELR <sup>106</sup>		M30 <sup>21</sup> KISSGALMALGV <sup>33</sup>	Y <sub>63</sub> -Y <sub>64</sub> -Y <sub>65</sub> -Y <sub>66</sub> -Y <sub>67</sub> -Y <sub>69</sub> -Y <sub>611</sub> -Y <sub>613</sub> -H <sub>2</sub> O, Y <sub>615</sub> -2H <sub>2</sub> O OR b <sub>615</sub> -H <sub>2</sub> O, b <sub>66</sub> -H <sub>2</sub> O, b <sub>67</sub> -H <sub>2</sub> O, b <sub>611</sub> -H <sub>2</sub> O, b <sub>614</sub> -NH <sub>2</sub> OR b <sub>610</sub> , NH <sub>2</sub> , b <sub>615</sub> -NH <sub>2</sub> OR b <sub>611</sub> -NH <sub>2</sub>	SBC4, SBC8
878.63	4390.112 (1 Met oxid.)	5+	-1.0	30nM	K77 <sup>76</sup> MKDTDSEEEIREAFRVFDKDGNGYISAAELR <sup>106</sup>		L1 <sup>1</sup> LMKR <sup>4</sup>	Y <sub>62</sub> -Y <sub>63</sub> -Y <sub>65</sub> -Y <sub>66</sub> -Y <sub>67</sub> -Y <sub>69</sub> -Y <sub>623</sub> -H <sub>2</sub> O, b <sub>69</sub> -b <sub>616</sub> -b <sub>619</sub> -NH <sub>2</sub> , b <sub>620</sub> -b <sub>622</sub> -b <sub>626</sub> -b <sub>630</sub> -H <sub>2</sub> O OR b <sub>613</sub> -H <sub>2</sub> O	SBC4
901.465	4504.276	5+	2.4	30nM	K77 <sup>76</sup> MKDTDSEEEIREAFRVFDK <sup>84</sup>		A16 <sup>6</sup> WKNFIAVSAANRAK <sup>21</sup>	Y <sub>67</sub> -Y <sub>67</sub> -Y <sub>614</sub> -H <sub>2</sub> O, b <sub>67</sub> -2H <sub>2</sub> O, b <sub>69</sub> -H <sub>2</sub> O, b <sub>610</sub> -2H <sub>2</sub> O, b <sub>614</sub> , b <sub>615</sub> OR b <sub>618</sub>	SBC4
1169.584	4675.305	4+	1.5	1mM	K21 <sup>1</sup> ADQLTEEQIAEFKAEAFSLFDKDGNGTITTK <sup>30</sup>		K8 <sup>6</sup> KNFIAVSAANR <sup>18</sup>	Y <sub>69</sub> -Y <sub>613</sub> -2H <sub>2</sub> O, Y <sub>616</sub> -Y <sub>617</sub> -Y <sub>621</sub> -Y <sub>622</sub> -Y <sub>623</sub> -Y <sub>624</sub> -Y <sub>625</sub> -Y <sub>627</sub> -Y <sub>628</sub> -NH <sub>2</sub> , Y <sub>64</sub> , b <sub>64</sub> , b <sub>65</sub> , b <sub>610</sub> , b <sub>611</sub>	BS <sup>2</sup> G
975.254	4872.240 (3 Met oxid.)	5+	0.9	30nM / 1mM	K75 <sup>38</sup> SLGQNPTEAELQDMINEVDADGNGTIDFPEFLTMMARK <sup>75</sup>		L1 <sup>1</sup> LMK <sup>3</sup>	Y <sub>67</sub> -Y <sub>69</sub> -Y <sub>612</sub> -H <sub>2</sub> O, Y <sub>613</sub> -Y <sub>618</sub> -H <sub>2</sub> O, Y <sub>621</sub> -2H <sub>2</sub> O, Y <sub>622</sub> -3H <sub>2</sub> O, Y <sub>639</sub> -Y <sub>633</sub> -3H <sub>2</sub> O, b <sub>61</sub> OR b <sub>61</sub> , b <sub>69</sub> -b <sub>611</sub> , b <sub>615</sub> -H <sub>2</sub> O, b <sub>627</sub> -NH <sub>2</sub> OR b <sub>62</sub> -2H <sub>2</sub> O	SBC4, SBC8
896.587	5374.493 (2 Met oxid.)	6+	-1.6	1mM	T70 <sup>37</sup> ELGTVMRSLGQNPTEAELQDMINEVDADGNGTIDFPEFLTMMAR <sup>74</sup>		K3 <sup>1</sup> LMK <sup>3</sup>	Y <sub>65</sub> -NH <sub>2</sub> , Y <sub>621</sub> -Y <sub>623</sub> -H <sub>2</sub> O, Y <sub>627</sub> -H <sub>2</sub> O, Y <sub>633</sub> -Y <sub>61</sub> -H <sub>2</sub> O, b <sub>68</sub> , b <sub>610</sub> , b <sub>612</sub> -H <sub>2</sub> O, b <sub>613</sub> , b <sub>622</sub> , b <sub>623</sub> , b <sub>634</sub> , b <sub>639</sub> , b <sub>67</sub> , b <sub>629</sub>	BS <sup>2</sup> G

4: irradiation energy of 4000 mJ/cm<sup>2</sup>; 8: irradiation energy of 8000 mJ/cm<sup>2</sup>



**Table A7. Cross-linking sites identified between CaM and the skMLCK F19E/L31W peptide.**

<i>m/z</i> measured	[M+H] <sup>+</sup> <sub>theor.</sub>	Charge state	Mass deviation (ppm)	[Ca <sup>2+</sup> ]	CaM	skMLCK F19E/L31W	Fragments	Sample
527.507	2107.009	4+	-1.3	1mM	K77 <sup>75</sup> KMKDSDSEEEIR <sup>86</sup>	L1, M2 <sup>1</sup> LMK <sup>3</sup>	Y <sub>61</sub> -Y <sub>62</sub> , Y <sub>63</sub> , Y <sub>64</sub> , Y <sub>65</sub> , Y <sub>66</sub> , b <sub>65</sub> -H <sub>2</sub> O or Y <sub>62</sub> , b <sub>67</sub> , b <sub>68</sub> -H <sub>2</sub> O, b <sub>69</sub> -NH <sub>3</sub> , b <sub>70</sub>	SBC4
596.051	2381.185	4+	0.7	1mM	K94 <sup>91</sup> VFDKDGNGYISAAELR <sup>106</sup>	L1, M2 <sup>1</sup> LMK <sup>3</sup>	Y <sub>61</sub> , Y <sub>62</sub> or Y <sub>611</sub> , Y <sub>63</sub> or Y <sub>612</sub> -H <sub>2</sub> O, Y <sub>64</sub> or b <sub>613</sub> -NH <sub>3</sub> , Y <sub>65</sub> or b <sub>62</sub> , Y <sub>66</sub> , Y <sub>67</sub> , b <sub>68</sub> , b <sub>69</sub> , b <sub>70</sub> , b <sub>71</sub> -NH <sub>3</sub> , b <sub>72</sub> -2NH <sub>3</sub> , b <sub>73</sub> , b <sub>74</sub> -H <sub>2</sub> O	SBC4, SBC8
603.552	2411.188	4+	0.5	1mM	K21 <sup>14</sup> EAFSLFDKDGDTITTK <sup>30</sup>	<sup>4</sup> RR <sup>5</sup>	Y <sub>62</sub> , Y <sub>63</sub> , Y <sub>64</sub> or b <sub>612</sub> , Y <sub>65</sub> -H <sub>2</sub> O, Y <sub>66</sub> , Y <sub>69</sub> , Y <sub>70</sub> , Y <sub>71</sub> , Y <sub>72</sub> , Y <sub>73</sub> -H <sub>2</sub> O or b <sub>714</sub> , NH <sub>3</sub> , b <sub>65</sub> -H <sub>2</sub> O, b <sub>67</sub> -H <sub>2</sub> O, b <sub>68</sub> -H <sub>2</sub> O, b <sub>69</sub> -NH <sub>3</sub>	SBC8
608.551	2431.185 (1 Met oxid.)	4+	-0.9	1mM	K13 <sup>1</sup> ADQLTEEQIAEFK <sup>13</sup>	K3 <sup>1</sup> LMKR <sup>4</sup>	Y <sub>64</sub> , Y <sub>67</sub> -NH <sub>3</sub> or b <sub>63</sub> , Y <sub>69</sub> , Y <sub>612</sub> -NH <sub>3</sub> , b <sub>65</sub> , b <sub>68</sub> -NH <sub>3</sub> , b <sub>67</sub> -2H <sub>2</sub> O, b <sub>610</sub>	BS <sup>2</sup> G
618.557	2471.205	4+	0.3	30nM, 1mM	K21 <sup>14</sup> EAFSLFDKDGDTITTK <sup>30</sup>	L1, M2 <sup>1</sup> LMK <sup>3</sup>	Y <sub>62</sub> , Y <sub>64</sub> , Y <sub>66</sub> , Y <sub>69</sub> , Y <sub>611</sub> -H <sub>2</sub> O, Y <sub>612</sub> -H <sub>2</sub> O, Y <sub>614</sub> -H <sub>2</sub> O, Y <sub>615</sub> -H <sub>2</sub> O, b <sub>65</sub> -H <sub>2</sub> O, b <sub>66</sub> -H <sub>2</sub> O or b <sub>62</sub> -H <sub>2</sub> O	SBC4, SBC8
621.296	2482.161	4+	-0.6	30nM	K77 <sup>76</sup> MKDTDSEEEIREAFR <sup>80</sup>	L1, M2 <sup>1</sup> LMK <sup>3</sup>	Y <sub>65</sub> , Y <sub>69</sub> or Y <sub>614</sub> , Y <sub>610</sub> , Y <sub>611</sub> , Y <sub>612</sub> , Y <sub>613</sub> , b <sub>63</sub> -NH <sub>3</sub> , b <sub>62</sub>	SBC8
635.577	2537.286	4+	-0.4	1mM	K94 <sup>91</sup> VFDKDGNGYISAAELR <sup>106</sup>	L1 <sup>1</sup> LMKR <sup>4</sup>	Y <sub>62</sub> or Y <sub>611</sub> , Y <sub>63</sub> , Y <sub>64</sub> , Y <sub>65</sub> or b <sub>62</sub> , Y <sub>66</sub> , Y <sub>67</sub> , b <sub>69</sub> -H <sub>2</sub> O, b <sub>610</sub> -H <sub>2</sub> O, b <sub>611</sub> -NH <sub>3</sub> , b <sub>612</sub> -NH <sub>3</sub> , b <sub>614</sub> -NH <sub>3</sub> , b <sub>61</sub>	SBC8
870.757	2610.258	3+	0	30nM / 1mM	K75 <sup>75</sup> KMKDSDSEEEIREAFR <sup>80</sup>	L1, M2 <sup>1</sup> LMK <sup>3</sup>	Y <sub>62</sub> , Y <sub>66</sub> , Y <sub>610</sub> , Y <sub>612</sub> , Y <sub>615</sub> or Y <sub>62</sub> -NH <sub>3</sub> , b <sub>62</sub>	SBC4
657.582	2627.306	4+	0.2	1mM	K21 <sup>14</sup> EAFSLFDKDGDTITTK <sup>30</sup>	L1, M2 <sup>1</sup> LMKR <sup>4</sup>	Y <sub>610</sub> -H <sub>2</sub> O, Y <sub>611</sub> , Y <sub>612</sub> -H <sub>2</sub> O, b <sub>63</sub> -H <sub>2</sub> O, b <sub>67</sub> -H <sub>2</sub> O, b <sub>613</sub> , b <sub>614</sub>	SBC4, SBC8
1.044.802	3132.389 (1Met oxid.)	3+	0.7	30nM / 1mM	K148 <sup>127</sup> EADIDGGQVNYEEFVQMMTA K <sup>148</sup>	L1, M2 <sup>1</sup> LMK <sup>3</sup>	Y <sub>61</sub> -H <sub>2</sub> O, Y <sub>63</sub> -H <sub>2</sub> O, Y <sub>66</sub> -NH <sub>3</sub> , Y <sub>611</sub> -H <sub>2</sub> O, Y <sub>612</sub> -H <sub>2</sub> O, Y <sub>613</sub> -H <sub>2</sub> O, Y <sub>614</sub> -H <sub>2</sub> O, Y <sub>615</sub> -NH <sub>3</sub> , Y <sub>616</sub> -NH <sub>3</sub> , Y <sub>617</sub> -NH <sub>3</sub> , Y <sub>618</sub> , Y <sub>619</sub> -NH <sub>3</sub> , Y <sub>620</sub> -NH <sub>3</sub> , Y <sub>621</sub> -NH <sub>3</sub> , b <sub>64</sub> -H <sub>2</sub> O, b <sub>65</sub> -H <sub>2</sub> O, b <sub>67</sub> -H <sub>2</sub> O, b <sub>69</sub> , b <sub>610</sub> -H <sub>2</sub> O	SBC4, SBC8
640.132	3196.633	5+	-1.6	30nM	K94 <sup>87</sup> EAFRVFDKDGNGYISAAELR <sup>106</sup>	L1, M2 <sup>1</sup> LMKRR <sup>5</sup>	Y <sub>63</sub> , Y <sub>66</sub> , Y <sub>611</sub> -H <sub>2</sub> O, Y <sub>612</sub> , Y <sub>613</sub> -2H <sub>2</sub> O, Y <sub>614</sub> -2H <sub>2</sub> O, Y <sub>615</sub> -3H <sub>2</sub> O, b <sub>65</sub> , b <sub>68</sub> , b <sub>615</sub> , b <sub>618</sub>	SBC4
828.168	3309.654	4+	-1.2	30nM	K94 <sup>91</sup> VFDKDGNGYISAAELR <sup>106</sup>	A12, V13 <sup>9</sup> NFIAVSAANREK <sup>20</sup>	Y <sub>62</sub> -H <sub>2</sub> O, Y <sub>64</sub> , Y <sub>65</sub> , Y <sub>66</sub> , Y <sub>67</sub> or b <sub>610</sub> , Y <sub>69</sub> or Y <sub>69</sub> , Y <sub>611</sub> , b <sub>65</sub> -H <sub>2</sub> O, b <sub>67</sub> -H <sub>2</sub> O, b <sub>610</sub> -H <sub>2</sub> O, Y <sub>610</sub> , b <sub>63</sub> , b <sub>64</sub> , b <sub>65</sub> , b <sub>69</sub>	SBC4
850.674	3399.672	4+	-0.6	1mM	K21 <sup>14</sup> EAFSLFDKDGDTITTK <sup>30</sup>	A16 <sup>9</sup> NFIAVSAANREK <sup>20</sup>	Y <sub>63</sub> , Y <sub>64</sub> , Y <sub>66</sub> , Y <sub>68</sub> , Y <sub>69</sub> , Y <sub>611</sub> , Y <sub>612</sub> or b <sub>68</sub> , Y <sub>614</sub> , Y <sub>615</sub> , b <sub>64</sub> -2H <sub>2</sub> O, b <sub>65</sub> , b <sub>66</sub> -H <sub>2</sub> O, b <sub>69</sub> , b <sub>613</sub> , Y <sub>69</sub> , Y <sub>610</sub> , b <sub>63</sub> , b <sub>64</sub> , NH <sub>3</sub>	SBC4, SBC8
945.675	3779.676	4+	0.2	1mM	K148 <sup>128</sup> EADIDGGQVNYEEFVQMMTA K <sup>148</sup>	S23, S24 <sup>22</sup> ISSGALMAWGV <sup>33</sup>	Y <sub>62</sub> -3H <sub>2</sub> O, Y <sub>66</sub> -H <sub>2</sub> O, Y <sub>67</sub> -H <sub>2</sub> O, Y <sub>613</sub> , Y <sub>614</sub> , Y <sub>619</sub> , b <sub>610</sub> -NH <sub>3</sub> , b <sub>615</sub> -3H <sub>2</sub> O, b <sub>620</sub> , Y <sub>68</sub> -H <sub>2</sub> O, Y <sub>69</sub> , b <sub>67</sub> , b <sub>610</sub> -2NH <sub>3</sub>	BS <sup>2</sup> G
975.254	4872.240 (3 Met oxid.)	5+	0.9	30nM / 1mM	K75 <sup>38</sup> SLGQNPTAEALDDMINEVDADG NGTIDFPEFLTMMARK <sup>75</sup>	L1 <sup>1</sup> LMK <sup>3</sup>	Y <sub>69</sub> , Y <sub>612</sub> -H <sub>2</sub> O, Y <sub>613</sub> , Y <sub>614</sub> -H <sub>2</sub> O, Y <sub>618</sub> -H <sub>2</sub> O, Y <sub>620</sub> -2H <sub>2</sub> O, Y <sub>623</sub> -H <sub>2</sub> O, Y <sub>630</sub> , Y <sub>633</sub> -3H <sub>2</sub> O, Y <sub>635</sub> -NH <sub>3</sub> , b <sub>61</sub> or b <sub>61</sub> , b <sub>69</sub> , b <sub>611</sub> , b <sub>616</sub> -H <sub>2</sub> O, b <sub>619</sub> -H <sub>2</sub> O, b <sub>622</sub> , b <sub>623</sub> -H <sub>2</sub> O, b <sub>627</sub> -NH <sub>3</sub> or b <sub>62</sub> -2H <sub>2</sub> O	SBC4, SBC8

4: irradiation energy of 4000 mJ/cm<sup>2</sup>; 8: irradiation energy of 8000 mJ/cm<sup>2</sup>

**Table A8. Cross-linking sites identified between CaM and the AC8-Nt peptide.**

<i>m/z</i> measured	[M+H] <sup>+</sup> <sub>theor.</sub>	Charge state	Mass deviation (ppm)	[Ca <sup>2+</sup> ]	CaM	CaM	AC8-Nt	Sample
689.682 (1 Met oxid.)	2067.031	3+	-0.7	1.4 mM	K77 <sup>75</sup> KMK <sup>77</sup>	E11 <sup>1</sup> ADQLTEEQIAEFK <sup>13</sup>		SDA 4, 8
694.095	2773.358	4+	0.5	1.4 mM	K94 <sup>91</sup> VFDKDGNGYISAAELR <sup>106</sup>		I16 <sup>15</sup> HITEQR <sup>20</sup>	SBC 4
903.784	2709.337	3+	0.4	1.4 mM	K21 <sup>14</sup> EAFSLFDKDGDTITTK <sup>30</sup>		I16/R20 <sup>15</sup> HITEQR <sup>20</sup>	SDA 4
941.460	2822.363	3+	0.3	1.4 mM	K21 <sup>14</sup> EAFSLFDKDGDTITTK <sup>30</sup>		R3 <sup>1</sup> GSRPQR <sup>6</sup>	SBC 4
955.132	2863.378	3+	1.0	1.4 mM	K21 <sup>14</sup> EAFSLFDKDGDTITTK <sup>30</sup>		I16 <sup>15</sup> HITEQR <sup>20</sup>	SBC 4
1156.522	3467.552 (3483.547; 3499.542)	3+	0	1.4 mM	K148 <sup>127</sup> EADIDGGQVNYEEFVQMMTA <sup>148</sup>		R6 <sup>1</sup> GSRPQR <sup>6</sup>	SBC 4
1086.529 (1 Met oxid.)	4343.095 (4359.089)	4+	-0.3	1.4 mM	K21 <sup>14</sup> EAFSLFDKDGDTITTK <sup>30</sup>	V108 <sup>107</sup> HVMTNLGEKLTDEEVDEMIR <sup>126</sup>		SDA 8

4: irradiation energy of 4000 mJ/cm<sup>2</sup>; 8: irradiation energy of 8000 mJ/cm<sup>2</sup>



**Table A9. Cross-linking sites identified between CaM and the AC8-C2b peptide.**

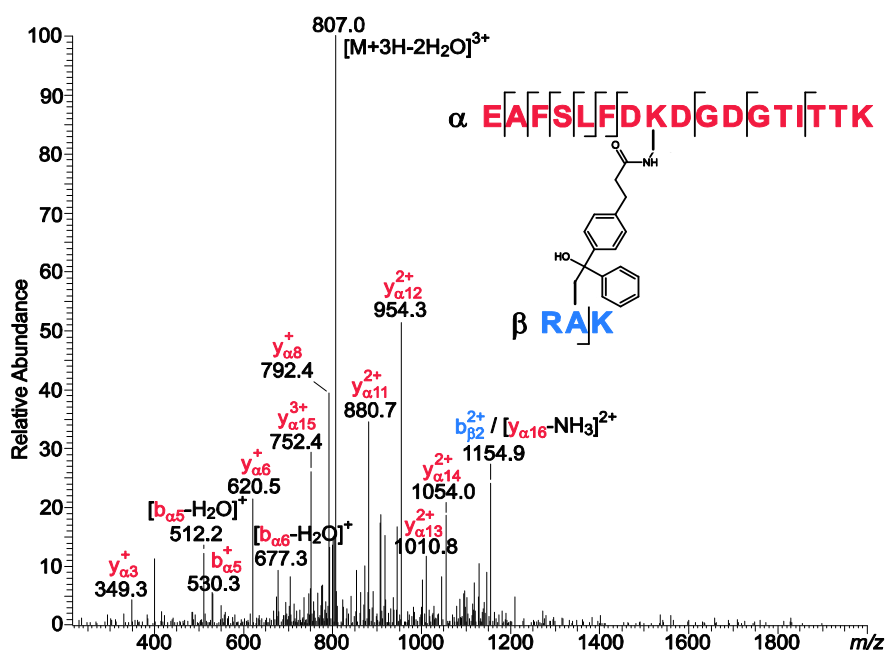
<i>m/z</i> measured	[M+H] <sup>+</sup> <sub>theor.</sub>	Charge state	Mass deviation (ppm)	[Ca <sup>2+</sup> ]	CaM	CaM	AC8-C2b	Sample
555.762	2220.025 (2236.020)	4+	0.5	1.4 mM	K77 76MKDTSDEEIR <sup>86</sup>		L22/L23 21QLLNEU <sup>27</sup>	SBC 0
660.580	2639.299	4+	-0.3	1.4 mM	K21 14EAFSLFDKDGDTITTK <sup>30</sup>		R18/K20 17QRQK <sup>20</sup>	SBC 8
684.350	2051.037 (2067.031)	3+	-0.1	1.4 mM	K77 75KMK <sup>77</sup>	I9/E11/F12 1ADQLTEEQIAEFK <sup>13</sup>		SDA 4, 8
782.126	3125.483 (3141.478)	4+	0	1.4 mM	K77 75KMKDTSDEEIR <sup>86</sup>	E11 1ADQLTEEQIAEFK <sup>13</sup>		SDA 4, 8
850.431	2549.278	3+	0.8	-	K94 91VFDKDGNGYISAAELR <sup>106</sup>		R18 17QRQK <sup>20</sup>	SBC 4
880.437	2639.299	3+	0.8	1.4 mM	K21 14EAFSLFDKDGDTITTK <sup>30</sup>		R18/K20 17QRQK <sup>20</sup>	SBC 8
907.939	3628.732 (3644.727)	4+	0.6	1.4 mM	K75/K77 75KMKDTSDEEIREAFR <sup>90</sup>	L4/K13 1ADQLTEEQIAEFK <sup>13</sup>		SDA 4, 8
932.462	2795.371	3+	0.3	1.4 mM	K94 91VFDKDGNGYISAAELR <sup>106</sup>	V35 31ELGTVMR <sup>37</sup>		SBC 8

4: irradiation energy of 4000 mJ/cm<sup>2</sup>; 8: irradiation energy of 8000 mJ/cm<sup>2</sup>

**Table A10. Cross-linking sites identified between CaM and both AC8 peptides.**

<i>m/z</i> measured	[M+H] <sup>+</sup> <sub>theor.</sub>	Charge state	Mass deviation (ppm)	[Ca <sup>2+</sup> ]	CaM	CaM	AC8-Nt	AC8-C2b	Sample
560.318	2238.254 (2254.249)	4+	-0.9	1.4 mM	K77 75KMK <sup>77</sup>		V13 7LLWQTAVRHTEQR <sup>20</sup>		SDA 4
655.584	2619.316	4+	-0.7	1.4 mM	K94 91VFDKDGNGYISAAELR <sup>106</sup>		I16R20 15HITEQR <sup>20</sup>		SDA 4
660.580	2639.299	4	0.8	1.4 mM	K21 14EAFSLFDKDGDTITTK <sup>30</sup>			R18/K20 17QRQK <sup>20</sup>	SBC 8
678.089	2709.337	4+	-0.3	1.4 mM / -	K21/K30 14EAFSLFDKDGDTITTK <sup>30</sup>		I16/E18/R20 15HITEQR <sup>20</sup>		SDA 4, 8
684.350	2051.037 (2067.031)	3+	0.1	1.4 mM / -	K77 75KMK <sup>77</sup>	E11/F12 1ADQLTEEQIAEFK <sup>13</sup>			SDA 4, 8
694.094	2773.358	4+	-1.0	1.4 mM	K94 91VFDKDGNGYISAAELR <sup>106</sup>		I16 15HITEQR <sup>20</sup>		SBC 4, 8
706.346	2822.363	4+	0.1	1.4 mM	K21 14EAFSLFDKDGDTITTK <sup>30</sup>		R3 1GSRPQR <sup>6</sup>		SBC 4, 8
716.601	2863.378	4+	0.8	1.4 mM	K21 14EAFSLFDKDGDTITTK <sup>30</sup>		I16 15HITEQR <sup>20</sup>		SBC 8
739.687	2217.045 (2233.040)	3+	0.4	-	K77 76MKDTSDEEIR <sup>86</sup>		I16R20 15HITEQR <sup>20</sup>		SDA 4, 8
782.125	3125.483	4+	-1.0	1.4 mM	K77 75KMKDTSDEEIR <sup>86</sup>	E11 1ADQLTEEQIAEFK <sup>13</sup>			SDA 4
787.716 (1 Met oxid.)	2361.135	3+	-0.3	1.4 mM	K77 75KMKDTSDEEIR <sup>86</sup>		R20 15HITEQR <sup>20</sup>		SDA 4
847.385 (2 Met oxid.)	3386.515	4+	0.4	1.4 mM	K148 127EADIDGGQVNYEEFVQMMTA K <sup>148</sup>		R20 15HITEQR <sup>20</sup>		SDA 4
1090.529 (2 Met oxid.)	4359.089	4+	0.8	-	K21 14EAFSLFDKDGDTITTK <sup>30</sup>	L112 107HVMTNLGKLTDEEVDE MIR <sup>126</sup>			SDA 4
1167.186 (2 Met oxid.)	3499.542	3+	0.7	1.4 mM	K148 127EADIDGGQVNYEEFVQMMTA K <sup>148</sup>		R3 1GSRPQR <sup>6</sup>		SBC 4

4: irradiation energy of 4000 mJ/cm<sup>2</sup>; 8: irradiation energy of 8000 mJ/cm<sup>2</sup>

**Figures**

**Figure A1.** Fragment ion mass spectrum of a cross-link between CaM and Munc13-1. MS/MS data were recorded at a retention time of 116.5 min, the triply charged precursor ( $m/z$  818.746) was selected that represents a cross-linked product between CaM and Munc13-1. The reaction contained a 50-fold excess of SBC and was irradiated with 8000  $\text{mJ}/\text{cm}^2$ . The cross-linked product is composed of amino acids 14-30 of CaM ( $\alpha$ -peptide, red) and 1-3 of Munc13-1 ( $\beta$ -peptide, blue), in which the cross-linker at Lys-21 of CaM had reacted with Ala-2 of Munc13-1.

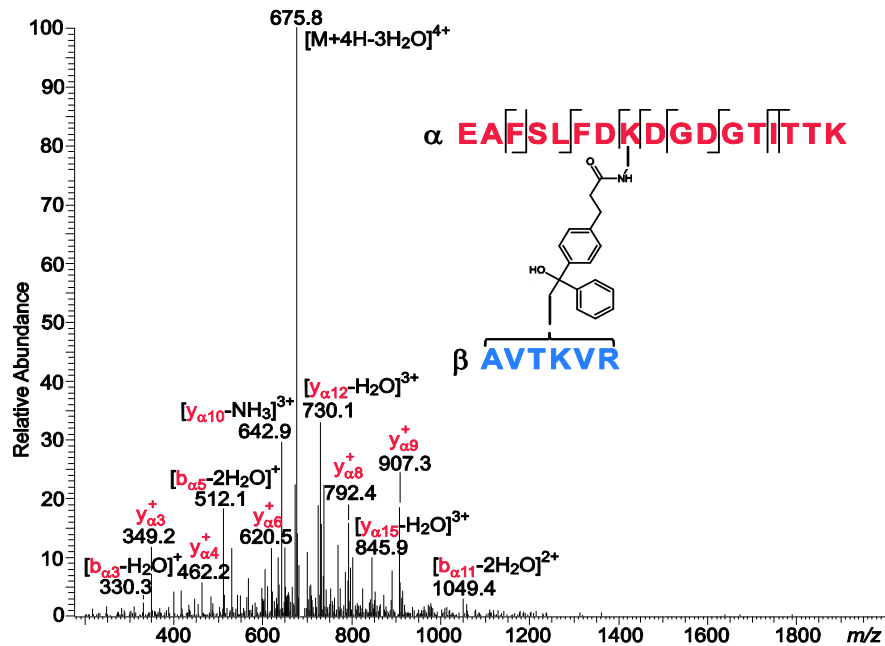


**Figure A2.** Fragment ion mass spectrum of a cross-link between CaM and ubMunc13-2. MS/MS data were recorded at a retention time of 77.3 min, the quadruply charged precursor ( $m/z$  689.107) was selected, representing a cross-linked product between CaM and ubMunc13-2. The reaction was carried out with a 20-fold excess of SBC and irradiated with 8000  $\text{mJ}/\text{cm}^2$ . The cross-linked product is composed of amino acids 14-30 of CaM ( $\alpha$ -peptide, red) and 10-15 of ubMunc13-2 ( $\beta$ -peptide, blue), in which Lys-21 of CaM is connected with ubMunc13-2. The exact cross-linking position could not be determined based on MS/MS data.

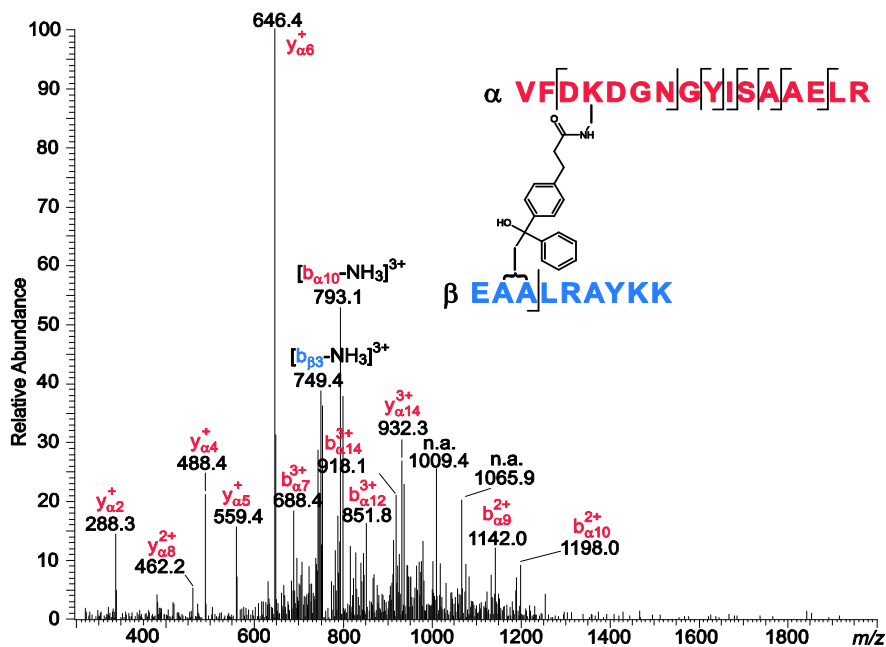


**Figure A3.** Fragment ion mass spectrum of a cross-link between CaM and Munc13-3. MS/MS data were recorded at a retention time of 67.7 min, the quadruply charged precursor ( $m/z$  760.646) was selected, representing a cross-linked product between CaM and Munc13-3. The reaction was conducted with a 20-fold excess of SBC and irradiated with 8000  $\text{mJ}/\text{cm}^2$ . The cross-linked product is composed of amino acids 91-106 of CaM ( $\alpha$ -peptide, red) and 5-13 of Munc13-3 ( $\beta$ -peptide, blue), in which Lys-94 of CaM is connected with Ala-6 or 7 of Munc13-3.

GST-bMunc13-2

*MSPILGYWKIKGLVQPTRLLLEYLEEKYEEHLYERDEGDKWRNKKFELGLEFPNLPYYIDGDVKLTQS  
MAIIRYIADKHNMLGGCPKERAEISMLEGAVLDIRYGVSR IAYS KDFETLKVDFLSKLP EMLKMFEDR  
LCHKTYLNGDHVTHPDFMLYDALDVVLYMDPMCLDAFPKLVCFKKRIEAI PQIDKYLKSSKYIAWPLQ  
GWQATFGGGDHPPKSDLVPRGSP E F HQGLSFLPKDGS AKQSDVSKLQDEVKGTSGAPQVISDPCGELS  
LLHQLEGSSPVLIPKEEDCGKLQIFKQDSQEHKACNVTKLQSDCNNAIKASSCLSLSGPLKAEKVNAE  
DRMLGGEDGLDILSPKQLEDLLADKSRRFATLNPDSAVEEVIIGPETFSNMVHIDLNEEETCTAQVLK  
NVFDKSSCVLGGSQEDEDVEIKFH TTKLSRAIHHFRLALQGVFQKLENNGSISPEDLESNESGSQSEN  
SDRLLWTVSSGGAHDCSVESPASQGSESLLSVVS GGVGISVQGDQTPQAPSNFSLASNNSPLTNSLLS  
FPLAPGLGNETCSRPDSPNQGKLSLEQVCAETIYLNKCINNFKNVLREKRLRQKLLQELVQTASHLS  
VEDIPSEGKREALQISDDGDPSLPQWLPEGP*

**Figure A4. Sequence of the GST-bMunc13-2 domain.** The bMunc13-2 domain used in this study was overexpressed as GST fusion protein containing the GST tag (*italic*), thrombin cleavage site (*red*), and amino acids 366 - 780 of full-length bMunc13-2.

GST-Munc13-3

*MSPILGYWKIKGLVQPTRLLLEYLEEKYEEHLYERDEGDKWRNKKFELGLEFPNLPYYIDGDVKLTQS  
MAIIRYIADKHNMLGGCPKERAEISMLEGAVLDIRYGVSR IAYS KDFETLKVDFLSKLP EMLKMFEDR  
LCHKTYLNGDHVTHPDFMLYDALDVVLYMDPMCLDAFPKLVCFKKRIEAI PQIDKYLKSSKYIAWPLQ  
GWQATFGGGDHPPKSDLVPRGSP E F SPCPLDNEPQGQWVGQYDSYQKTNSNDLYPNQSHPSMMYRSQ  
SELQSDDSEAAQPKSWHSRLSIDLSDKTFKFPKFGSTLQRAKSALEVVWNKSTQSLSGCEDSGSSLMG  
RFRTLSQSTANESSTTLDSDIYTEPYYYKAE E E E E D Y C E P V A D S E T D Y V E V M E Q V L A K L E N R T S V T E V D  
EHIKEYDHPSYETPYETPQDEGYDGQADDI ISEGELETLN E P A V E M E L V E D E S Q N L P V E P P E V M K P K R  
IRPSFKEAALRAYKKQMAELEEKILAGDSSSVDEKARIVSGNDLDASKFSALQVFGGAGRGLYGIDSM  
PDLRRKKTLP I V R D V A M T L A A R K S G L S L A M V I R T S L N N*

**Figure A5. Sequence of the GST-Munc13-3 domain.** The Munc13-3 domain used in this study was overexpressed as GST fusion protein containing the GSTtag (*italic*), thrombin cleavage site (*red*), and amino acids 711 - 1063 of full-length Munc13-3.

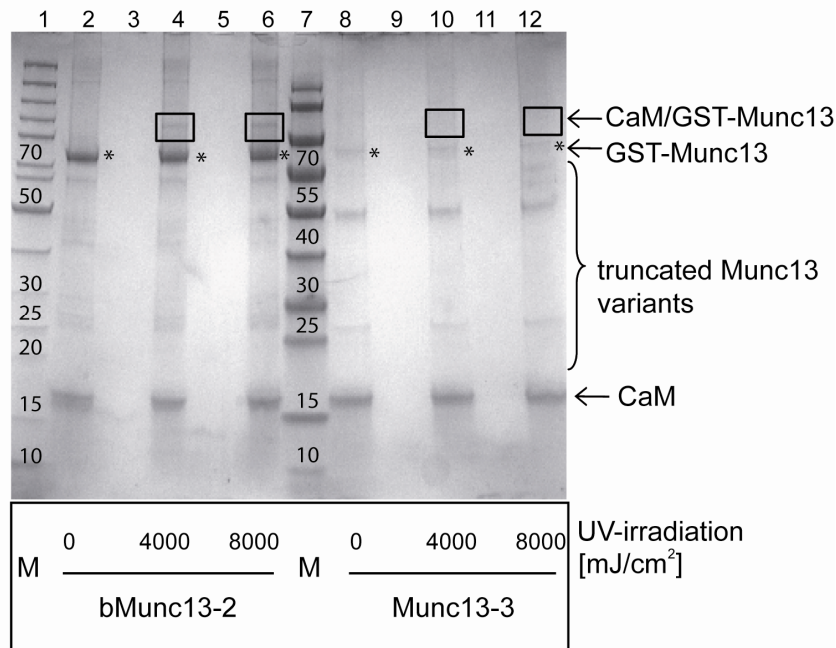


**Figure A6. Cross-linking experiment between and CaM and GST-Munc13 domains.** Cross-linking reaction mixtures, conducted with SBC (30 min reaction time, 50-fold excess), were irradiated with UV-A light (0, 4000, or 8000 mJ/cm<sup>2</sup>). A band migrating at ~75 kDa was detected representing the GST-Munc13 domains (asterisks). In the case of the reaction with GST-bMunc13-2, a band between 80 and 100 kDa is visible that might represent the CaM/Munc13 (1:1) complex (black boxes). For Munc13-3, no distinct band appeared upon irradiation. Lanes 1 and 7 contain molecular weight marker (M).

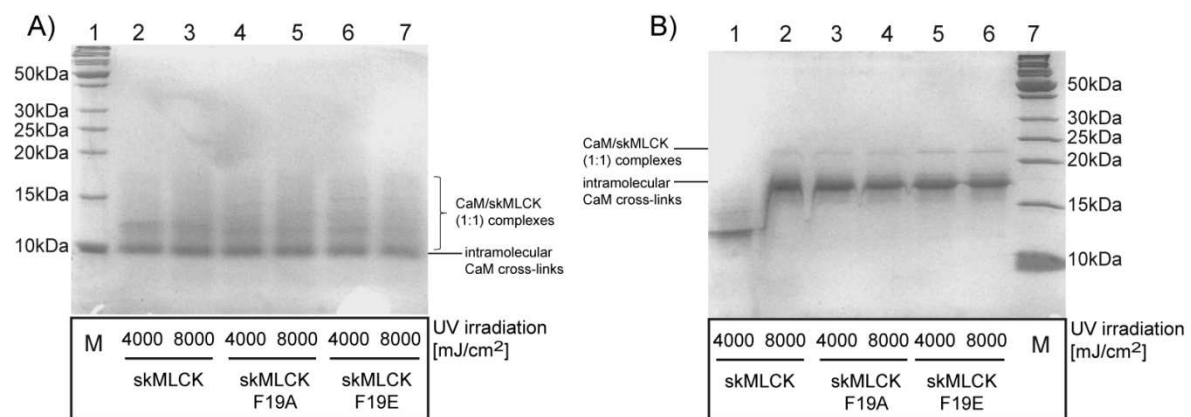


**Figure A7. SDS-PAGE analysis of cross-linking reactions between CaM and different skMLCK peptide variants.** Cross-linking reaction mixtures resulting from SBC (30 min reaction time, 50-fold excess) were irradiated with long-wavelength UV light (4000 or 8000 mJ/cm<sup>2</sup>). A) Reactions at 1 mM Ca<sup>2+</sup> revealed different bands for cross-linker-modified CaM (intramolecular cross-links) and CaM/peptide complexes. B) Reactions at 30 nM Ca<sup>2+</sup> revealed distinct bands for cross-linker-modified CaM (intramolecular cross-links) and CaM/peptide complexes. The control reactions (without irradiation; 0 mJ/cm<sup>2</sup>) were not loaded on the gel. M: molecular weight marker.

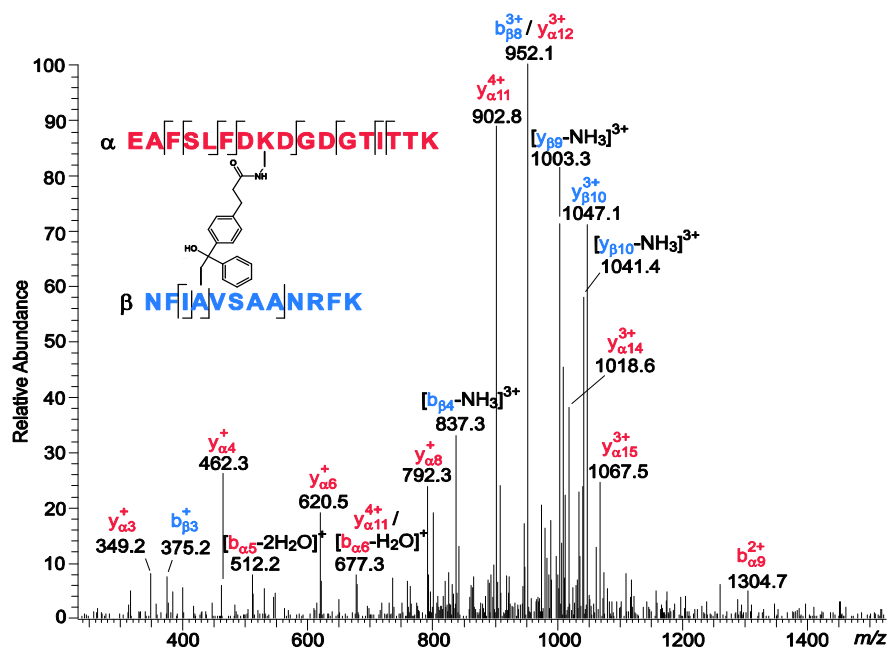


**Figure A8.** Fragment ion mass spectrum of a cross-link between CaM and the skMLCK peptide. MS/MS data were recorded at a retention time of 73.5 min, the quadruply charged precursor ( $m/z$  850.674) was selected, representing a cross-linked product between CaM and the skMLCK peptide. The reaction was conducted at 1 mM  $Ca^{2+}$  with a 50-fold excess of SBC (30 min reaction time; amine-reactive site) followed by irradiation with UV-A light ( $4000 \text{ mJ/cm}^2$ ). The cross-linked adduct contains amino acids 14-30 of CaM ( $\alpha$ -peptide, red) and amino acids 9-20 of skMLCK ( $\beta$ -peptide, blue), in which Lys-21 of CaM is connected with Ala-12 of the skMLCK peptide.

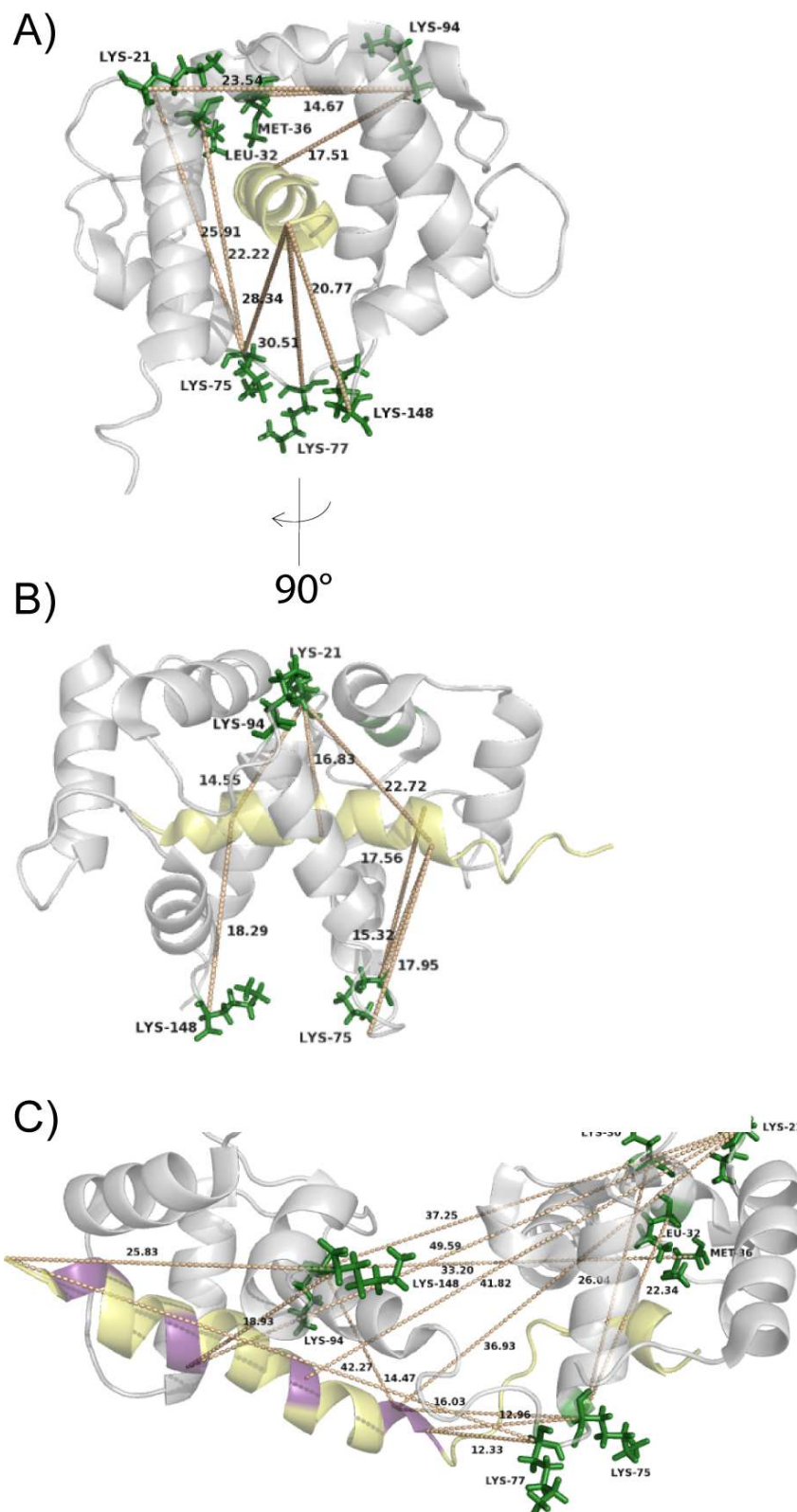


**Figure A9. Identified cross-linked products between CaM and the skMLCK peptide.** Ca-Ca distances [in Å] between cross-linked amino acids are depicted in the NMR structures of (A, B) the CaM/M13 peptide complex (pdb 2bbm, (98)); viewed from two angles and (C) the CaM/Munc13-1 peptide complex (pdb 2kdu, (54)). CaM is colored in grey, the peptide is shown in yellow. Reacted amino acids in CaM are displayed as green sticks, while these of the peptide are shown in purple.

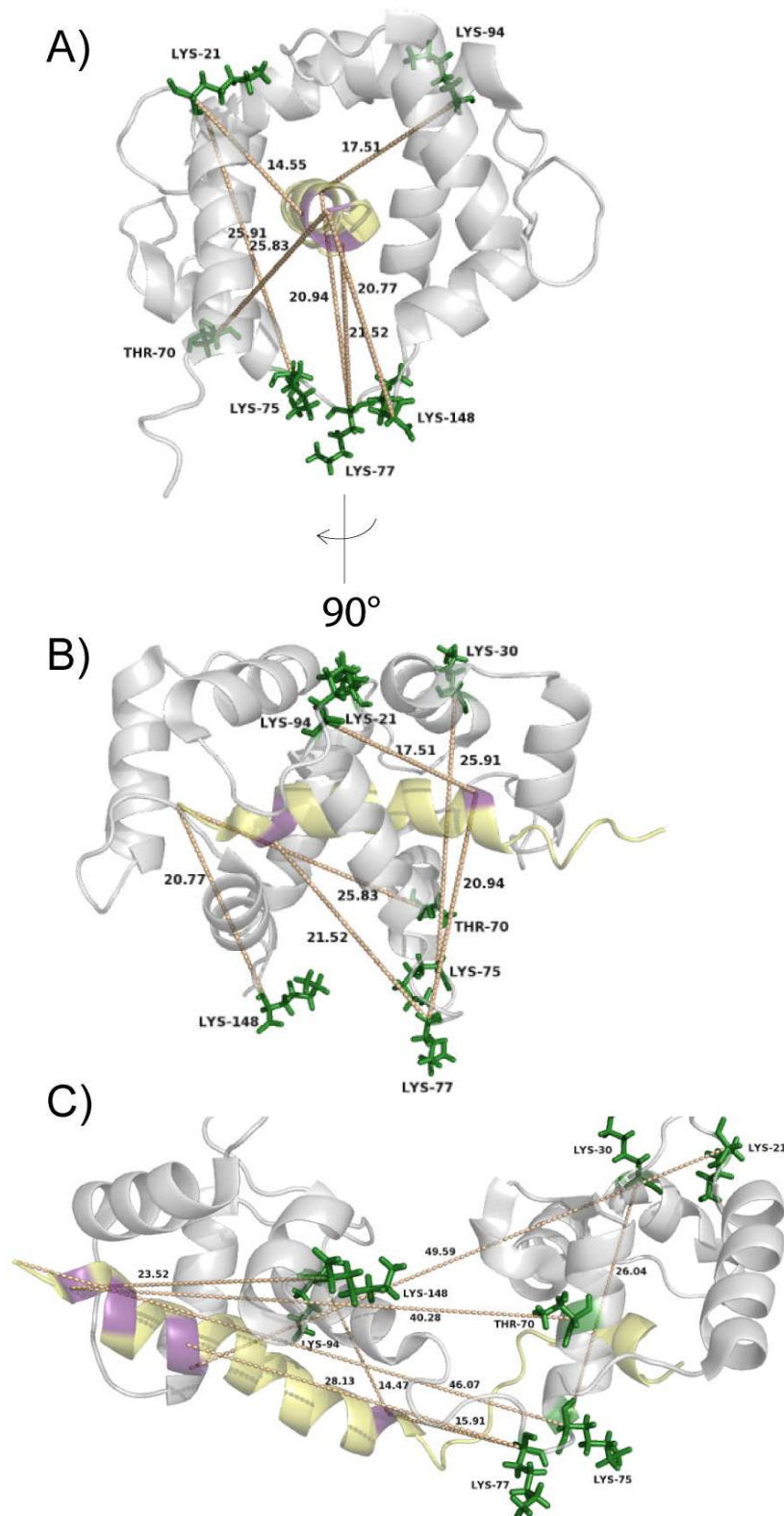


**Figure A10. Identified cross-linked products between CaM and the skMLCK F19A peptide.** Ca-Ca distances [in Å] between cross-linked amino acids are depicted in the NMR structures of (A, B) the CaM/M13 peptide complex (pdb 2bbm, (98)); viewed from two angles and (C) the CaM/Munc13-1 peptide complex (pdb 2kdu, (54)). CaM is colored in grey, the peptide is shown in yellow. Reacted amino acids in CaM are displayed as green sticks, while those of the peptide are shown in purple.



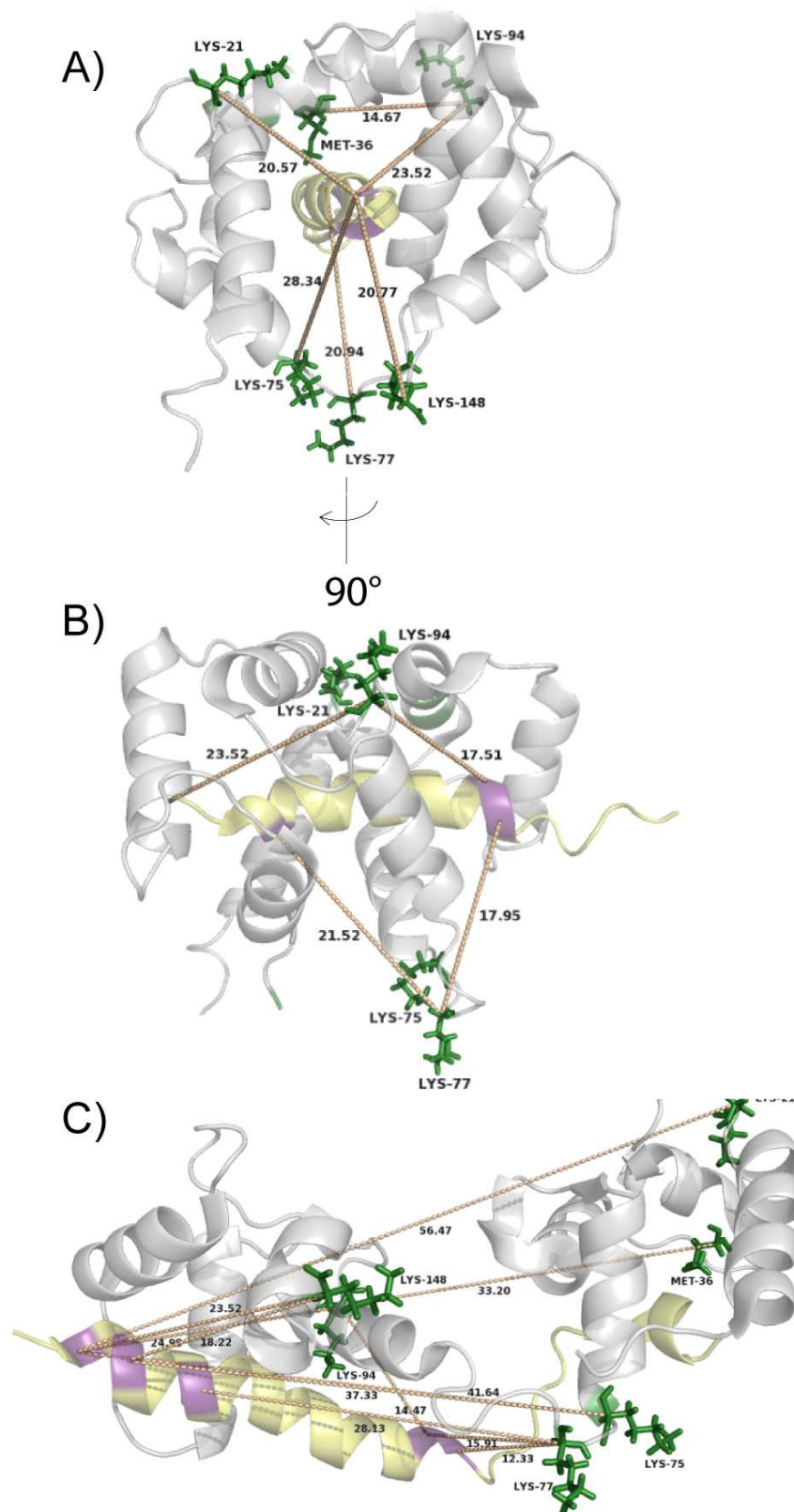


**Figure A11. Identified cross-linked products between CaM and the skMLCK F19E peptide.**  $\alpha$ - $\alpha$  distances [ in Å] between cross-linked amino acids are depicted in the NMR structures of (A, B) the CaM/M13 peptide complex (pdb 2bbm, (98)); viewed from two angles and (C) the CaM/Munc13-1 peptide complex (pdb 2kdu, (54)). CaM is colored in grey, the peptide is shown in yellow. Reacted amino acids in CaM are displayed as green sticks, while those of the peptide are shown in purple.

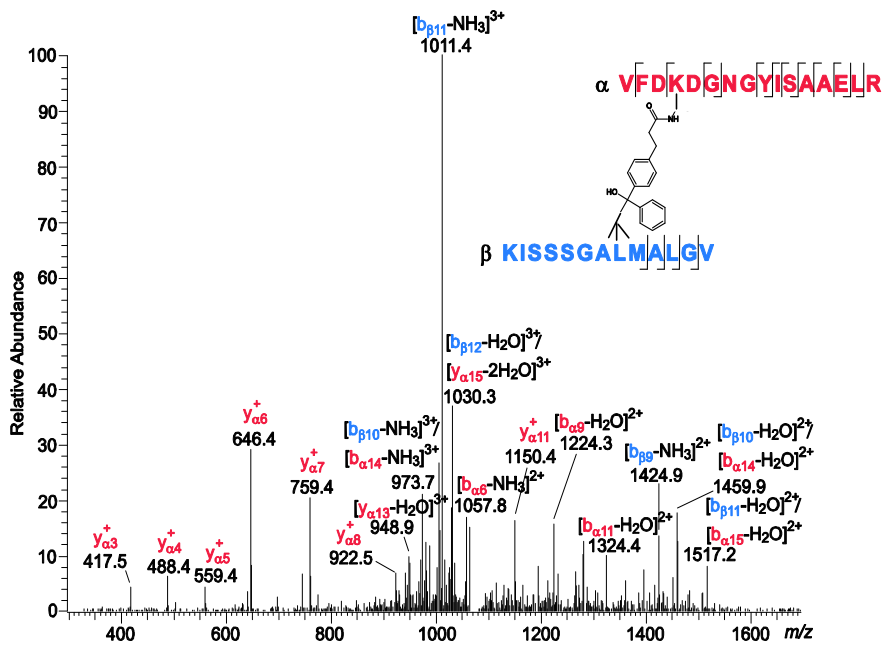


**Figure A12.** Fragment ion mass spectrum of a cross-link between CaM and the skMLCK F19A peptide. MS/MS data were recorded at a retention time of 78.6 min, the triply charged precursor ( $m/z$  1074.209) was selected, representing a cross-linked product between CaM and skMLCK F19A. The reaction was conducted at a  $Ca^{2+}$  concentration of 30 nM and with a 50-fold molar excess of SBC (30 min reaction time for the amine-reactive site) followed by irradiation with UV-A light ( $4000 \text{ mJ/cm}^2$ ). The cross-linked adduct contains amino acids 91-106 of CaM ( $\alpha$ -peptide, red) and amino acids 21-34 of skMLCK F19A ( $\beta$ -peptide, blue), in which Lys-94 of CaM is connected with Ala-27, Leu-28, or Met-29 of the skMLCK F19A peptide. The exact cross-linking position could not be determined based on MS/MS data.

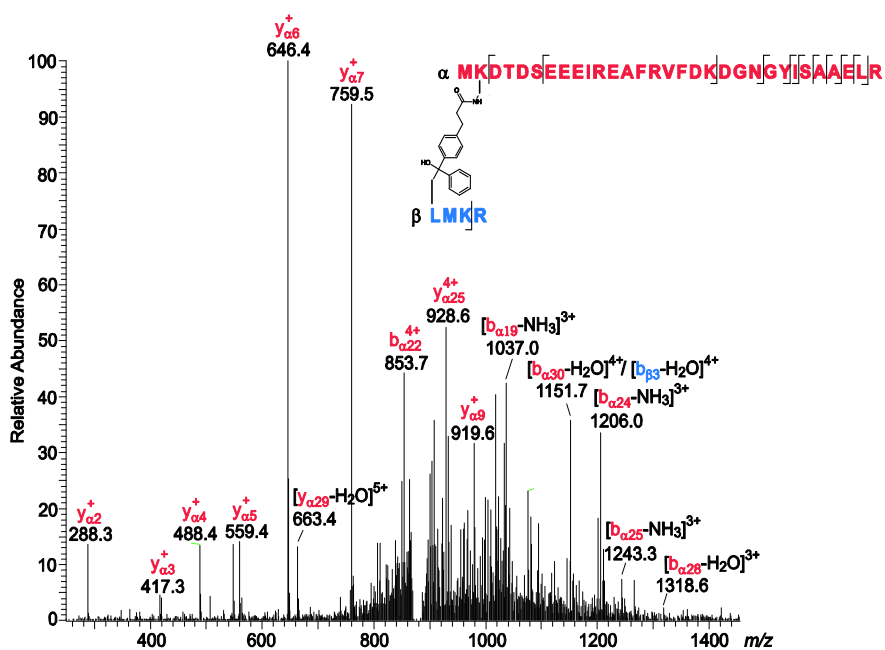


**Figure A13. Fragment ion mass spectrum of a cross-link between CaM and the skMLCK F19E peptide.** MS/MS data were recorded at a retention time of 75.0 min, the fivefold charged precursor ( $m/z$  878.627) was selected, representing a cross-linked product between CaM and skMLCK F19E. The reaction was conducted at a  $Ca^{2+}$  concentration of 30 nM and with a 50-fold molar excess of SBC (30 min reaction time for the amine-reactive site) followed by irradiation with UV-A light ( $4000 \text{ mJ/cm}^2$ ). The cross-linked adduct contains amino acids 76-106 of CaM ( $\alpha$ -peptide, red) and amino acids 1-4 of skMLCK F19E ( $\beta$ -peptide, blue), in which Lys-77 of CaM is connected to Leu-1, Met-2 or Lys-3 of the skMLCK F19E peptide.

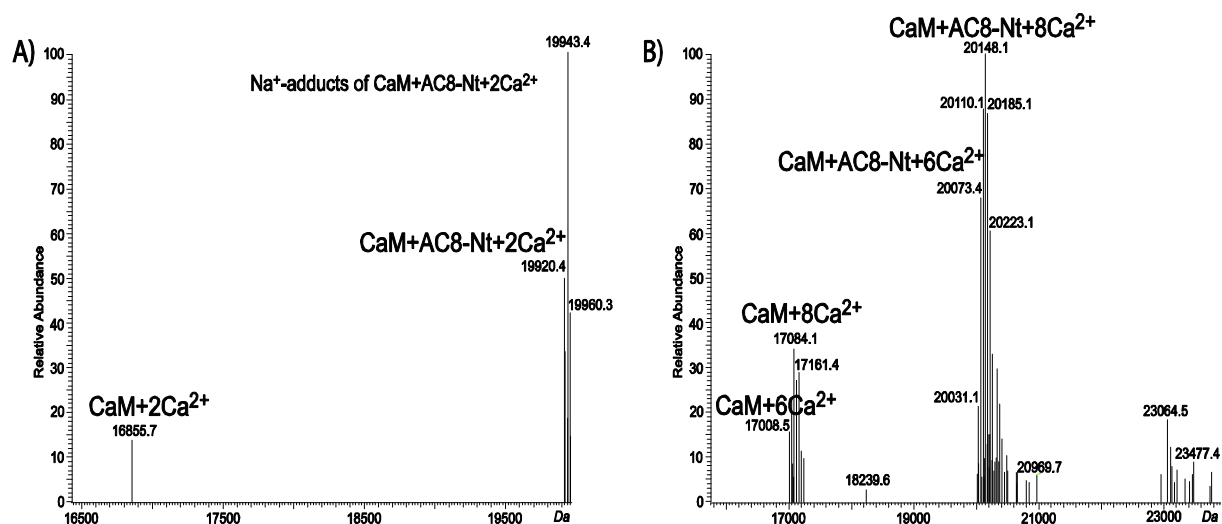


**Figure A14.** *Offline nano-ESI-MS* of a solution containing CaM and both AC8 peptides. Both AC8 peptides comprising the two CaM-binding sites (AC8-Nt and AC8-C2b) of AC8 were added to a CaM solution containing either A) 200  $\mu\text{M}$  EGTA or B) 1 mM  $\text{Ca}^{2+}$ . Deconvoluted singly charged mass spectra are presented.

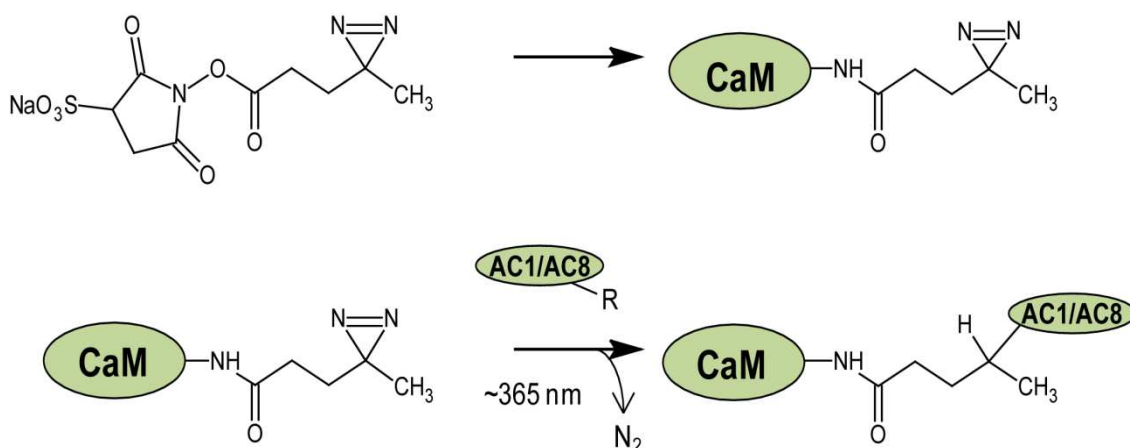


**Figure A15.** Scheme of cross-linking reactions using sulfo-SDA. The cross-linking reagent sulfo-SDA was reacted in a two-step fashion. First, the amine-reactive site of the cross-linker was reacted with CaM (30 min, 50-fold excess of cross-linker). After quenching and separation of excess cross-linker, sulfo-SDA-labeled CaM was added to the AC peptide and the reaction mixtures were irradiated with long-wavelength UV light, resulting in cross-linked products.

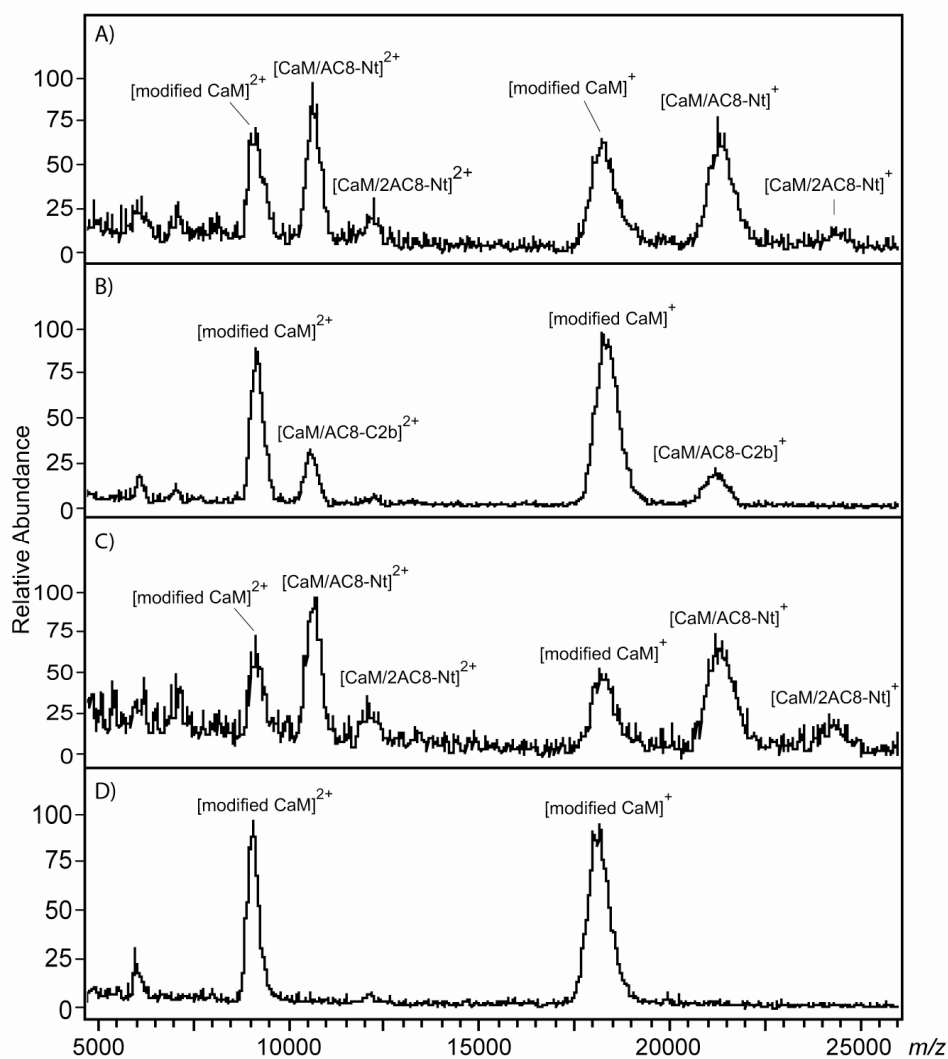


**Figure A16. MALDI-TOF-MS analysis of cross-linking reaction mixtures between CaM and AC peptides.** MALDI-TOF mass spectra of cross-linking reactions conducted at 1.4 mM Ca<sup>2+</sup> with a 50-fold molar excess of SBC, which were irradiated with UV-A light (8000 mJ/cm<sup>2</sup>). Analyses of reaction mixtures between CaM and A) AC8-Nt, B) AC8-C2b, C) AC8-Nt + AC8-C2b, and D) AC1-C1b are shown. Singly ( $m/z$  range 16,000-21,000) and doubly ( $m/z$  range 8,000-11,000) charged ions of cross-linker-modified CaM as well as CaM/AC peptide complexes are visible.

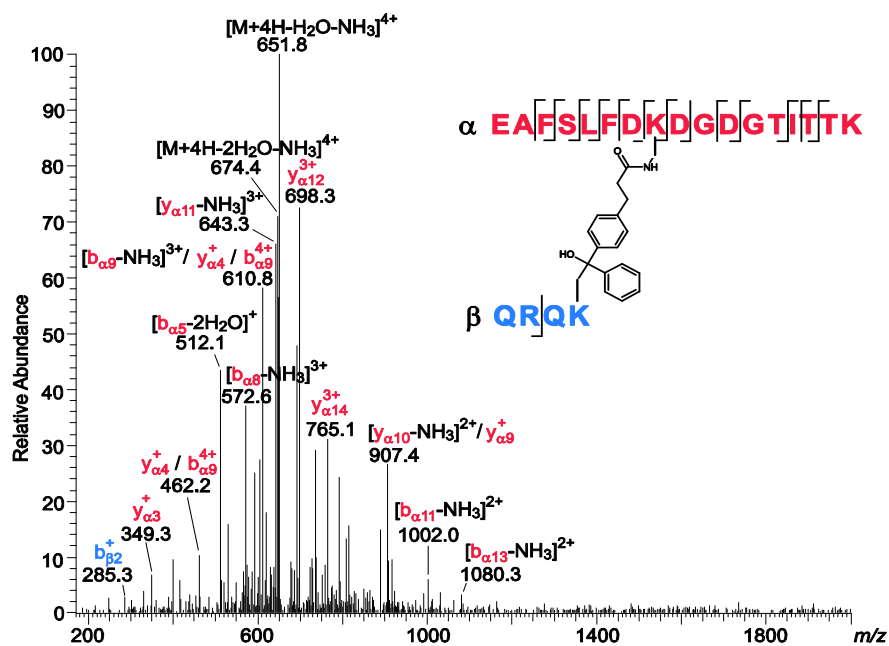


**Figure A17. Fragment ion mass spectrum of a cross-link between CaM and the AC8-C2b peptide.** MS/MS data were recorded at a retention time of 59.7 min and the quadruply charged precursor ( $m/z$  660.327) was selected, representing a cross-linked product between CaM and AC8-C2b. The reaction was conducted at a  $Ca^{2+}$  concentration of 1.4 mM with a 50-fold molar excess of SBC (30 min reaction for the amine-reactive site), and was irradiated with UV-A light (8000  $mJ/cm^2$ ). The cross-linked adduct contains the amino acid sequence 14-30 of CaM ( $\alpha$ -peptide, red) and 17-20 of AC8-C2b ( $\beta$ -peptide, blue), in which Lys-21 of CaM is connected with Lys-20 of the AC8-C2b peptide.

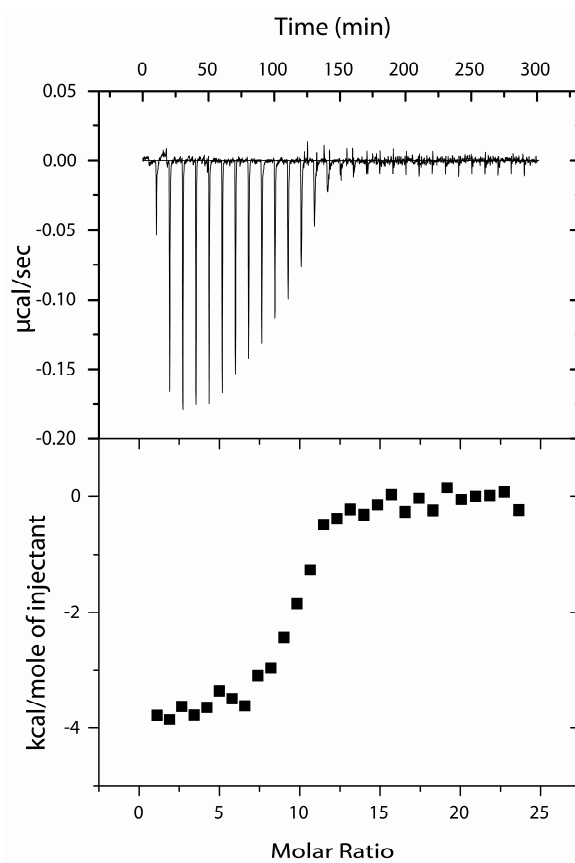


**Figure A18.** ITC analysis of the interaction between CaM and the AC1-C1b peptide. The AC1-C1b peptide ( $100\ \mu\text{M}$  in the syringe) was titrated to CaM ( $10\ \mu\text{M}$  in the reaction cell). One binding event is detectable with a stoichiometry of ca. 10.

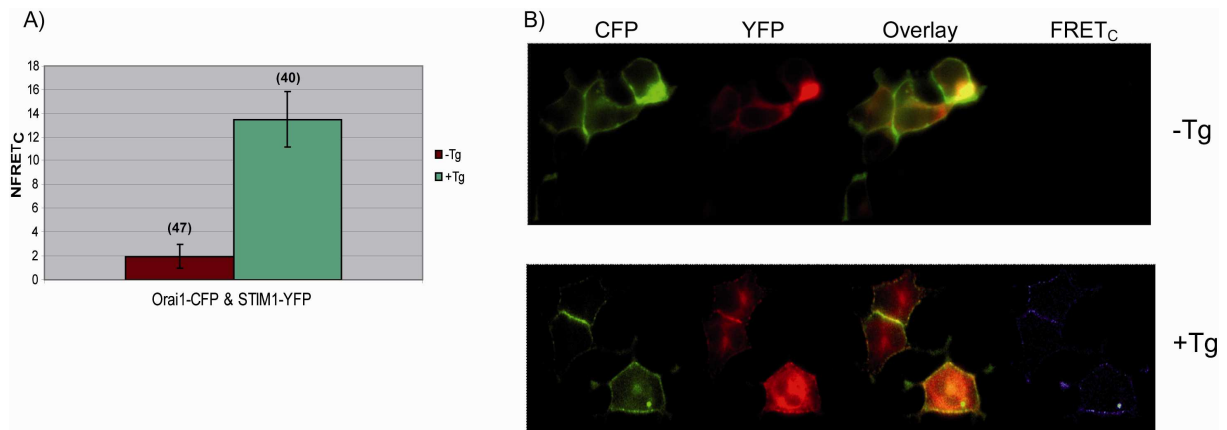


**Figure A19. FRET between Orai1-CFP and STIM1-YFP.** A) Only low NFRET<sub>C</sub> values were calculated before addition of Tg (-Tg, red), while a significant increase in FRET is observed upon store depletion (+Tg, green). B) The images of CFP and YFP fluorescence are shown. Overlay of both images indicates a colocalization upon addition of Tg, which is not detected without Tg. The corrected FRET image (FRET<sub>C</sub>) shows a FRET signal after store depletion.

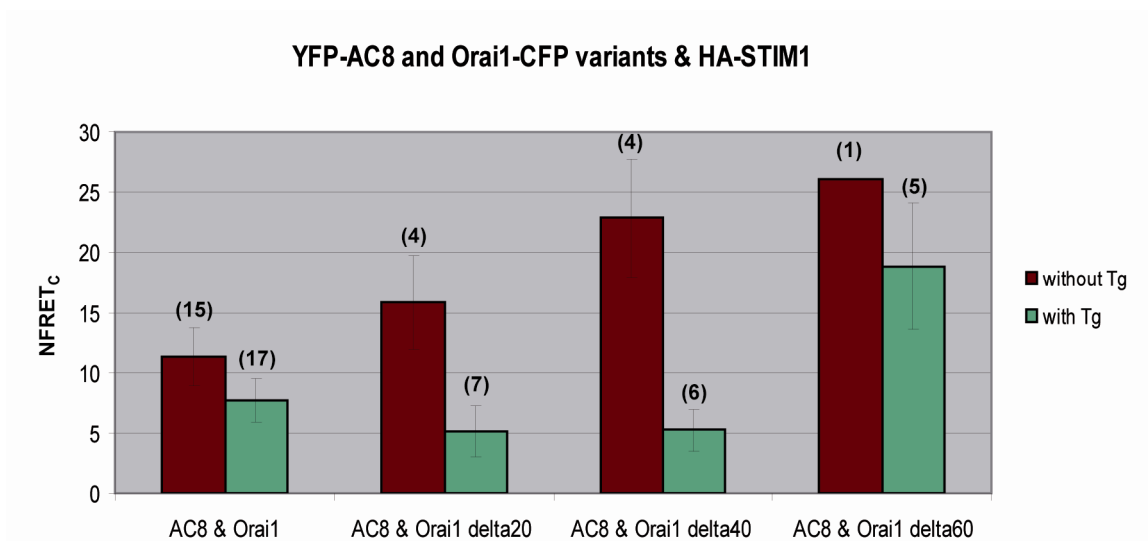


**Figure A20. FRET between YFP-AC8 and Orai1-CFP in the presence of HA-STIM1.** The calculated NFRET<sub>C</sub> values for FRET between YFP-AC8 and Orai1-CFP were higher in the absence of Tg (red) than upon addition of Tg (green), indicating an affect of HA-STIM1 on the interaction between Orai1 and AC8 when the Ca<sup>2+</sup> stores are empty. The numbers in brackets represent the number of single cells, which were averaged.



## REFERENCES

1. Yang, S. H., Sharrocks, A. D., and Whitmarsh, A. J. (2013) MAP kinase signalling cascades and transcriptional regulation, *Gene* 513, 1-13.
2. Black, J. C., Van Rechem, C., and Whetstine, J. R. (2012) Histone lysine methylation dynamics: establishment, regulation, and biological impact, *Mol Cell* 48, 491-507.
3. Huxley, H. E. (1969) The mechanism of muscular contraction, *Science* 164, 1356-1365.
4. Stull, J. T., Kamm, K. E., and Vandenoorn, R. (2011) Myosin light chain kinase and the role of myosin light chain phosphorylation in skeletal muscle, *Arch Biochem Biophys* 510, 120-128.
5. Ren, L., Emery, D., Kaboord, B., Chang, E., and Qoronfleh, M. W. (2003) Improved immunomatrix methods to detect protein:protein interactions, *J Biochem Biophys Methods* 57, 143-157.
6. Fields, S., and Song, O. (1989) A novel genetic system to detect protein-protein interactions, *Nature* 340, 245-246.
7. Fields, S. (2009) Interactive learning: lessons from two hybrids over two decades, *Proteomics* 9, 5209-5213.
8. Gavin, A. C., Bosche, M., Krause, R., Grandi, P., Marzioch, M., Bauer, A., Schultz, J., Rick, J. M., Michon, A. M., Cruciat, C. M., Remor, M., Hofert, C., Schelder, M., Brajenovic, M., Ruffner, H., Merino, A., Klein, K., Hudak, M., Dickson, D., Rudi, T., Gnau, V., Bauch, A., Bastuck, S., Huhse, B., Leutwein, C., Heurtier, M. A., Copley, R. R., Edlmann, A., Querfurth, E., Rybin, V., Drewes, G., Raida, M., Bouwmeester, T., Bork, P., Seraphin, B., Kuster, B., Neubauer, G., and Superti-Furga, G. (2002) Functional organization of the yeast proteome by systematic analysis of protein complexes, *Nature* 415, 141-147.
9. Phillips, K. S., and Cheng, Q. (2007) Recent advances in surface plasmon resonance based techniques for bioanalysis, *Anal Bioanal Chem* 387, 1831-1840.
10. Ababou, A., and Ladbury, J. E. (2006) Survey of the year 2005: literature on applications of isothermal titration calorimetry, *J Mol Recognit* 19, 79-89.
11. Fernandez-Duenas, V., Llorente, J., Gandia, J., Borroto-Escuela, D. O., Agnati, L. F., Tasca, C. I., Fuxe, K., and Ciruela, F. (2012) Fluorescence resonance energy transfer-based technologies in the study of protein-protein interactions at the cell surface, *Methods* 57, 467-472.
12. Milne, J. L., Borgnia, M. J., Bartesaghi, A., Tran, E. E., Earl, L. A., Schauder, D. M., Lengyel, J., Pierson, J., Patwardhan, A., and Subramaniam, S. (2013) Cryo-electron microscopy--a primer for the non-microscopist, *FEBS J* 280, 28-45.
13. Rowe, A. J. (2011) Ultra-weak reversible protein-protein interactions, *Methods* 54, 157-166.
14. Jensen, M. R., Ortega-Roldan, J. L., Salmon, L., van Nuland, N., and Blackledge, M. (2011) Characterizing weak protein-protein complexes by NMR residual dipolar couplings, *Eur Biophys J* 40, 1371-1381.
15. Durbin, S. D., and Feher, G. (1996) Protein crystallization, *Annu Rev Phys Chem* 47, 171-204.
16. Mozzarelli, A., and Rossi, G. L. (1996) Protein function in the crystal, *Annu Rev Biophys Biomol Struct* 25, 343-365.
17. Sinz, A. (2006) Chemical cross-linking and mass spectrometry to map three-dimensional protein structures and protein-protein interactions, *Mass Spectrom Rev* 25, 663-682.

18. Sinz, A. (2010) Investigation of protein-protein interactions in living cells by chemical crosslinking and mass spectrometry, *Anal Bioanal Chem* 397, 3433-3440.
19. Schaks, S., Kalkhof, S., Krauth, F., Jahn, O., and Sinz, A. (2011) Chemisches Cross-Linking und MS zur Untersuchung von Proteinkomplexen, *BIOspektrum* 17, 524-527.
20. Chin, D., and Means, A. R. (2000) Calmodulin: a prototypical calcium sensor, *Trends Cell Biol* 10, 322-328.
21. Katz, B., and Miledi, R. (1968) The role of calcium in neuromuscular facilitation, *J Physiol* 195, 481-492.
22. Burgoyne, R. D., and Morgan, A. (1995) Ca<sup>2+</sup> and secretory-vesicle dynamics, *Trends Neurosci* 18, 191-196.
23. Nishizuka, Y. (1986) Studies and perspectives of protein kinase C, *Science* 233, 305-312.
24. Denton, R. M. (2009) Regulation of mitochondrial dehydrogenases by calcium ions, *Biochim Biophys Acta* 1787, 1309-1316.
25. Ikura, M., and Ames, J. B. (2006) Genetic polymorphism and protein conformational plasticity in the calmodulin superfamily: two ways to promote multifunctionality, *Proc Natl Acad Sci U S A* 103, 1159-1164.
26. Cheung, W. Y. (1970) Cyclic 3',5'-nucleotide phosphodiesterase. Demonstration of an activator, *Biochem Biophys Res Commun* 38, 533-538.
27. Kakiuchi, S., and Yamazaki, R. (1970) Calcium dependent phosphodiesterase activity and its activating factor (PAF) from brain studies on cyclic 3',5'-nucleotide phosphodiesterase (3), *Biochem Biophys Res Commun* 41, 1104-1110.
28. Fallon, J. L., and Quiocho, F. A. (2003) A closed compact structure of native Ca<sup>2+</sup>-calmodulin, *Structure* 11, 1303-1307.
29. Babu, Y. S., Sack, J. S., Greenhough, T. J., Bugg, C. E., Means, A. R., and Cook, W. J. (1985) Three-dimensional structure of calmodulin, *Nature* 315, 37-40.
30. Kuboniwa, H., Tjandra, N., Grzesiek, S., Ren, H., Klee, C. B., and Bax, A. (1995) Solution structure of calcium-free calmodulin, *Nat Struct Biol* 2, 768-776.
31. Copley, R. R., Schultz, J., Ponting, C. P., and Bork, P. (1999) Protein families in multicellular organisms, *Curr Opin Struct Biol* 9, 408-415.
32. Friedberg, F., and Rhoads, A. R. (2001) Evolutionary aspects of calmodulin, *IUBMB Life* 51, 215-221.
33. Friedberg, F., and Rhoads, A. R. (2001) Sequence homology of the 3'-untranslated region of calmodulin III in mammals, *Mol Biol Rep* 28, 27-30.
34. Friedberg, F., and Taliaferro, L. (2005) Calmodulin genes in zebrafish (revisited), *Mol Biol Rep* 32, 55-60.
35. Chattopadhyaya, R., Meador, W. E., Means, A. R., and Quiocho, F. A. (1992) Calmodulin structure refined at 1.7 Å resolution, *J Mol Biol* 228, 1177-1192.
36. Zhang, M., Tanaka, T., and Ikura, M. (1995) Calcium-induced conformational transition revealed by the solution structure of apo calmodulin, *Nat Struct Biol* 2, 758-767.
37. Kawasaki, H., and Kretsinger, R. H. (1994) Calcium-binding proteins. 1: EF-hands, *Protein Profile* 1, 343-517.
38. Kawasaki, H., Nakayama, S., and Kretsinger, R. H. (1998) Classification and evolution of EF-hand proteins, *Biometals* 11, 277-295.
39. Burgoyne, R. D., and Clague, M. J. (2003) Calcium and calmodulin in membrane fusion, *Biochim Biophys Acta* 1641, 137-143.
40. Michiels, J., Xi, C., Verhaert, J., and Vanderleyden, J. (2002) The functions of Ca(2+) in bacteria: a role for EF-hand proteins?, *Trends Microbiol* 10, 87-93.

41. Zhou, Y., Yang, W., Kirberger, M., Lee, H. W., Ayalasomayajula, G., and Yang, J. J. (2006) Prediction of EF-hand calcium-binding proteins and analysis of bacterial EF-hand proteins, *Proteins* 65, 643-655.
42. Potter, J. D., Stang-Brown, P., Walker, P. L., and Lida, S. (1983) Ca<sup>2+</sup> binding to Calmodulin, *Methods Enzymol.* 102, 135-143.
43. Ogawa, Y., and Tanokura, M. (1984) Calcium binding to calmodulin: effects of ionic strength, Mg<sup>2+</sup>, pH and temperature, *J Biochem* 95, 19-28.
44. Bhattacharya, S., Bunick, C. G., and Chazin, W. J. (2004) Target selectivity in EF-hand calcium binding proteins, *Biochim Biophys Acta* 1742, 69-79.
45. Swindells, M. B., and Ikura, M. (1996) Pre-formation of the semi-open conformation by the apo-calmodulin C-terminal domain and implications binding IQ-motifs, *Nat Struct Biol* 3, 501-504.
46. Vetter, S. W., and Leclerc, E. (2003) Novel aspects of calmodulin target recognition and activation, *Eur J Biochem* 270, 404-414.
47. Crivici, A., and Ikura, M. (1995) Molecular and structural basis of target recognition by calmodulin, *Annu Rev Biophys Biomol Struct* 24, 85-116.
48. Ikura, M. (1996) Calcium binding and conformational response in EF-hand proteins, *Trends Biochem Sci* 21, 14-17.
49. Cox, J. A., Comte, M., Fitton, J. E., and DeGrado, W. F. (1985) The interaction of calmodulin with amphiphilic peptides, *J Biol Chem* 260, 2527-2534.
50. O'Neil, K. T., and DeGrado, W. F. (1990) How calmodulin binds its targets: sequence independent recognition of amphiphilic alpha-helices, *Trends Biochem Sci* 15, 59-64.
51. Rhoads, A. R., and Friedberg, F. (1997) Sequence motifs for calmodulin recognition, *FASEB J* 11, 331-340.
52. O'Connell, D. J., Bauer, M. C., O'Brien, J., Johnson, W. M., Divizio, C. A., O'Kane, S. L., Berggard, T., Merino, A., Akerfeldt, K. S., Linse, S., and Cahill, D. J. (2010) Integrated protein array screening and high throughput validation of 70 novel neural calmodulin-binding proteins, *Mol Cell Proteomics* 9, 1118-1132.
53. Juranic, N., Atanasova, E., Filoteo, A. G., Macura, S., Prendergast, F. G., Penniston, J. T., and Strehler, E. E. (2010) Calmodulin wraps around its binding domain in the plasma membrane Ca<sup>2+</sup> pump anchored by a novel 18-1 motif, *J Biol Chem* 285, 4015-4024.
54. Rodriguez-Castaneda, F., Maestre-Martinez, M., Coudeville, N., Dimova, K., Junge, H., Lipstein, N., Lee, D., Becker, S., Brose, N., Jahn, O., Carlomagno, T., and Griesinger, C. (2009) Modular architecture of Munc13/calmodulin complexes: dual regulation by Ca<sup>2+</sup> and possible function in short-term synaptic plasticity, *EMBO J* 29, 680-691.
55. Brose, N., Hofmann, K., Hata, Y., and Sudhof, T. C. (1995) Mammalian homologues of *Caenorhabditis elegans* unc-13 gene define novel family of C2-domain proteins, *J Biol Chem* 270, 25273-25280.
56. Brenner, S. (1974) The genetics of *Caenorhabditis elegans*, *Genetics* 77, 71-94.
57. Hosono, R., Sassa, T., and Kuno, S. (1987) Mutations affecting acetylcholine levels in the nematode *Caenorhabditis elegans*, *J Neurochem* 49, 1820-1823.
58. Hosono, R., and Kamiya, Y. (1991) Additional genes which result in an elevation of acetylcholine levels by mutations in *Caenorhabditis elegans*, *Neurosci Lett* 128, 243-244.
59. Aravamudan, B., Fergestad, T., Davis, W. S., Rodesch, C. K., and Broadie, K. (1999) *Drosophila* UNC-13 is essential for synaptic transmission, *Nat Neurosci* 2, 965-971.
60. Augustin, I., Betz, A., Herrmann, C., Jo, T., and Brose, N. (1999) Differential expression of two novel Munc13 proteins in rat brain, *Biochem J* 337 ( Pt 3), 363-371.

61. Song, Y., Ailenberg, M., and Silverman, M. (1998) Cloning of a novel gene in the human kidney homologous to rat munc13s: its potential role in diabetic nephropathy, *Kidney Int* 53, 1689-1695.
62. Betz, A., Thakur, P., Junge, H. J., Ashery, U., Rhee, J. S., Scheuss, V., Rosenmund, C., Rettig, J., and Brose, N. (2001) Functional interaction of the active zone proteins Munc13-1 and RIM1 in synaptic vesicle priming, *Neuron* 30, 183-196.
63. Augustin, I., Rosenmund, C., Südhof, T. C., and Brose, N. (1999) Munc13-1 is essential for fusion competence of glutamatergic synaptic vesicles, *Nature* 400, 457-461.
64. Varoqueaux, F., Sigler, A., Rhee, J. S., Brose, N., Enk, C., Reim, K., and Rosenmund, C. (2002) Total arrest of spontaneous and evoked synaptic transmission but normal synaptogenesis in the absence of Munc13-mediated vesicle priming, *Proc Natl Acad Sci U S A* 99, 9037-9042.
65. Rosenmund, C., Sigler, A., Augustin, I., Reim, K., Brose, N., and Rhee, J. S. (2002) Differential control of vesicle priming and short-term plasticity by Munc13 isoforms, *Neuron* 33, 411-424.
66. Rizo, J., and Rosenmund, C. (2008) Synaptic vesicle fusion, *Nat Struct Mol Biol* 15, 665-674.
67. Basu, J., Shen, N., Dulubova, I., Lu, J., Guan, R., Guryev, O., Grishin, N. V., Rosenmund, C., and Rizo, J. (2005) A minimal domain responsible for Munc13 activity, *Nat Struct Mol Biol* 12, 1017-1018.
68. Richmond, J. E., Weimer, R. M., and Jorgensen, E. M. (2001) An open form of syntaxin bypasses the requirement for UNC-13 in vesicle priming, *Nature* 412, 338-341.
69. Betz, A., Okamoto, M., Benseler, F., and Brose, N. (1997) Direct interaction of the rat unc-13 homologue Munc13-1 with the N terminus of syntaxin, *J Biol Chem* 272, 2520-2526.
70. Brose, N., Rosenmund, C., and Rettig, J. (2000) Regulation of transmitter release by Unc-13 and its homologues, *Curr Opin Neurobiol* 10, 303-311.
71. Guan, R., Dai, H., and Rizo, J. (2008) Binding of the Munc13-1 MUN domain to membrane-anchored SNARE complexes, *Biochemistry* 47, 1474-1481.
72. Wenginger, K., Bowen, M. E., Choi, U. B., Chu, S., and Brunger, A. T. (2008) Accessory proteins stabilize the acceptor complex for synaptobrevin, the 1:1 syntaxin/SNAP-25 complex, *Structure* 16, 308-320.
73. Ma, C., Su, L., Seven, A. B., Xu, Y., and Rizo, J. (2013) Reconstitution of the vital functions of Munc18 and Munc13 in neurotransmitter release, *Science* 339, 421-425.
74. Zucker, R. S., and Regehr, W. G. (2002) Short-term synaptic plasticity, *Annu Rev Physiol* 64, 355-405.
75. Junge, H. J., Rhee, J. S., Jahn, O., Varoqueaux, F., Spiess, J., Waxham, M. N., Rosenmund, C., and Brose, N. (2004) Calmodulin and Munc13 form a Ca<sup>2+</sup> sensor/effector complex that controls short-term synaptic plasticity, *Cell* 118, 389-401.
76. Betz, A., Ashery, U., Rickmann, M., Augustin, I., Neher, E., Südhof, T. C., Rettig, J., and Brose, N. (1998) Munc13-1 is a presynaptic phorbol ester receptor that enhances neurotransmitter release, *Neuron* 21, 123-136.
77. Rizo, J., and Südhof, T. C. (1998) C2-domains, structure and function of a universal Ca<sup>2+</sup>-binding domain, *J Biol Chem* 273, 15879-15882.
78. Koch, H., Hofmann, K., and Brose, N. (2000) Definition of Munc13-homology-domains and characterization of a novel ubiquitously expressed Munc13 isoform, *Biochem J* 349, 247-253.

79. Dimova, K., Kawabe, H., Betz, A., Brose, N., and Jahn, O. (2006) Characterization of the Munc13-calmodulin interaction by photoaffinity labeling, *Biochim Biophys Acta* 1763, 1256-1265.
80. Shin, O. H., Lu, J., Rhee, J. S., Tomchick, D. R., Pang, Z. P., Wojcik, S. M., Camacho-Perez, M., Brose, N., Machius, M., Rizo, J., Rosenmund, C., and Sudhof, T. C. (2010) Munc13 C2B domain is an activity-dependent Ca<sup>2+</sup> regulator of synaptic exocytosis, *Nat Struct Mol Biol* 17, 280-288.
81. Shen, N., Guryev, O., and Rizo, J. (2005) Intramolecular occlusion of the diacylglycerol-binding site in the C1 domain of munc13-1, *Biochemistry* 44, 1089-1096.
82. Li, W., Ma, C., Guan, R., Xu, Y., Tomchick, D. R., and Rizo, J. (2011) The crystal structure of a Munc13 C-terminal module exhibits a remarkable similarity to vesicle tethering factors, *Structure* 19, 1443-1455.
83. Xu, X. Z., Wes, P. D., Chen, H., Li, H. S., Yu, M., Morgan, S., Liu, Y., and Montell, C. (1998) Retinal targets for calmodulin include proteins implicated in synaptic transmission, *J Biol Chem* 273, 31297-31307.
84. Dimova, K., Kalkhof, S., Pottratz, I., Ihling, C., Rodriguez-Castaneda, F., Liepold, T., Griesinger, C., Brose, N., Sinz, A., and Jahn, O. (2009) Structural insights into the calmodulin-Munc13 interaction obtained by cross-linking and mass spectrometry, *Biochemistry* 48, 5908-5921.
85. Lipstein, N., Schaks, S., Dimova, K., Kalkhof, S., Ihling, C., Kölbel, K., Ashery, U., Rhee, J., Brose, N., Sinz, A., and Jahn, O. (2012) Nonconserved Ca<sup>2+</sup>/Calmodulin Binding Sites in Munc13s Differentially Control Synaptic Short-Term Plasticity, *Molecular and Cellular Biology* 32, 4628-4641.
86. Kamm, K. E., and Stull, J. T. (2001) Dedicated myosin light chain kinases with diverse cellular functions, *J Biol Chem* 276, 4527-4530.
87. Hanks, S. K., Quinn, A. M., and Hunter, T. (1988) The protein kinase family: conserved features and deduced phylogeny of the catalytic domains, *Science* 241, 42-52.
88. Blumenthal, D. K., Takio, K., Edelman, A. M., Charbonneau, H., Titani, K., Walsh, K. A., and Krebs, E. G. (1985) Identification of the calmodulin-binding domain of skeletal muscle myosin light chain kinase, *Proc Natl Acad Sci U S A* 82, 3187-3191.
89. Herring, B. P., Stull, J. T., and Gallagher, P. J. (1990) Domain characterization of rabbit skeletal muscle myosin light chain kinase, *J Biol Chem* 265, 1724-1730.
90. Kennelly, P. J., Edelman, A. M., Blumenthal, D. K., and Krebs, E. G. (1987) Rabbit skeletal muscle myosin light chain kinase. The calmodulin binding domain as a potential active site-directed inhibitory domain, *J Biol Chem* 262, 11958-11963.
91. Takashima, S. (2009) Phosphorylation of myosin regulatory light chain by myosin light chain kinase, and muscle contraction, *Circ J* 73, 208-213.
92. Krueger, J. K., Bishop, N. A., Blumenthal, D. K., Zhi, G., Beckingham, K., Stull, J. T., and Trewella, J. (1998) Calmodulin binding to myosin light chain kinase begins at substoichiometric Ca<sup>2+</sup> concentrations: a small-angle scattering study of binding and conformational transitions, *Biochemistry* 37, 17810-17817.
93. Krueger, J. K., Zhi, G., Stull, J. T., and Trewella, J. (1998) Neutron-scattering studies reveal further details of the Ca<sup>2+</sup>/calmodulin-dependent activation mechanism of myosin light chain kinase, *Biochemistry* 37, 13997-14004.
94. Gallagher, P. J., Herring, B. P., Trafny, A., Sowadski, J., and Stull, J. T. (1993) A molecular mechanism for autoinhibition of myosin light chain kinases, *J Biol Chem* 268, 26578-26582.

95. Persechini, A., Yano, K., and Stemmer, P. M. (2000)  $\text{Ca}^{2+}$  binding and energy coupling in the calmodulin-myosin light chain kinase complex, *J Biol Chem* 275, 4199-4204.
96. Findlay, W. A., Martin, S. R., Beckingham, K., and Bayley, P. M. (1995) Recovery of native structure by calcium binding site mutants of calmodulin upon binding of sk-MLCK target peptides, *Biochemistry* 34, 2087-2094.
97. Kalkhof, S., Ihling, C., Mechtler, K., and Sinz, A. (2005) Chemical cross-linking and high-performance Fourier transform ion cyclotron resonance mass spectrometry for protein interaction analysis: application to a calmodulin/target peptide complex, *Anal Chem* 77, 495-503.
98. Ikura, M., Clore, G. M., Gronenborn, A. M., Zhu, G., Klee, C. B., and Bax, A. (1992) Solution structure of a calmodulin-target peptide complex by multidimensional NMR, *Science* 256, 632-638.
99. Bowman, B. F., Peterson, J. A., and Stull, J. T. (1992) Pre-steady-state kinetics of the activation of rabbit skeletal muscle myosin light chain kinase by  $\text{Ca}^{2+}$ /calmodulin, *J Biol Chem* 267, 5346-5354.
100. Hultschig, C., Hecht, H. J., and Frank, R. (2004) Systematic delineation of a calmodulin peptide interaction, *J Mol Biol* 343, 559-568.
101. Krupinski, J., Coussen, F., Bakalyar, H. A., Tang, W. J., Feinstein, P. G., Orth, K., Slaughter, C., Reed, R. R., and Gilman, A. G. (1989) Adenylyl cyclase amino acid sequence: possible channel- or transporter-like structure, *Science* 244, 1558-1564.
102. Tesmer, J. J., Sunahara, R. K., Gilman, A. G., and Sprang, S. R. (1997) Crystal structure of the catalytic domains of adenylyl cyclase in a complex with G $\alpha$ .GTP $\gamma$ S, *Science* 278, 1907-1916.
103. Zhang, G., Liu, Y., Ruoho, A. E., and Hurley, J. H. (1997) Structure of the adenylyl cyclase catalytic core, *Nature* 386, 247-253.
104. Tesmer, J. J., Sunahara, R. K., Johnson, R. A., Gosselin, G., Gilman, A. G., and Sprang, S. R. (1999) Two-metal-ion catalysis in adenylyl cyclase, *Science* 285, 756-760.
105. Cooper, D. M. (2003) Regulation and organization of adenylyl cyclases and cAMP, *Biochem J* 375, 517-529.
106. Tang, W. J., and Hurley, J. H. (1998) Catalytic mechanism and regulation of mammalian adenylyl cyclases, *Mol Pharmacol* 54, 231-240.
107. Masada, N., Ciruela, A., Macdougall, D. A., and Cooper, D. M. (2009) Distinct mechanisms of regulation by  $\text{Ca}^{2+}$ /calmodulin of type 1 and 8 adenylyl cyclases support their different physiological roles, *J Biol Chem* 284, 4451-4463.
108. Vorherr, T., Knopfel, L., Hofmann, F., Mollner, S., Pfeuffer, T., and Carafoli, E. (1993) The calmodulin binding domain of nitric oxide synthase and adenylyl cyclase, *Biochemistry* 32, 6081-6088.
109. Levin, L. R., and Reed, R. R. (1995) Identification of functional domains of adenylyl cyclase using in vivo chimeras, *J Biol Chem* 270, 7573-7579.
110. Gu, C., and Cooper, D. M. (1999) Calmodulin-binding sites on adenylyl cyclase type VIII, *J Biol Chem* 274, 8012-8021.
111. Simpson, R. E., Ciruela, A., and Cooper, D. M. (2006) The role of calmodulin recruitment in  $\text{Ca}^{2+}$  stimulation of adenylyl cyclase type 8, *J Biol Chem* 281, 17379-17389.
112. Macdougall, D. A., Wachten, S., Ciruela, A., Sinz, A., and Cooper, D. M. (2009) Separate elements within a single IQ-like motif in adenylyl cyclase type 8 impart  $\text{Ca}^{2+}$ /calmodulin binding and autoinhibition, *J Biol Chem* 284, 15573-15588.

113. Fagan, K. A., Mahey, R., and Cooper, D. M. (1996) Functional co-localization of transfected Ca<sup>2+</sup>-stimulable adenylyl cyclases with capacitative Ca<sup>2+</sup> entry sites, *J Biol Chem* 271, 12438-12444.
114. Fagan, K. A., Mons, N., and Cooper, D. M. (1998) Dependence of the Ca<sup>2+</sup>-inhibitable adenylyl cyclase of C6-2B glioma cells on capacitative Ca<sup>2+</sup> entry, *J Biol Chem* 273, 9297-9305.
115. Prakriya, M., Feske, S., Gwack, Y., Srikanth, S., Rao, A., and Hogan, P. G. (2006) Orai1 is an essential pore subunit of the CRAC channel, *Nature* 443, 230-233.
116. Vig, M., Beck, A., Billingsley, J. M., Lis, A., Parvez, S., Peinelt, C., Koomoa, D. L., Soboloff, J., Gill, D. L., Fleig, A., Kinet, J. P., and Penner, R. (2006) CRACM1 multimers form the ion-selective pore of the CRAC channel, *Curr Biol* 16, 2073-2079.
117. Yeromin, A. V., Zhang, S. L., Jiang, W., Yu, Y., Safrina, O., and Cahalan, M. D. (2006) Molecular identification of the CRAC channel by altered ion selectivity in a mutant of Orai, *Nature* 443, 226-229.
118. Lewis, R. S., and Cahalan, M. D. (1989) Mitogen-induced oscillations of cytosolic Ca<sup>2+</sup> and transmembrane Ca<sup>2+</sup> current in human leukemic T cells, *Cell Regul* 1, 99-112.
119. Zweifach, A., and Lewis, R. S. (1993) Mitogen-regulated Ca<sup>2+</sup> current of T lymphocytes is activated by depletion of intracellular Ca<sup>2+</sup> stores, *Proc Natl Acad Sci U S A* 90, 6295-6299.
120. Lis, A., Peinelt, C., Beck, A., Parvez, S., Monteilh-Zoller, M., Fleig, A., and Penner, R. (2007) CRACM1, CRACM2, and CRACM3 are store-operated Ca<sup>2+</sup> channels with distinct functional properties, *Curr Biol* 17, 794-800.
121. Liou, J., Kim, M. L., Heo, W. D., Jones, J. T., Myers, J. W., Ferrell, J. E., Jr., and Meyer, T. (2005) STIM is a Ca<sup>2+</sup> sensor essential for Ca<sup>2+</sup>-store-depletion-triggered Ca<sup>2+</sup> influx, *Curr Biol* 15, 1235-1241.
122. Kawasaki, T., Lange, I., and Feske, S. (2009) A minimal regulatory domain in the C-terminus of STIM1 binds to and activates ORAI1 CRAC channels, *Biochem Biophys Res Commun* 385, 49-54.
123. Deng, X., Wang, Y., Zhou, Y., Soboloff, J., and Gill, D. L. (2009) STIM and Orai: dynamic intermembrane coupling to control cellular calcium signals, *J Biol Chem* 284, 22501-22505.
124. Martin, A. C., Willoughby, D., Ciruela, A., Ayling, L. J., Pagano, M., Wachten, S., Tengholm, A., and Cooper, D. M. (2009) Capacitative Ca<sup>2+</sup> entry via Orai1 and stromal interacting molecule 1 (STIM1) regulates adenylyl cyclase type 8, *Mol Pharmacol* 75, 830-842.
125. Willoughby, D., Everett, K. L., Halls, M. L., Pacheco, J., Skroblin, P., Vaca, L., Klussmann, E., and Cooper, D. M. (2012) Direct binding between Orai1 and AC8 mediates dynamic interplay between Ca<sup>2+</sup> and cAMP signaling, *Sci Signal* 5, ra29.
126. Lewis, R. S. (2007) The molecular choreography of a store-operated calcium channel, *Nature* 446, 284-287.
127. Spassova, M. A., Soboloff, J., He, L. P., Xu, W., Dziadek, M. A., and Gill, D. L. (2006) STIM1 has a plasma membrane role in the activation of store-operated Ca(2+) channels, *Proc Natl Acad Sci U S A* 103, 4040-4045.
128. Young, M. M., Tang, N., Hempel, J. C., Oshiro, C. M., Taylor, E. W., Kuntz, I. D., Gibson, B. W., and Dollinger, G. (2000) High throughput protein fold identification by using experimental constraints derived from intramolecular cross-links and mass spectrometry, *Proc Natl Acad Sci U S A* 97, 5802-5806.
129. Sinz, A. (2003) Chemical cross-linking and mass spectrometry for mapping three-dimensional structures of proteins and protein complexes, *J Mass Spectrom* 38, 1225-1237.

130. Fritzsche, R., Ihling, C. H., Götze, M., and Sinz, A. (2012) Optimizing the enrichment of cross-linked products for mass spectrometric protein analysis, *Rapid Commun Mass Spectrom* 26, 653-658.
131. Trester-Zedlitz, M., Kamada, K., Burley, S. K., Fenyo, D., Chait, B. T., and Muir, T. W. (2003) A modular cross-linking approach for exploring protein interactions, *J Am Chem Soc* 125, 2416-2425.
132. Sinz, A., Kalkhof, S., and Ihling, C. (2005) Mapping protein interfaces by a trifunctional cross-linker combined with MALDI-TOF and ESI-FTICR mass spectrometry, *J Am Soc Mass Spectrom* 16, 1921-1931.
133. Müller, D. R., Schindler, P., Towbin, H., Wirth, U., Voshol, H., Hoving, S., and Steinmetz, M. O. (2001) Isotope-tagged cross-linking reagents. A new tool in mass spectrometric protein interaction analysis, *Anal Chem* 73, 1927-1934.
134. Pearson, K. M., Pannell, L. K., and Fales, H. M. (2002) Intramolecular cross-linking experiments on cytochrome c and ribonuclease A using an isotope multiplet method, *Rapid Commun Mass Spectrom* 16, 149-159.
135. Taverner, T., Hall, N. E., O'Hair, R. A., and Simpson, R. J. (2002) Characterization of an antagonist interleukin-6 dimer by stable isotope labeling, cross-linking, and mass spectrometry, *J Biol Chem* 277, 46487-46492.
136. Back, J. W., Sanz, M. A., De Jong, L., De Koning, L. J., Nijtmans, L. G., De Koster, C. G., Grivell, L. A., Van Der Spek, H., and Muijsers, A. O. (2002) A structure for the yeast prohibitin complex: Structure prediction and evidence from chemical crosslinking and mass spectrometry, *Protein Sci* 11, 2471-2478.
137. Müller, M. Q., Dreiocker, F., Ihling, C. H., Schäfer, M., and Sinz, A. (2010) Cleavable cross-linker for protein structure analysis: reliable identification of cross-linking products by tandem MS, *Anal Chem* 82, 6958-6968.
138. Müller, M. Q., Ihling, C. H., and Sinz, A. (2013) Analyzing PPARalpha/ligand interactions by chemical cross-linking and high-resolution mass spectrometry, *Methods Mol Biol* 952, 287-299.
139. Hermanson, G. T. (2010) *Bioconjugate Techniques*, 2nd ed., Academic Press, London.
140. Kalkhof, S., and Sinz, A. (2008) Chances and pitfalls of chemical cross-linking with amine-reactive N-hydroxysuccinimide esters, *Anal Bioanal Chem* 392, 305-312.
141. Leavell, M. D., Novak, P., Behrens, C. R., Schoeniger, J. S., and Kruppa, G. H. (2004) Strategy for selective chemical cross-linking of tyrosine and lysine residues, *J Am Soc Mass Spectrom* 15, 1604-1611.
142. Madler, S., Bich, C., Touboul, D., and Zenobi, R. (2009) Chemical cross-linking with NHS esters: a systematic study on amino acid reactivities, *J Mass Spectrom* 44, 694-706.
143. Brunner, J. (1993) New photolabeling and crosslinking methods, *Annu Rev Biochem* 62, 483-514.
144. Dorman, G., and Prestwich, G. D. (1994) Benzophenone photophores in biochemistry, *Biochemistry* 33, 5661-5673.
145. Krauth, F., Ihling, C. H., Rüttinger, H. H., and Sinz, A. (2009) Heterobifunctional isotope-labeled amine-reactive photo-cross-linker for structural investigation of proteins by matrix-assisted laser desorption/ionization tandem time-of-flight and electrospray ionization LTQ-Orbitrap mass spectrometry, *Rapid Commun Mass Spectrom* 23, 2811-2818.
146. Wittelsberger, A., Thomas, B. E., Mierke, D. F., and Rosenblatt, M. (2006) Methionine acts as a "magnet" in photoaffinity crosslinking experiments, *FEBS Lett* 580, 1872-1876.
147. Hermanson, G. T. (1996) *Bioconjugate Techniques*, Academic Press, San Diego, CA.



148. Peri, S., Steen, H., and Pandey, A. (2001) GPMAW--a software tool for analyzing proteins and peptides, *Trends Biochem Sci* 26, 687-689.
149. Götze, M., Pettelkau, J., Schaks, S., Bosse, K., Ihling, C. H., Krauth, F., Fritzsche, R., Kühn, U., and Sinz, A. (2012) StavroX--a software for analyzing crosslinked products in protein interaction studies, *J Am Soc Mass Spectrom* 23, 76-87.
150. Roepstorff, P., and Fohlman, J. (1984) Proposal for a common nomenclature for sequence ions in mass spectra of peptides, *Biomed Mass Spectrom* 11, 601.
151. Schilling, B., Row, R. H., Gibson, B. W., Guo, X., and Young, M. M. (2003) MS2Assign, automated assignment and nomenclature of tandem mass spectra of chemically crosslinked peptides, *J. Am. Soc. Mass. Spectrom.* 14, 834-850.
152. Kalkhof, S., Haehn, S., Paulsson, M., Smyth, N., Meiler, J., and Sinz, A. (2010) Computational modeling of laminin N-terminal domains using sparse distance constraints from disulfide bonds and chemical cross-linking, *Proteins* 78, 3409-3427.
153. Suchanek, M., Radzikowska, A., and Thiele, C. (2005) Photo-leucine and photo-methionine allow identification of protein-protein interactions in living cells, *Nat Methods* 2, 261-267.
154. Chin, J. W., Martin, A. B., King, D. S., Wang, L., and Schultz, P. G. (2002) Addition of a photocrosslinking amino acid to the genetic code of Escherichiacoli, *Proc Natl Acad Sci U S A* 99, 11020-11024.
155. Young, T. S., Ahmad, I., Yin, J. A., and Schultz, P. G. (2010) An enhanced system for unnatural amino acid mutagenesis in E. coli, *J Mol Biol* 395, 361-374.
156. Xie, J., and Schultz, P. G. (2006) A chemical toolkit for proteins--an expanded genetic code, *Nat Rev Mol Cell Biol* 7, 775-782.
157. Karas, M., Bachmann, D., and Hillenkamp, F. (1985) Influence of the wavelength in high-irradiance ultraviolet laser desorption mass spectrometry of organic molecules, *Anal. Chem.* 57, 2935-2939.
158. Karas, M., Bachmann, D., Bahr, U., and Hillenkamp, F. (1987) Matrix-assisted ultraviolet laser desorption of non-volatile compounds, *Int. J. Mass Spectrom. Ion Processes* 78, 53-68.
159. Strupat, K., Karas, M., and Hillenkamp, F. (1991) 2,5-Dihydroxybenzoic acid: a new matrix for laser desorption--ionization mass spectrometry, *Int. J. Mass Spectrom. Ion Processes* 111, 89-102.
160. Zenobi, R., and Knochenmuss, R. (1998) Ion formation in MALDI mass spectrometry, *Mass Spectrom. Rev.* 17, 337-366.
161. Stephens, W. E. (1946) A Pulsed Mass Spectrometer with Time Dispersion, *Phys Rev* 69, 691.
162. Mamyrin, B. A., Karataev, V. I., Shmikk, D. V., and Zagulin, V. A. (1973) The mass-reflectron, a new nonmagnetic time-of-flight mass spectrometer with high resolution, *Sov. Phys. JETP* 37, 45.
163. Mamyrin, B. A. (1994) Laser assisted reflectron time-of-flight mass spectrometry, *Int. J. Mass Spectrom. Ion Processes* 131, 1-19.
164. Brown, R. S., and Lennon, J. J. (1995) Mass resolution improvement by incorporation of pulsed ion extraction in a matrix-assisted laser desorption/ionization linear time-of-flight mass spectrometer, *Anal Chem* 67, 1998-2003.
165. Whittal, R. M., and Li, L. (1995) High-resolution matrix-assisted laser desorption/ionization in a linear time-of-flight mass spectrometer, *Anal Chem* 67, 1950-1954.
166. Cotter, R. J. (1992) Time-of-flight mass spectrometry for the structural analysis of biological molecules, *Anal Chem* 64, 1027A-1039A.

167. Guilhaus, M. (1995) Special feature: Tutorial. Principles and instrumentation in time-of-flight mass spectrometry. Physical and instrumental concepts, *J. Mass Spectrom.* 30, 1519-1532.
168. Suckau, D., Resemann, A., Schuerenberg, M., Hufnagel, P., Franzen, J., and Holle, A. (2003) A novel MALDI LIFT-TOF/TOF mass spectrometer for proteomics, *Anal Bioanal Chem* 376, 952-965.
169. Horning, E. C., Horning, M. G., Carroll, D. I., Dzidic, I., and Stillwell, R. N. (1973) New picogram detection system based on a mass spectrometer with an external ionization source at atmospheric pressure, *Anal Chem* 45, 936-943.
170. Yamashita, M., and Fenn, J. B. (1984) Electrospray ion source. Another variation on the free-jet theme, *J Phys Chem* 88, 4451-4459.
171. Fenn, J. B., Mann, M., Meng, C. K., Wong, S. F., and Whitehouse, C. M. (1989) Electrospray ionization for mass spectrometry of large biomolecules, *Science* 246, 64-71.
172. Dole, M., Mack, L. L., Hines, R. L., Mobley, R. C., Ferguson, L. D., and Alice, M. B. (1968) Molecular Beams of Macroions, *J Chem Phys* 49, 2240-2249.
173. Taylor, G. (1964) Disintegration of Water Drops in an Electric Field, *Proc Royal Soc London A* 280, 383-397.
174. Rayleigh, L. (1982) On the Equilibrium of Liquid Conducting Masses Charged With Electricity, *London, Edinburgh, Dublin Phil Mag J Sci* 14, 184-186.
175. Kebarle, P., and Tang, L. (1993) From ions in solution to ions in the gas phase, *Anal. Chem.* 65, 972A-986A.
176. Konermann, L. (2009) A Simple Model for the Disintegration of Highly Charged Solvent Droplets during Electrospray Ionization, *J. Am. Soc. Mass. Spectrom.* 20, 496-506.
177. Winger, B. E., Light-Wahl, K. J., Ogorzalek Loo, R. R., Udseth, H. R., and Smith, R. D. (1993) Observation and implications of high mass-to-charge ratio ions from electrospray ionization mass spectrometry, *J. Am. Soc. Mass. Spectrom.* 4, 536-545.
178. Iribarne, J. V., and Thomson, B. A. (1976) On the evaporation of small ions from charged droplets, *J Chem Phys* 64, 2287-2294.
179. Thomson, B. A., and Iribarne, J. V. (1979) Field induced ion evaporation from liquid surfaces at atmospheric pressure, *J Chem Phys* 71, 4451-4463.
180. Loo, J. A., Edmonds, C. G., Udseth, H. R., and Smith, R. D. (1990) Effect of reducing disulfide-containing proteins on electrospray ionization mass spectra, *Anal. Chem.* 62, 693-698.
181. Wilm, M. S., and Mann, M. (1994) Electrospray and Taylor-Cone theory, Dole's beam of macromolecules at last?, *Int. J. Mass Spectrom. Ion Processes* 136, 167-180.
182. Wilm, M., and Mann, M. (1996) Analytical Properties of the Nanoelectrospray Ion Source, *Anal. Chem.* 68, 1-8.
183. Schwartz, J. C., Senko, M. W., and Syka, J. E. P. (2002) A two-dimensional quadrupole ion trap mass spectrometer, *J. Am. Soc. Mass. Spectrom.* 13, 659-669.
184. Douglas, D. J., Frank, A. J., and Mao, D. (2005) Linear ion traps in mass spectrometry, *Mass Spectrom. Rev.* 24, 1-29.
185. Schwartz, J. C., Zhou, X. G., and Bier, M. E. U.S. Patent 5,572,022.
186. Makarov, A., Denisov, E., Kholomeev, A., Balschun, W., Lange, O., Strupat, K., and Horning, S. (2006) Performance evaluation of a hybrid linear ion trap/orbitrap mass spectrometer, *Anal Chem* 78, 2113-2120.
187. Cooks, R. G. (1995) Special feature: Historical. Collision-induced dissociation: Readings and commentary, *J. Mass Spectrom.* 30, 1215-1221.
188. Kingdon, K. H. (1923) A Method for the Neutralization of Electron Space Charge by Positive Ionization at Very Low Gas Pressures, *Phys. Rev.* 21, 408-418.

189. Makarov, A. (1999) U.S. Patent 5, 5,886,346.
190. Makarov, A. (2000) Electrostatic Axially Harmonic Orbital Trapping: A High-Performance Technique of Mass Analysis, *Anal. Chem.* **72**, 1156-1162.
191. Hu, Q., Noll, R. J., Li, H., Makarov, A., Hardman, M., and Graham Cooks, R. (2005) The Orbitrap: a new mass spectrometer, *J. Mass Spectrom.* **40**, 430-443.
192. Correa, D. H. A., and Ramos, C. H. I. (2009) The use of circular dichroism spectroscopy to study protein folding, form and function, *African J. Biochem. Res.* **3**, 164-173.
193. Greenfield, N., and Fasman, G. D. (1969) Computed circular dichroism spectra for the evaluation of protein conformation, *Biochemistry* **8**, 4108-4116.
194. Fandrich, M., and Dobson, C. M. (2002) The behaviour of polyamino acids reveals an inverse side chain effect in amyloid structure formation, *EMBO J* **21**, 5682-5690.
195. Greff, D., Toma, F., Fermandjian, S., Low, M., and Kisfaludy, L. (1976) Conformational studies of corticotropin1-32 and constitutive peptides by circular dichroism, *Biochim Biophys Acta* **439**, 219-231.
196. Llinas, M., and Klein, M. P. (1975) Solution conformation of the ferrichromes. VI. Charge relay at the peptide bond. Proton magnetic resonance study of solvation effects on the amide electron density distribution, *J. Am. Chem. Soc.* **97**, 4731-4737.
197. Nelson, J. W., and Kallenbach, N. R. (1986) Stabilization of the ribonuclease S-peptide alpha-helix by trifluoroethanol, *Proteins* **1**, 211-217.
198. Christensen, J. J., Izatt, R. M., and Hansen, L. D. (1965) New Precision Thermometric Titration Calorimeter, *Review of Scientific Instruments* **36**, 779-783.
199. Beaudette, N. V., and Langerman, N. (1980) The thermodynamics of nucleotide binding to proteins, *CRC Crit Rev Biochem* **9**, 145-170.
200. Perozzo, R., Folkers, G., and Scapozza, L. (2004) Thermodynamics of protein-ligand interactions: history, presence, and future aspects, *J Recept Signal Transduct Res* **24**, 1-52.
201. Freyer, M. W., and Lewis, E. A. (2008) Isothermal titration calorimetry: experimental design, data analysis, and probing macromolecule/ligand binding and kinetic interactions, *Methods Cell Biol* **84**, 79-113.
202. Ladbury, J. E., Klebe, G., and Freire, E. (2010) Adding calorimetric data to decision making in lead discovery: a hot tip, *Nat Rev Drug Discov* **9**, 23-27.
203. Zhou, X., Sun, Q., Kini, R. M., and Sivaraman, J. (2008) A universal method for fishing target proteins from mixtures of biomolecules using isothermal titration calorimetry, *Protein Sci* **17**, 1798-1804.
204. Nunez, S., Venhorst, J., and Kruse, C. G. (2012) Target-drug interactions: first principles and their application to drug discovery, *Drug Discov Today* **17**, 10-22.
205. Ince, R., and Narayanaswamy, R. (2006) Analysis of the performance of interferometry, surface plasmon resonance and luminescence as biosensors and chemosensors, *Anal. Chim. Acta* **569**, 1-20.
206. Katsamba, P. S., Navratilova, I., Calderon-Cacia, M., Fan, L., Thornton, K., Zhu, M., Bos, T. V., Forte, C., Friend, D., Laird-Offringa, I., Tavares, G., Whatley, J., Shi, E., Widom, A., Lindquist, K. C., Klakamp, S., Drake, A., Bohmann, D., Roell, M., Rose, L., Dorocke, J., Roth, B., Luginbuhl, B., and Myszka, D. G. (2006) Kinetic analysis of a high-affinity antibody/antigen interaction performed by multiple Biacore users, *Anal Biochem* **352**, 208-221.
207. Cooper, M. A. (2002) Optical biosensors in drug discovery, *Nat Rev Drug Discov* **1**, 515-528.
208. Sorkin, A., McClure, M., Huang, F., and Carter, R. (2000) Interaction of EGF receptor and grb2 in living cells visualized by fluorescence resonance energy transfer (FRET) microscopy, *Curr Biol* **10**, 1395-1398.

209. Sambrook, J., and Russell, D. W., (Eds.) (2001) *Molecular cloning: A laboratory manual.*, 3rd ed., NY.
210. Neuhoff, V., Arold, N., Taube, D., and Ehrhardt, W. (1988) Improved staining of proteins in polyacrylamide gels including isoelectric focusing gels with clear background at nanogram sensitivity using Coomassie Brilliant Blue G-250 and R-250, *Electrophoresis* 9, 255-262.
211. de Koning, L. J., Kasper, P. T., Back, J. W., Nessen, M. A., Vanrobaeys, F., Van Beeumen, J., Gherardi, E., de Koster, C. G., and de Jong, L. (2006) Computer-assisted mass spectrometric analysis of naturally occurring and artificially introduced cross-links in proteins and protein complexes, *FEBS J* 273, 281-291.
212. Maupetit, J., Derreumaux, P., and Tuffery, P. (2010) A fast method for large-scale de novo peptide and miniprotein structure prediction, *J Comput Chem* 31, 726-738.
213. Meiler, J., Müller, M., Zeidler, A., and Schmäschke, F. (2001) Generation and evaluation of dimension-reduced amino acid parameter representations by artificial neural networks, *J Mol Model* 7, 360-369.
214. McGuffin, L. J., Bryson, K., and Jones, D. T. (2000) The PSIPRED protein structure prediction server, *Bioinformatics* 16, 404-405.
215. Duhovny, D., Nussinov, R., and Wolfson, H. J. (2002) *Efficient Unbound Docking of Rigid Molecules*, Springer, Berlin.
216. Lyskov, S., and Gray, J. J. (2008) The RosettaDock server for local protein-protein docking, *Nucleic Acids Res* 36, W233-238.
217. Dimova, K. (2009) Characterization of the Munc13-Calmodulin Interaction (PhD Thesis), In *Faculty of Biology*, Georg August University, Göttingen.
218. Chang, J. Y. (1985) Thrombin specificity. Requirement for apolar amino acids adjacent to the thrombin cleavage site of polypeptide substrate, *Eur J Biochem* 151, 217-224.
219. Worms, C. S. (2012) Expression und Reinigung von Munc13-Varianten als GST-Fusionsproteine (Bachelor Thesis Biochemistry), In *Institute of Pharmacy*, Martin-Luther University, Halle-Saale.
220. Maucher, D. (2011) Interaktionsstudien zwischen Calmodulin und skeletaler Myosin leichte-Ketten-Kinase (skMLCK) mit chemischem Cross-Linking und Massenspektrometrie (Bachelor Thesis Biochemistry), In *Institut of Pharmacy*, Martin-Luther-University Halle-Wittenberg, Halle.
221. Chagot, B., and Chazin, W. J. (2011) Solution NMR Structure of Apo-Calmodulin in Complex with the IQ Motif of Human Cardiac Sodium Channel NaV1.5, *Journal of Molecular Biology* 406, 106-119.
222. Masada, N., Schaks, S., Jackson, S. E., Sinz, A., and Cooper, D. M. (2012) Distinct mechanisms of calmodulin binding and regulation of adenylyl cyclases 1 and 8, *Biochemistry* 51, 7917-7929.
223. Li, Z., Lu, J., Xu, P., Xie, X., Chen, L., and Xu, T. (2007) Mapping the interacting domains of STIM1 and Orai1 in Ca<sup>2+</sup> release-activated Ca<sup>2+</sup> channel activation, *J Biol Chem* 282, 29448-29456.
224. Willoughby, D., Masada, N., Wachten, S., Pagano, M., Halls, M. L., Everett, K. L., Ciruela, A., and Cooper, D. M. (2010) AKAP79/150 interacts with AC8 and regulates Ca<sup>2+</sup>-dependent cAMP synthesis in pancreatic and neuronal systems, *J Biol Chem* 285, 20328-20342.
225. Cutler, P. (2004) *Protein Purification Protocols*, 2nd ed., Humana Press.

## ACKNOWLEDGEMENT

Ich möchte mich bei Prof. Andrea Sinz für die Möglichkeit bedanken, im Rahmen des Graduiertenkollegs 1026 in ihrer Arbeitsgruppe promovieren zu können, und vor allem dafür, dass sie sich für Fragen und Diskussionen immer Zeit genommen hat.

Dr. Christian Ihling danke ich für die praktische Einführung in die Massenspektrometrie und viele hilfreiche Tipps zu meinen Experimenten. Auch Knut Kölbel danke ich für die Hilfe im Labor und bei den CD-Messungen.

Bei der gesamten Arbeitsgruppe möchte ich mich für eine angenehme, sehr lustige Atmosphäre bedanken (auch während der Stunden außerhalb der Arbeit), aber auch für hilfreiche und kritische Diskussionen, die meine Arbeit immer wieder bereichern konnten.

Dr. Stefan Kalkhof danke ich für die Durchführung des Modelings der CaM/Munc13-Peptidkomplexe und für viele weitere ausführliche Erklärungen und Diskussion rund um die CaM/Munc13-Interaktion.

Marian Schneider und der Arbeitsgruppe von Dr. Sven Pfeifer danke ich sehr für die vielen investierten Stunden zur Bestimmung der CaM-Affinität der skMLCK-Peptide mittels SPR.

Dr. Olaf Jahn möchte ich für die Synthese der Munc13- und skMLCK-Peptide danken und für seine stetige Diskussionsbereitschaft per Telefon oder E-Mail, aber auch bei unseren Treffen.

Dr. Kalina Dimova und Dr. Noa Lipstein danke ich für die Bereitstellung verschiedener Munc13-Konstrukte.

Ich bedanke mich bei Caroline Worms für die Mitarbeit an der Klonierung und Expression von GST-Munc13-1 und GST-ubMunc13-2 sowie bei Daniel Maucher für die Durchführung und Auswertung der BS<sup>2</sup>G-Cross-linking-Experimente zwischen CaM und skMLCK im Rahmen einer Bachelorarbeit.

Auch allen Wahlpflichtstudenten und Praktikantinnen, die an der Expression der Munc13-Domänen mitgearbeitet haben, möchte ich danken.

## Acknowledgement

---

Bei den Arbeitsgruppen von Prof. Milton Stubbs und Prof. Elisabeth Schwarz möchte ich mich für die Möglichkeit bedanken, ITC (zusammen mit Sabrina Pfennig) und CD messen zu können, aber auch für die geduldige Beantwortung meiner Fragen.

Den Mitgliedern des Graduiertenkollegs 1026, vor allem PD Dr. Ralph Golbik, Prof. Gary Sawers, PD Dr. Hauke Lilie, Sabrina Pfennig, Claudia Simon, Marian Schneider, Johannes Taubert und Tobias Schmidt, danke ich für die Kooperationen und zahlreiche Hilfestellungen verschiedenster Art.

Prof. Dermot Cooper und seiner Arbeitsgruppe danke ich für die herzliche Aufnahme in die Gruppe während meines Aufenthaltes in Cambridge, ich habe viel gelernt (vor allem von Debby und Katy) und habe mich sehr wohl gefühlt.

Vielen Dank an Silke Kuhfahl, Sabrina Pfennig und meinen Mann für die Korrektur dieser Arbeit und die vielseitige Hilfe während meiner ganzen Promotion.

Meinen Freunden, meiner Familie und meinem Mann danke ich für viel Geduld, viele schöne Stunden und die riesige Unterstützung, ohne euch wäre das alles nicht möglich gewesen!

## PUBLICATIONS

### Publications in peer-reviewed journals:

Götze M, Pettelkau J, Schaks S, Bosse K, Ihling CH, Krauth F, Fritzsche R, Kühn U, Sinz A. **StavroX--a software for analyzing crosslinked products in protein interaction studies.** *J Am Soc Mass Spectrom.* **2012** 23 (1), 76-87

Lipstein N\*, Schaks S\*, Dimova K\*, Kalkhof S, Ihling C, Kölbel K, Ashery U, Rhee J, Brose N, Sinz A, Jahn O. **Non-conserved Ca<sup>2+</sup>/calmodulin binding sites in Munc13s differentially control synaptic short-term plasticity.** *Mol Cell Biol.* **2012** 32 (22):4628-41

\*Authors contributed equally

Masada N, Schaks S, Jackson SE, Sinz A, Cooper DM. **Distinct mechanisms of calmodulin binding and regulation of adenylyl cyclases 1 and 8.** *Biochemistry.* **2012** 9; 51(40), 7917-29

Herbst S, Maucher D, Schneider M, Ihling CH, Jahn O, and Sinz A. **Munc13 Exhibits a Unique Calmodulin Binding Mode as Evidenced by Chemical Cross-Linking and Mass Spectrometry.** *PLOS ONE*, *in press*.

Herbst S, Masada N, Pfennig S, Ihling CH, Cooper DMF, and Sinz A. **Structural Insights into Calmodulin / Adenylyl Cyclase 8 Interaction.** *Analytical and Bioanalytical Chemistry*, *in press*.

Simon C, Klose T, Herbst S, Han BG, Sinz A, Glaeser RM, Stubbs MT, and Lilie H. **Disulfide linkage and structure of highly stable yeast-derived virus-like particles of murine polyomavirus.** *submitted to J Biol. Chem.*

### Publication in a journal without peer-review:

Schaks S, Kalkhof S, Krauth F, Jahn O, Sinz A. **Chemisches Cross-Linking und MS zur Untersuchung von Proteinkomplexen.** *Biospektrum* **2011** 5, 524-527

### Book Chapter

Schaks S, Maucher D, Ihling C, and Sinz A. **Investigation of a Calmodulin/Peptide Complex by Chemical Cross-Linking and High-Resolution Mass Spectrometry.** *Biomacromolecular Mass Spectrometry*, König, S (ed.), Nova Science Publishers, **2012** (ISSN: 1936-444X)

### Oral Presentations:

Investigation of Calmodulin/Munc13 Interaction. *Fall Meeting GRK 1026, Dessau 2009*

## Publications

---

Structural Insights into Calmodulin/Munc13 Interaction. *Spring Meeting GRK 1026, Halle 2010*

A Closer Look into the Interaction Site Between CaM and Munc13 Proteins. *Fall Meeting GRK 1026, Blankenburg 2010*

A closer look into the interaction site between CaM and Munc13 proteins. *International Meeting GRK 1026, Halle 2011*

A closer look into the interaction site between CaM and Munc13 proteins. *Jahrestagung der Deutschen Gesellschaft für Massenspektrometrie (DGMS) 2011, Dortmund*

A closer look into the interaction site between CaM and Munc13 proteins. *5th Mass Spectrometry in Biotechnology & Medicine Summer School, Dubrovnik 2011*

Further insights into CaM/target interactions. *Fall Meeting GRK 1026, Leuna 2011*

Further Insights Into CaM/Target Interactions - The best things come in threes. *Spring Meeting GRK 1026, Eisenach 2012*

Untersuchung von CaM/Munc13-Komplexen mittels chemischer Quervernetzung und hochauflösender Massenspektrometrie. *19. Arbeitstagung Micromethods in Protein Chemistry, Bochum 2012*

Non-conserved Ca<sup>2+</sup>/calmodulin binding sites in Munc13s differentially control synaptic short-term plasticity. *Fall Meeting GRK 1026, Naumburg 2012*

### Poster:

**S. Schaks, F. Krauth, M. Q. Müller, C. Ihling, O. Jahn, and A. Sinz. Investigation of Calmodulin/Munc13 Peptide Interaction by Chemical Cross-Linking, MALDI-TOF/TOF-MS and ESI-LTQ-Orbitrap-MS.** *Jahrestagung der Deutschen Gesellschaft für Massenspektrometrie (DGMS) 2010, Halle*

**S. Schaks, F. Krauth, M. Q. Müller, C. Ihling, O. Jahn, and A. Sinz. Investigation of Calmodulin/Munc13 Peptide Interaction by Chemical Cross-Linking, MALDI-TOF/TOF-MS and ESI-LTQ-Orbitrap-MS.** *5th Mass Spectrometry in Biotechnology & Medicine Summer school, Dubrovnik 2011*

**S. Schaks, D. Maucher, C. Ihling, O. Jahn, and A. Sinz. Investigation of Calmodulin/Peptide Complexes by Chemical Cross-Linking and LTQ-Orbitrap-MS.** *Joint Conference of German Mass Spectrometry Society (DGMS) and Polish Mass Spectrometry Society 2012, Poznań, Poland*

**S. Schaks, D. Maucher, C. Ihling, O. Jahn, and A. Sinz. Investigation of Calmodulin/Peptide Complexes by Chemical Cross-Linking and LTQ-Orbitrap-MS.** *Horizons in Molecular Biology 2012, Göttingen*



S. Schaks, D. Maucher, C. Ihling, O. Jahn, and A. Sinz. **Investigation of Calmodulin/Peptide Complexes by Chemical Cross-Linking and LTQ-Orbitrap-MS.** *Jahrestagung der Deutschen Gesellschaft für Massenspektrometrie (DGMS) 2013, Berlin*

# Selbständigkeitserklärung

Ich versichere hiermit, die vorliegende Dissertation selbständig und ohne unerlaubte fremde Hilfe angefertigt zu haben. Ich habe keine anderen als die im Literaturverzeichnis angeführten Quellen genutzt und sämtliche Textstellen, die wörtlich oder sinngemäß aus veröffentlichten oder unveröffentlichten Schriften entnommen wurden, und alle Angaben, die auf mündlichen Auskünften beruhen, als solche kenntlich gemacht. Ebenfalls sind alle von anderen Personen bereitgestellten Materialien oder erbrachten Dienstleistungen als solche gekennzeichnet. Bei der Auswahl und Auswertung des Materials, bei der Herstellung des Manuskripts, sowie bei der geistigen Herstellung der vorgelegten Arbeit waren keine anderen Personen beteiligt. Insbesondere wurde weder die Hilfe eines Promotionsberaters in Anspruch genommen, noch haben Dritte von mir unmittelbar oder mittelbar geldwerte Leistungen für Arbeiten erhalten, die im Zusammenhang mit dem Inhalt der vorgelegten Dissertation stehen. Die vorgelegte Arbeit ist weder im Inland noch im Ausland in gleicher oder ähnlicher Form einer anderen Prüfungsbehörde zum Zweck einer Promotion oder eines anderen Prüfungsverfahrens vorgelegt worden. Ich habe keine früheren erfolglosen Promotionsversuche unternommen.

Halle (Saale), den 26.09.2013

Sabine Herbst

# LEBENS LAUF

## Persönliche Daten

geboren am 10.06.1984 in Merseburg  
verheiratet (geb. Schaks), keine Kinder  
Staatsangehörigkeit: deutsch

## Schul Ausbildung

09/1991 – 07/1995      Grundschule Schafstädt  
09/1995 – 07/2004      J.-G.-Herder-Gymnasium in Merseburg  
Abschluss: Abitur (Gesamtnote: 1,7)

## Hochschulausbildung

10/2004                      Studium Biochemie/Diplom an der  
Martin-Luther-Universität Halle-Wittenberg  
Vertiefungsrichtung: Protein- u. Enzymchemie  
10/2008 – 08/2009      Anfertigung der Diplomarbeit (Arbeitsgruppe Prof. Elmar  
Wahle) zum Thema: Analyse der Interaktion zwischen der  
Poly(A)-Polymerase und PABPN1  
08/2009                      Abschluss: Diplom Biochemikerin (Prädikat *sehr gut*)

## Promotion

seit 06/2013                Wissenschaftlicher Mitarbeiter am Institut für Pharmazie der  
Martin-Luther-Universität Halle-Wittenberg (Arbeitsgruppe  
Prof. Thomas Groth)  
09/2009 – 05/2013      Wissenschaftlicher Mitarbeiter am Institut für Pharmazie der  
Martin-Luther-Universität Halle-Wittenberg (Arbeitsgruppe  
Prof. Andrea Sinz)  
Thema: Investigation of Calmodulin/Target Interactions by  
Mass Spectrometry  
03/2011 – 06/2011      Auslandsaufenthalt in der Arbeitsgruppe von  
Prof. Dermot Cooper, Department of Pharmacology, University  
of Cambridge (UK)